TECHNISCHE UNIVERSITÄT WIEN
Vienna University of Technology

DISSERTATION

RELIABILITY OF SILVER SINTERED LARGE AREA JOINTS: TEMPERATURE DEPENDENT MECHANICAL PROPERTIES UNDER STATIC AND CYCLIC LOADING

carried out for the purpose of obtaining the degree of Dr. techn.

under the supervision of

Associate Prof. Mag.a rer.nat. Dr.in techn. Golta KHATIBI DAMAVANDI

and

Mag. Dr. rer.nat Martin LEDERER

submitted at

Institute of Chemical Technologies and Analytics

Faculty of Technical Chemistry, TU Wien

by

Dipl. Ing. Zeynep Gökçe GÖKDENİZ

Mat.Nr.: 00026261

Vienna, October 2022 _____

THIS THESIS IS ACCOMPLISHED WITHIN THE FRAMEWORK OF CHRISTIAN DOPPLER LABORATORY FOR LIFETIME AND RELIABILITY OF INTERFACES IN COMPLEX MULTI-MATERIAL ELECTRONICS

To my grandmother: C.Sevim, Selam.

KURZFASSUNG

In der Leistungselektronik werden seit Jahrzehnten bleihaltige Lote als Verbindungsmaterial verwendet. Die Erhöhung der Packungsdichte bei immer geringerer Chipgröße hat jedoch zu steigenden Anforderungen an das Wärmemanagement geführt. Bei erhöhter Betriebstemperatur können Unterschiede von Wärmeausdehnungskoeffizienten hohe Spannungen in benachbarten Bauteilen verursachen. Daher führen plastische Verformung und Kriechen zu einer ernsthaften Beeinträchtigung der Zuverlässigkeit von Materialverbindungen bzw. der eingeschränkten Produktlebensdauer.

Silbersintern ist eine mit Kupfer verträgliche, bleifreie Alternative hinsichtlich der Verbindungstechnik für Module der Leistungselektronik. Silber hat nicht nur eine hohe elektrische und thermische Leitfähigkeit, sondern auch eine hohe Schmelztemperatur (ca. 960 °C) und ist deshalb ein vielversprechendes Material für Anwendungen bei erhöhter Temperatur. Obwohl die grundlegenden Eigenschaften von Sintermaterialien wie Kupfer und Silber gut bekannt sind, ist es erforderlich Prozessparameter an Materialien und deren Geometrie anzupassen, um die Lebensdauererwartung der Verbindungen zu steigern.

In dieser Arbeit wurden charakteristische Eigenschaften wie Dichte, elektrischer Widerstand, Zug- und Scherfestigkeit von gesintertem Silber analysiert, wobei der Einfluss der Porosität der Struktur zu berücksichtigen war. Die Porosität hängt ihrerseits von der Herstellungsmethode und den Sinterbedingungen (Druck, Temperatur und Zeit) ab. Für die Untersuchungen wurden hauptsächlich zwei Arten von Proben produziert: gesintertes Ag als freistehende Streifenschicht, sowie als Cu-Ag-Cu Überlappungsverbindung. Weiters wurden definierte Serien der Probenarten hergestellt. Die thermomechanischen Eigenschaften, die Lebensdauer und das Verhalten der Spannungsrelaxation von Kupferverbindungen wurden bei verschiedenen Testtemperaturen untersucht.

Im Vergleich zu den frisch gesinterten, sogenannten 0-Stunden Proben, wurden einige Probenserien vor der Prüfung 250-Stunden bei 250 °C wärmebehandelt, entweder an Luft oder in einem versiegelten Glasschutz mit reduzierter Sauerstoffzufuhr. Die dadurch bewirkte Mikrostruktur wurde untersucht. In Gegenwart von Sauerstoff wurde ein Wachstum der Korngröße des gesinterten Silbers beobachtet, und im Fall der Cu-Ag-Cu Überlappungsverbindungen trat eine Kupferoxidbildung auf.

Das Elastizitätsmodul von ohne Wärmebehandlung hergestellten, hantelförmigen Ag-Proben wurde mit einem Laser-Speckle-Extensometer bestimmt, welches eine kontaktlose Dehnungsmessung ermöglichte. Zusammenfassend kann gesagt werden, dass Proben, die 250-Stunden bei 250 °C gealtert wurden, ein niedrigeres Elastizitätsmodul aufweisen als die nicht wärmebehandelten Proben. Außerdem wurde bei der höheren Prüftemperatur von 200 °C eine Abnahme des E-Moduls beobachtet.

Für die Dichtemessung des porösen Silbers wurden zwei Methoden verwendet: die Masse/Volumen-Methode und die optische Methode der digitalen Bildverarbeitung. Für die

Charakterisierung wurden die Proben entweder in flüssigem Stickstoff gebrochen oder bereits bei den Tests gebrochene Proben untersucht, eventuell in Harz eingebettet und geschliffen. Ein lokaler Schnitt mit fokussiertem Ionenstrahl (FIB) ermöglichte den Einblick in die poröse Struktur der Ag-Schicht unter der Oberfläche. Mit dieser optischen Methode wurde aber keine signifikante Dichteänderung durch Wärmebehandlung bei 250°C festgestellt.
Im Vergleich dazu wurden mit der Masse/Volumen-Methode im Allgemeinen niedrigere Dichtewerte gemessen. Bei den drucklos gesinterten Proben wurde nach 250-stündiger Alterung bei 250 °C eine Veränderung der Porosität beobachtet, die Proben wurden dichter.

Die elektrischen Messungen lieferten mit zunehmender Porosität einen zunehmenden spezifischen Widerstand, und mit zunehmender Prüftemperatur (200 °C) wurde erwartungsgemäß ein Anstieg des spezifischen elektrischen Widerstands beobachtet.

Die mittlere Zugfestigkeit von hantelförmigen Proben aus gesintertem Silber, sowie die mittlere Scherfestigkeit der Cu-Ag-Cu Verbindungen zeigten im Allgemeinen eine Abnahme für Testtemperaturen von 130 °C und 200 °C, im Vergleich zu 25 °C. Mit steigender Temperatur ändert sich das Sprödbruchverhalten tiefer Temperaturen in ein duktiles Verhalten.

Die mechanisch-zyklische Lebensdauer wurde für Verbindungen der Cu-Ag-Cu Proben verschiedener Sinterparameter bestimmt. Schließlich wurden solche Proben für die weiterführende Prüfung ausgewählt, bei denen zuerst das Kupfersubstrat mit einer dünnen Ag-Schicht vorbesputtert wurde. Danach wurden Schablonen mit Ag-Paste bedruckt und schließlich unter Druck gesintert. Das zyklische Ermüdungsverhalten dieser Proben bei Raumtemperatur und bei erhöhten Temperaturen wurde verglichen, wobei Proben mit und ohne 250-Stunden Alterung unterschieden wurden. Die Anzahl N_f der Zyklen bis zum Versagen wurde mit Weibull-Wahrscheinlichkeitsdiagrammen analysiert. Im Allgemeinen wurde bei hohen Temperaturen eine reduzierte Lebensdauer beobachtet. Eine Wärmebehandlung vor der mechanischen Prüfung verbesserte jedoch die zyklische Lebensdauer der Cu-Ag-Cu Verbindungen erheblich.

Die Kriecheigenschaft der drucklos und druckunterstützt gesinterten Proben wurde untersucht, indem die Proben auf ein definiertes Spannungsniveau gedehnt wurden, woraufhin der Abfall der Spannung über eine Stunde beobachtet wurde. Dabei wurde das Spannungsniveau jeweils nach der mittleren Endfestigkeit der Probenserie festgelegt. Diese Tests wurden bei 25 °C, 130 °C und 200 °C durchgeführt.

Die Ergebnisse der durchgeführten Tests und Analysen konnten durch die Parameter eines theoretischen Materialmodells angepasst werden, welches auf einer Kombination aus Norton-Kriechen und Gurson-Plastizität basiert. Die konstitutiven Gleichungen des Modells beschreiben die Kriecheigenschaften von gesintertem Silber in Abhängigkeit von seiner Porosität. Dabei wurde die Temperaturabhängigkeit durch einen Arrhenius-Term mit Aktivierungsenergie Q beschrieben. Das Materialmodell wurde in der kommerziellen Software ABAQUS durch das Benutzerunterprogramm UMAT implementiert und kann nun für die Zuverlässigkeitsbewertung von Ag-gesinterten Kupferverbindungen eingesetzt werden.

ABSTRACT

In power electronics Pb-containing solders have been used over decades as bonding material. However, increase of packaging density at lower chip weight and size has led to increasing requirements regarding thermal management during operation. Especially at elevated operation temperature, the mismatch of the coefficients of thermal expansion can cause high stresses in constrained materials, and therefore plastic deformation and creep failure become a serious issue of joint reliability.

Silver sintering is a copper compatible and lead-free alternative interconnection technology for power modules. In addition to high electrical and thermal conductivity, silver has a high melting point (960 °C) in comparison to conventional solder alloys. Hence, silver is a promising material for applications at elevated temperature. Although the basic characteristics of sintering materials such as copper and silver are well understood, adjustments of process parameters, material combinations and geometry are required to enhance lifetime expectations based on reliability prognosis of the interconnects.

In this work, characteristic features such as density, electrical resistivity, tensile and shear strength of sintered Ag were analyzed, which are influenced by the porous structure arising in consequence of sample preparation and sintering conditions (pressure, temperature, and time). Two main types of samples were produced: either as sintered Ag-film or as Cu-Ag-Cu lap joint. Further, series of pressureless and pressure-assisted sintered specimen were defined. The thermo-mechanical properties, fatigue lifetime and stress relaxation behaviour of copper joints were investigated at various testing temperatures.

In comparison to the as-sintered, so-called 0-hour samples, some sample series were heat treated for 250 hours at 250 °C prior to testing, either in air or in sealed glass protection with restricted oxygen content. The correlating microstructure was investigated. In the presence of oxygen, a growth in the grain size of the sintered silver was observed, and in case of the Cu-Ag-Cu lap-joints, copper-oxide formation occurred.

The Young's modulus of the dumbbell shaped samples prepared without the heat treatment was measured by a setup including a laser speckle extensometer, which enabled contactless strain measurement of the sintered silver. In conclusion, samples aged for 250 hours at elevated temperature showed a reduced elastic modulus compared to samples, which were not heat treated. A decrease of the Young's modulus was also observed for the elevated test temperature of 200 °C.

For the density measurement of the porous silver two methods were used: the mass/volume method and the optical method of digital image processing. For the latter, to reveal the cross-sectional surface, the samples were either fractured (also in liquid nitrogen) or embedded in resin

and grinded. A local cut with focused ion beam (FIB) enabled the insight into the porous structure below the surface showing pitch holes of the Ag-layer. With this optical method, no significant change in density arising from heat treatment at 250°C could be measured.
In comparison, in general lower density values were measured with use of the mass/volume method. For the pressureless sintered specimens, after ageing at 250 °C for 250 hours, a change in the porosities was observed, the samples got denser.

The electrical measurements delivered increasing resistivity with increasing porosity, and with increasing testing temperature (200 °C), an increase of the electrical resistivity was observed, as expected.

The mean ultimate tensile strength of dumbbell shaped specimens of sintered silver as well as the mean shear strength of the copper lap-joints showed in general a decrease for testing temperatures of 130 °C and 200 °C, compared to 25 °C. With the increase of temperature, the brittle fracture characteristics of low temperatures changed into a ductile behavior.

The mechanical cyclic lifetime was determined for various specimen of the Cu-Ag-Cu lap-joints sintered under different parameters. Finally, the samples of which the copper substrate was pre-sputtered with a thin Ag-layer, then stencil printed with Ag-paste and sintered under pressure were selected for the main test series. The behaviour of cyclic fatigue of these samples at room and elevated temperatures were compared for the 0-hour and 250-hours aged types. The number of cycles to failure N_f were analyzed with Weibull probability plots. In general, the cyclic fatigue life was significantly reduced, when samples were tested at high temperature. However, heat treatment prior to mechanical testing improved the cyclic lifetime of the lap-joints significantly.

The creep properties of the pressureless and pressure assisted sintered specimens were examined with experiments, where samples were stretched to a defined stress level, depending on the ultimate strength of the specimens, and the relaxation was observed over one hour. Tests were carried out at 25 °C, 130 °C and 200 °C.

The results of the performed tests and analyses could be fitted by the parameters of a theoretical material model based on a combination of Norton creep and Gurson plasticity. The constitutive equations of the model describe the creep properties of sintered silver in dependence of its porosity. Thereby, the temperature dependence was described by an Arrhenius term using the activation energy Q. The material model was implemented in the commercial software of ABAQUS through user subroutine UMAT and can now be used as helpful tool for reliability assessment of Ag-sintered copper joints.

TABLE of CONTENTS

CHAPTER 1

INTRODUCTION and MOTIVATION

A lot happened in the 20th century, also in the field of science. New technologies based on electricity were developed such as the incandescent light bulb, thermionic vacuum-tube diodes, transistors, and integrated circuits, leading to a huge evolution of semiconductor devices in the first quarter of the 21st century. Probably one of the famous pictures is the one of three researches (Fig.1.1.a) awarded with the Nobel prize in 1956 for their discovery of the transistor effect in 1947. Please note the solder joints, on the realistic sized replica of ca. 4 cm, connecting the wires in Fig.1.1.b. Flash forwarding to the present day, a processor from Intel, the Penryn, has on a die of the size of 107 mm^2, less than the area of a cent, 410 million transistors for each dual-core chip. A wafer with several chips is shown in Fig.1.2. The typical operating temperature for the processor of this kind is ca. 105 °C. With this vast concentration of electronic elements on smaller area, also the interconnection technology of the modules faces new challenges. The probability that the interconnect, e.g. die attach or solder joint, of a particular package in a product performing its intended function for a specified period of time under a given operating condition without failure is considered by reliability engineering [11].

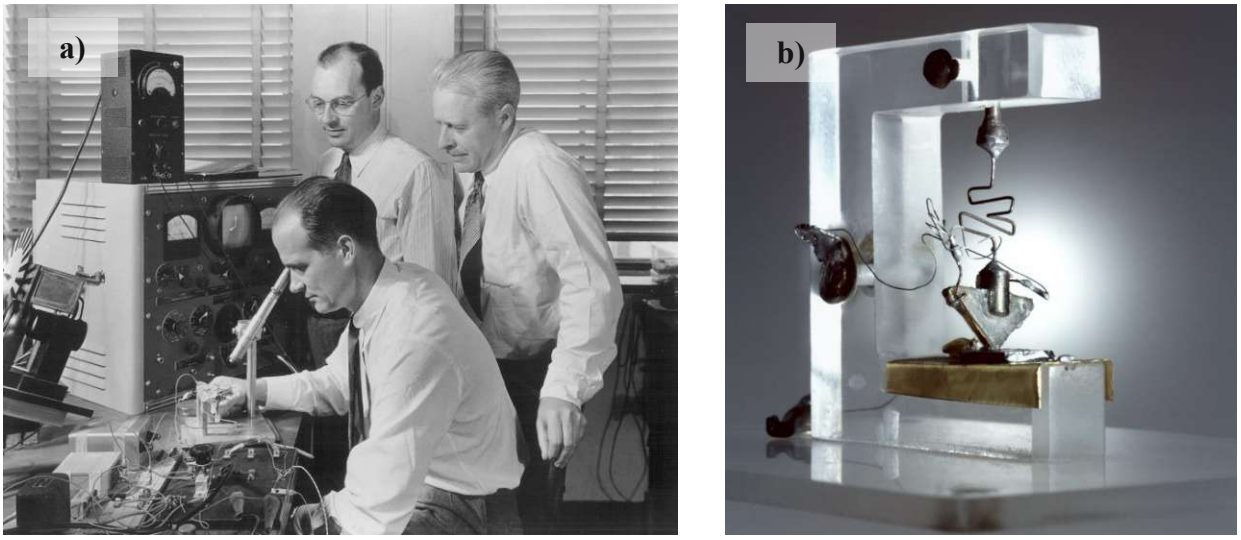

Fig.1.1: At the end of the year 1947 John Bardeen, Walter Brattain, and William Shockley (a) managed to make the first working transistor (b).

The reliability assessment is a major point in the application field for high-power electronics such as aircrafts, automotive, space exploration, etc. For example, an electronic component for a power module is the insulated gate bipolar transistor (IGBT). Fig.1.3. shows the typical application spectrum of IGBTs (Fig.1.3.a) with an actual sample of the module from transportation field (Fig.1.3.b) and interconnections of the IGBT such as wire bonds and solder joints to produce a mechanically acceptable and functional conductive bond between the metal surfaces.

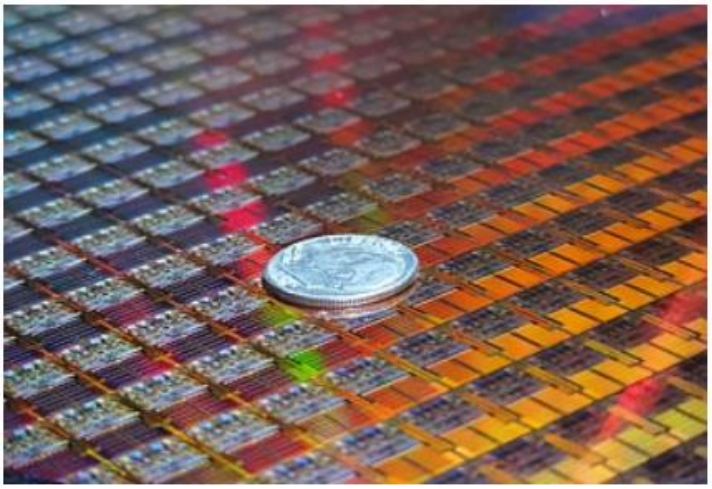

Fig.1.2: A wafer with several Intel processors with each processor, smaller than a dime, containing several hundreds of millions of transistors, invisible to the naked eye.

Wire bonding is used for instance between the semiconductor device and its baseplate such as DCB (direct copper bonded) or to other integrated circuits (IC). Common materials used as wire are gold, silver, copper and aluminum. Thick wires are several hundred micrometers of diameter, thin wires under 100 µm [13].

For thin gold wires usually the ball bonding process is applied. This process starts with the formation of a sphere with ca. twice the diameter of the wire by melting the wire tip in an electric arc. The wire with the sphere at its end, called ball, is placed on the contact metallization of the preheated semiconductor, typically over 150°C. While pressing onto it like a nail head, the intimate contact between the mating partners is supported by ultrasonic vibrations. Though, ball bonding as a process might sound expensive with a series of serial process steps, it is still by far the most frequently applied interconnection process for semiconductors. It is performed fully automated at speeds up to 20 bondings per second including all necessary precision positioning steps. However, ball bonding is limited to gold wires and thus not applicable for power semiconductors.

The wedge bonding process utilizes ultrasonic energy and pressure as well. In contrast to ball bonding, the wire end is welded directly onto the substrate metallization without the need of the ball formation. This process is applicable also to thick wires, e.g. several 100 µm thick Al-wires. However, for wedge bonding the entire assembly needs to be moved from bond to bond with the orientation of the longer pad side in direction of the wire axis and, therefore, wedge bonding is much slower than ball bonding.

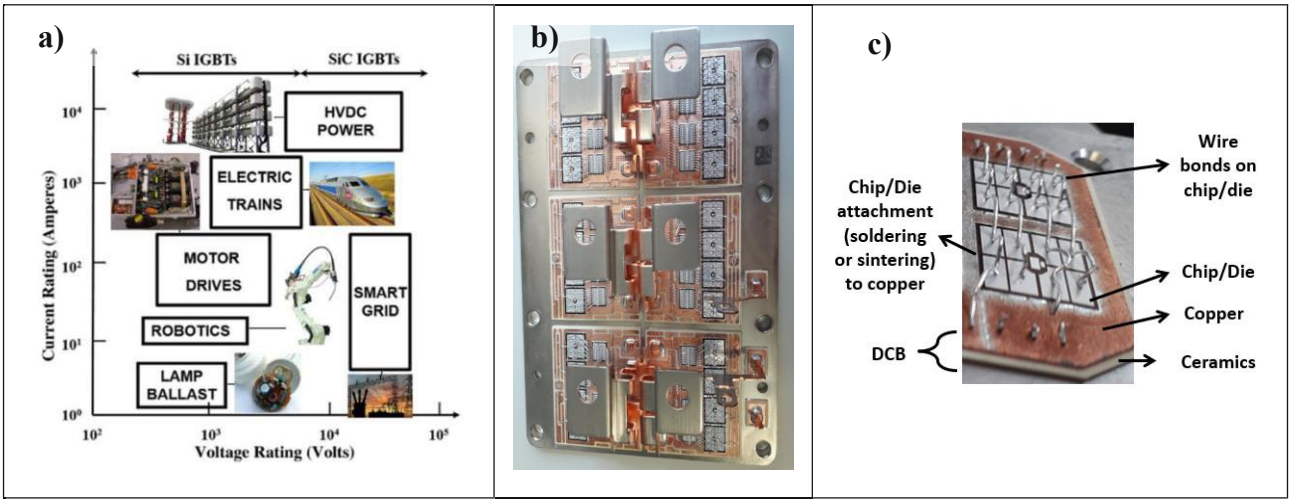

Fig.1.3: Application spectrum for IGBTs [17] [18,p.3] **(a), several IGBT modules on a baseplate (b) and two individual IGBTs with connecting bonds (c).**

To contact large areas such as for die bonding or component mounting solder pastes are commonly used. During soldering process, the components are joined by the filler which has a lower melting point than the adjoining metals. Most established solder material is probably lead and its tin alloys. An overview of the melting temperature of the solder alloys is given in Fig.1.4. PbSn or PbSnAg combinations have been used over decades for soldering components on printed circuit board (PCB) and for die attach placed inside molded components as packaging, but due to environmental aspects European Restriction of Certain Hazardous Substances (RoHS) Directive (2011/65/EU) restricts the use of certain hazardous substances such as lead in electrical and electronic equipment. For this reason, lead had to be replaced by other metals like Ag and Bi. For the SnAg-based solders this change shifted their melting points by around 40 K to a level of ca. 220°C, while the soldering temperature of SnBi-alloys allowed to widen the melting range in a lower temperature regime. On the other hand, major obstacles on the way to increase operation temperature using soldering techniques for mounting power chips are related to several unavoidable effects such as: the need of fluxes and therewith the enclosure of flux residues during soldering; an effect that particularly applies to large-area solder joints (i.e.: lateral dimension of the solder layer is large compared to its thickness) as most frequently the case for the attachment particularly of power semiconductor chips; the formation of brittle intermetallic layers and Kirkendall voids at the solder/metallization interfaces at elevated temperature; grain coarsening and recrystallization of the solder layer due to different coefficient of thermal expansion during natural cycling of temperature by power on/off state changes.

As the process temperature of the used materials differ, high operating temperature can be a relative value. Though, the bare Si-based semiconductors can resist more than 400 °C for a short time without remaining changes of their characteristics, for traditional power electronic assemblies an ambient temperature of only up to 100 °C may be allowed.

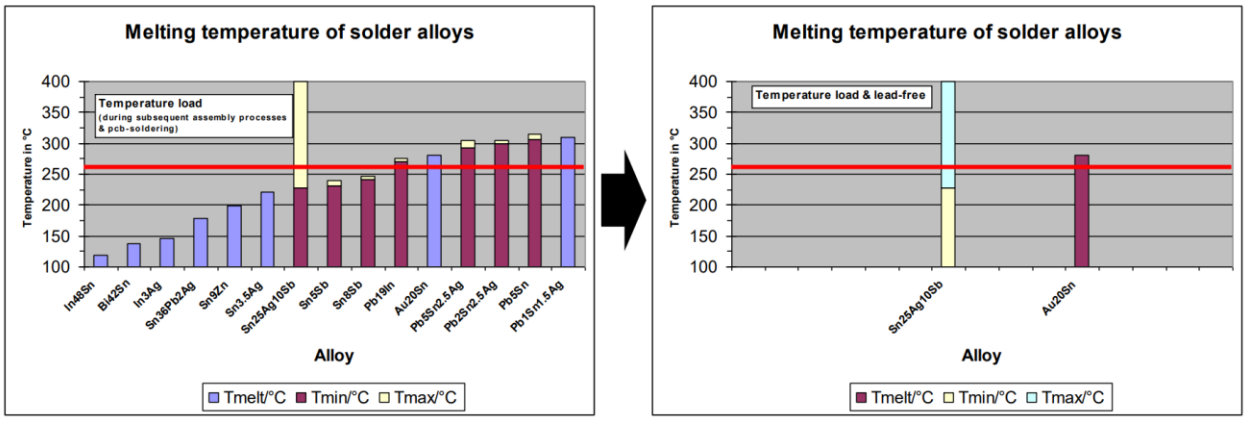

Fig.1.4: Melting temperature of solder filler alloys [14].

The reason for this limitation is given by the interconnection and packaging technology. An interconnection technique allowing to resist 200 °C and more would allow for increasing the power density i.e., increasing the miniaturization degree, and saving cost for cooling means. The application of wide band gap semiconductors like SiC allows power devices operating at very high voltages (up to ca. 1700 V) and high temperature, in theory more than 1000°C [66]. Moreover, SiC exhibits superior thermal properties [15].

One still state-of-the-art attachment technique of power semiconductor chips on ceramic substrates relies on the use of solders with a lead content of more than 90% allowing to raise the operation temperature by around 50 K with respect to power modules fabricated with conventional tin-based solders. However, there is a strong ambition to replace this technique by a lead-free alternative.

Pressure silver sintering offers significant advantages regarding thermal properties compared to conventional soldering [16]. Additionally, it is assumed that the higher melting point of sintered silver in comparison to solder leads to results of improved reliability, reducing expenses for cooling measures and supporting further miniaturization.

As a promising alternative to soldering the basic idea of the silver sintering process comprises the following process steps: applying the metal paste by stencil printing or pipetting similarly as a solder paste on one or both of the metallizations to be mated, drying the paste, and sintering at a temperature comparable to the peak temperature of conventional soldering processes. From this simple process description one could conclude that sintering is somewhat similar to soldering. However, the formation of the metallic bond is significantly different from the metallurgical point of view and so is the macroscopic behavior of the sintered joints: Due to the fact that sintering takes place at a very low homologue temperature (of only around 0.55 instead of close to 1) interdiffusion of atoms at the contact points between micrometer sized particles and metallization occurs primarily by the content of nanoparticles in the paste. Consequently, since sintering is terminated already in an extremely early state at these low temperatures, only a truss-like framework of silver or copper remains as bonding layer which explains its comparatively low modulus of elasticity and a pronounced creep behavior.

Both of these mechanical peculiarities - as they contribute to a very high compliance between bonding partners with different thermal expansion - are extremely important from the applicant's viewpoint of lifetime and reliability of the products. The binary system of silver and copper is an eutectic system with a reaction temperature of around 740°C (so, far beyond any thinkable operation temperature); the formation of brittle intermetallic layers as in case of e.g. tin-based solder joints are avoided by principle. This is particularly important to withstand a high number of temperature cycles (long life) and to keep bonding forces at their initial level also at high operation temperature (high temperature stability).

Despite the circumstance that the basic characteristics as mentioned here are known since more than a decade, the replacement of soldering processes by sintering in a part of applications is going on only stepwise because the final properties of interconnections including lifetime prediction require a thorough understanding of relations between process parameters, material combinations, and last but not least geometry parameters of the entire set-up.

This thesis follows the goals of establishing the time and temperature dependence of mechanical properties of silver sintered joints in an experimental approach and providing this experience in form of a material model to allow its engineering use in a commercial Finite Element program. Systematic experimental investigations were targeted on establishing the mechanical behavior of sintered layers of silver under shear and under tensile loads at various testing temperatures.

The following chapters summarize basic theoretical aspects with the focus kept on low-temperature silver sintering and applied methods for data evaluation (chapter 2), the setup design and fabrication of appropriate samples for measurements (chapter 3), deduced mechanical properties (chapter 4-5), and outlining the main discussion points (chapter 6).

CHAPTER 2

THEORY and METHODS

This chapter shall give an overview to the theory of the sintering process, to the general terminology used in material science along with the research methods to determine the characteristics and on which the evaluation of the results base. Investigations include mechanical properties such as tensile and shear strength, creep behaviour, fatigue lifetime and characteristics such as electrical conductivity/resistivity and density of porous material.

2.1. Sintering

What is sintering? Sintering is the transformation of a material in the powder form into a new stable dense or porous material with different physical properties. Consolidation of the powder occurs using the thermal energy. According to International Organization for Standardization (ISO) sintering is defined as "*the heat treatment of a powder or a compact below the melting point of the main constituent for the purpose of increasing the strength by bonding together of the particles*".

The powder containing nano- or micro-sized metal particles is usually combined into additives, solvents, and binders to a viscous paste as indicated in Fig.2.1 [19, p.46], which enables processing for example with stencil printing for a defined geometry of shape and thickness. As a pre-step of sintering the heating at a lower temperature first (in case of silver below 180 °C) allows the evaporation of these volatile dispersants. Sintering process itself takes place at a higher level of temperature (in case of silver above 200 °C).

The driving force of sintering is the reduction of the surface energy, causing the neighboring metal particles to merge to minimize the total surface area, initiating necking connections at the interface as indicated in Fig.2.2 [19, p.18].

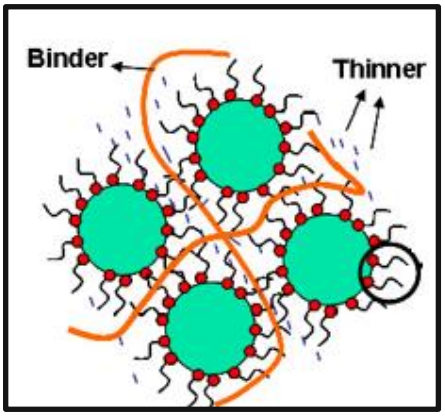

Fig. 2.1 [19, p.46]: Metal powder particles are mixed with solvents, binders and thinners to obtain an applicable paste for example for stencil printing.

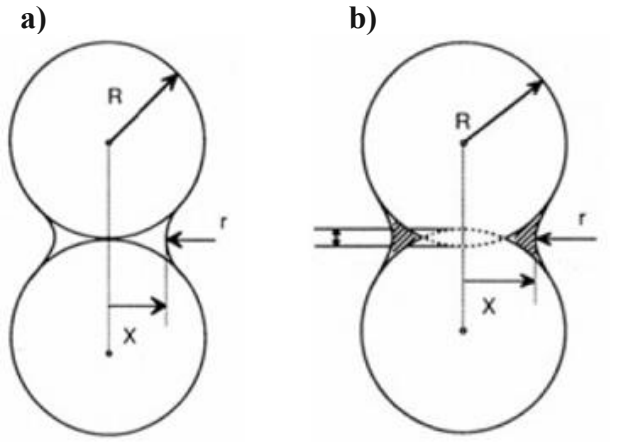

Fig. 2.2 [19, p.18]: Two particles of the metal powder with a radius of R merging together to minimize the surface energy, creating necking connection with the radius r, and further grain coarsening.

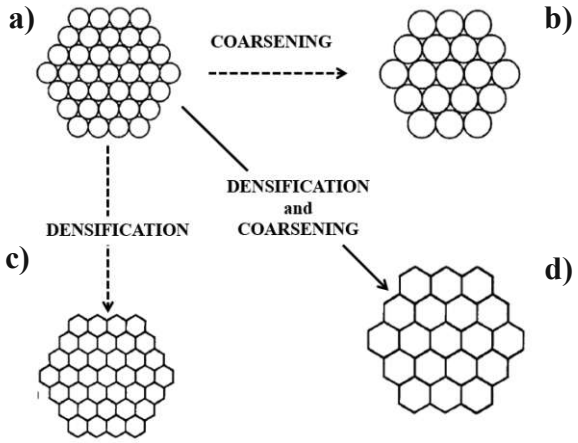

Fig. 2.3 [20, p.7]: Powder particles (a) undergoing grain coarsening (b) and densification (c) under heating, resulting in the change of surface area and interfacial energy, leading to dense sintered material (d).

The reduction of the total energy can be expressed as

$$\Delta(\gamma A) = \gamma \Delta A + \Delta \gamma A \tag{1}$$

where A is the total surface area and γ the specific interface energy [20, p.6].

The regular sintering is a solid-state reaction which does not go through a liquid-to-solid transition, resulting in the absence of self-alignment [9, page xiv]. But sintering allows a certain control of the microstructure and density over the parameter such as process time, temperature, and pressure. Densification can be increased by applying external compression force during the sintering process. The compactness as well as higher level of grain coarsening can be achieved at higher sintering temperatures [22]. The sintering atmosphere can also play an important role in the grain size of

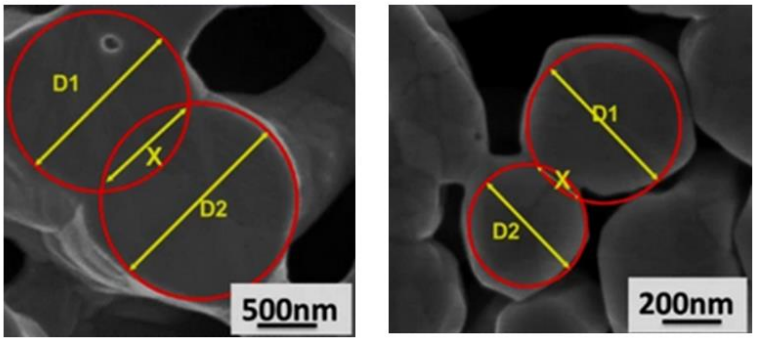

Fig.2.4 [21]: SEM images of the sintered silver in air (a) and nitrogen (b) atmosphere showing grain size and neck growth of the Ag-particles: ca. 1.5µm for the former and under 0.5 µm for the latter case.

the bonding layer. Fig. 2.4 shows the neck-building of the Ag-particles after pressureless sintering at 250 °C in air (a) and nitrogen (b) ambient [21].

Besides the solid-state sintering there are various types of sintering such as liquid phase sintering, which occurs when a powder compact is present in liquid phase during sintering; and Transient Liquid Phase (TLP) sintering where a liquid phase in the compact is formed at an early stage of sintering but disappears as sintering proceeds and densification is completed in the solid state [20, p.5]. An overview plot of the variants in form of a phase diagram is given in Fig.2.5. In comparison, the phase diagram of silver and copper is given in Fig.2.6. Below the eutectic point of 779 °C, at typical sintering temperatures between 200-300 °C both metals, Ag and Cu, are in solid state and as a pure eutectic system do not form intermetallic phases.

To achieve an optimal degree of sintering several factors should be considered, including the formulation (shape and size) of the filler paste, the sintering process with heating rate profile and time. Carefully chosen time allows for effective course of diffusion mechanisms in a material and limits also the process of grains growth [12, p.126]. In case of silver sintering as interconnection material in die attach, also the design of the electronic assembly including die size, joint thickness, surface roughness and metallization of the substrate matters. These factors, along with the microstructure such as grain size and porosity of the sintered layer, affect the interface properties and all together the electrical, thermal, and mechanical reliability of the joint [9, p.70] [23].

The next section should give an overview to the theory of the mechanical properties for the material characterization as response to various types of stressing.

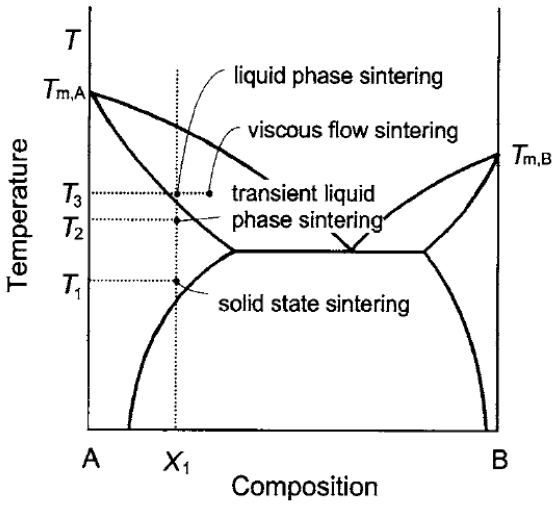

Fig.2.5 [20, p.5]: Illustration of various types of sintering.

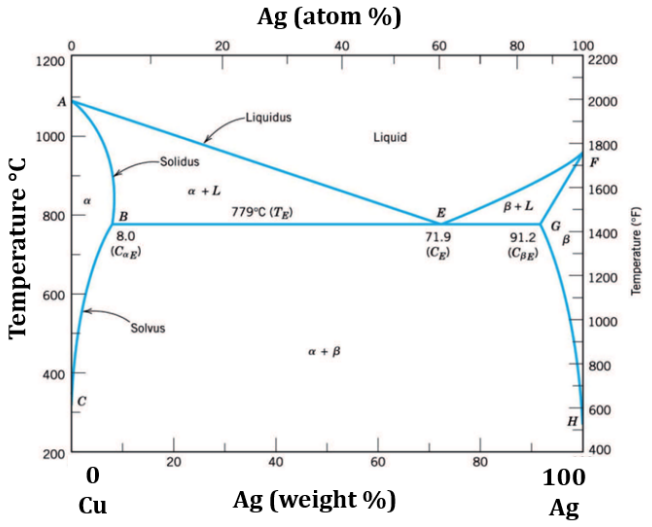

Fig.2.6: Phase diagram of silver and copper.

2.2. Mechanical Properties

Materials in general and in electronics can be exposed to various kinds of mechanical stresses such as tensile, tensile-compressive alternating stress, shear, torsion or bending. Static and dynamic behaviour along with the thermal are critical for the usage of a material in specific applications. Thermomechanical loading below the yield stress level leads to elastic deformation of the subjected material. With the increase of load level permanent plastic deformation or fracture occurs, leading to malfunction or breakdown of the component. The types and characteristics of the stress-strain relationship are discussed in the next section.

2.2.1. Stress-Strain Relationship

Reversible elastic deformation is defined by the feature of the material turning back into its original state after it is exposed to stress, such as in Fig.2.7., under a certain level. The nominal stress, also known as the engineering stress

$$\sigma = \frac{F}{A_0} \tag{2}$$

is the ratio between the force F and its applied original cross-sectional area A_0, measured in N/m^2 or Pa. In comparison, the true stress is inversely proportional to the cross-sectional area A, which decreases due to necking during ductile fracture process:

$$\sigma_t = \frac{F}{A} \tag{3}$$

The longitudinal nominal strain, also known as (longitudinal) engineering strain

$$\varepsilon = \frac{l - l_o}{l_o} = \frac{\Delta l}{l_o} \tag{4}$$

is the relative elongation of the material resulting from the applied stress, with l_0 as the original length, and l as the length after the load is applied, as shown in Fig.2.8. In comparison, the true strain can be expressed as the natural logarithm of the ratio of the current length l and the original length l_0.

$$\varepsilon_t = \ln \frac{l}{l_o} = \ln\,(1 + \varepsilon) \tag{5}$$

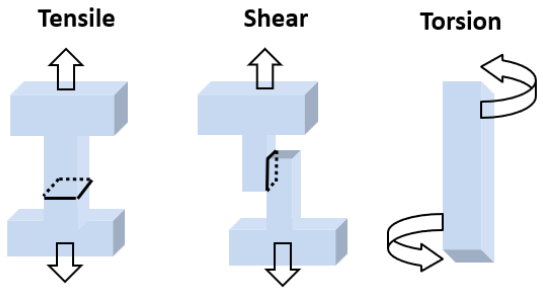

Fig.2.7: Possible directions of force exposure.

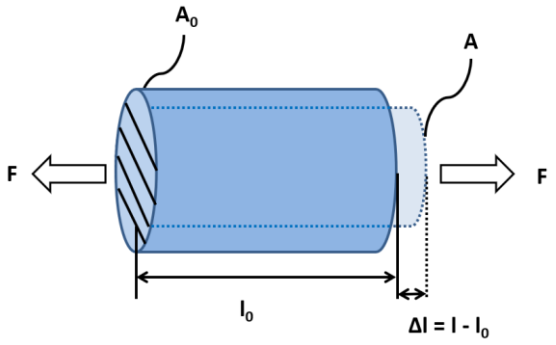

Fig.2.8: Change in length and cross-sectional area of the material due to loading.

The definition of the shear stain, strictly speaking engineering shear strain, γ is illustrated in Fig.2.9:

$$\gamma = \tan(\theta) = \frac{\Delta x}{d} \qquad (6)$$

where Δx is the transversal displacement, and d is the initial distance.

The shear stress is given with:

$$\tau = \frac{F}{A_o} \; . \qquad (7)$$

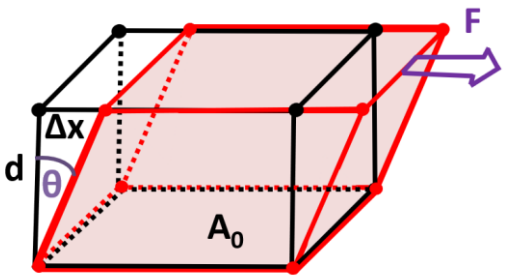

Fig.2.9: Illustration of the shear strain

$$\boldsymbol{\gamma = \tan(\theta) = \frac{\Delta x}{d}} \; .$$

The load a material can withstand at ambient temperature before fracture occurs can be plotted on a stress-strain diagram (Fig. 2.10). The elastic region is marked with an A and is limited by the so-called yield strength. Above the yield strength, marked with B, the material shows plastic deformation defined by the irreversible modification of its shape. Strain hardening is the increase of yield stress during ongoing plastic deformation. It originates from defects of the crystal lattice called dislocations, which are generated during plastic deformation of the material. On the way reaching the ultimate strength level (UTS), marked with C, some materials suffer from instant brittle fracture. On the other hand, some materials show a ductile behaviour and undergo a necking process, section C-D, where the cross-sectional area becomes increasingly thinner before breaking finally [24].

In the elastic range A, the σ-ε-relationship has a linear characteristic and is described by Hooke's law:

$$E = \frac{\sigma}{\varepsilon} . \qquad (8)$$

with E defined as tensile elasticity modulus, also known as Young's modulus. The stiffer the material is, the greater is the E-value. It is worth mentioning that the E-modulus is also temperature dependent and decreases with increasing temperature in general. The E-modulus is ca. 80 GPa for bulk silver (Ag) [75] [78], ca. 120 GPa for copper (Cu) [74] and ca. 35 GPa for lead (Pb) [74] at room temperature. For the annealed bulk silver, the ultimate tensile strength (σ_{US}) is around 125 MPa and the yield strength (σ_y) is around 55 MPa [78].

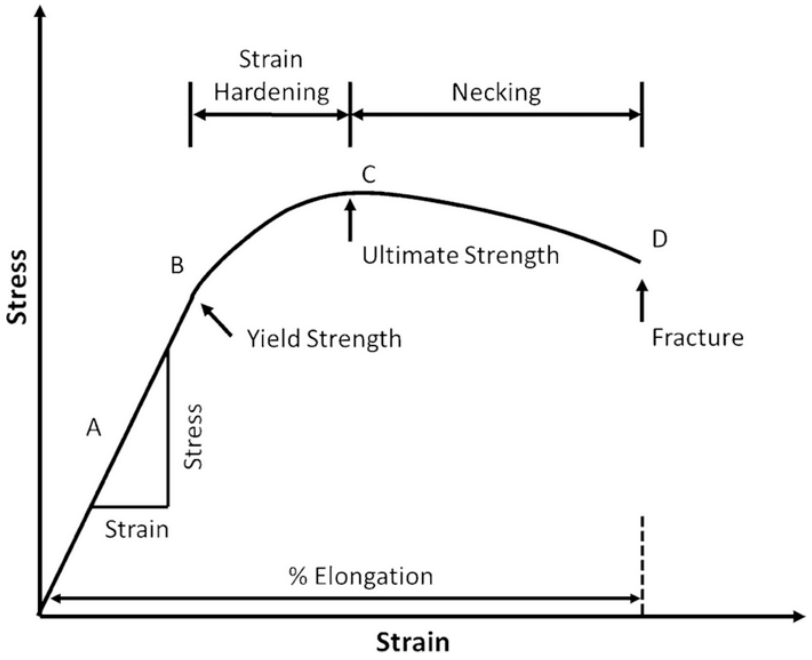

Fig.2.10 [24]: Possible stress (σ) –strain (ε) relationship of materials such as some metals showing the linear-elastic regime A, plastic deformation region above the yield strength B, passing the ultimate strength point C for ductile materials, until the fracture failure at D.

The shear modulus is denoted by a G and is defined by the ratio of shear stress τ to shear strain γ:

$$G = \frac{\tau}{\gamma}. \qquad (9)$$

G-modulus, modulus of rigidity, is around 45 GPa for bulk silver [76], 45 GPa for copper [74] and 10 GPa for lead [74].

When a triaxial stress (σ) from all sides causes an alteration (ΔV) in the volume (V) without phase change of the material, then the elastic modulus describing this proportionality factor is called compression or bulk modulus K:

$$\sigma = K \cdot \frac{\Delta V}{V}. \qquad (10)$$

For isotropic elastic materials, these moduli satisfy the relationship:

$$E = 2G(1 + \nu) = 3\,K(1 - 2\nu). \qquad (11)$$

where ν is called Poisson's ratio. The ν is calculated as 0.368 for bulk silver (with E_{Ag} = 82.4 GPa and K_{Ag} =103.8 GPa at room temperature) [75]. Further, ν is around 0.326 for copper [74] and 0.425 for lead [74].

2.2.2. Creep Behaviour and Stress Relaxation

Exerting a force on a material causing stress and strain, i.e. adding mechanical work to the material means loading it with energy. The area under the stress-strain curve (as in Fig.2.9) can be interpreted as representing the absorbed energy density. In the plastic deformation regime, this leads to dislocation movement along crystallographic slip planes. Thus, the material becomes increasingly saturated with new dislocations and manifests itself. Thermal annealing the material to rearrange the lattice formation of dislocations would be one possibility to lower the resistance to plastic deformation. But especially when the homologous temperature T_H

$$T_H = \frac{T}{T_m} \tag{12}$$

i.e. the ratio of the temperature (T) to the materials melting point (T_m) increases, diffusion creep failure becomes a dominant issue in the joint reliability. For example, Nabarro-Herring creep is based on vacancy diffusion through the crystal, and it occurs at rather low stresses in fine-grained materials. Other low-stress creep types are described by Coble creep as grain boundary diffusion or Harper-Dorn creep as viscous creep for some pure materials near melting point.

When the stress is held constant (σ = const.), the change in the strain over time $\Delta\varepsilon/\Delta t$ as creep rate can be measured like in Fig.2.11 [25]. Creep evolution consists of three stages: primary transient creep, steady-state creep and tertiary creep. The transient stage is characterized by an initial sharp increase in creep strain. The steady-state stage has the longest duration in which the rate of increase of strain is almost constant. The tertiary stage shows an accelerated increase in creep strain leading to ultimate failure [26].

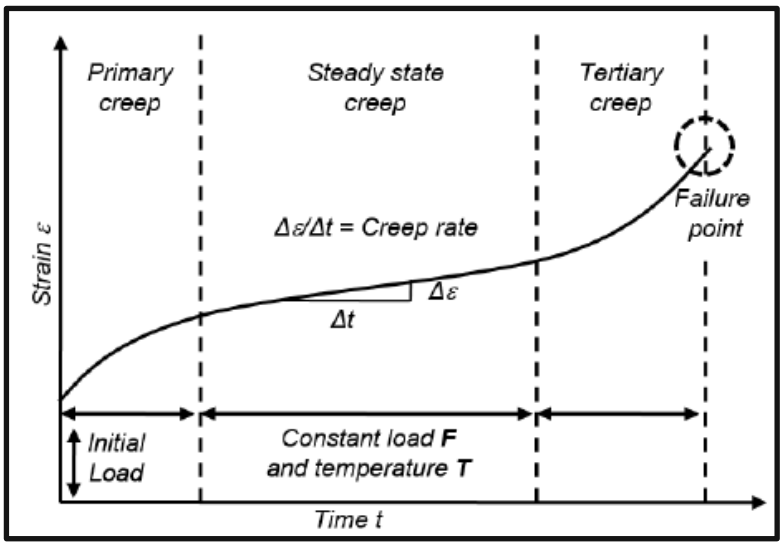

Fig. 2.11 [25]: Creep evolution can be described in three stages: primary, steady-state and tertiary creep.

Another test method consists in keeping the initiated strain at a constant level (ε = const., $\Delta\varepsilon = \Delta\varepsilon_e + \Delta\varepsilon_p = 0$) and observing the stress behaviour as plotted in Fig.2.12 [27]. The decrease of the peak stress over time can be described by the relaxation rate $\Delta\sigma/\Delta t$.

Reminding the Hook's law in elastic region, the relationship can be expressed as:

$$\frac{\Delta\sigma}{\Delta t} = E \cdot \frac{\Delta\varepsilon_e}{\Delta t} \tag{13}$$

Norton creep is a model based on a power law, which is commonly used to describe the phase of steady state creep as stress-dependent mechanism:

$$\frac{d\varepsilon}{dt} = \dot{\varepsilon} = C_m \cdot \sigma^n \tag{14}$$

with C_m as temperature-dependent material constant and n as stress exponent.

Thus, one obtains the expression

$$\dot{\varepsilon} = C \cdot e^{\frac{-Q}{kT}} \cdot {\sigma_{vM}}^n \tag{15}$$

as stress relaxation curve including an Arrhenius term $e^{\frac{-Q}{kT}}$ with the activation energy Q, the Boltzmann constant k and the absolute temperature T. The temperature dependence is implemented in the material constant C, σ_{vM} stands for the von Mises stress equivalent considering multiaxial states of stress, and n is the stress exponent.

The equations shall give the basis for the estimation of end of lifetime emerging from creep and fatigue. The determination of the data, which is characteristic for a material, is obtained by various standardised testing and recognised experimental methods.

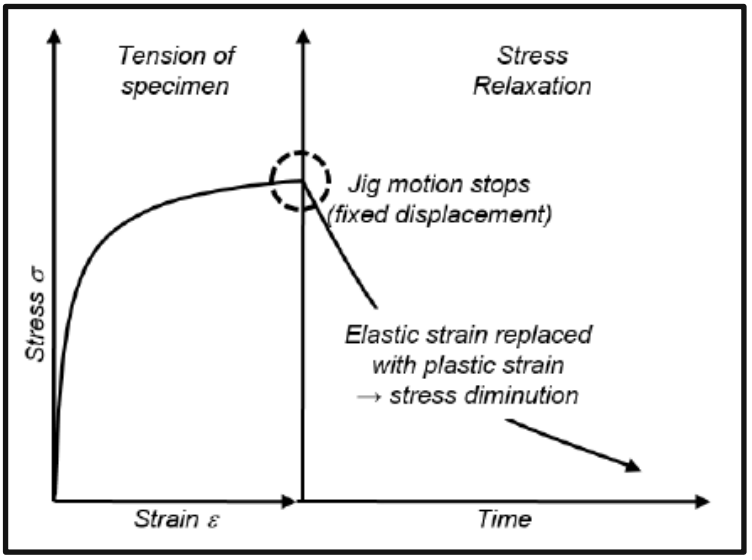

Fig. 2.12: Stress relaxation plot [27]: straining the sample to initiation level ε =const., and measuring the decay in stress over time as $\Delta\sigma/\Delta t$.

2.3. Fatigue and Lifetime Testing

2.3.1. Fatigue

When metals are confronted with repetitive loading, first cracks are initiated in the material in form of microscopic notches or defects on grain interfaces. Depending on the stress level and frequency, the fracture propagates and the damage grows, which is called fatigue. Failure mechanisms such as crack propagation lead to irreversible structural change in a material, which does not recover after resting.

Upon heating during operation, different substances of a module expand by different amounts and the mismatch of the coefficients of thermal expansion (CTE) can seriously affect the reliability at elevated temperatures. The linear CTE is described by

$$\alpha \cdot \Delta T = \frac{\Delta l}{l_0} \tag{16}$$

where α represents the CTE, l_0 the original length of the material and Δl its change due to the change in temperature ΔT. A schematic view of the mechanical bending of interconnected layers is given in Fig.2.13.a., and a SEM image of an actual Si-die soldered on a DCB showing a crack on the connecting interface induced by stress loading is given in Fig.13.b. *(1)*

Under real operation conditions materials are not only exposed to static stresses but also cyclic ones, where the stressing load changes with time, such as on revolving shafts or bending of the interfaces due to thermal expansion during operational on-and-off switching.

Practical laboratory investigations in accelerated testing use loading cycles such as triangle- or sinus waveform as in Fig. 2.14. Representative parameters of the devolution are the under (σ_{min}) and upper (σ_{max}) level of the applied stress. The stress range is given by

$$\Delta\sigma = \sigma_r = \sigma_{max} - \sigma_{min} \tag{17}$$

Negative values of σ express compressive stress, thus negative values of R indicate alternating compressive and tensile stress [67].

---

(1) As a sintering material in microelectronic packaging, Ag has numerous benefits with its excellent thermal and electrical conductivity, its relatively well matching CTE (ca. 19.5 10^{-6} / K) with copper (ca. 16.5 $\cdot 10^{-6}$ / K) compared to lead (ca. 29 $\cdot 10^{-6}$ / K). Silver's high melting point (960 °C) lead to a lower homologous temperature compared to Pb-solder or alloys, which could be advantageous in regards of creep-based dislocation fatigue.

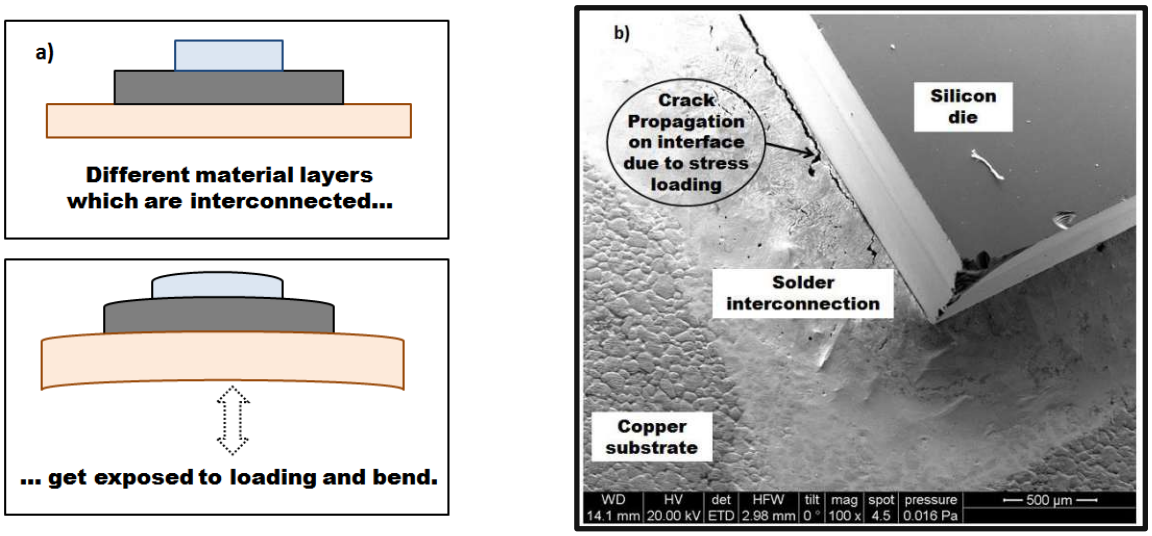

Fig.2.13: Schematic view of layers with different materials which are interconnected i.e. on an electronic module (a) and actual SEM image of a common sample (b).

$$\sigma_m = \frac{\sigma_{max} + \sigma_{min}}{2} \qquad (18)$$

is the mean stress value.

$$\sigma_a = \frac{\sigma_{max} - \sigma_{min}}{2} \qquad (19)$$

is the stress amplitude.

The ratio of σ_{min} and σ_{max}:

$$R = \frac{\sigma_{min}}{\sigma_{max}} \qquad (20)$$

is the R value.

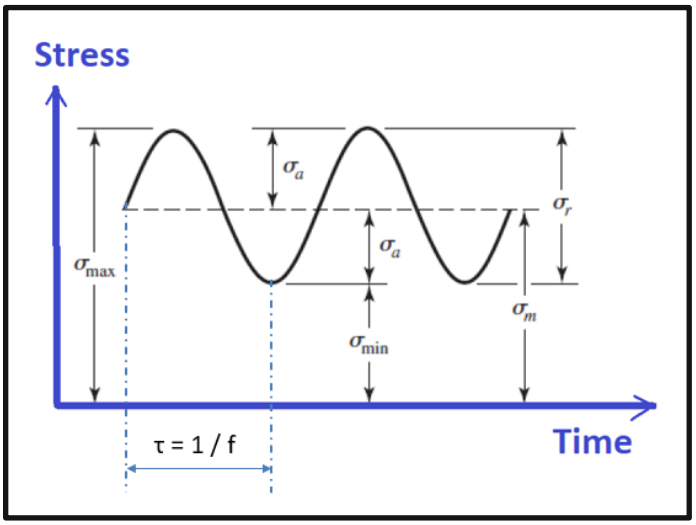

Fig.2.14 [65]: Stress loading in accelerated testing.

The frequency f is defined as the reciprocal of the period τ:

$$f = \frac{1}{\tau} \qquad (21)$$

Two regimes of the number of loading cycles N_f until total failure can be distinguished the so-called High Cycle Fatigue (HCF) which occurs when the stress amplitude σ_a is relatively low leading to cycle numbers of more than 10^4-10^5, and Low Cycle Fatigue (LCF) when number of cycles are under 10^3-10^4.

The lifetime of materials under cyclic load is represented by a Wöhler diagram, also known as S-N diagram. The stress amplitude σ_a is plotted versus the logarithmic number of load cycles. The resulting plots are useful guides for lifetime prediction.

Several lifetime models are known in literature. In the regime of LCF, the Coffin-Manson model is usually preferred. This model relates the plastic strain accumulated per loading cycle:

$$\frac{\Delta\varepsilon_p}{2} = \varepsilon'_f \cdot \left(2 \cdot N_f\right)^c \tag{22}$$

Here $\Delta\varepsilon_p/2$ is the plastic strain amplitude, ε'_f is empiric fatigue ductility coefficient corresponding to strain at fracture level, N_f is the number of cycles to failure (one complete cycle contains two reversals, i.e. two half cycling loops), c is the material dependent fatigue ductility exponent. The Coffin-Manson-diagram tends to be temperature and strain rate dependent during cycling tests because solder joints undergo deformation and hardening due to creep.

In the regime of HCF deformations occur mainly in the elastic range, where the loading is close to but still less than the yield stress of the material. The lifetime in the HCF regime is well described by the Basquin equation:

$$\frac{\Delta\sigma}{2} = \sigma'_f \cdot \left(2 \cdot N_f\right)^b \tag{23}$$

where $\Delta\sigma/2$ is the stress amplitude (σ_a), σ'_f is the fatigue strength coefficient and b the fatigue strength exponent.

However, Figure 2.15 illustrates that neither the Coffin-Manson equation nor the Basquin equation can describe the entire fatigue life ranging from low to high cycles. Therefore, Morrow [28] suggested a combined model considering both lifetime models. In this model, the total strain is related to the number of loading cycles to failure.

The constitutive equation of this model was derived by adding the equations of the Coffin-Manson model and the Basquin equation.

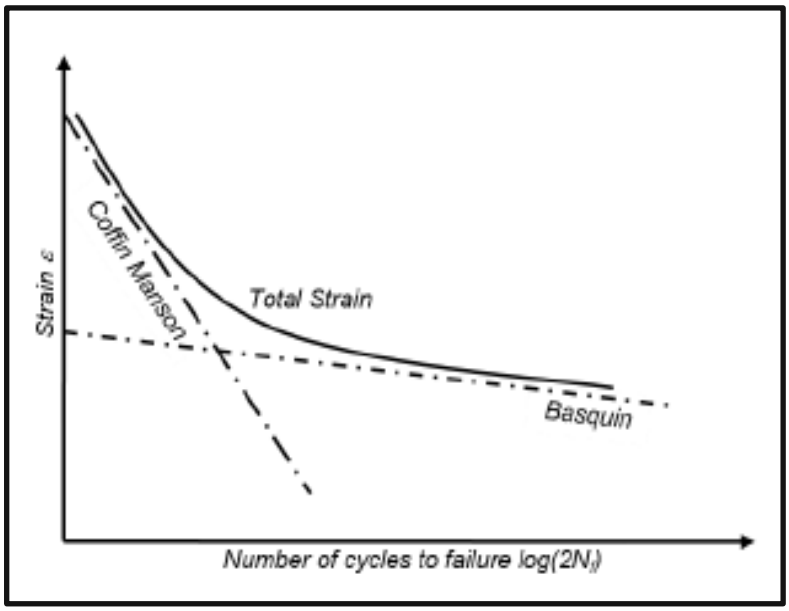

Fig.2.15 [27, p.18]: Total strain versus lifetime equation.

One half of the total strain reads as

$$\frac{\Delta\varepsilon}{2} = \frac{\Delta\varepsilon_p}{2} + \frac{\Delta\varepsilon_e}{2}. \tag{24}$$

Consequently, considering also the right-hand sides of the equations, the lifetime model reads as

$$\frac{\Delta\varepsilon}{2} = \varepsilon'_f \cdot \left(2 \cdot N_f\right)^c + \frac{\sigma'_f}{E} \cdot \left(2 \cdot N_f\right)^b \tag{25}$$

In conclusion, the lifetime of a strained sample is well described by a four-parameter model.

There are several factors which influence the lifetime of a component such as the material itself including microstructure, the medium it is exposed to (corrosion potential, thermal conditions, electrochemical elements, etc.), design boundaries and mechanical limitations [29]. The bathtub curve, which is commonly used in reliability engineering, represents the probability of failure over time and has three distinct phases, as plotted in Fig. 2.16 [30]. At the early-stage failures occur due to manufacturing errors such as design problems and installation defects called “infant mortality” in the lifetime. This is followed by the useful adult life period, where a constant low failure rate dominates with random errors such as operational overload e.g. due to material erosion. Approaching the late life, the so called wear-out phase is reached where the observed failure rate starts increasing gradually. The end of life is usually defined in this last regime.

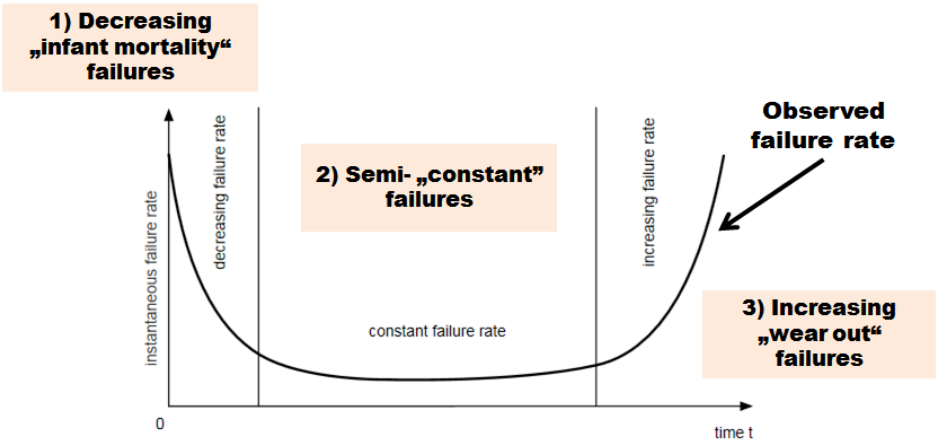

Fig.2.16 [30]: The bathtub curve outlining the three lifetime stages.

2.3.2. Cyclic Tests: PC, TC, MC

Accelerated cycling tests with low and high frequencies at various stress and temperature conditions are used to determine a predictable lifetime for the components, for example in electronic assemblies. Cycling tests are usually destructive for the device under test (DUT) to detect the numbers of cycles until fracture of function failure. The obtained data with material characteristics can be applied in simulation programs to estimate the statically long-term reliability.

Power Cycling:

When a high current flows through the electronic circuit of the power semiconductor module, the temperature of the module begins to rise within a short time due to the self-generated heat. A power cycle test is an accelerated test mimicking such situations. Usually a direct current (DC) source provides voltage pulses while the temperature, voltage, and current are recorded continuously [9, p.109].

Thermal Cycling:

The thermal expansion mismatches between neighboring and interconnected layers are the primary source of stress and strain. To examine the reliability limits for the joint itself, various chip and base plates with various level of mismatch of CTE can be used and the temperature changes during periods can be set to distinct levels as plotted in Fig.2.17 [9, p.194].
The linear thermal expansion is assumed to be a constant average within a defined temperature interval. But the CTE may be also a function of temperature, leading to nonlinearities in the expansion behavior which need to be taken into account.

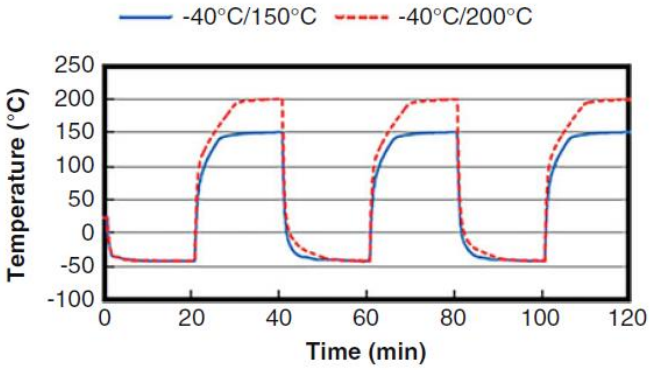

Fig.2.17 [9, p.194]: The specimens were exposed to load cycles with a duration of 40 min per each unit of 20 min, at the temperatures between -40 °C/150 °C and -40 °C/200 °C.

Mechanical Cycling:

Depending on the direction of the applied loading force, mechanical stressing can be flexural or multi-axial. Classical uni-axial shear or tensile-compression tests are performed in a displacement machine with a load cell for measuring the force and strain on the DUT (usually dumbbell shaped specimen). Alternatively bending tests can be applied depending on the number of pressure points as 1-point, 3-point or 4-point. In the case of 3point bending, the bending stress is applied in the middle of the sample which is supported on two ends. The test can be performed in static or dynamic ways. Depending on the dimension of the DUT it can be exited to resonate in ultrasonic range, so that also high cycle fatigue determination is possible in rather short time.

2.4. Electrical Resistivity Measurement
Van-der-Pauw Method

The Van der Pauw Method is a four-point measurement technique which allows deriving an average resistivity of a specimen with the shape of a thin layer whereby 'thin' means that the thickness of the specimen is small with respect to the distance of the measuring points (needle-like electrodes). Two electrodes are used to conduct current through the specimen and the other two electrodes to measure the voltage drop caused by this current as it can be seen in Fig. 2.18. In this case a thin (50-100 µm) sintered Ag sample is placed under the needles in a thermal chamber (Fig.2.18.a) to collect data also at elevated temperatures. The function of the electrodes is permuted as shown in Fig.18.b [31]. With this approach the influence of the contact resistance between electrodes and sample on the measurement results can be eliminated. Another advantage of the Van der Pauw method is that it can be applied for almost arbitrarily shaped thin specimen even with very low resistivity [32]. However it is important to have a homogeneous sample with uniform thickness [33].

The mean resistance R is obtained by averaging eight single resistance values of one sample. A possible start for series is the implementation of the current I_{AB} while the voltage V_{CD} is obtained. By reversing the polarities, one eliminates the offset inaccuracies arising from contact potential, therefore the implementation of the current I_{BA} was pursued while measuring again the corresponding voltage V_{CD}. Then rotating to the implementation of I_{BC} and of I_{CB} while obtaining V_{AD}, and so on for the 4 variations. With the mean value of R and the known Ag-thickness d of the sample, its resistivity ρ can be calculated with the following formula [34],[35]:

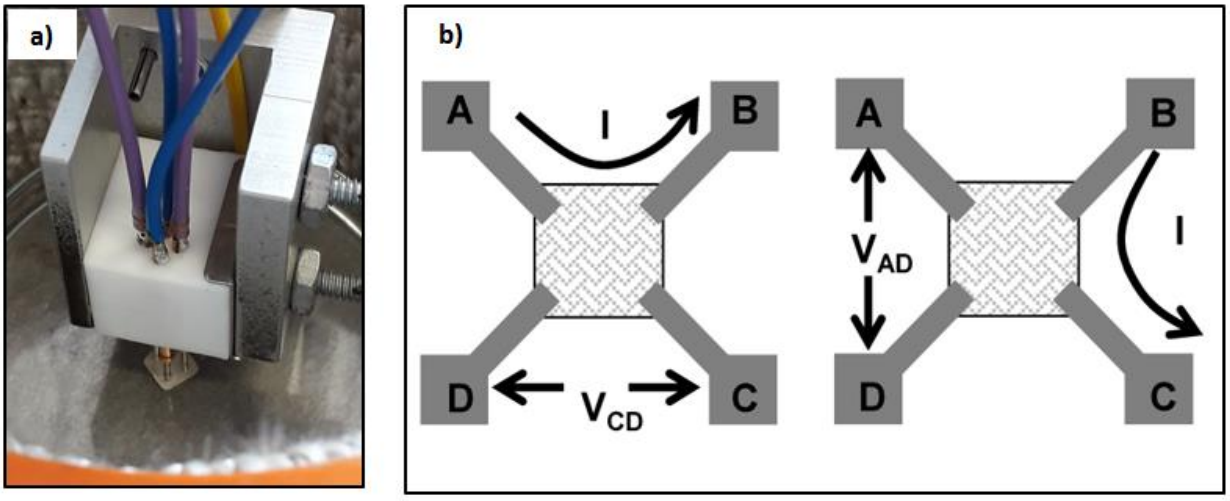

Fig.2.18: A square shaped sintered silver sample is placed under 4 electrodes (a). Schematics of the Van der Pauw method for measuring the sheet resistance (b) [31].

$$\rho = R \cdot \frac{\pi \cdot d}{ln(2)} \tag{26}$$

With the Wiedemann-Franz-Lorenz law for metals, the thermal conductivity λ can be deduced from the electric resistivity ρ according to the relation

$$\lambda = \frac{1}{\rho} \cdot L \cdot T \tag{27}$$

where T is the temperature and L the Lorenz number:

$$L = \frac{1}{3} \cdot \left(\frac{\pi \cdot k_B}{e}\right)^2 \tag{28}$$

with the Boltzmann constant $k_B = 1.38 \cdot 10^{-23}$ J/K and the elementary charge $e = 1.6 \cdot 10^{-19}$ As. In other words, the ratio of thermal conductivity (λ) to electrical conductivity ($\frac{1}{\rho}$) is proportional to the temperature (T) with a constant factor (L = 2.44 x 10^{-8} W·Ω·K^{-2}). The relationship considers that both heat and electrical transport are based on the free electrons in the metal, therefore the Wiedemann-Franz-Lorenz law does not hold a good approximation at very low temperatures. In the present work however, investigations were considered above room temperature.

The thermal and electrical conductivities for bulk silver are 430 W/m·K and $60 \cdot 10^6$ S/m at room temperature [36], for pure copper ca. 400 W/m·K and $58 \cdot 10^6$ S/m, respectively [37].

2.5. Density Evaluation

For the density measurement of solid, liquid, and gaseous materials there are several methods to determine the mass and volume relationship. For porous solid state metals the geometric information can be also determined by image processing methods.

2.5.1. Mass/Volume Method

One of the simplest methods to evaluate the density ϱ of a porous layer is by measuring its mass m and the outer volume V which is defined by the enveloping surfaces [10]:

$$\varrho = \frac{m}{V} \tag{29}$$

Determination of the volume with Archimedes principle would be one possibility. This would be by measuring the weight of the sample first in air then in an auxiliary liquid, mostly water to calculate over the known density of the liquid. Apart from the disadvantage of this method being temperature sensitive, the sample may have an unknown structure of holes which might be open or closed pores, where the liquid pours in an unpredictable amount. In case of a material with unknown relation of closed and open porosity one can make use of the He pycnometry allowing to establish the volume of the open pores in a separate measurement [38].

Another method could be gas pycnometer measurement based on Boyle–Mariotte law. A disadvantage here could be that application of pressure leading to a possible deformation and change of the volume itself.

To determine the volume using the geometrical dimension, for example with the help of a 3D-microscope as shown in Fig.2.19, is another option. A 5 mm x 5 mm square shaped stencil printed and sintered specimen is measured optically. The disadvantage of this method might show itself when the flatness or shape imperfection of the sample increases. It is also only for one sort of material, volume of different material layers cannot be differentiated without extra investigation.

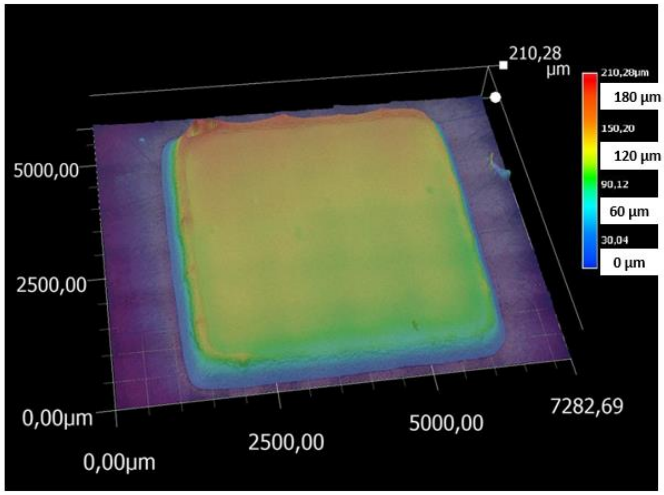

Fig.2.19: Image of sintered silver and height measurement by 3D-microscope.

2.5.2. Imaging Method

Direct determination of porosity proportion is possible by contrast imaging after revealing the region of interest (roi) accordingly. This could be done by grinding or etching the surface to expose the microstructure. SEM images of the roi reveal usually metal surface as white-grey areas, and pores as black voids. It is common to use a semi-automatic image program to set a threshold and convert the roi in total black-white areas to determine the volume percentage of voids and dense parts which is reversibly unique in case of isotropic samples [39]. This method can also be applied on fracture surfaces. The broken surfaces are defined to be the areas that show significant brightness changes within a small distance [40]. To reveal the leading pores and load bearing cross section, contacts should be broken at lower temperatures e.g. in liquid nitrogen. Changes in total porosity or the change in ratio of isolated to interconnected pores can strongly affect the load bearing cross section and therefore the mechanical properties of the material [41].

The disadvantage of the imaging method in general is converting the three-dimensional information into a two dimension format. Marginal fracture areas cannot be detected correctly since the gray tone in shadows are too shallow. The disadvantage of etching is the less well control of the process within the pores which leads to over-etching. The disadvantage of grinding is smearing of the pores on surface in the Ag-dense area. One could try to impregnate the surface with resin, but it does not penetrate in smaller voids due to its viscosity, so this could be an option rather for large pores (diameter more than 3µm).

Another option to reveal the pores in the roi is focused ion beam (FIB) milling as shown in Fig.2.20 [42]. A 3D characterization of thin films, as shown in Figure Fig.2.21, using a SEM/FIB microscope and studying porosity slice by slice from the segmented data with various techniques is also possible [43].

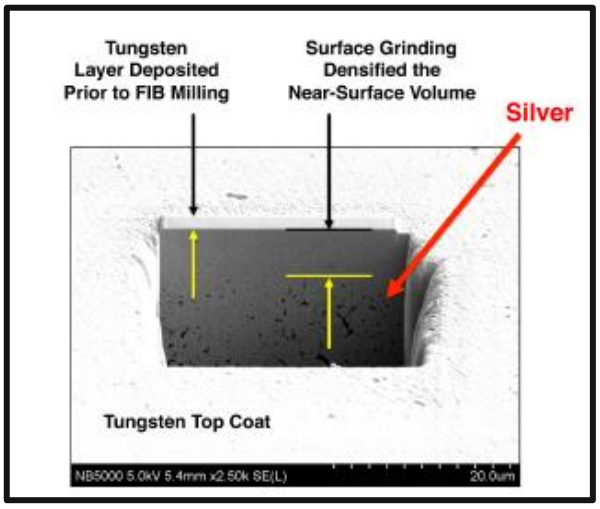

Fig.2.20: Example of a focused ion beam (FIB) milled trench [42].

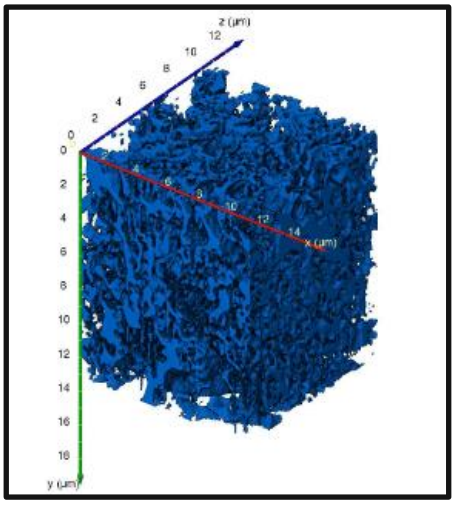

Fig.2.21: FIB-nt image and pore network segmentation (blue) [43].

CHAPTER 3

SAMPLE PREPARATION and TESTING SETUP

This chapter is devoted to the preparation of samples and description of testing procedures to establish the temperature dependent mechanical properties of the sintered silver itself (as coupons) and as interconnection between copper stripes (as lap-joints). The effect of interfacial processes on the joining quality are important for reliability and time of use until failure of an interconnection. Since the alloying of bulk copper and silver in any concentration leads to a ductile solid compound, the interdiffusion of these metals at the interface appears less critical to the joining technology. However, the open-porous structure of the sintered silver layer allows lateral penetration of atmospheric oxygen and reaction with the mating copper surfaces. The preparation of samples and experiments are designed to obtain mechanical properties such as tensile and shear strength at room and elevated temperatures, and to reveal the effect of oxygen reactions at the interfaces and their meaning for fatigue lifetime.

Two main types of samples were prepared for mechanical tests. Firstly, the Ag-coupons as sintered silver itself. Secondly, the Cu-Ag-Cu lap joint samples as interconnection. Different sintering parameters (sintering temperature, time, and pressure) were chosen to create the various series of samples.

For the investigations two types of commercial Ag-paste from Heraeus were used: ASP-016-63 and ASP-338-14/28. In this thesis mainly the testing results of the samples produced with the last one are discussed, if not otherwise stated. To mention the difference, the ASP-016-63 is produced for large area (1-2.5 cm^2) die attach of DCB (direct copper bonded) modules and contains 88% of flake-shaped silver particles of 1-10 µm size whereas the ASP-338-28 contains 73% of silver metal and has a more fluent consistency. The micro-sized Ag-particles are mingled under ultrasonic agitation with an organic solvent containing binders (e.g. polyvinyl butyral) and solvents (e.g. terpineol). According to the data sheet the ASP-338 series can be applied on silver, gold and copper surfaces and allow to produce layers with a CTE of 19 ppm/K, thermal conductivity above 150 - 200 (W/m·K) and electrical resistivity under 0.010 mΩ·cm. The paste is usually applied by stencil printing, first dried at a lower temperature under 180 °C (within nitrogen atmosphere) for organic compounds to volatilize and then sintered over 230 °C. In comparison to conventional soldering, no solder-flux is used. Therefore, no cleaning is required.

3.1. The Ag-Coupons

To obtain the sintered silver as free standing coupons, the Ag-paste was applied by stencil printing (Fig.3.1.a) either on glass for pressureless sintering or on ceramic plates (Fig.3.1.b) in case of sintering with pressure. To be able to detach the silver from the substrate, boron nitride was sprayed prior to the printing process on the plates.

Two main shapes of the Ag-coupons were printed: the 5 mm x 5 mm square pads for density measurements over the mass-volume method and the dumbbells for tensile testing. The dumbbell shaped specimens of sintered silver were produced in three sizes in length: 20 mm, 30 mm or 40 mm (Fig.3.1.c). The smaller ones were used for serial testing of tensile strength (including the setup system), whereas the bigger ones also enabled measurement with laser speckle extensometer (LSE) to determine the strain of the porous silver material itself.

The applied Ag-paste was first dried in a non-sealed oven under nitrogen influx (N_2 > 100 l/h) with a temperature profile slowly approaching to 130 °C to avoid both overshooting of the oven temperature and bubble formation of the volatile components within the silver. The electron microscope image of the dried silver paste is given in Fig.3.2.

The surface roughness of the dried Ag-paste was investigated under an optical 3D-microscope of Keyence (Fig.3.3) with a theoretical resolution of 0.2 µm. When the Ag-paste was printed correctly, i.e. the pressure was applied evenly and uniformly, a surface roughness of 10 -15 µm on top of the dried silver paste could be observed as shown in Fig.3.3.c, which is in the range of big sized Ag-flakes. After the drying procedure, various sintering conditions (combinations of sintering time, temperature and pressure) were chosen to fabricate different series of samples. The main series of the sintered Ag-coupons investigated in this thesis were produced with a stencil thickness of 200 µm and were named as A, B, C, and D. Their parameters are listed in Table 3.1.

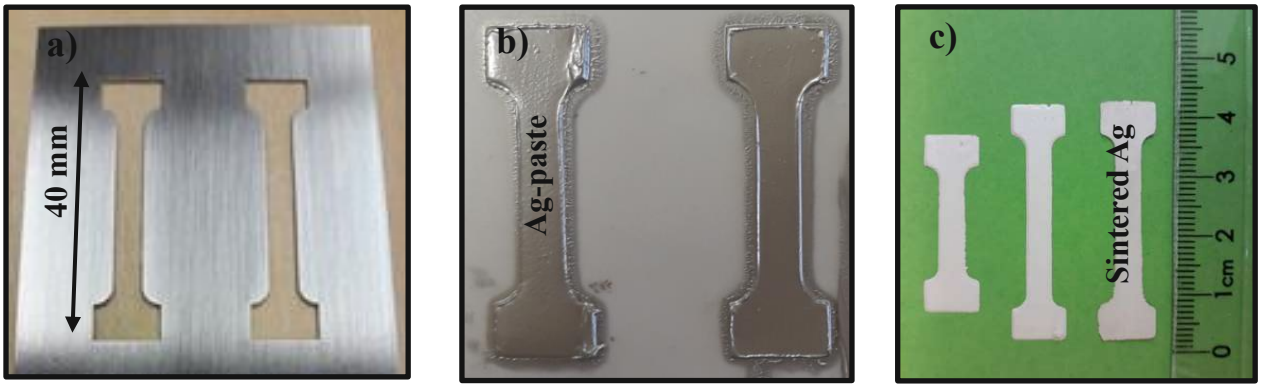

Fig.3.1: Steel stencil (a) used to print dumbbell shaped Ag-paste on a ceramic base (b) which is first dried at 130°C and then sintered at elevated temperature (230°C or 300°C) (c).

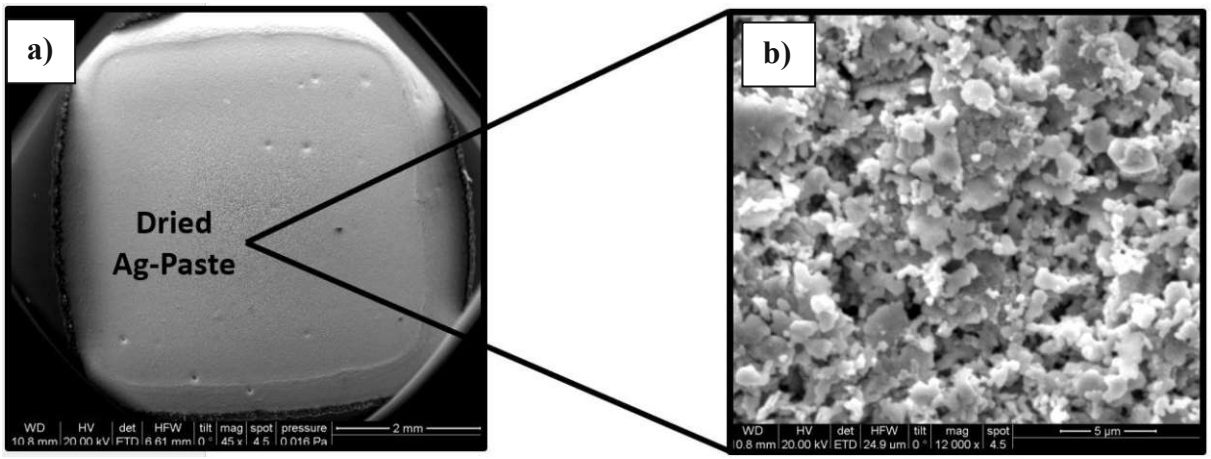

Fig.3.2: Picture of the dried Ag-paste as a 5 mm x 5 mm square printed with a stencil of 200 µm thickness (a) and SEM image of the surface at a magnification of 12K showing the micro sized Ag-flakes (b).

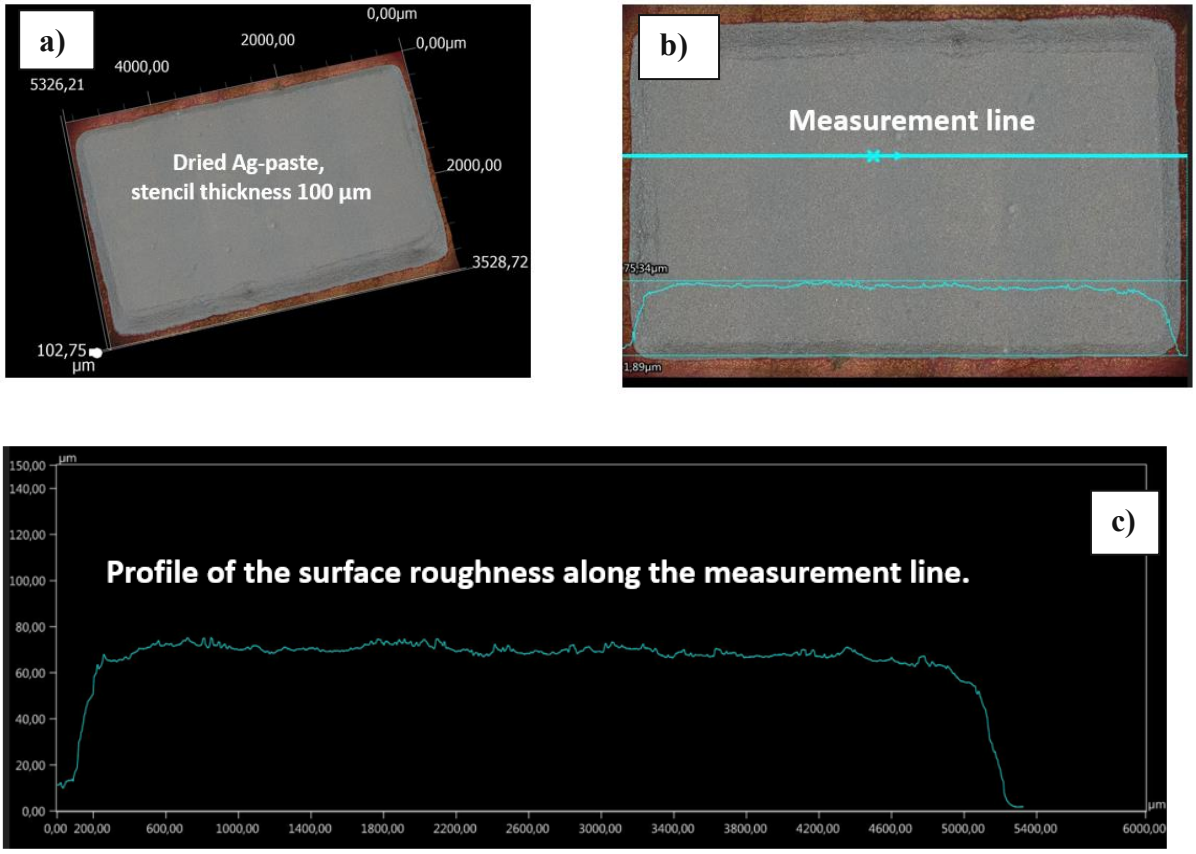

Fig.3.3: 3D microscope image of the dried Ag-paste (a) (b) and the surface profile (c).

Table 3.1: Sintered Silver Dumbbell Sample Series				
Series	**Stencil thickness**	**Sintering Pressure**	**Sintering Temperature**	**Sintering Time**
A	200 µm	0 MPa	230 °C	30 min
B	200 µm	0 MPa	300 °C	30 min
C	200 µm	70 MPa	230 °C	30 min
D	200 µm	70 MPa	300 °C	30 min

3.2. The Cu-Ag-Cu Lap Joints

Cu-Ag-Cu lap joint series with varying geometry, sintering conditions and surface preparation were produced for shear and 3-Point-Bending (3PB) tests.

Lap joint button type samples, which are shortly called button samples, had a square sintering area of ca. 19-20 mm^2 as shown in Fig.3.4. The top buttons were sintered on a copper base, either in neighbouring pads as in Fig.3.4.a for serial shear strength measurement, or individual on 20 mm long bases with the width of 10 mm and thickness of 2 mm as in Fig.3.4.c to integrate in the 3PB setup with a resonance frequency of 20 kHz. The corresponding results are published in the first paper of this thesis in chapter 5.1: *Temperature Dependant Mechanical Properties of Sintered Silver Copper Joints*.

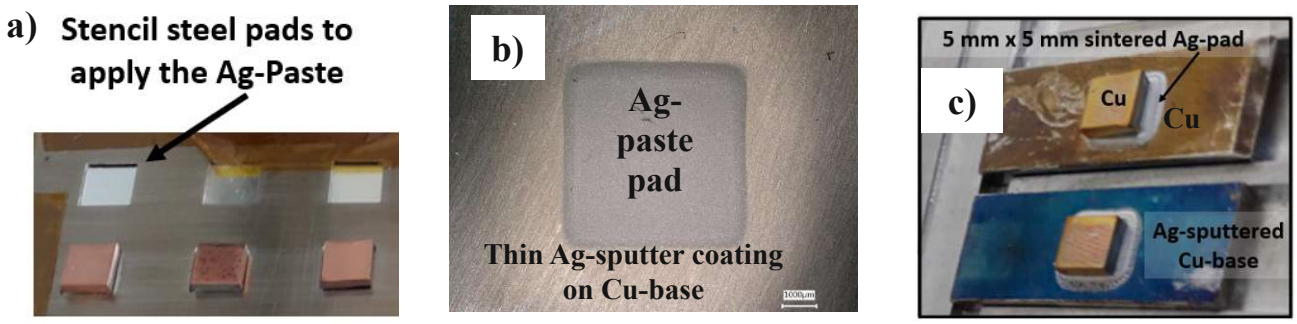

Fig.3.4: A stencil with a thickness of 100 µm and square windows (a) is used to apply the Ag-paste on the Ag-sputtered Cu-base (b). Copper tops of ca. 20 mm^2 area are then sintered under pressure to produce the button samples (c).

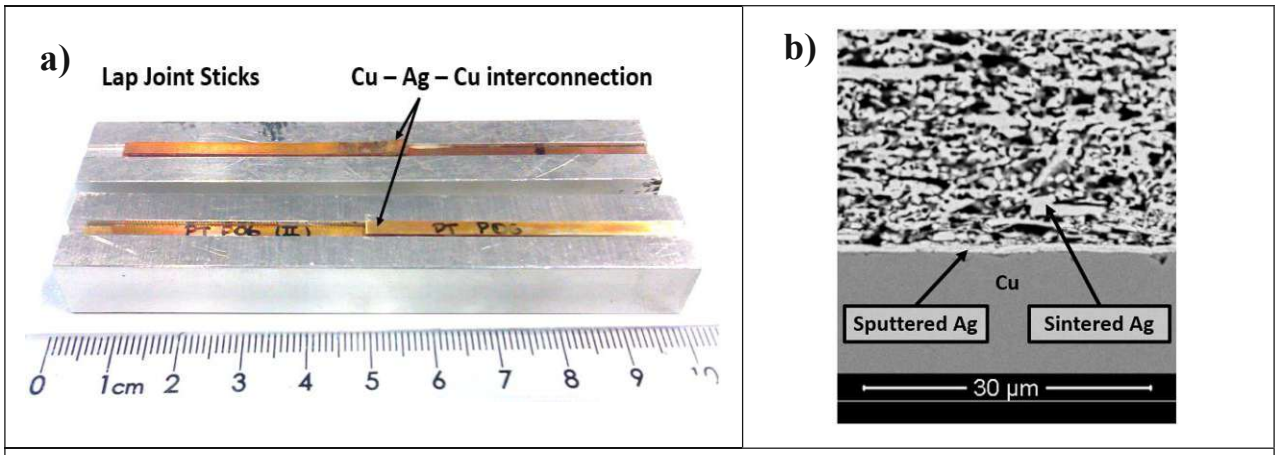

Fig.3.5: Lap-joint samples in specifically designed aluminum sample holders for sintering (a). Cross-sectional SEM image of the Cu-Ag interconnection from the mid-region (b).

Lap joint strips (as shown in Fig.3.5.a), which are shortly called lap-joints in this work, had a sintering area of ca. 10 mm^2. The long copper material pieces had a cross section of 3 x 1 mm and a length of 50 mm. The Ag-interconnected lap-joint samples were used for shear strength and cyclic lifetime measurements and stress relaxation tests.

Prior to application of Ag-paste, the surface of the Cu-base is grinded on sandpaper with sequential decreasing grain sizes down to 10 µm to remove the surface oxidation. Then the copper was rinsed in ethanol and dried by air blowing. For the production of some sample series the Ag-paste was dried directly on the cleaned copper. For the production of some other sample series, the copper surface was Ag-coated (500 nm – 1 µm) by sputtering as shown in Fig.3.5.b. The silver sintering of the lap joints was performed using an automatic programmable heating press with active cooling function and a plate size of 40 cm x 40 cm as in Fig.3.6.

Fig.3.6: Press machine with heating plates.

The lap-joint series were named as P, PT, PTP and PTS and their sintering parameters are listed in the Table 3.2. The first series were subject to studies to optimise the sintering process for shear type cyclic experiments and the results are plotted in chapter 6. Although there were mechanical cyclic lifetime measurements with the blank copper samples (PT and PTP), for the comparison of thermal effects on fatigue lifetime mainly the last PTS series were investigated. The name P stands short for 'Probe' and PT for 'Probe-Twosided', marking the application of the 100 µm Ag-paste on both copper strip sides of the interconnection (short 2x100 µm). PTS stands short for Probe-TwoSided-Sputtered. With a total thickness of 200 µm of applied silver, the sintering conditions of this last lap-joint series corresponds to the C-series of dumbbell shaped Ag-coupons, which in total gives the information both on shear and tensile testing behavior.

Table 3.2: Cu-Ag-Cu Lap-Joint (Rods) Series

Series	Surface	Stencil thickness	Sintering Pressure	Sintering Temperature	Sintering Time
P	blank Cu	100 µm	ca. 25 MPa	230 °C	60 min
PT	blank Cu	2 x 100 µm	ca. 25 MPa	230 °C	60 min
PTP	blank Cu	2 x 100 µm	> 70 MPa	230 °C	30 min
PTS	Ag-sputter metallization	2 x 100 µm	70 MPa	230 °C	30 min

3.3. Heat Treatment and Metallurgic Preparation

A thermal aging test measures changes in characteristic parameters, such as strength, void size in material or creep behaviour after the material is subjected to a constant high-temperature environment for a fixed duration [9, pp.136] and has therefore undergone microstructural changes. To study the effect of ageing on microstructure and mechanical behavior, both the Ag-coupons and lap-joints were thermally treated. Some of the samples investigated were heated up to 250 °C for 250 hours in air ambient oven, the other ones were sealed in a glass capsule to prevent further oxygen inflow as depicted in Fig.3.7. Since the porous structure of the sintered silver form a complex comb with random void paths, the penetration depth of the oxygen is not fully predictable. Especially for the lap-joints, while a clear difference of the Ag-grain size could be measured on the edges, no significant chance was observed deep inside of the samples.

The microscopic examinations were made on both the fracture surface and the grinding surface. For the latter one, the samples were embedded in resin as shown in Fig.3.8. and polished up to 1 µm. It shall be mentioned that also the method of the investigation may play an important role. For example, to determine the density of the 3-dimensional porous structure by the optical method usually the 2-dimesional conversion of a region is reckoned. As mentioned, a specific segment of the sample such as corners, can give a different information than another segment. Also, the preparation of a section e.g. by etching may influence the resulting outcome.

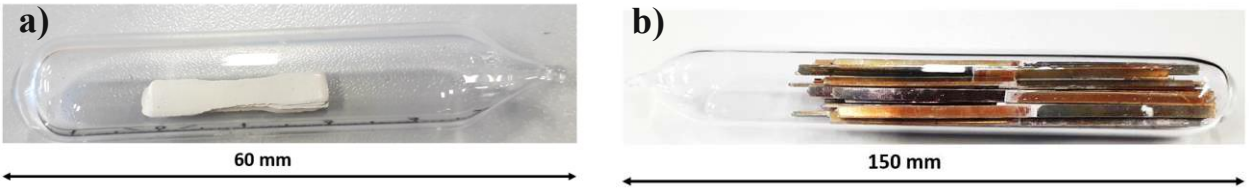

Fig.3.7: Dumbbell shaped sintered Ag-coupons (a) and Cu-Ag-Cu lap-joints are placed in sealed glass to prevent oxygen income during thermal treatment.

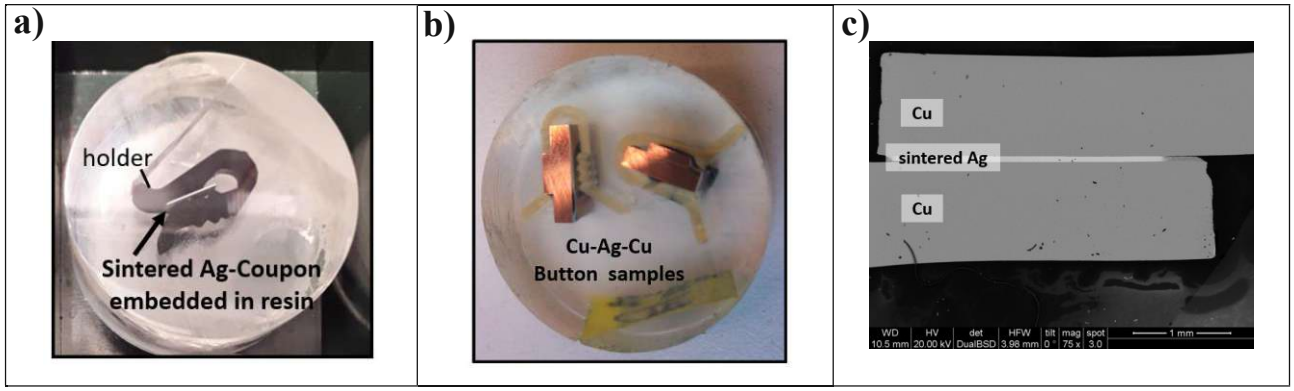

Fig.3.8: Cross-section of an Ag-Coupon (a), Cu-Ag-Cu Button samples (b) and SEM image of a Lap-Joint (c) embedded in resin.

3.4. Testing Setup

To perform the shear, tensile, stress relaxation, and cyclic fatigue tests a tensile machine of MESSPHYSIK Materials Testing (max. strength capacity 1 kN) in combination with various sample holders and load cells (capacity 100 N, 500 N and 1 kN) of AEP Transducers with a resolution up to 0,1 mN was used. One setup type is shown in Fig.3.9 for shear testing of button style lap joints, where the scraper tip pushes down while measuring the force to detach the sintered joint.

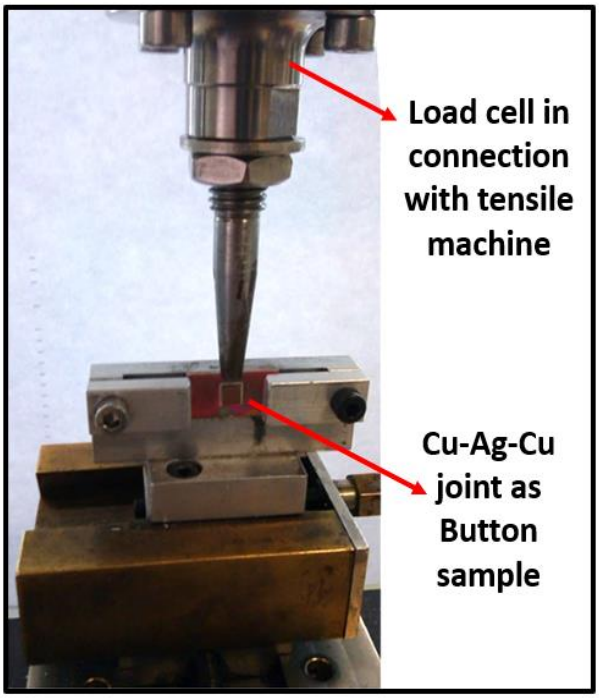

Fig.3.9: Testing setup for shearing button samples.

Another setup type is shown in Fig.3.10 for tensile testing of Cu-Ag-Cu lap-joint strips or sintered Ag-coupons with dumbbell shape. The latter one was equipped with a laser speckle extensometer (LSE) which enabled contactless strain measurement of the investigated material. Two laser beams are directed at the sample surface at a calibrated distance. The created speckle pattern is captured by the two cameras (Fig.3.10.a). When testing was performed, the movement of the marked regions was envisaged and the displacements remotedly measured with a resolution of 0,1 µm (Fig.3.10.b) along with the force applied by the tensile machine. This setup was mainly used to obtain the elastic modulus in-situ during tensile testing, and to compare the stress-strain behaviour measured locally on the sintered and relatively small Cu-Ag-Cu area with the behaviour of the lap-joint for depicted representative samples.

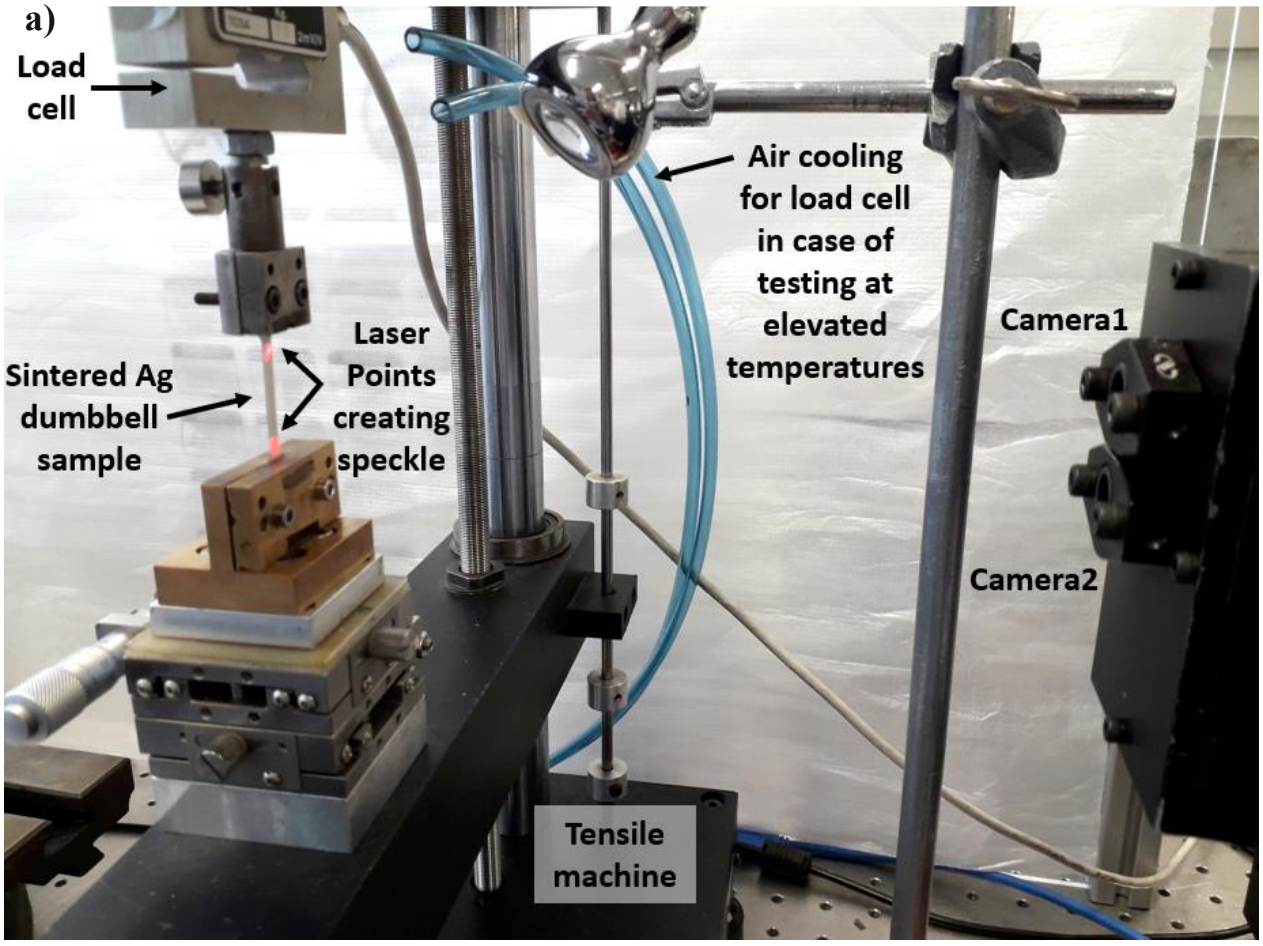

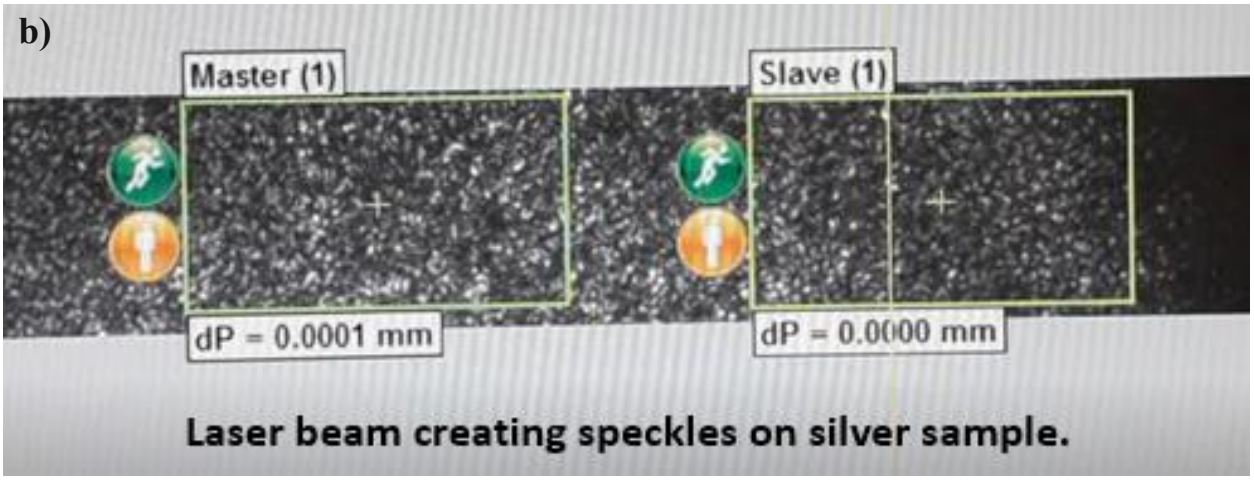

Fig.3.10: Testing setup with Laser Speckle Extensometer (a) and strain measurement directly on the sintered silver (b).

3.5. Thermal Calibration

To perform the stress tests at elevated temperatures mainly two methods were carried out: heating of the lap-joints by eddy currents and convection heating of the dumbbell Ag-coupons in a constructed chamber around the sample in the tensile machine.

As shown in Fig.3.11.a the lap-joint sample was placed in a solenoid as inductor, while being clamped in the stress-strain machine. The temperature was measured with both a thermal camera and a thermocouple. The advantage of this setup is that the main heat is created in the coil region and the testing machine is not directly affected as shown in Fig.3.11.b. Both copper and silver being diamagnetic materials with the relative permeability $\mu_r \approx 1$ temperatures only up to 150 °C could be observed. To reach temperatures above this level, an iron wire was wrapped around the sample. In this case to prevent overheating over the preset 200 °C, a thermocouple connected to the lap-joint with heat paste as shown in Fig.3.11.c served as feedback to the circuit controller. The off-and-on regulation caused an ongoing fluctuation of the sample's temperature in the range of ca. 10-15 °C, which was not preferable especially during relaxation experiments. The method with convection heating was chosen for most of the tested samples. For this purpose the tensile testing machine was covered with a thermal chamber as in Fig.3.12.a. The heating source was a hot air blower connected to the chamber, and again a thermocouple was placed on the sample. The preset temperature levels of the heater were observed along with the actual sample temperature levels (Fig.3.12.b) and calibration curve in the temperature range of the tests was plotted (Fig.3.12.c). The silver coupons had a steeper slope than the Cu-Ag-Cu joints and reached the 200 °C sample temperature already at around 300 °C setting value. Because the heat convection reached also other elements of the setup such as the load cell, additional air cooling was turned on during operation of the heater.

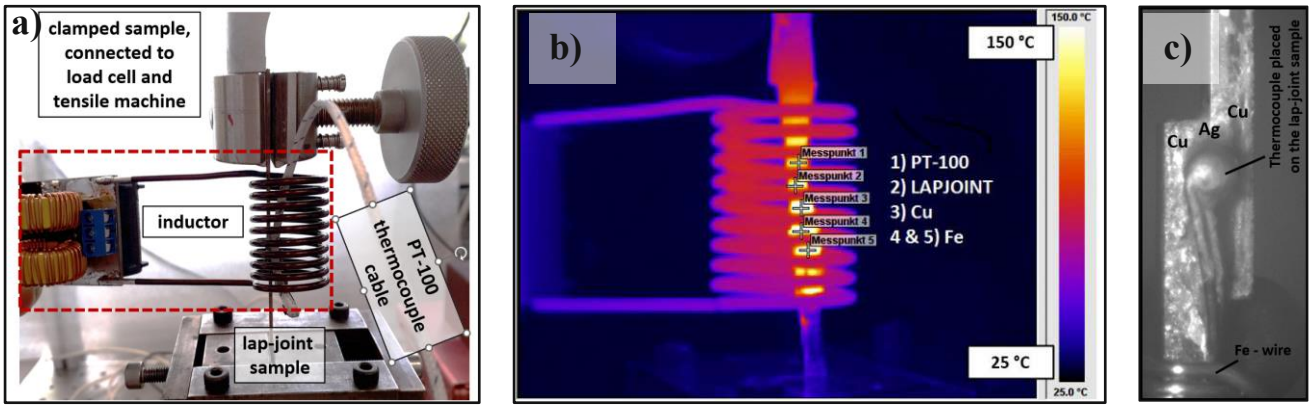

Fig.3.11: To create a heating effect the lap-joint was placed in an inductor circuit (a) and the temperature was measured with both a thermal camera (b) and thermocouple (c).

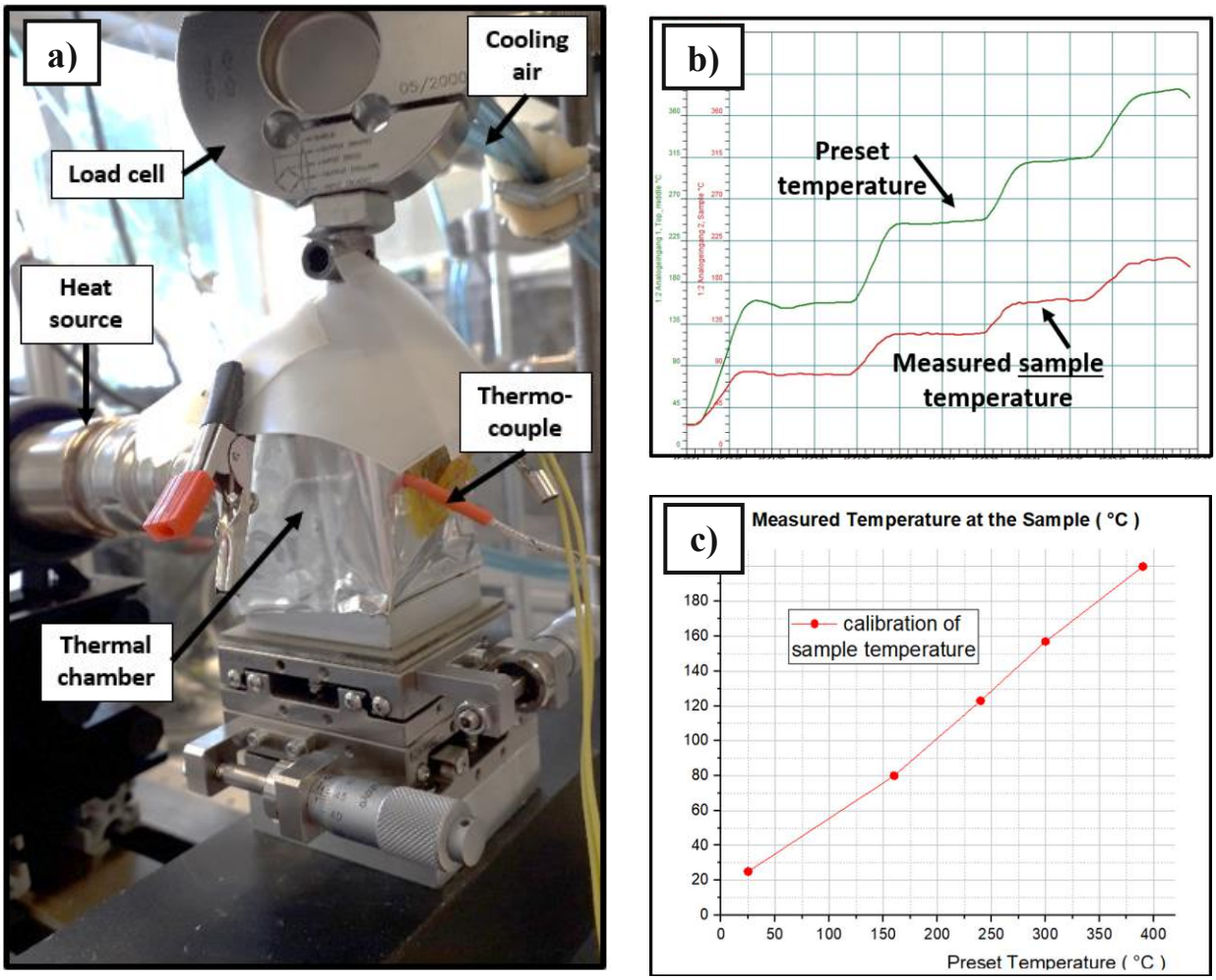

Fig.3.12: Tensile machine with a thermal chamber covering the sample under test (a). The calibration of the heater and sample temperature (b) delivering a near linear behaviour in the experimental range (c).

CHAPTER 4

TEMPERATURE DEPENDENCE of MATERIAL BEHAVIOUR

In the previous chapter the preparation of the various sintered silver dumbbell series for tensile experiments and the silver sintered copper lap joints for shear experiments are described, also the preparation of the samples with thermal treatment and the procedure for the microscopic investigations. Furthermore, the testing setup for the studies on the mechanical properties at room and elevated temperatures and cyclic lifetime is described.

In this chapter the focus lies on the presentation of the obtained results, emphasizing the influence of oxygen containing atmosphere during thermal treatment after sintering and the influence of testing temperature on the mechanical behaviour of the sintered silver samples. The investigation on failure characteristics provides the information required for the end-of-life estimation of the sintered silver joints in various thermal conditions.

4.1. Investigation Results Obtained With Ag-Coupons

The dumbbell shaped samples of porous silver are gained by sintering a commercial Ag-paste of Heraeus the ASP-338 series. The various sintering conditions in preparation of the main series are listed in the Table 3.1. Further, the thermal treated samples are marked either with 'A-Aged' meaning thermally aged in air atmosphere or with 'G-Aged' meaning thermally aged in a sealed glass tube with restricted oxygen content, in both cases at 250 °C for 250-hours, as described in chapter 3.3. Samples as sintered (without thermal treatment) are marked with '0-hour'. The series were subject to investigations on density evaluation, electrical measurement, tensile strength and relaxation testing at room and elevated temperatures.

4.1.1. Investigation of Microstructure

The characteristic microstructure of the sintered silver varies with the sintering conditions (pressure, temperature, and time). A dense microstructure composition is anticipated by applying a high pressure of 70 MPa and coarsening of the pores is expected at the higher sintering temperature of 300 °C. The electron microscopy images from the fracture cross section of the Ag-dumbbells for the sample series A, B, C, and D are shown in Fig.4.1.a-d at a magnification of $6x10^3$, as well as the images of the other selected sample series sintered at various pressures in Fig.4.2.a-c, all after the same sintering duration of 30 minutes.

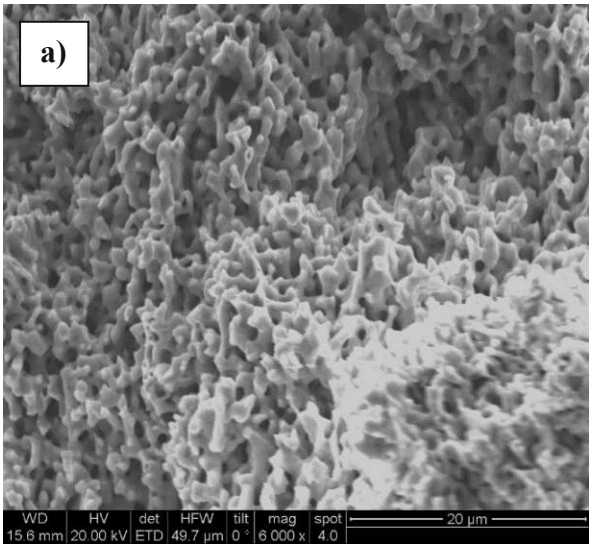

A: 0 MPa, 230 °C, 30 min

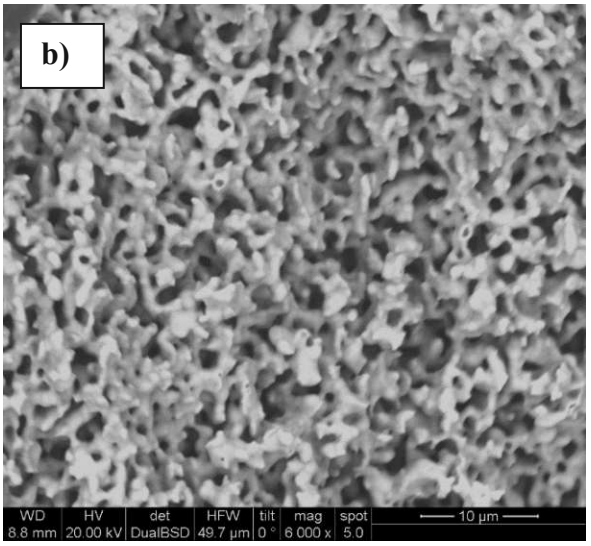

B: 0 MPa, 300 °C, 30 min

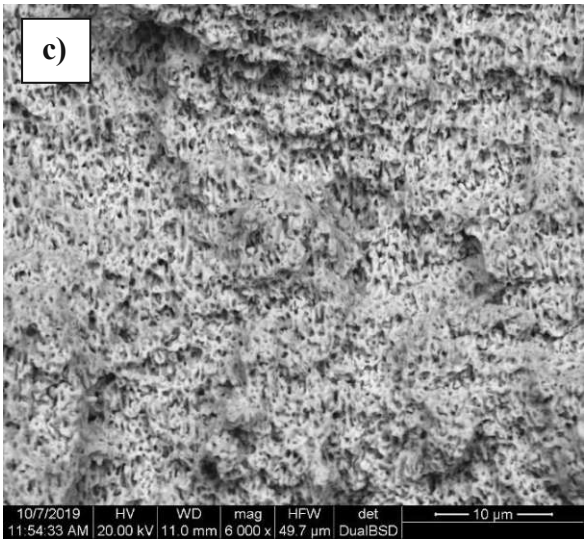

C: 70 MPa, 230 °C, 30 min

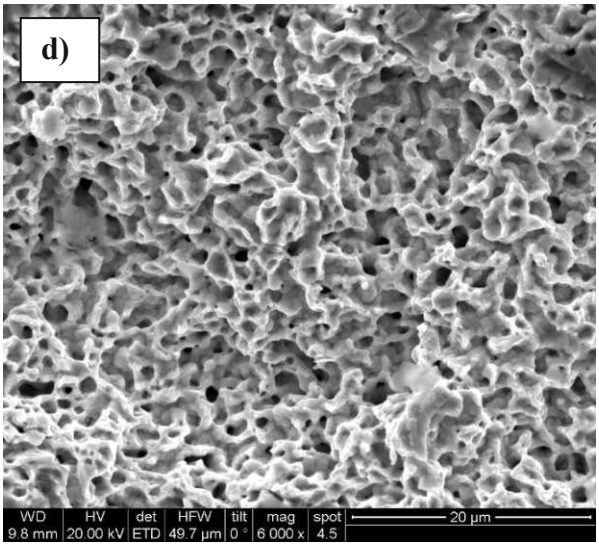

D: 70 MPa, 300 °C, 30 min

Fig.4.1: 0-hour, Fracture surface SEM images of the sintered silver for the main series A (a), B (b), C (c) and D (d) with sintering conditions as in Table 3.1.

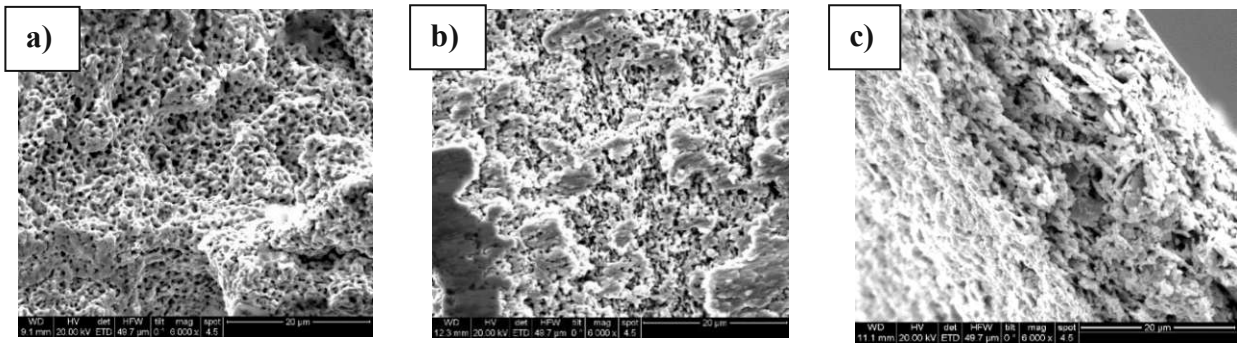

35 MPa, 230 °C, 30 min. 50 MPa, 230 °C, 30 min. 90 MPa, 230 °C, 30 min.

Fig.4.2: 0-hour, Fracture surface SEM images of the silver which is sintered under various pressures of 35 MPa (a), 50 MPa (b) and 90 MPa (c) at 230 °C and for 30 minutes.

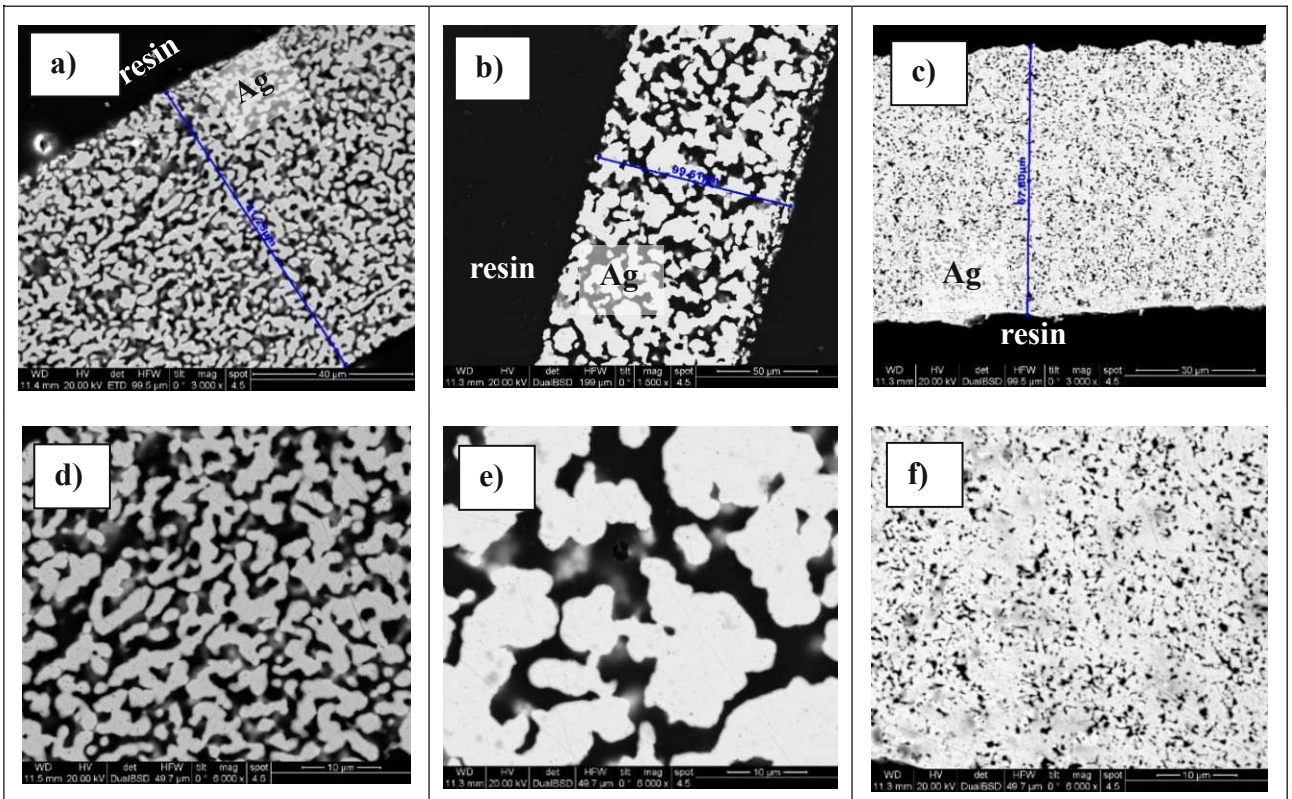

A: 0 MPa, 230 °C, 30 min B: 0 MPa, 300 °C, 30 min C: 70 MPa, 230 °C, 30 min

Fig.4.3: Grinding surface of the sample series A (a)(d), B (b)(e) and C (c)(f) which were embedded in epoxy resin after ageing in a sealed glass tube at 250 °C for 250-hours.

In comparison to the 0-hour samples in Fig.4.1, the microscopic images of the G-Aged and A-Aged ones are shown in Fig.4.3-4.4 and Fig.4.5.

Compared to the 3D fraction zone in Fig.4.4, Fig.4.3 shows the electron microscope images of the grinded 2D surface for the G-Aged series A, B and C. This perspective directly revealed the necking connections and the size of the voids in the sintered silver, for the observed segment slice. The comparison of Fig.4.3.d and Fig.4.3.e showed that apart from the diameter size of the Ag-particles, the consolidation of the interconnecting paths is strongly dependent on the temperature. This might be the result of the self-diffusion of silver atoms due to thermal kinetics. The density analysis of the grinded surfaces with the monochromic imaging method gave for both the 0-hour and G-Aged series of A-type samples a porosity of around 40 %. A comparison to the mass/volume evaluation of the density is discussed in chapter 5.

The most obvious change due to thermal treatment in air atmosphere was the growth of the round shaped Ag-particles for the pressureless sintered series A (Fig.4.5.a) and B (Fig.4.5.b), whereas no significant enlargement of the grain size could be observed (Fig.4.4.a-b) in case of the sealed glass with confined oxygen.

Beside the grain growth another ongoing process under heat treatment is the accumulation of the pores. Chuantong Chen et al. [44] reported, in comparison to the samples aged for 1000 hours in vacuum which almost kept the initial state, a coarsening of the sintered silver's microstructure after aging at 250 °C in air for 100 hours; and a decrease in pore number while the average pore size increased from 0.6 µm up to 1.5 µm with thermal exposure time after 250 hours in air.

For our series of type C which were sintered under high pressure, the dimple-like structure of the A-Aged pores showed diameters up to ca. 4 µm as in Fig.4.5.c., whereas only a small enlargement of the voids was observable when fracture surface images of the 0-hour (Fig.4.1.c) and G-Aged (Fig.4.4.c) samples are compared.

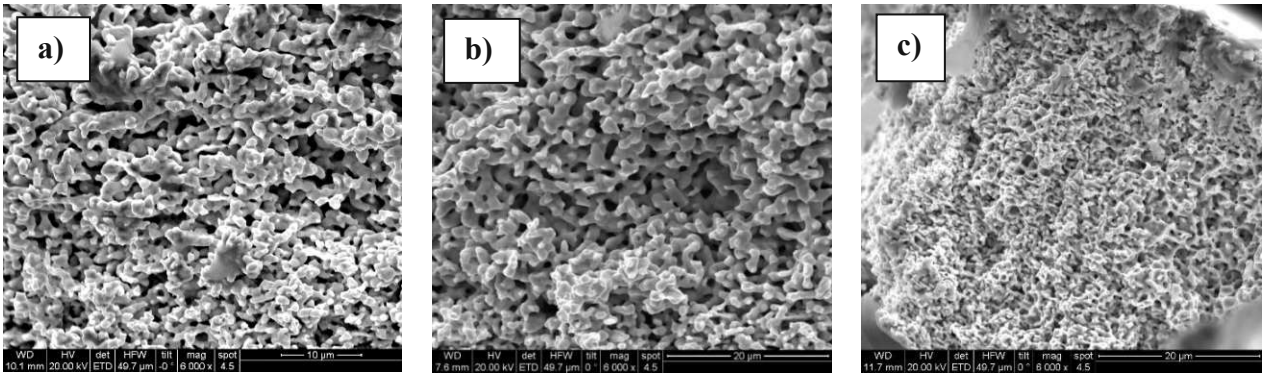

A: 0 MPa, 230 °C, 30 min B: 0 MPa, 300 °C, 30 min C: 70 MPa, 230 °C, 30 min

Fig.4.4: Fracture surface of the sample series A (a), B (b) and C (c) which were aged in sealed glass tube at 250 °C for 250-hours.

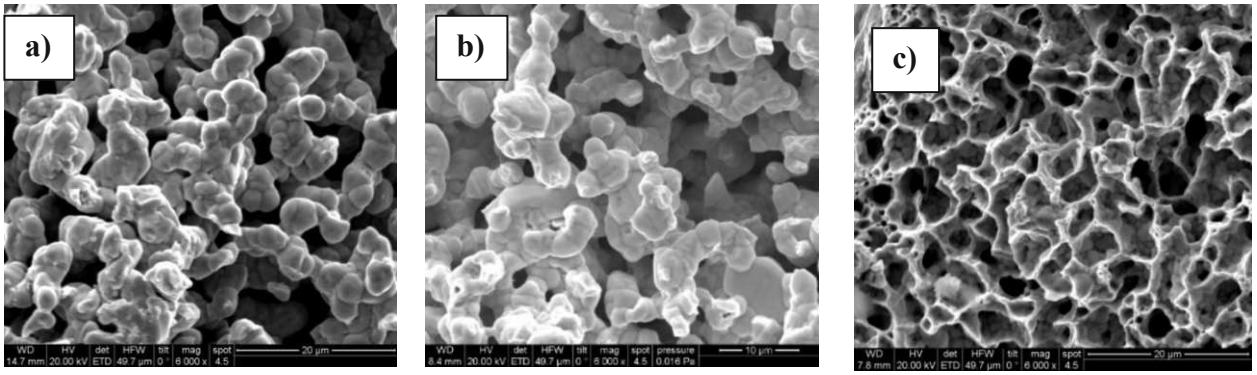

A: 0 MPa, 230 °C, 30 min B: 0 MPa, 300 °C, 30 min C: 70 MPa, 230 °C, 30 min

Fig.4.5: Fracture surface of the sample series A (a), B (b) and C (c) which were aged in air ambient at 250 °C for 250-hours.

Silver at room temperature has a rather stable condition considering the oxidation. But the presence of oxygen seems to play a significant role on the microstructure of the sintered silver at elevated temperature and hence its mechanical properties. A possible explanation is the formation of Ag_2O at 250 °C and the follow-up decomposition of the unstable silver oxide into silver nanoparticles, filling up the voids between neighbouring particles and finally merging into a bigger Ag-particle together with the neighbouring elements to minimise the surface energy [44]. This would also explain the self-healing of the cracks in the range of 10 nm in the Ag-layer after heating at 200 °C up to 100 hours as described by Chuantong Chen et al. [45]. In the latter case, the heat treatment increased the tension strength. C. Choe et al. [46] reported a variation of the tensile strength for pressureless sintered silver (sintering parameter 250 °C, 1 hour) after isothermal ageing at 250 °C depending on the exposure time.

It should be noted that the thermal treatment in the literature is assumed as being performed in air, if not stated otherwise or specifically stated as vacuum ageing, especially when accompanying grain coarsening and pore accretion is reported.

The newly performed bonds of sintered silver after heat treatment may have a different response to the stress than as-sintered condition, and the cycling lifetime may alter as the change in grain size and boundaries can influence the mechanical behaviour. In the next sections the influence of thermal treatment on the stress-strain characteristics will be investigated.

4.1.2. Tensile Strength

From the various specimen of produced samples, the stress-strain characteristics particularly of the three main series A, B, and C were investigated. The tensile strength was obtained at three testing temperatures of 25°C, 130°C and 200°C with a crosshead speed of 1 mm/min, as depicted in Fig.4.6. The tensile measurements of the 250-hours G-Aged samples are also plotted in the same figure on the right sides. For each series 4 – 14 samples were tested. The porous silver sintered without pressure i.e., the A and B series have mean tensile strength values of ca. 14 MPa and 17 MPa, whereas the high pressure sintered series C has a mean value of 56 MPa with a maximum reaching up to 95 MPa at room temperature. Comparing the individual average values of the 0-hour and 250-hours series we observe both, enhancement and deterioration of the tensile strength. The fall of the tensile strength with increasing testing temperature can well be recognized in all cases Fig.4.6.a-c with the exception of the G-aged samples of the C-series tested at 25 °C / 130 °C. In this latter case only 5 samples were tested and one of these exhibited an exceptionally high strength (the test run of this sample is depicted in Fig. 4.9.d, sample test identification #517). This exception causes the high maximum value in the strength diagram (Fig. 4.6.c, right side).

Figures 4.7 - 4.9 show the stress (σ) - strain (ε) behaviour of the corresponding series A, B and C at the testing temperatures of 25 °C, 130 °C and 200 °C, again with the same testing speed of 1 mm/min, respectively. The 0-hour series are plotted in the left columns, the 250-hours G-Aged series are plotted in the right columns. Three selected samples for each of the 18 test series represent the maximum tensile strength region. At room temperature: A clear brittle fracture characteristic is given for the 0-hour series A, B and C. At the stress level of 20 MPa, in the elastic region, the system strain is approximately around 0.4 % for the pressureless sintered samples (Fig.4.7.a and Fig.4.8.a) with more porous Ag-structure, and 0.1 % for the pressure sintered hence dense samples (Fig.4.9.a). The 250-hours G-Aged series also show a rather brittle behaviour. In the latter case, a clear increase of strain above 0.3 % corresponding to 20 MPa is observed for the C samples (Fig.4.9.b).

With increasing testing temperature: especially at 200 °C a clear ductile characteristic is given for all the series A, B, and C; and for both 0-hour (Fig.4.7.d, Fig.4.8.d and Fig.4.9.d) as well as 250-hours G-Aged (Fig.4.7.e, Fig.4.8.e and Fig.4.9.e). At the testing temperature of 200 °C the yield point of the 0-hour series is observed around 10 MPa for the pressureless sintered samples A and B, and 30 MPa for the pressure sintered samples C.

Fig.4.10 shows an example of the automatic in-situ evaluation of the elastic modulus during measurement with the LSE directly at the sintered silver bulk as described in chapter 3. The load-unload hysteresis was measured at a testing speed of 0.2 mm/min. At room temperature especially for the 0-hour samples no significant ductile characteristic was observable in the stress-strain plot because the samples fractured immediately after reaching the ultimate tensile strength (UTS), hence no specific yield point as transition into plastic regime could be defined.

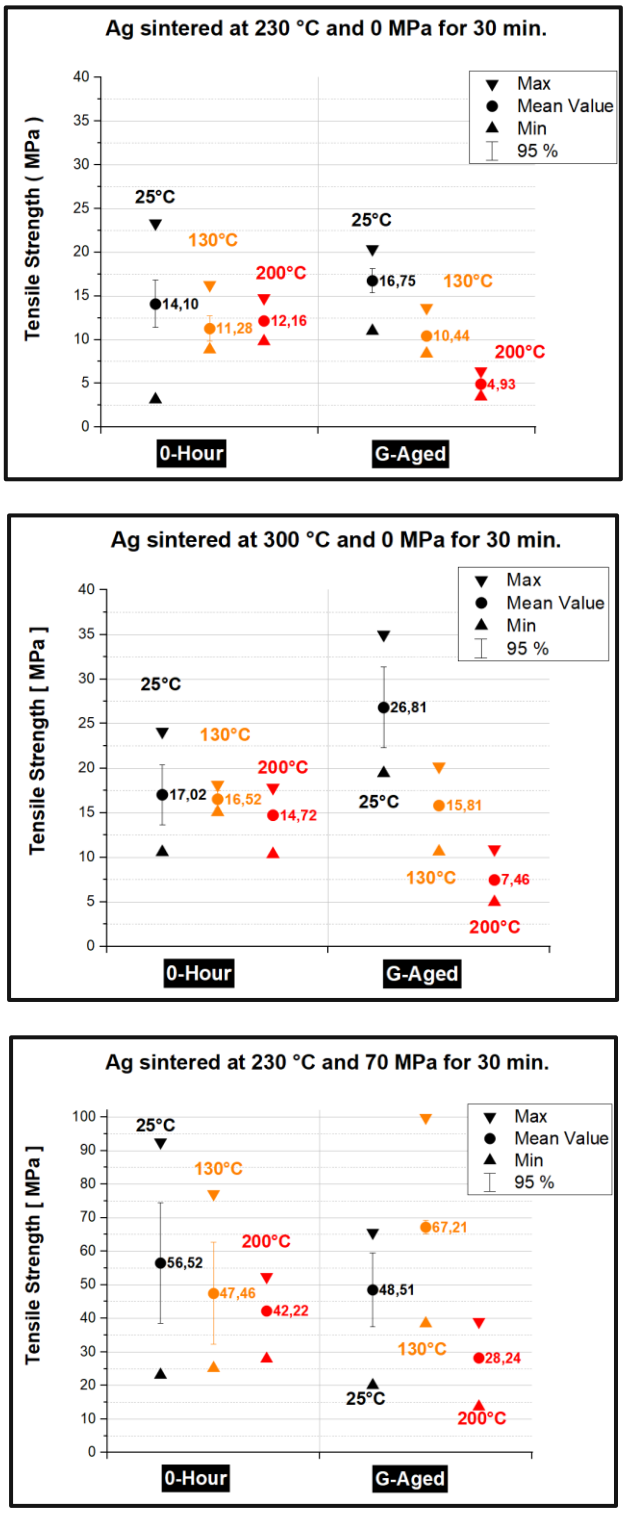

Fig 4.6: Comparison of tensile behavior for the dumbbell shaped sample series A (a), B (b) and C (c) of sintered silver; at testing temperatures of 25 °C, 130 °C and 200 °C; at the testing speed of 1 mm/min; for 0-hour vs. 250-hours at 250 °C thermal treatment (G-Aged).

Series A: 0-hour (no thermal treatment)	**Series A: 250-hours thermal treatment** at 250 °C in protective glass
a) 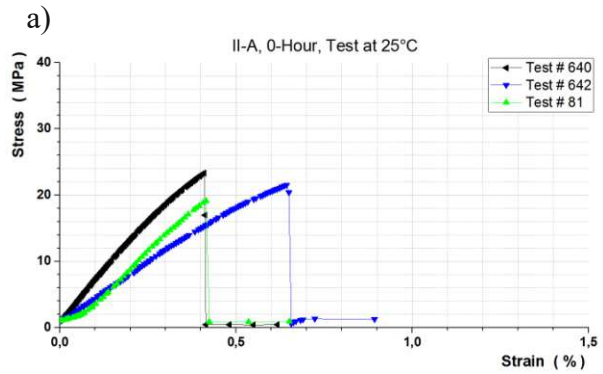	b) 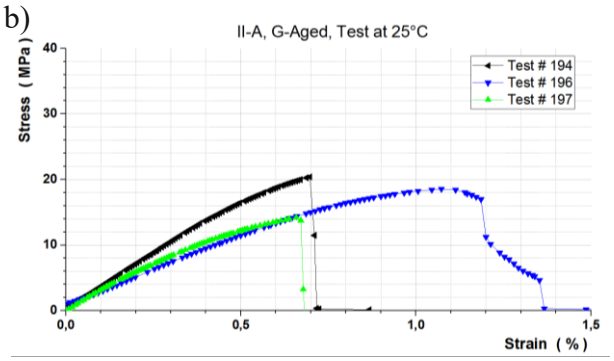
c) 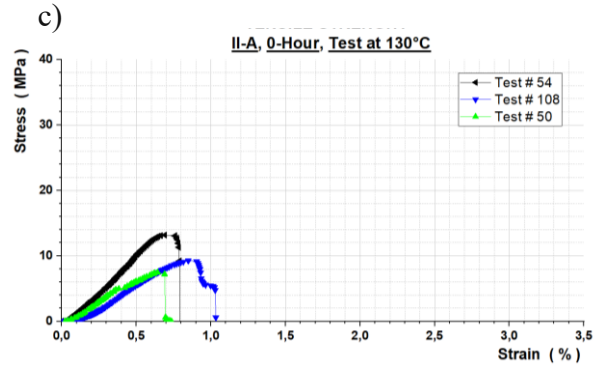	d) 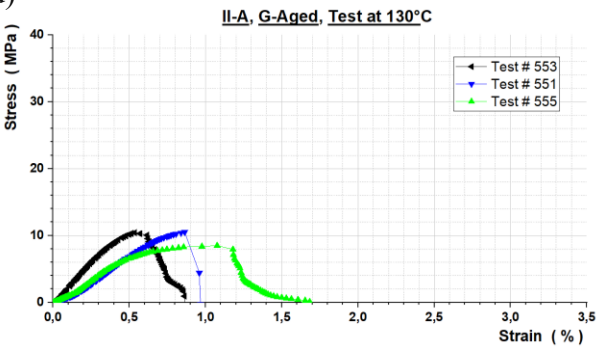
e) 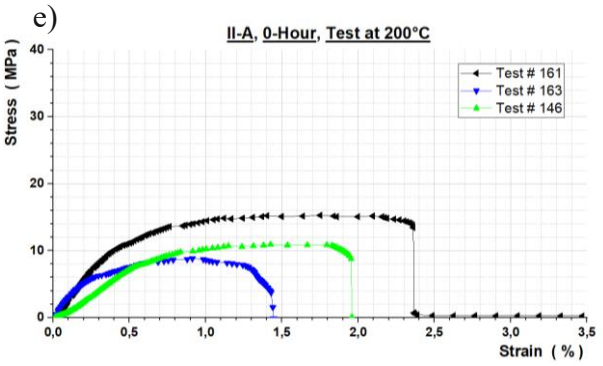	f) 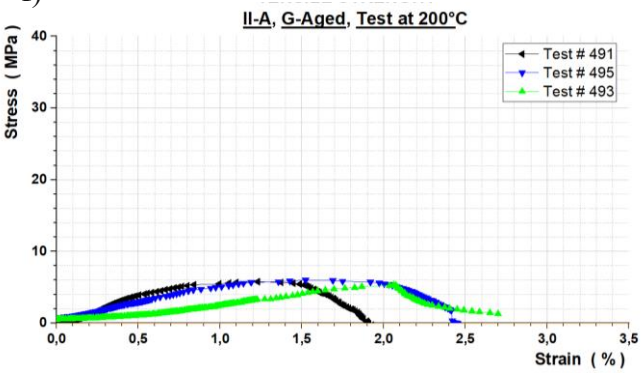

Fig.4.7: Tensile stress-strain behavior for the dumbbell sample series of porous silver A, pressureless sintered at 230 °C for 30 minutes. Comparison of 0-hour (a)(c)(e) vs. 250-hours (b)(d)(f) thermal treatment (G-Aged) at testing temperatures of 25 °C, 130 °C and 200 °C and testing speed of 1 mm/min.

Series B: 0-hour (no thermal treatment)	**Series B: 250-hours thermal treatment** at 250 °C in protective glass
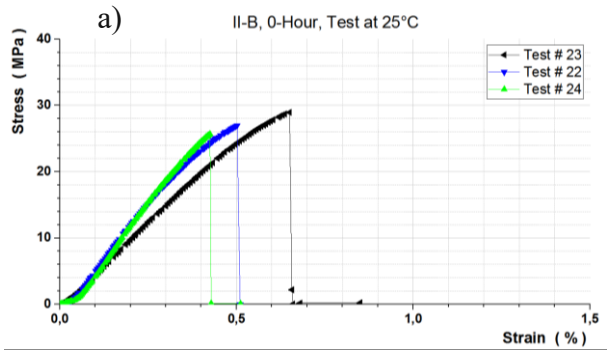	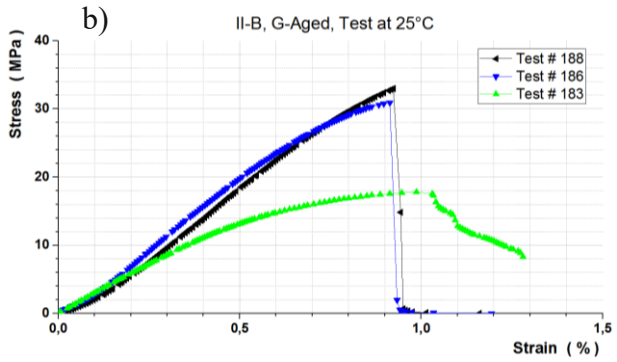
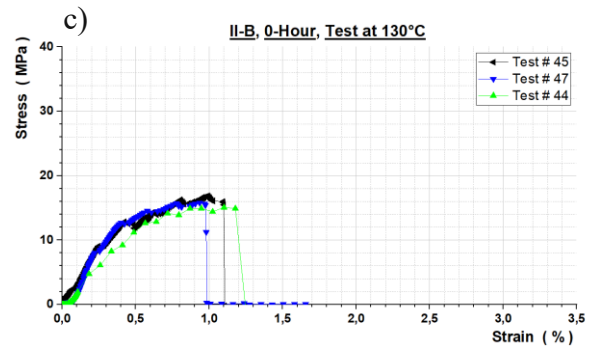	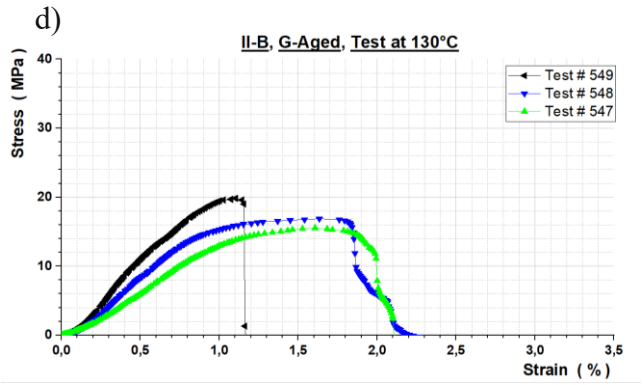
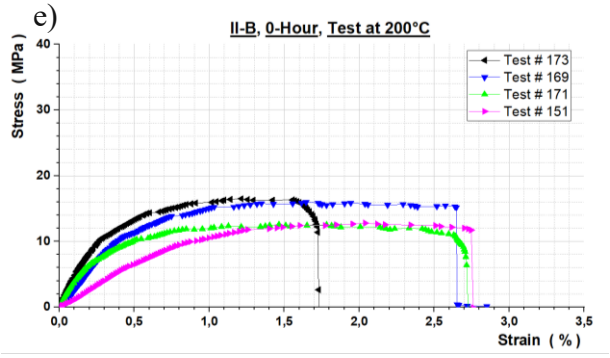	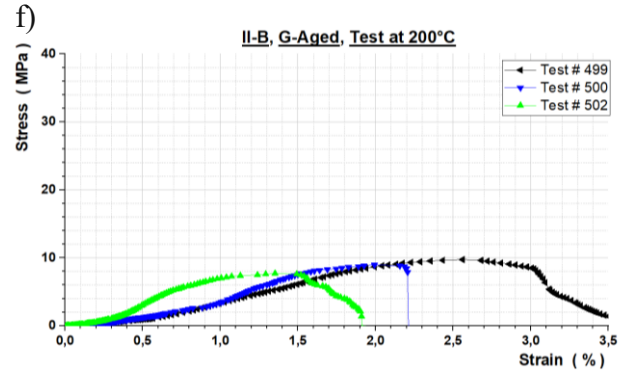

Fig.4.8: Tensile stress-strain behaviour for the dumbbell sample series of porous silver B, pressureless sintered at 300 °C for 30 minutes. Comparison of 0-hour (a)(c)(e) vs. 250-hours (b)(d)(f) thermal treatment (G-Aged) at testing temperatures of 25 °C, 130 °C and 200 °C and testing speed of 1 mm/min.

Series C: 0-hour (no thermal treatment)	**Series C: 250-hours thermal treatment** at 250 °C in protective glass
a) 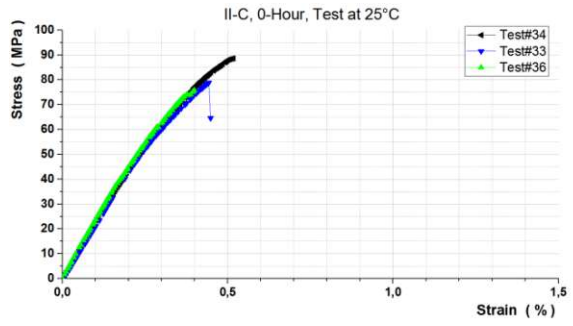	b) 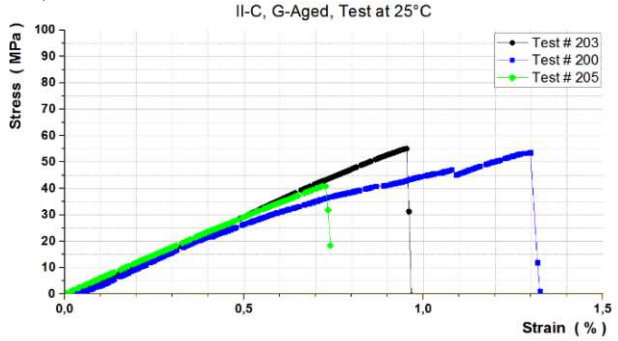
c) 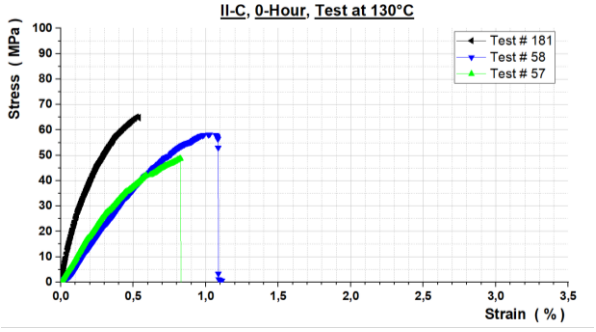	d) 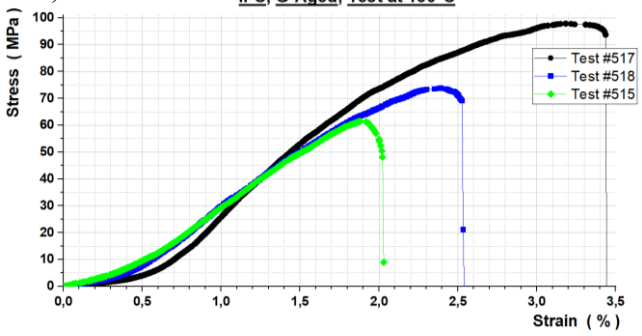
e) 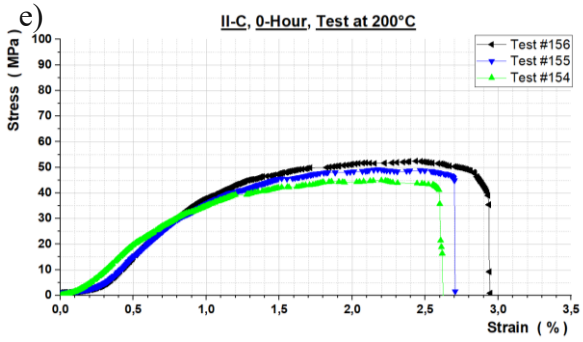	f) 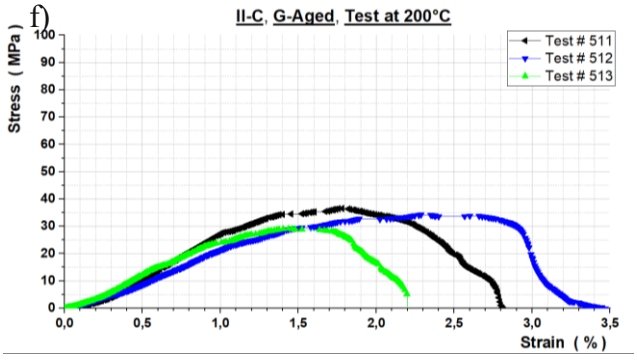

Fig.4.9: Tensile stress-strain behaviour for the dumbbell sample series of dense silver C, sintered at 70 MPa and 230 °C for 30 minutes. Comparison of 0-hour (a)(c)(e) vs. 250-hours (b)(d)(e) thermal treatment (G-Aged) at testing temperatures of 25 °C, 130 °C and 200 °C and testing speed of 1 mm/min.

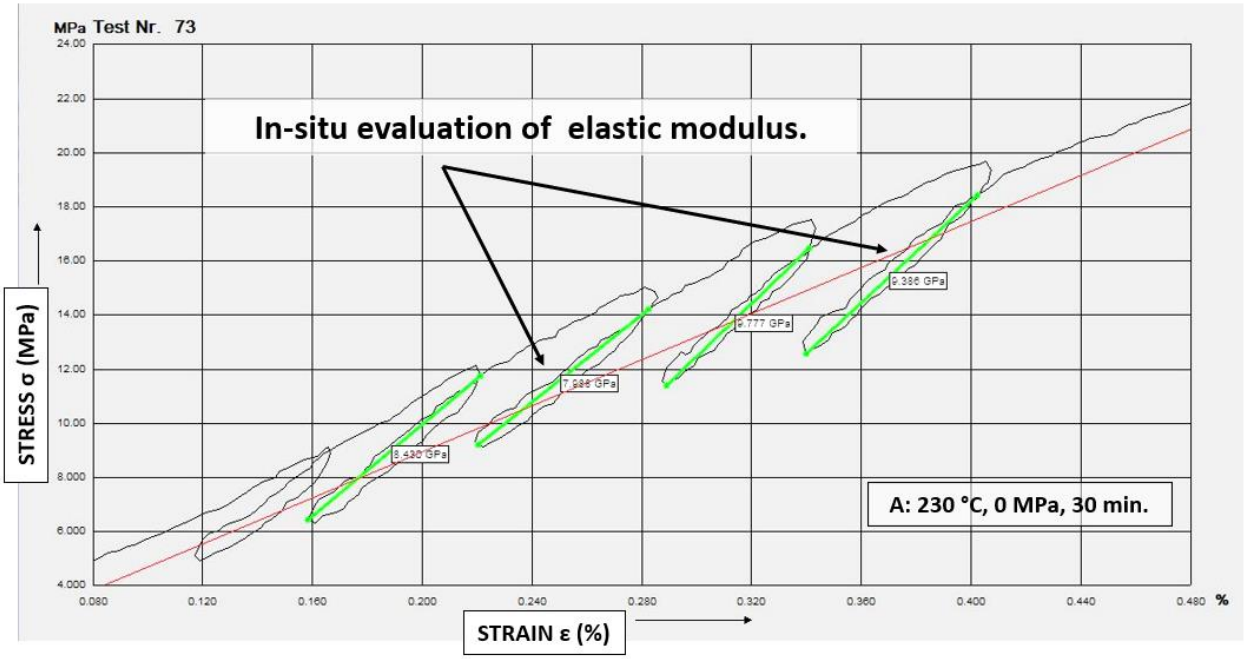

Fig 4.10: In-situ measurement of the elastic modulus of an Ag-dumbbell sample (series A) during stress-strain measurement with LSE (and testing speed of 0.2 mm/min).

In comparison to E-modulus for bulk silver which is around 80 GPa [75] [78], for the sintered silver series the averaged values for the elastic modulus *E* determined from the experiments are given in Table 4.1. The column 4.1.b of the system shows in general a lower value than the column 4.1.a of the LSE due to the distinction of the setup elasticity. Similar observation is made for the steeper stress-strain measurement with the LSE in the linear elastic regime of the lap-joint (Fig.4.24).

Table 4.1: E-Modulus of sintered Ag-dumbbells measured at room temperature, determined with LSE directly at the silver material (a) and determined from experimental slope of the stress-strain plots (b-c).

Sample Series	(a) 0-hour LSE insitu	(b) 0-hour System	(c) 250-hours G-Aged System
A	8.9 GPa	5 GPa	2.5 GPa
B	5.6 GPa	5 GPa	3.3 GPa
C	38 GPa	20 GPa	6 GPa

4.2. Results of Cu-Ag-Cu Joints Investigation

The Cu-Ag-Cu lap-joint samples are produced by sintering under 70 MPa pressure and at 230 °C for 30 minutes, corresponding to the C dumbbell series. Again, samples as sintered (without thermal treatment) are marked with '0-hour' and the thermal treated samples are marked either with 'A-Aged' meaning thermally aged in air atmosphere or with 'G-Aged' meaning thermally aged in protective glass ambient, in both cases at 250 °C. 250-hous or 500-hours duration is given depending on the time kept in the reflow oven. On the base of naming different series, to this chapter relevant lap-joint samples are called PTS. For the practical reason of being able to trace back the individual samples, this tag from the experimental days in the laboratory is kept in this work.

4.2.1. Microstructural Characterization

The microscopic characterization of the Cu-Ag-Cu lap-joint samples include the scanning electron microscope (SEM) images, the focused ion beam (FIB) processed area of the sintered silver with neighboring copper region, the energy dispersive x-ray (EDX) scan of the section, the electron backscatter diffraction (EBSD) mapping, transmission electron microscope (TEM) images and electron energy loss spectroscopy (EELS) line scan.

The SEM images of the FIB processed areas of the sintered silver within the Cu-Ag-Cu lap-joints are given Fig. 4.11. The first image belongs to silver as sintered under 70 MPa (Fig.4.11.a) exhibiting a dense character of the Ag section. The second image (Fig.4.11.b) is taken after thermal treatment of the sample at 250 °C for 250 hours in protective glass ambient, where a confined growth of the pores can be observed. The Ostwald ripening, driven by the surface-to-volume energy, describes the increase of the pore diameter due to agglomeration inside the sintered volume. In the following images the change in the states of the pores after 250 hours (Fig.4.11.c) and 500 hours (Fig.4.11.d) in air atmosphere is clearly noticeable. The comparison of the A-Aged and G-Aged samples at the same temperature and for the same duration show the role of the air in the pore growth.

The evaluation of the silver density for these four sample types are pursued based on monochromatic image analyzing method. For the 0-hour sample (as sintered) the porosity obtained by imaging processing is around 5-6 %, for the 250-hours A-Aged and G-Aged samples 6-9 % and for the 500-hours A-Aged sample around 20 %. The vast difference in density obtained versus the mass/volume method is discussed in chapter 6.

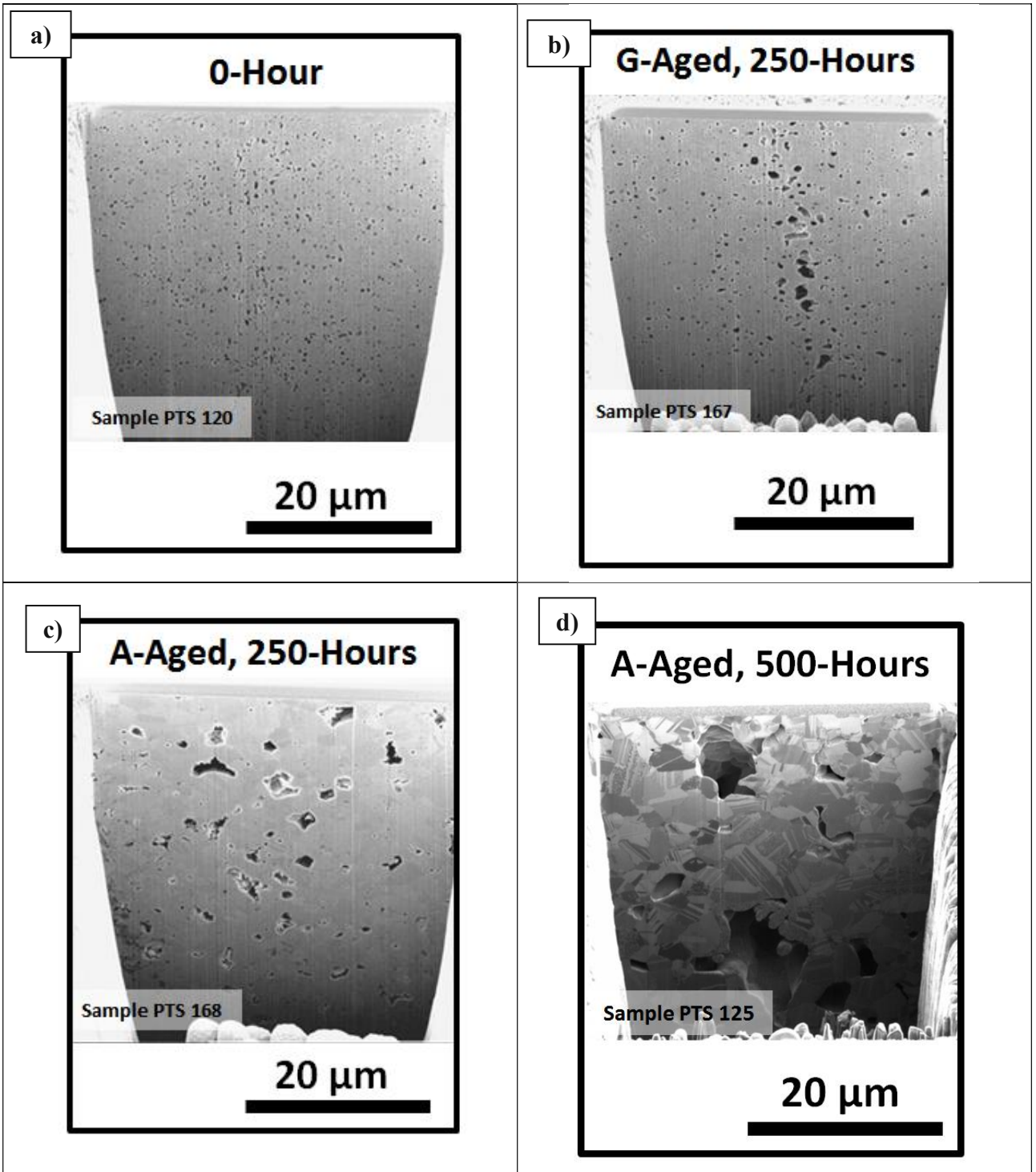

Fig.4.11: The FIB processed area of the sintered silver within the Cu-Ag-Cu lap-joint as sintered (a) and after thermal treatment at 250 °C for 250 hours in protective glass ambient (b) vs. 250 hours (c) and 500 hours (d) in air atmosphere.

The grinded surface of an A-Aged lap-joint is given in Fig.4.12. Fig.4.12.a shows an overview of the cross-section where a distinction of the pores shape is remarkable between the joint's center as in Fig.4.12.b and the margin of the joint as in Fig.4.12.c. Jie Li et al. [47] remarks that the outgassing of the organics in the sinter paste may hinder a deeper oxygen diffusion into the inner zone. The EDX analysis as in Fig.4.12.d reveal the oxygen existence on the copper-silver junction and the oxide layer actually continues some way along the interface to the inner section of the joint as in Fig.4.12.b.

The SEM images and EBSD analyses of the lap-joints' surfaces for G-Aged and A-Aged samples are given in Fig.4.13. Thermal treatment at 250 °C for 250 hours in protective glass ambient has no further effect on the pores' diameter (which is under 1 µm) and grain size. Thermal treatment at the same temperature in air ambient for 500 hours leads to pores up to 10 µm diameter and growth of grain size, which effects the crack propagation and mechanical response of the material.

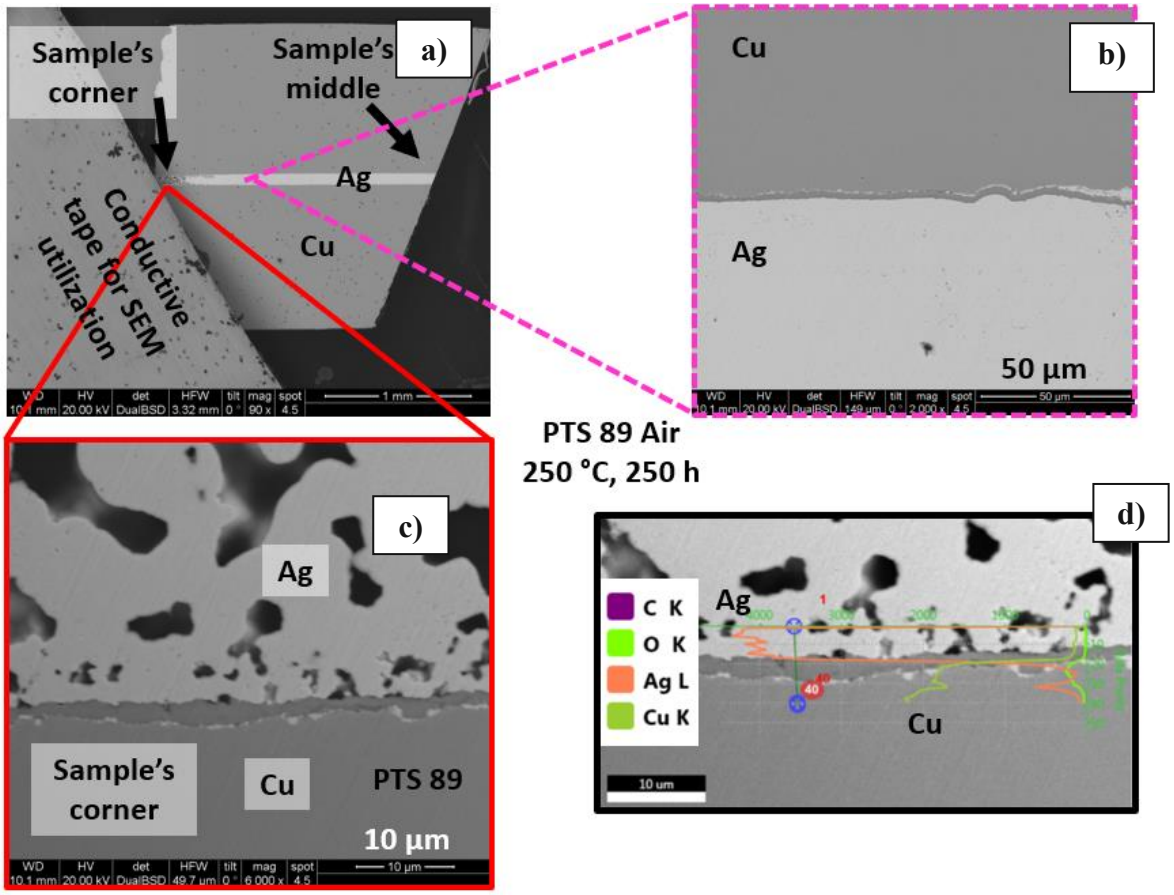

Fig.4.12: Grinding surface of an A-Aged lap-joint showing (a) the effect of the oxygen in the middle of the sample (b) vs. near corner (c) and EDX analyses of the latter (d).

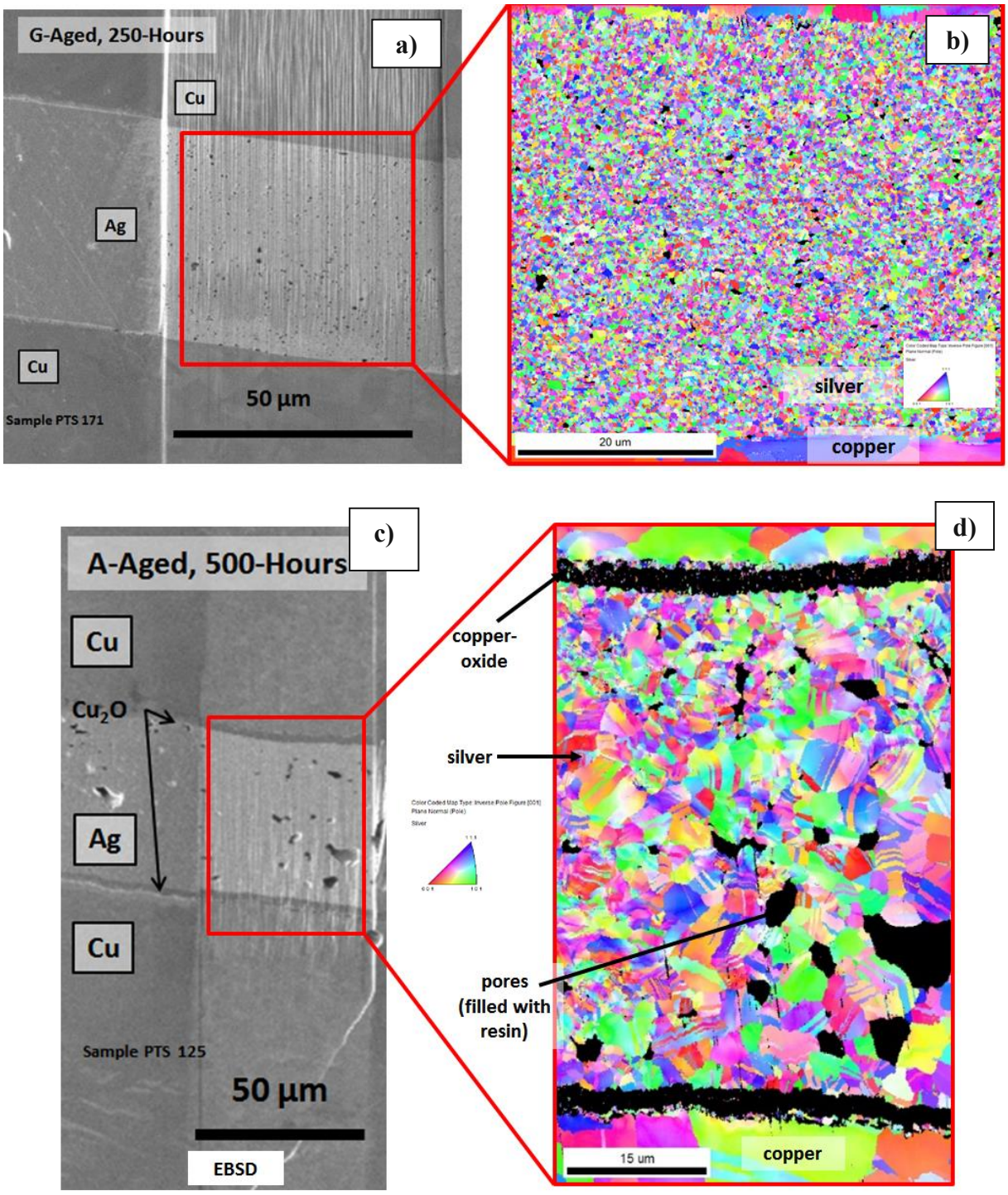

Fig.4.13: SEM images (a)(c) and EBSD analysis (b)(d) of the Cu-Ag-Cu lap-joints showing the states of the pores and silver grains after thermal treatment at 250 °C in protective glass ambient for 250 hours (a)(b) and in air ambient for 500 hours (c)(d).

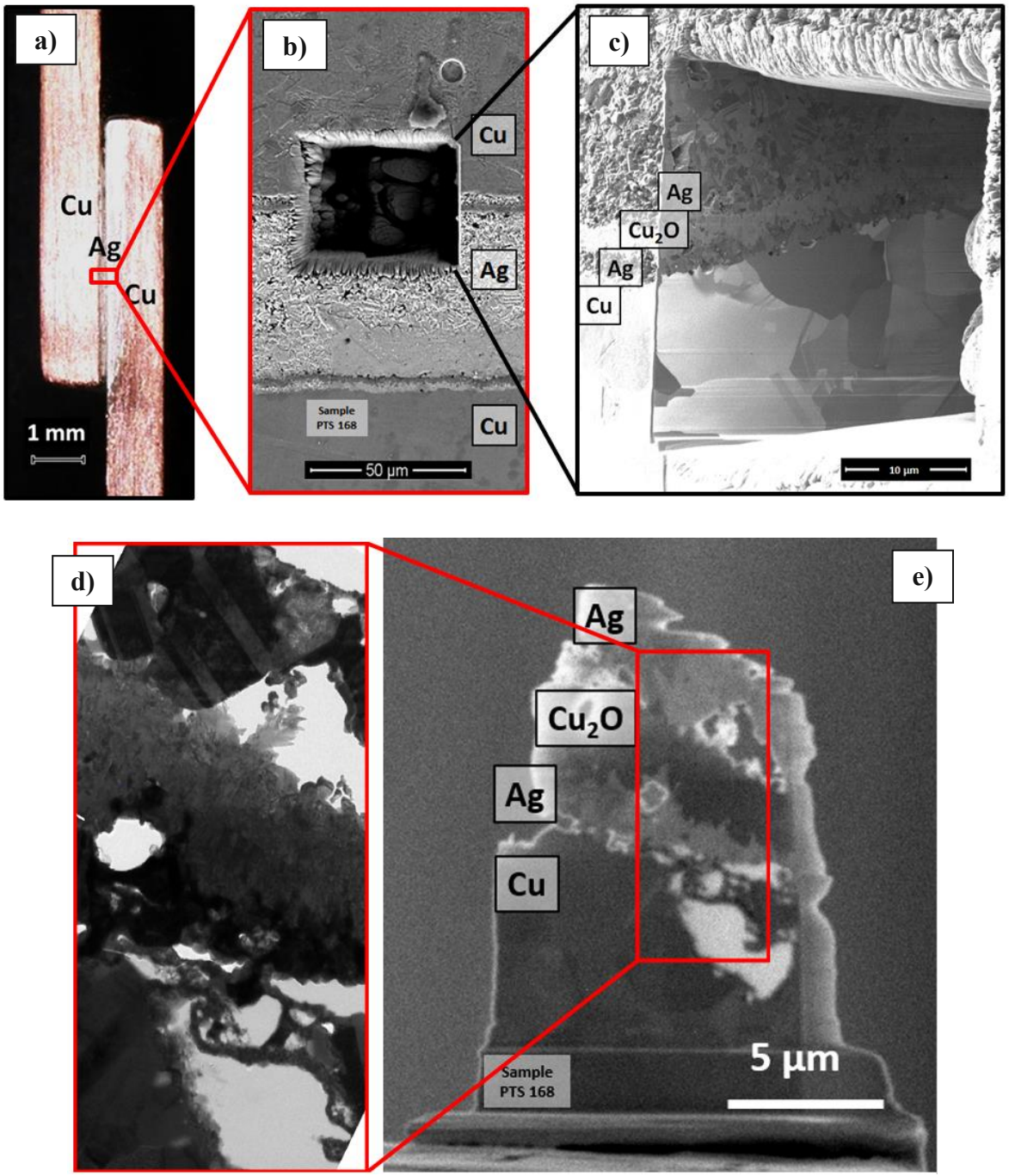

Fig.4.14: Cu-Ag-Cu sample thermal treated at 250 °C for 250 hours at air ambient. Microscopic image of the lap-joint (a) and SEM image of the sample's middle section with focused ion beam (FIB) processed region (b) showing the silver-copper interface (c). TEM image containing the copper-oxide layer (d) from the lamella of the shown pit area (e).

Apart from the state of the silver grains and pores in the sintering area, the other region of interest, the silver-copper interface, for the A-Aged specimen can be seen closely as pictured in Fig.4.14. While no oxidation is observed after thermal treatment in the protective atmosphere subsequent to sintering (Fig.4.13), the SEM images of the FIBed area in Fig.4.14.b-c show the penetration of the copper-oxide layer into the sintered silver bulk after thermal treatment in air ambient. For particular analyses two TEM lamellas of the Cu-Ag interface section from A-Aged lap-joints were prepared as shown in Fig.4.14.d-e and Fig.4.16.a-c. The EELS scans and EDX mappings confirmed the formation of Cu_2O as in Fig.4.15.b-c and Fig.4.16.d. Furthermore, carbon polymer, probably remaining of the Ag-coating from the sinter paste, could be detected.

The SEM images of the fracture surface from the G-Aged and A-Aged lap-joints after shearing is given in Figure 4.17. The comparison of the Ag-grain size for the G-Aged (Fig.4.17.c) and A-Aged (Fig.4.17.f and Fig.4.17.i) series is pointed out for the marginal section of the joint, where the oxygen presence was given in equal condition, at a magnification of 10 thousand. The former is around 1 µm and the latter up to 3-4 µm. The crack propagation due to shearing stress is observed either on the Cu-Ag interface as shown in Fig.4.17.a or through sintered Ag-bulk as shown in Fig.4.17.g. An overview to the fracture characteristics is given in the Appendix A.1.

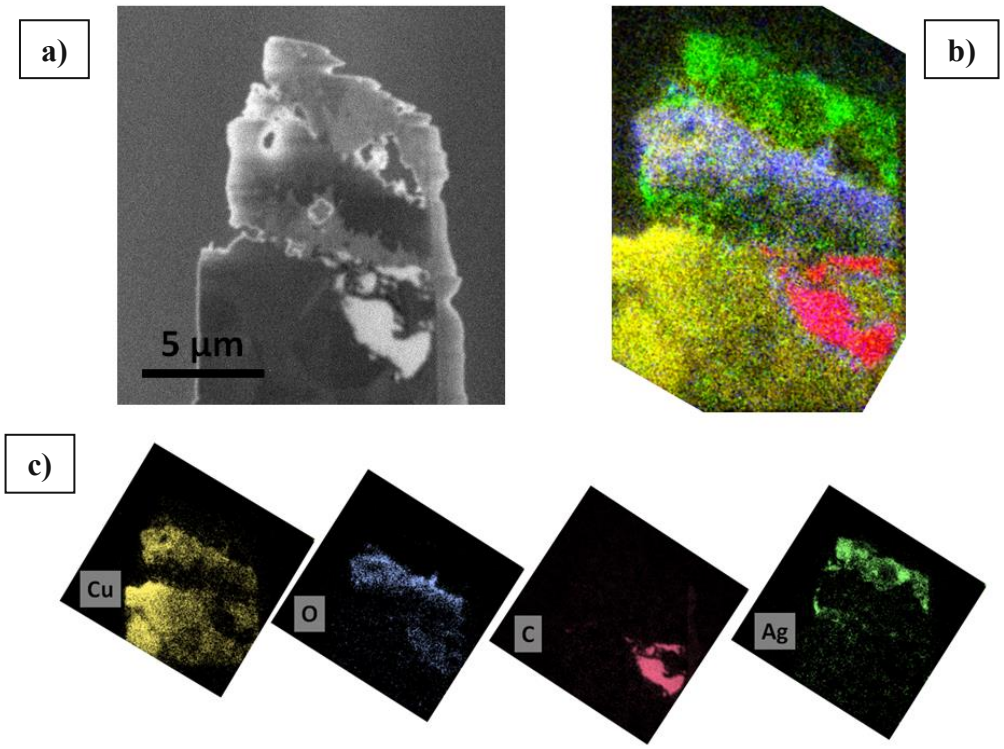

Fig.4.15: TEM image of the Cu-Ag interface of the sintered lap-joint sample (a). EDX analysis confirming the formation of copper-oxide as yellow+blue section (b)(c) after thermal treatment in air ambient (at 250 °C for 250 hours).

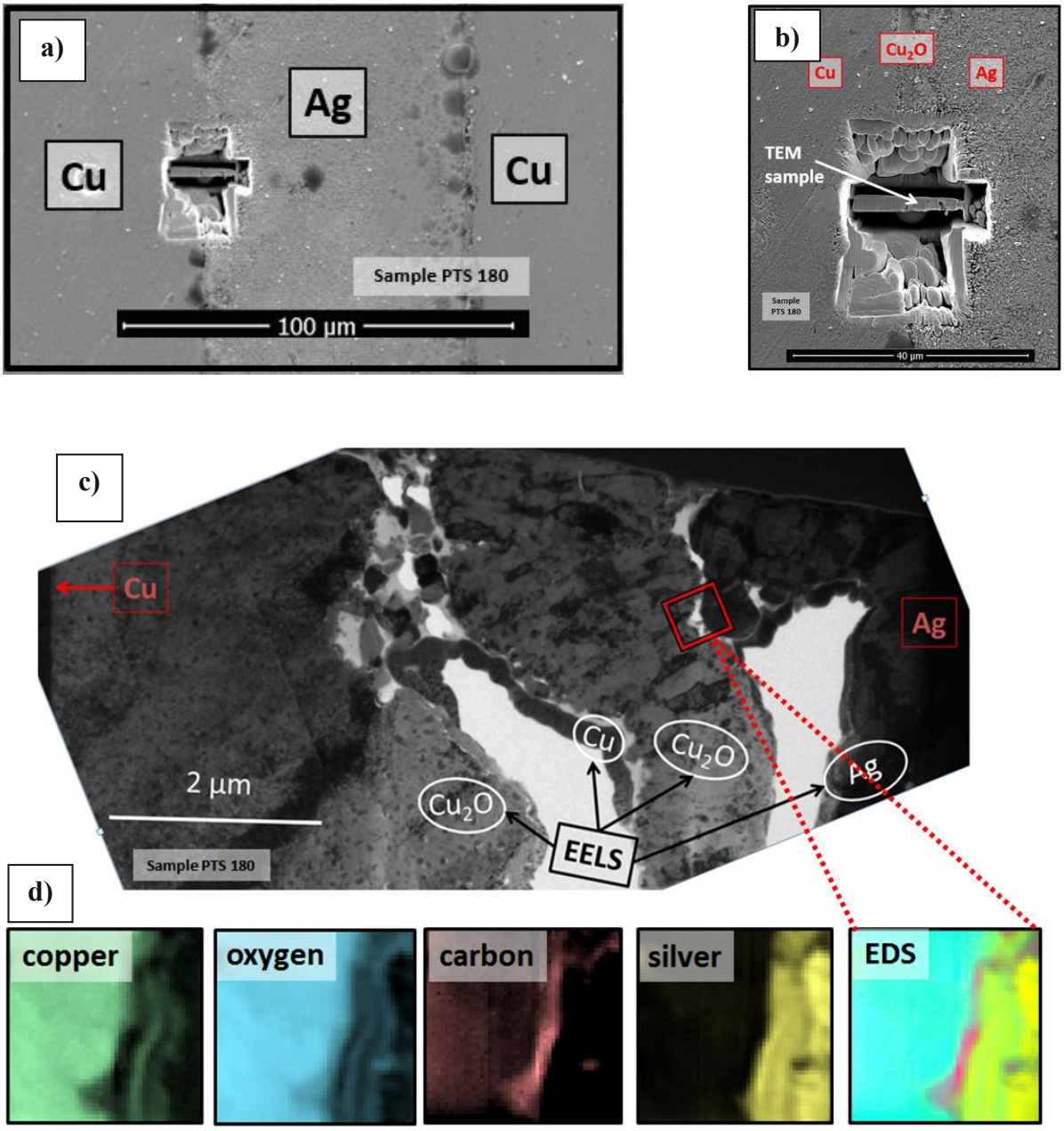

Fig.4.16: Cu-Ag-Cu lap-joints sample series (PTS) sintered at 70 MPa pressure and 230 °C for 30 minutes and thermal treated at 250 °C for 250 hours at air ambient. SEM image of the Ag-sintered Cu-lap-joint (a), SEM (b) and TEM (c) images of the sintered silver with neighboring copper-oxide section and the red marked square area (ca. 0,5 x 0,5 µm²) was EDX mapped (d).

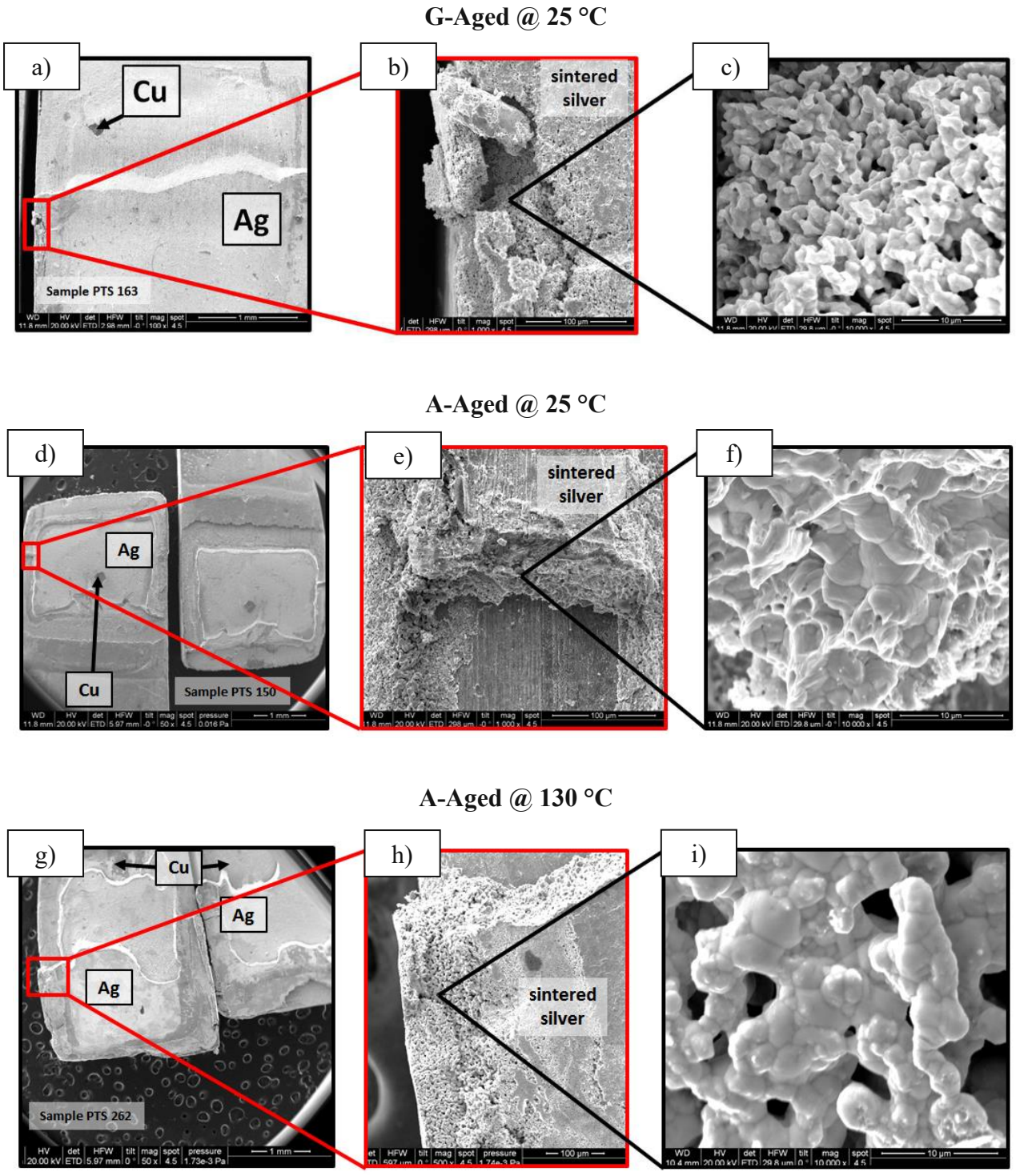

Fig.4.17: Cu-Ag-Cu lap-joints sintered at 70 MPa pressure and 230 °C for 30 minutes. G-Aged sample tested at 25 °C (a)(b)(c). A-Aged sample tested at 25 °C (d)(e)(f). A-Aged sample tested at 130 °C (g)(h)(i).

4.2.2. Shear Strength

In this section the response of the Cu-Ag-Cu lap-joints to shear stress shall be investigated. The obtained strength profile for the given specimen 0-hour, G-Aged and A-Aged is plotted in Fig. 4.18. Two testing temperatures of 25 °C (black plots) and 130 °C (red plots) are given for the testing speed of 2 mm/min. Here again, in general the shear strength is declining with increasing testing temperature. The mean value of the shear strength of the 0-hour samples tested at room temperature should be higher than the one received at the testing temperature of 130°C. An explanation for this might be the large deviation of the measured strength values, though, the number of samples (34) were already comparatively high.

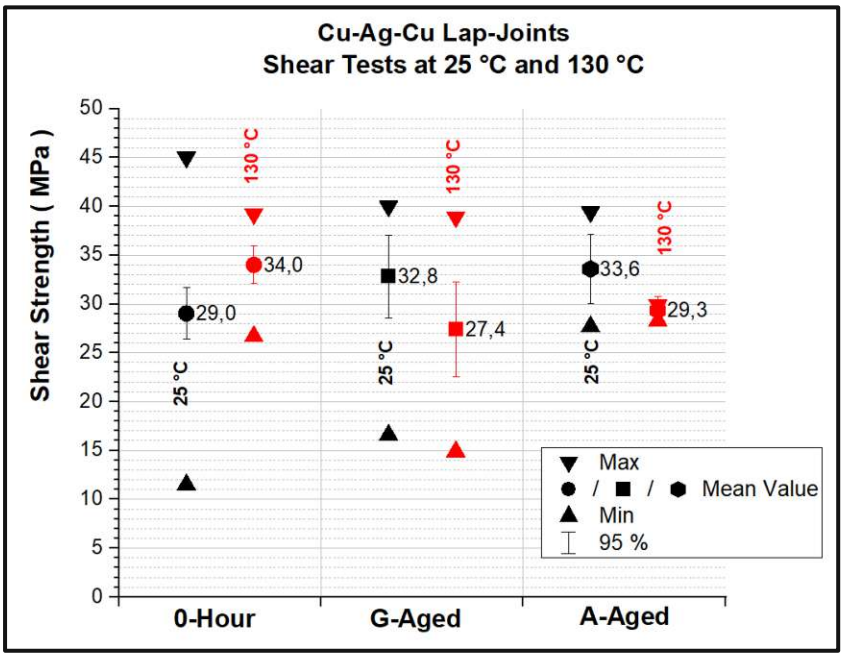

Fig 4.18.: Shear strength for the Cu-Ag-Cu lap-joint series. Comparison of shear behaviour for 0-hour vs. 250-hours thermal treatment (G-Aged and A-Aged at 250 °C) at testing temperatures of 25 °C and 130 °C, for the testing speed of 2 mm/min.

The maximum measured shear strength here is around 46 MPa. For the same sintering conditions of time, temperature, pressure, and atmosphere, the maximum tensile strength at room temperature was of 120 MPa. The relationship between the shear strength τ_{sh} and yield strength σ_y are commonly given by the equation

$$\tau_{sh} = x * \sigma_y \tag{30}$$

where x is ca. 0.5 depending on which failure theory (such as Tresca's or von Mises) one adopts [77]. Georgi Genov [77] suggests a revisited rule-of-thumb dependency for the shear strength and the ultimate strength σ_{US}:

$$\tau_{sh} = 0.6 * \sigma_{US} - 25, \tag{31}$$

which fits very well to our above-mentioned measurement results of ultimate tensile and shear strengths.

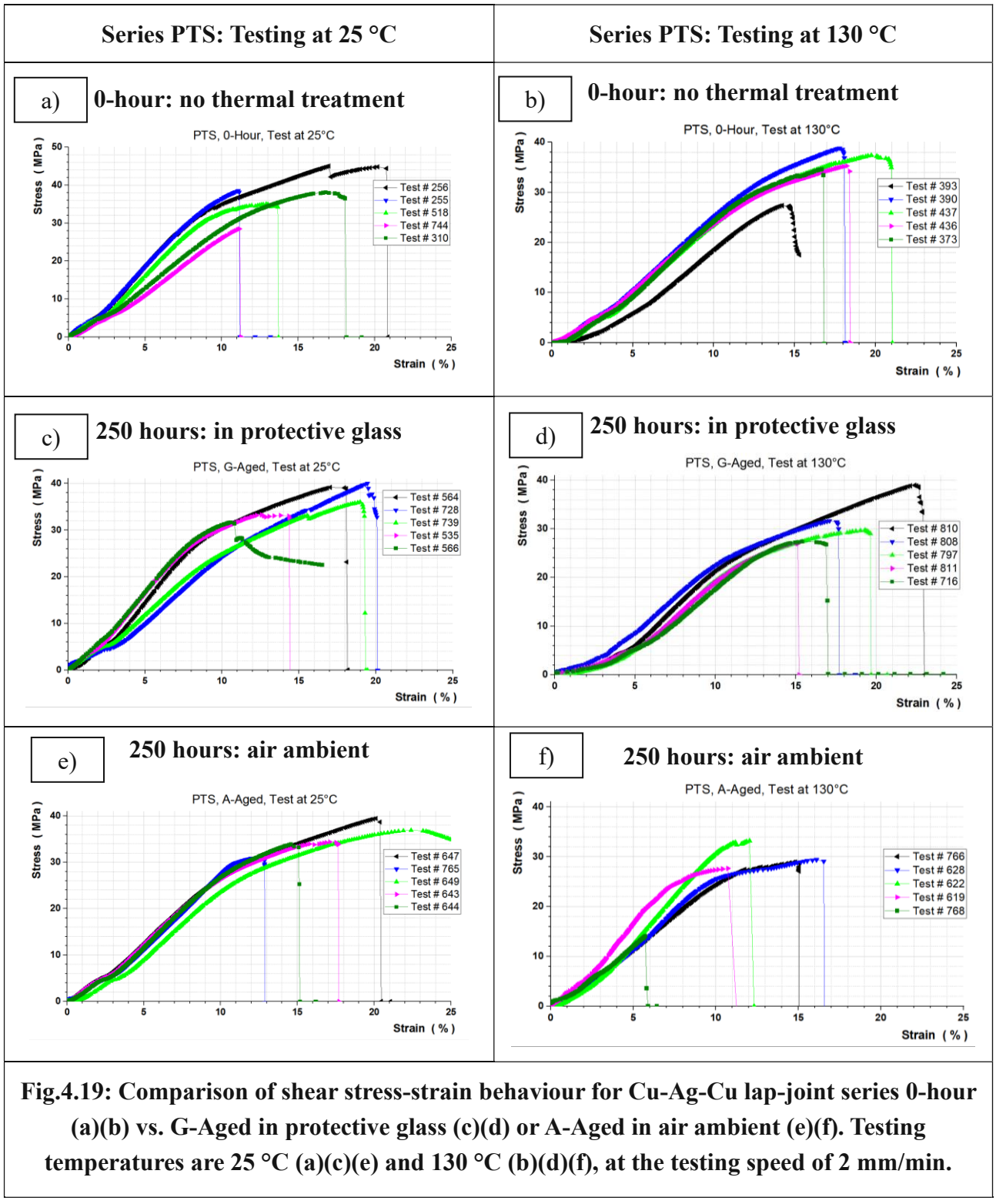

Fig.4.19: Comparison of shear stress-strain behaviour for Cu-Ag-Cu lap-joint series 0-hour (a)(b) vs. G-Aged in protective glass (c)(d) or A-Aged in air ambient (e)(f). Testing temperatures are 25 °C (a)(c)(e) and 130 °C (b)(d)(f), at the testing speed of 2 mm/min.

To compare the shear behaviour, Khazaka, R. et al. [69] reviewed the relationship between the joint shear strength of nano-silver paste for die attach technology and various parameters such as the applied bonding temperature, sintering pressure and time, sintering atmosphere, interconnection area and joint thickness, thermal cycling, and storage time at different temperatures. A summary of the latter is given as follows: for the storage at 85 °C [70], 250 °C [71] and 300 °C [72] a relatively small variation between 20 MPa and 30 MPa of the die shear strength is given. For the storage at 500 °C [73] in air, while the shear strength of 100 µm thick films remained constant, for thin joints of 15 µm a decrease from 50 MPa to the half was observed.

For our samples with an average silver thickness layer of ca. 70 µm after sintering, the mean shear strength of the Cu-Ag-Cu lap-joints was ca. 29 MPa for the 0-hour specimen. The mean shear strengths of the 250-hours aged samples were around 33 MPa at room temperature and showed descending tendency at the testing temperature of 130 °C.

The stress (τ) – strain (ε) behaviour for the lap-joint series is given in Fig.4.19. Tests at room temperature are plotted in the left column, tests at elevated temperature in the right column. Five selected samples for each of the 6 test series represent the maximum shear strength region.

4.2.3. Cyclic Loading

After the investigations on tensile behaviour of the pressure assisted sintered silver and investigations on shear behaviour of the lap-joints sintered with the same parameters (70 MPa, 230 °C, 30 min) and characterization of the microscopic structure of the corresponding sample series, in this section the studies on the lifetime estimation are presented. The mechanical cycling tests were performed again at room temperature and an elevated temperature.

The ratcheting behaviour for the first 10 cycles of the 0-hour PTS lap-joints at 25 °C is given in Fig.4.20: with a stress maximum of 40 MPa (40max) and mean value of 25 MPa in Fig.4.20.a, and with a stress maximum of 30 MPa (30max) and mean value of 20 MPa in Fig.4.20.b. In comparison to the latter, the first 10 cycles of the 250-hours A-Aged and G-Aged samples are given in Fig.4.21.a-b. Each diagram includes three individual tests of random samples from the series to represent the range in compliance of the stress-strain behaviour. Annotated is also the number of cycles (N_f) till end of life (EOL) for each individual test. It should be noted that the average shear strength for the specimen is around 30 MPa, which means that the cyclic amplitude was highly stressing.

The strain maxima of the 0-hour samples measured at room temperature are about 14-16 % for 40max specimen and about 8-10 % for 30max specimen, for the first 10 cycles. As described in section 5.2, an average asymptote value of ca. 22 % and 16 % of ratcheting strains respectively are given for EOL fracture at 25 °C.

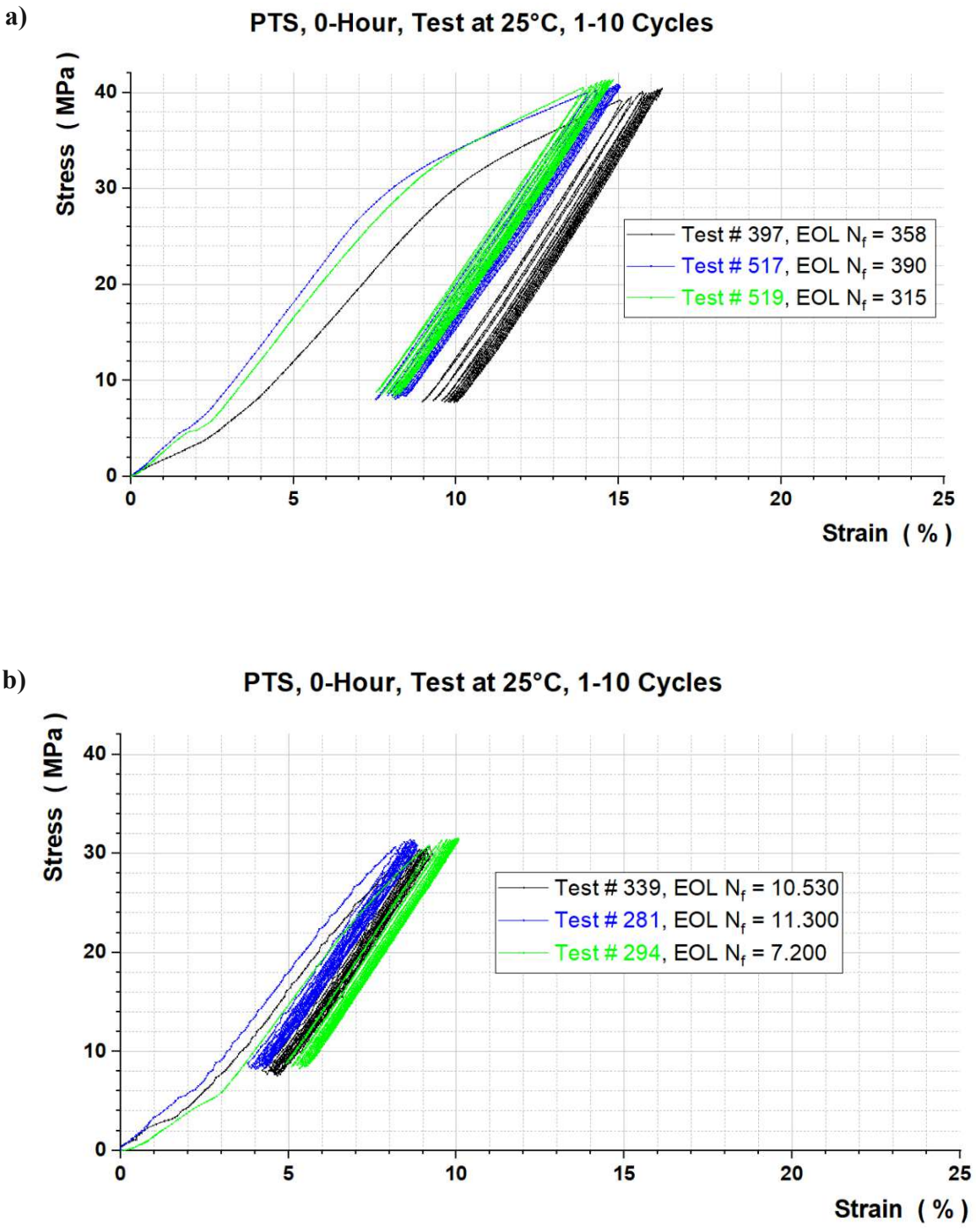

Fig 4.20: Comparison of shear cyclic for 0-hour Cu-Ag-Cu lap-joints for two stress maximum levels: 40 MPa (a) and 30 MPa (b). Each series include three individual tests of representative samples. Testing was performed at room temperature and only the first 10 cycles are shown.

a)

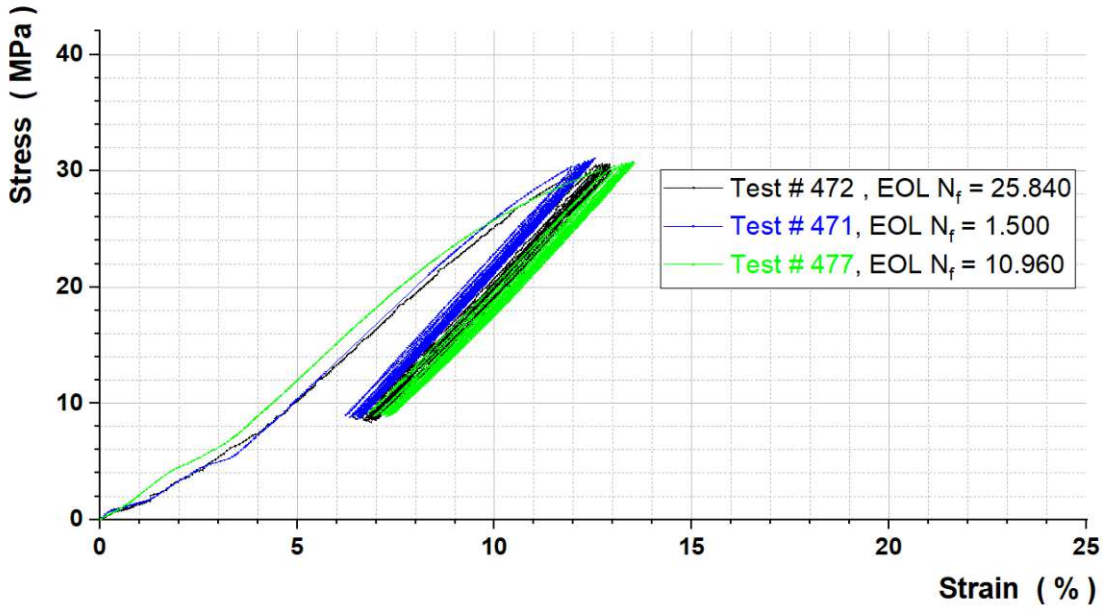

b)

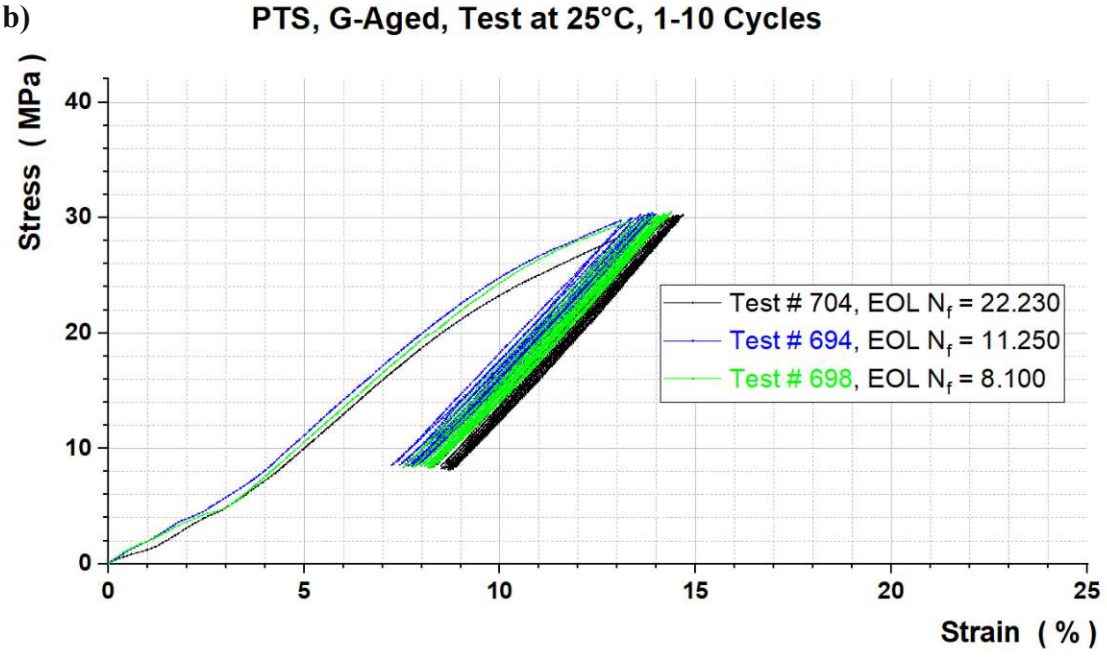

Fig 4.21: Comparison of shear cyclic for Cu-Ag-Cu lap-joints which are 250-hours thermal treated at air ambient (a) or in glass (b). Each series include three individual tests of representative samples. Testing was performed at room temperature and only the first 10 cycles are shown.

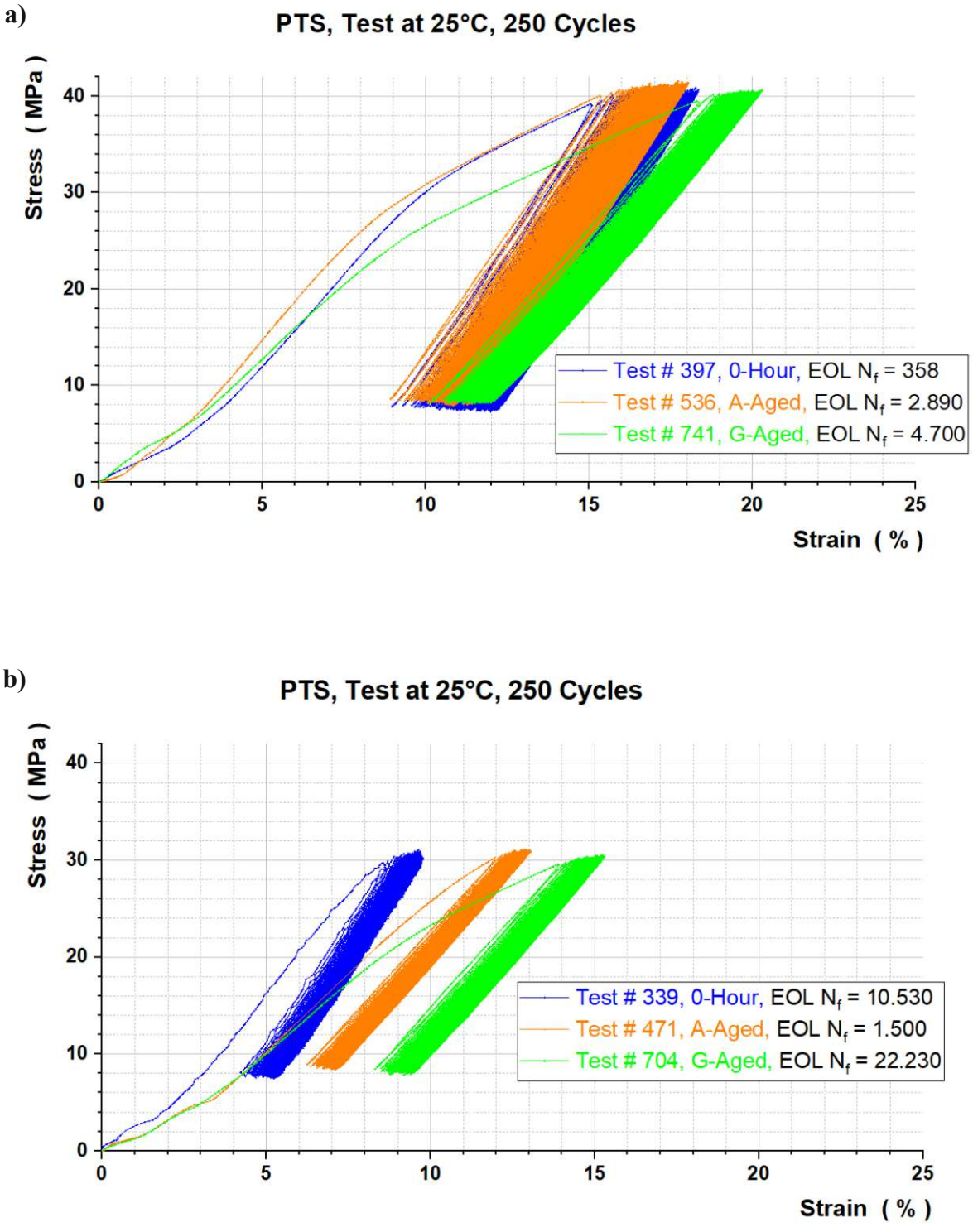

Fig 4.22: Comparison of shear cyclic for 0-hour (blue), 250-hours A-Aged (orange) and G-Aged (green) Cu-Ag-Cu lap-joints for two stress maxima: 40 MPa (a) and 30 MPa (b). Testing was performed at room temperature and only the first 250 cycles are shown.

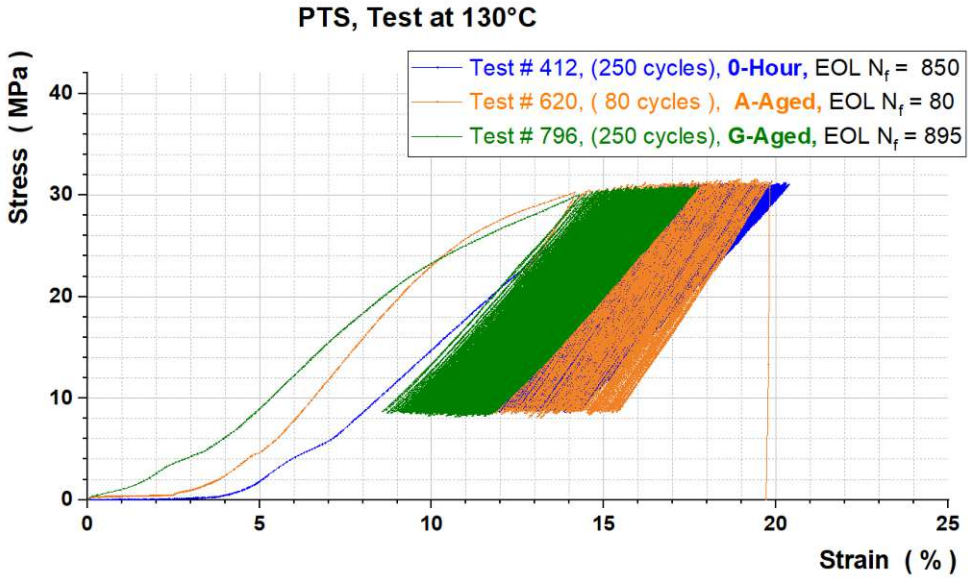

Fig 4.23: Comparison of shear cyclic for 0-hour (blue), 250-hours A-Aged (orange) and G-Aged (green) Cu-Ag-Cu lap-joints at the elevated testing temperature of 130 °C for the maximal stress amplitude level of 30 MPa.

a)

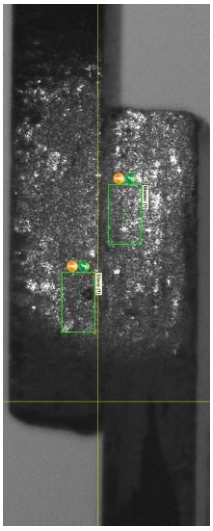

b)

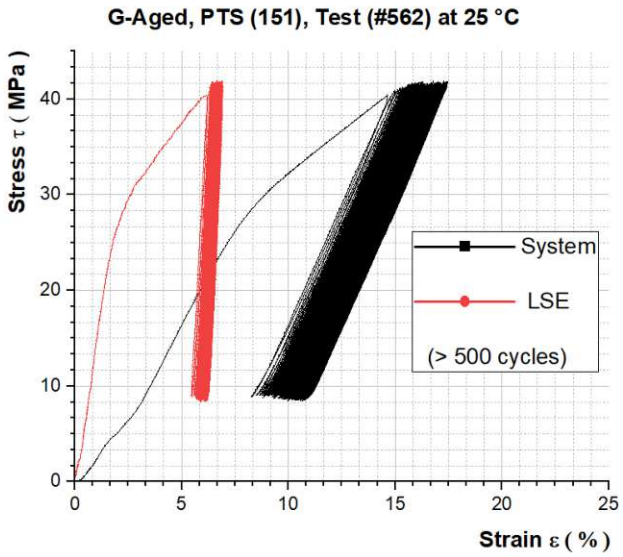

Fig 4.24: The master-slave region of laser speckles on the lap-joint were placed as near as possible to the sintered Ag interface and were calibrated on 1 mm in vertical distance (left) to compare the stress-strain measurement of the lap-joint sample with (red plot) and without (black plot) LSE (right).

The direct comparison of the 0-hour and aged specimen for the first 250 cycles is shown in Fig.4.22. The samples with a ratcheting stress maximum of 40 MPa are given in Fig.4.22.a and the samples with a ratcheting stress maximum of 30 MPa are given in Fig.4.22.b. Here we note the comment to the diagram 4.22.a where we can distinguish the slope of the stress/strain curves (in the hook's regime) of the 0-hour and A-Aged samples from the one of the G-Aged, the latter appears softer. At this point one could believe that the reason for this deviation could be the microstructure, as we can observe a significant difference in the pore size (Fig. 4.11). However, with view on the diagram 4.22.b the A-Aged samples exhibit another slope than the 0-hour samples. For this reason, the explanation for the different slopes has to be found in tolerances of the silver layer thickness. Although the geometry of the Ag-pads was predefined by the stencil printing and the samples were placed in holders, a contact shift during the alignment of the pressing plates and the high press application was possible, leading to slight variations of the joint area.

Fig.4.23 shows the stress-strain behaviour of the latter specimen at the elevated testing temperature of 130 °C. Hardening is observed especially for the G-Aged samples, 4.20.b vs 4.21.b, above the 30 MPa level and at elevated temperature.

Measurement with the LSE was performed to determine the strain of the sintered silver layer. As shown in Fig.4.24 a region of 1 mm in vertical length at the Ag-Cu interface was marked to be traced. The evaluation for a G-Aged sample with over 500 mechanical stress cycles is plotted on the right side. The black plot considers the entire strain (of the system including the sample). Thus, it has a softer characteristic than the red plot which, thanks to the LSE measurement, uses the pure sample strain.

The influence of thermal ageing and testing temperature on the failure probability is shown in Fig.4.25 as Weibull plot. The Weibull statistical distribution can be characterized with various estimator methods such as Benard and Bos-Levenbach, Hazen or Blom [48]. In this study the automatic evaluation was made with a program called Origin, reckoning according to Blom method [49] with the formula

$$\frac{i - 0.375}{n + 0.25}. \tag{32}$$

The number of the data points corresponding to the test values is represented by n and i is the rank of the samples in ascending order.

The samples are tested with a frequency of ca. 0.1 Hz, either until the sintered lap-joint is fully detached to obtain the cycles number N_f (as end of life) or were assumed as 'run-through' after 30.000 cycles. The three types 0-hour, 250-hours A-Aged and G-Aged sample series are tested at room temperature and compared in Fig. 4.25.a. An improvement of mechanical cycling lifetime in shear loading with 30 MPa maxima and tested at room temperature is observed for the thermally treated series. The comparison at the elevated testing temperature of 130 °C for the G-Aged versus 0-hour series is shown in Fig. 4.25.b, where the enhancement of the 250-hours series is not noticeable

anymore. The stress concentration around the lattice irregularities and pores are considered as rather leading to crack propagation. The dislocations in sintered Ag could be mobilized by the elevated temperature and lead to a reduction of life due to fatigue [50].

a)

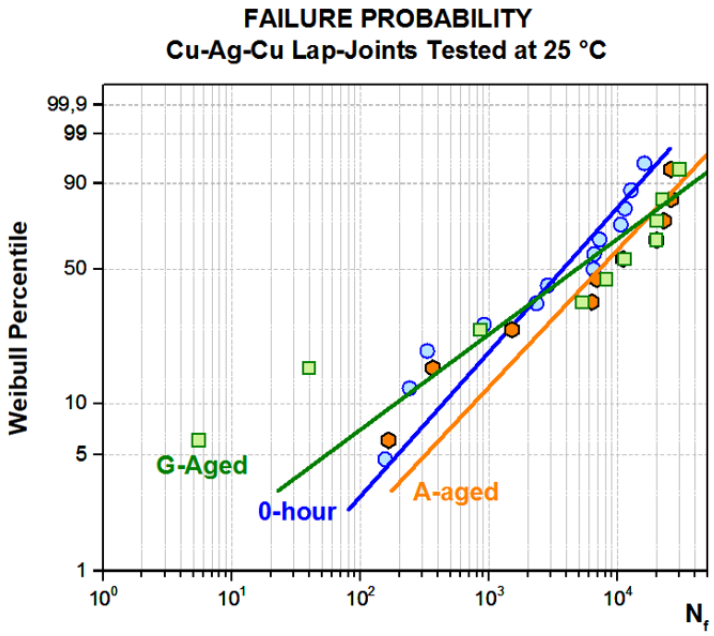

b)

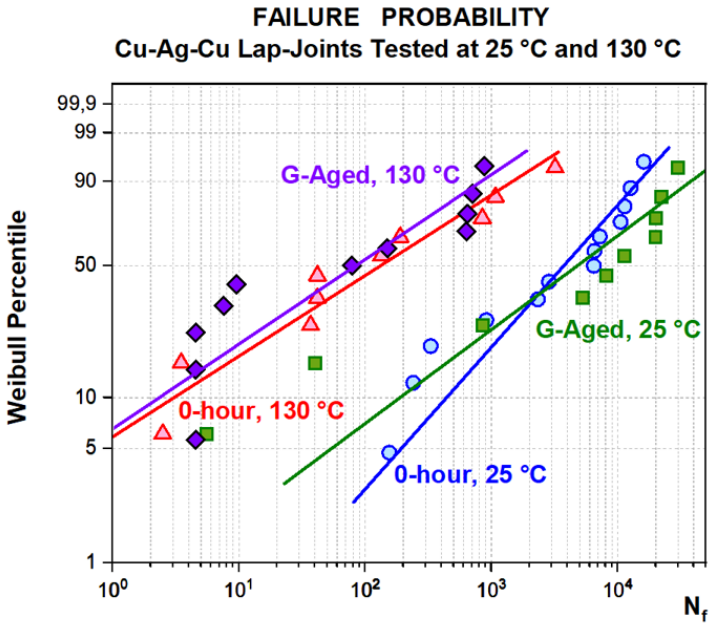

Fig 4.25: Comparison of uniaxial shear cyclic lifetime of Cu-Ag-Cu lap-joints for 0-hour and 250-hours thermal treated samples at testing temperatures of 25 °C and 130 °C with maximal stress amplitude levels of 30 MPa.

The Wöhler plot as an S-N diagram in Fig.4.26 shows the influence of the temperature on the Cu-Ag-Cu joining quality for various stress levels (30 MPa, 35 MPa, and 40 MPa). The diagram was plotted with ProFatigue software, which is a statistical tool to predict the Wöhler field, based on Weibull or Gumbel distribution. For the former method, the number of cycles corresponding to the 50 % failure probability (as given in Fig.4.25) are listed in Table 4.2.

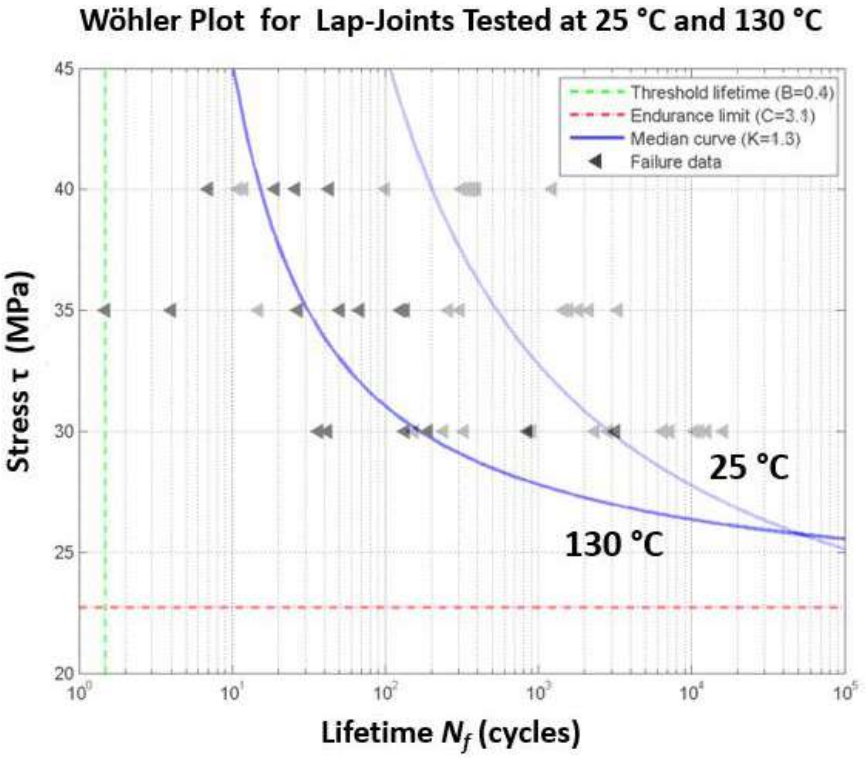

Fig.4.26: Comparison of uniaxial shear cyclic lifetime N_f (as EOL) of Cu-Ag-Cu lap-joints with maximal stress amplitude levels of 30 MPa, 35 MPa, and 40 MPa; testing at ca. 0,1 Hz.

Table 4.2: Number of Cycles to Failure for the 50 % Weibull Probability (WP) corresponding to Fig. 4.25.

Number of Cycles for 50 % WP	max. 30 MPa mean 20 MPa	max. 35 MPa mean 22.5 MPa	max. 40 MPa mean 25 MPa	Testing Temperature
0-hour	3600	900	220	**25 °C**
G-Aged	5000		8500	
A-Aged	7200			
0-hour	150	110	12	**130 °C**
G-Aged	80			

CHAPTER 5

PUBLISHED PAPERS

Previous chapters contain the motivation and goals of our research including the main aspects of the related theory and the investigation methodology. This chapter is devoted to the summary of the published results obtained through the research years on the thermomechanical properties of sintered silver. Papers have been peer reviewed, five have been released with IEEE, and a sixth one in Microelectronics Reliability with Elsevier. This was possible with the competent and most valuable supervision of Prof. Golta Khatibi and enlightening discussions with Prof. Johann Nicolics. In the last three papers of this thesis co-supervisor Dr. Martin Lederer contributed with developing a material model for porous silver based on the evaluated data. The test samples have been manufactured at the TU Wien laboratories inhouse by the PhD student. The required equipment was modified, experiments were carried out, examination and analysis were pursued accordingly. For each paper the contribution of the co-authors and support of the colleagues is annotated.

The first paper ***Temperature Dependent Mechanical Properties of Sintered Silver*** **[1]** investigated the shear strength of Cu-Ag-Cu joints sintered under various preparation conditions for optimization purposes, along with the stress relaxation behaviour of a lap-joint type at room and elevated temperatures, and 3-Point-Bending (3PB) mechanical fatigue of the button type samples. Special thanks are devoted to Dr. Agnieszka Betzwar for her practical advice and contribution during the high frequency lifetime measurements, and Dipl.Ing. Thomas Walter for his support with the setups.

The second paper ***Behaviour of Silver-Sintered Joints by Cyclic Mechanical Loading and Influence of Temperature*** **[2]** investigated the low cycle mechanical lifetime of the depicted lap-joint series, the S-N curve have been plotted for room and elevated temperatures. The ratcheting strain as an indicator of the residual stress of the cyclic hysteresis and creep behaviour was evaluated for two stress peak levels, near and above the hardening benchmark. The effect of thermal treatment on microstructure and fatigue characteristics was investigated. Failure probabilities were evaluated with Weibull distribution (based on Blom methodology). For the electron microscopy images, the focused ion beam (FIB) millings in the region of interest were made by Dipl. Ing. Andreas Steiger-Thirsfeld. The results of these investigations were also presented at the 10th Workshop of the German Association for Welding and Allied Processes e.V. and published in conference proceedings **[3]**.

The third paper ***Temperature Dependent Physical Properties of Silver-Sintered Layers for Power Electronics*** **[4]** investigated the main characteristics of the porous silver which were sintered under selected preparation conditions. Tensile strengths for the series of the dumbbell shaped Ag-coupons were deduced for room and elevated testing temperatures, as well as the electrical resistivity. The mass/volume densities of the samples were determined by Markus Lunzer, BSc. The thermal

analysis TG and DTA of the dried Ag-paste prior to sintering was performed by Prof. Christian Gierl-Mayer. The factual data of a high-power LED module developed by ESCATEC using silver sintering as interconnection technology was provided by Dr. Martin Mündlein.

The fourth and fifth papers ***Temperature Dependent Relaxation Behavior of Pressureless and Pressures Assisted Sintered Silver*** **[5]** and ***Temperature Dependent Relaxation Behavior of Ag-Sintered Copper Joints*** **[6]** investigated specifically the creep characteristics of the porous silver dumbbells and the lap-joints, respectively. For this purpose, the samples were exposed to defined stress levels consequent on the studies of the series, and the relaxation behaviour was observed. The experiments were again performed at room and elevated temperatures in alignment with prior research. Regarding that mechanical lifetime for low cyclic fatigue of thermal treated (250 hours aged) lap-joints was conspicuously high compared to as sintered (0-hour) samples, stress relaxation data of both 0-hour and A-Aged lap-joints were collected. The numerical results could be well implemented in the Norton power law and the stress exponent values were determined. Considering that the inelastic deformation in the material due to stress application leads to the end-of-life damage, a unified model of Gurson plasticity and Norton creep was developed by Dr. Martin Lederer. Also a certain activation energy, which is the energy necessary for the transportation of the lattice atoms during creep phenomena, could be elaborated for the tested and in numerical fitting evaluated samples.

For the sixth paper ***Constitutive equations for strain rate and temperature dependent mechanical behaviour of porous Ag-sintered joints in electronic packages*** **[7]** the constitutive data of the stress-strain characteristics including tensile, shear and relaxation behaviour for sintered silver at selected temperatures was available along with the density analysis of the corresponding sample series. Dr. Martin Lederer has determined the specific material parameters from fits to mechanical tests and accomplished the implementation of finite element method (FEM) on the commercial ABAQUS simulation software. Combined with the investigations on microstructural features and mechanical cyclic lifetime, the material model developed can be used for reliability assessments of Ag-sintering. The results were also published in German at the conference proceedings of the 11th Workshop of DSV/GMM Elektronische Baugruppe und Leiterplatten (EBL) in 2022 **[8]**.

In the following sections the published papers are given respectively. In the sections 5.1-5.6 the enumeration and lists of the references in each paper is given as published, at the end of the corresponding paper. Therefore, these lists of the references cited in this chapter 5 should be differentiated from the list of references given separately in an own section at the end of the thesis.

Complementary results and a thorough discussion of the main investigation points such as porosity of sintered silver, mechanical properties and effect of thermal treatment is provided on the base of comparisons with outcomes of other research works in chapter 6.

5.1. Temperature Dependent Mechanical Properties of Sintered Silver-Copper Joints

Zeynep Gökdeniz[1)], Golta Khatibi[1)], Thomas Walter[1)], and Johann Nicolics[2)]

[1)] Christian Doppler Laboratory for Lifetime and Reliability of Interfaces in Complex Multi-Material Electronics, Inst. for Chemical Technologies and Analytics, TU Wien, Getreidemarkt 9, 1060 Vienna, Austria

[2)] Dep. of Electronic Materials, Inst. of Sensor and Actuator Systems, Gusshausstraße 27-29, TU Wien, Austria

zeynep.goekdeniz@tuwien.ac.at

Abstract: *The focus of this work is investigation of the mechanical properties of low-temperature Ag-sintered large area joints which were prepared by using silver coated and blank copper substrates. Shear tests and stress relaxation experiments were conducted at various temperatures by using a micro tensile testing machine equipped with a thermal chamber. Fatigue behavior was studied by using a high frequency three point cyclic bending testing system. In order to compare the relaxation behavior at higher temperatures the stress exponents were deduced from measured data according to the creep law. Failure probability curves of sintered silver interconnections were plotted and compared with those of solder joints prepared with lead-tin-silver alloy. It was found that the sintering parameters, Ag-sinter layer thickness and the substrate material strongly affect the shear strength and fatigue response of the joints. Using scanning electron microscopy (SEM) and 3D-microscopy techniques allowed to obtain an insight into the failure mechanisms of the Ag-sinter joints subjected to static shear test and fatigue loading.*

1. Introduction

The applications of power electronic devices target the trend in requirements such as high operation temperatures and controlled power loss density while demanding challenging methods for packaging such as low pressure joining technologies at low temperature. With its high thermal and electrical conductivities, silver sintering is a promising lead-free, environmental friendly alternative bonding technology. It is also compatible with multilayer processing where direct soldering is not always possible.

For silver sintering, commercially available Ag-pastes from different suppliers may consist of nano- or micro-particles of different size and shapes and a variety of organic additives. They are used to form silver joints by pressureless sintering and sintering under pressure up to 40 MPa [1-3] under different atmosphere such as air or nitrogen. The paste composition and sintering parameters have a strong impact on the porosity of the sintered silver layer which determines the elastic and thermomechanical behaviour of the joint. Furthermore, a size effect, i.e. increase of shear strength maximum with decreased bonding area, is reported [3]. Hence the studies of the mechanical behaviour of the sintered Ag-paste in different applications are still topic of ongoing research and are essential for reliable lifetime prediction.

2. Experimental

2.1. Sample design

Shear and stress relaxation tests were performed with Cu-Ag-Cu lap-joints. Each joint was prepared by using a pair of copper strips with a length of 50 mm, width of 3 mm and thickness of 1 mm. The surface of the copper strips was grinded to remove the surface oxides, put in an isopropyl-ultrasonic bath for rinsing and dried by air blowing. The Ag-paste was applied on copper by stencil printing to maintain a certain thickness with a pad area of 10–15 mm² (Fig. 1.a). Fatigue test samples consisted of Cu strips with a length of 20 mm, width of 10 mm and thickness of 2 mm. On the top of the strips rectangular pieces of Cu with an average area of 19.5 mm² were sintered on a silver pad with an area of 25 mm² (Fig. 1.b, 1.c). The contact surface of the Cu tops was sputtered with

978-1-5386-5731-7/18/$31.00 ©2018 IEEE

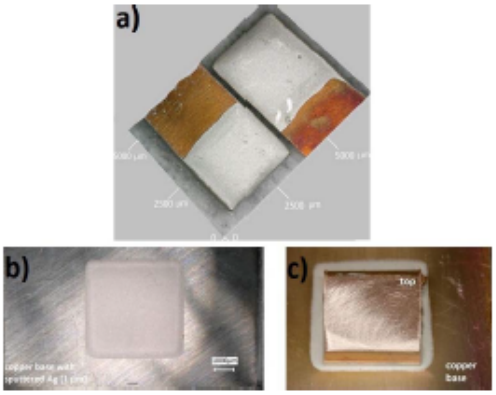

Fig. 1. Example of sample preparation: Ag-paste of 100 µm thickness is stencil printed a) on the edge of 3 mm wide and 50 mm long copper sticks for lap-joints by sintering to each other; b) by 5 mm x 5 mm mask template on copper base with pre-sputtered silver layer of 1 µm. c) A top of copper, also silver sputtered on the connection side, is placed in the middle of the dried paste on the base to be sintered under pressure.

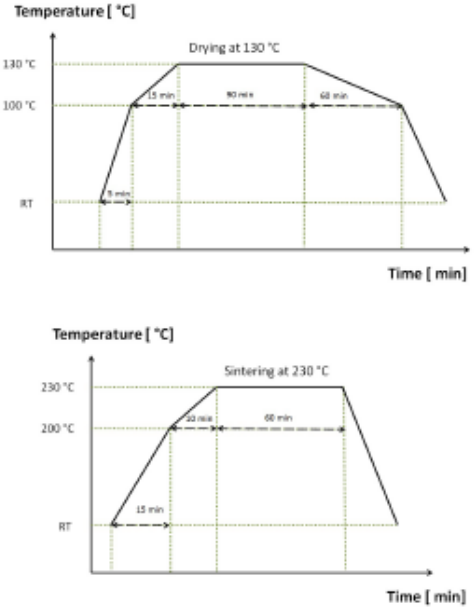

Fig. 2. Temperature profile of drying and sintering procedure for the used silver interconnection paste.

silver to obtain a 1 µm thick coating on the sintering area. The surface of Cu strips (bottom pieces) were either blank (1c) or coated by Ag- sputtering (1b).

The Ag-paste was dried at 130 °C under the flow of N_2 >2 l/min; the temperature profile is shown in Fig. 2. For 50 µm and 100 µm stencil mask the thickness of the applied silver paste (Heraeus mAgic paste) was reduced around half of original Ag-thickness after sintering at 230 °C for an hour. Both sintering in air and in nitrogen are studied, the former lead to higher shear strength than the latter ones. This is consistent with the analyses of Stanislas Hascoët et.al where processing under nitrogen lead to a weaker bond than under oxidizing atmoshere [6]. Therefore, sintering in air is preferred for sample preparation on further tests.

2.2. Microstructure

Sintering with different applied pressure leads to a noticeable difference in the microstructure. SEM images of various silver layers are shown in Fig. 3. The samples were sintered without (a) or under a pressure of around 25 MPa (b) and over 50 MPa (c).

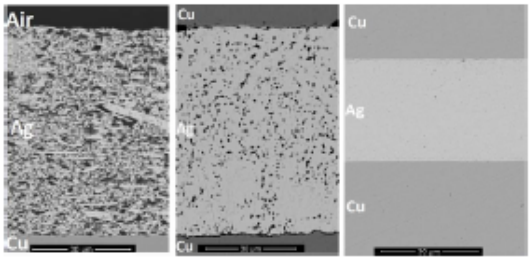

Fig. 3. Microstructure of silver paste sintered at different pressures: a) pressureless b) 25 MPa c) >50 MPa

Image analyses give an overview of the ratio of the pores: no sintering pressure leads to a porosity between 35–40 %, whereas a pressure over 50 MPa results in a porosity under 5 %. In the latter case of high pressure also a compression of the sintered silver layer was observed (e.g. 33.6 µm thickness) compared to layers sintered without pressure (50.7 µm thickness).

2.3. Test set-up

Tensile experiments were performed using a microstrain machine ME30-1 with a 500 N load cell (with a resolution of 10 mN) for stress measuring and a portable thermal chamber with heating element controlled by the regulator JUMO Imago 500, which

also enables recording of temperature data of the thermal element that is mounted on the sample during testing.

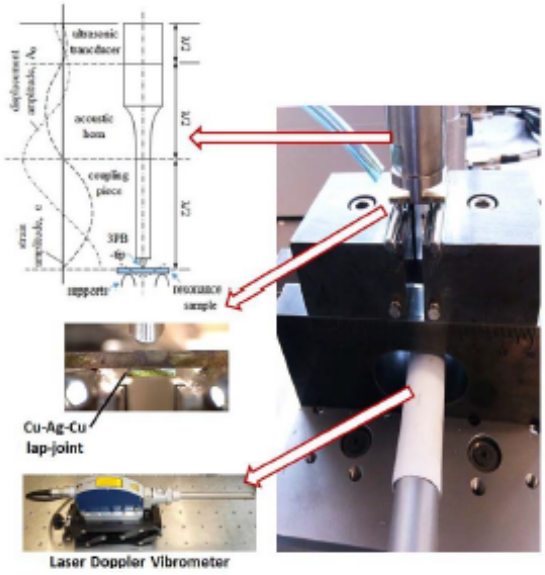

Fig. 4. Schematic image of the ultrasonic resonance fatigue testing system with three point bending set-up [4], picture of Cu-Ag-Cu sample placed under the excitation tip and laser Doppler vibrometer for capturing the resonance displacement of the specimen at the maximum.

Fatigue experiment set-up utilizes an ultrasonic resonance testing system consisting of a power supply, a transducer and an acoustic horn as schematically shown in Fig. 4. The sample below the tip of the horn is placed on the two steel supports of the bending stage. The system is connected to the load cell of a tensile machine which allows to adjustment a constant preload by the control software. This is required to prevent the movement of the specimen during excitation. For this purpose the configured set-up with the necessary application of 130 N preload induced a displacement amplitude of 5 µm during excitation. This was measured at the 1 mm thick and 19.5 mm^2 square copper side of silver sintering junction, of which the detachment is defined as the failure criteria. The vibrating system induces a resonance frequency of 20 kHz and is coupled to the adjusted sample at the position of maximum displacement, of which the amplitude is measured by means of a laser Doppler vibrometer during the excitation [4].

3. Results

3.1. Shear tests

Prior tests revealed increasing shear strength for higher sintering pressure [3]. Therefore, for the lap-joints within the area 10–15 mm^2 of applied silver

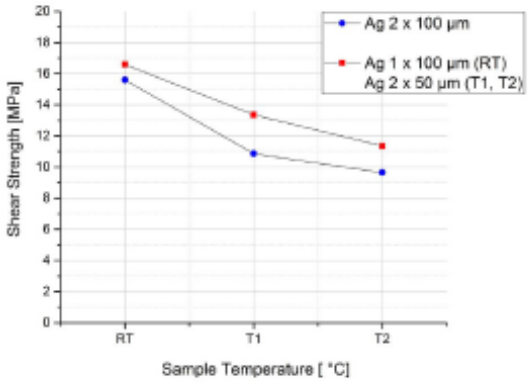

Fig. 5. Shear strength of large area (>10 mm^2) silver sintered samples at 25 MPa for different stencil thickness of applied paste and at different sample testing temperatures (RT = 26 °C, T_1 = 100 °C, T_2 = 140 °C).

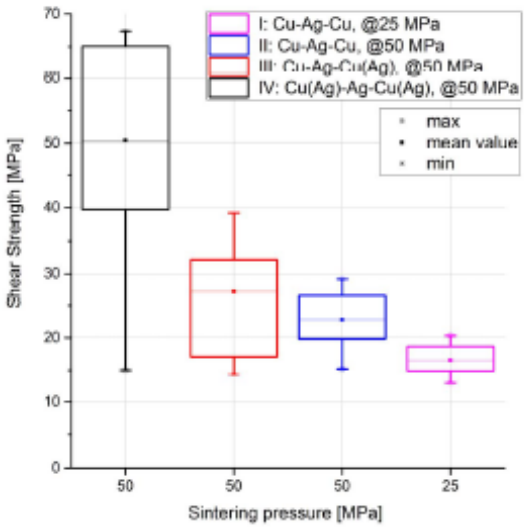

Fig. 6. Shear strength at room temperature of Cu-Ag-Cu interconnections are collated: Series I and II sintered at 25 MPa and 50 MPa respectively, where the silver paste was directly put on copper; series III and IV where copper were pre-sputtered with 1 µm silver layer either on one or on both sides of the sintering contact.

paste, a sintering pressure of approximately 25 MPa was chosen. These samples were shear tested at different temperatures. A decrease in shear strength with higher temperatures was observed as plotted in Fig. 5. Experiments also showed higher shear strength for Ag-thickness of 100 µm vs. 200 µm stencil print. For large area lap-joints of around 20 mm^2 sintering pressure over 50 MPa was adjusted.

Using the 100 µm thick stencil for the silver interface, the influence of applied sintering pressure to the shear strength measured at room temperature is plotted in Fig. 6. Samples series marked with I and II in the diagram are sintered with 25 MPa and 50 MPa, respectively, where the Ag-paste was directly put on copper. Set number III Cu-Ag-Cu(Ag) layers consists of a blank copper base on which the Ag-paste was applied with a 5 mm × 5 mm mask template, and a copper top which was pre-sputtered with 1 µm silver layer on the connection side (Fig. 1.c). In the series IV Cu(Ag)-Ag-Cu(Ag) both, base and top sides of the copper were pre-sputtered with silver. An increase of the average shear strength from 16.5 MPa to 21.8 MPa

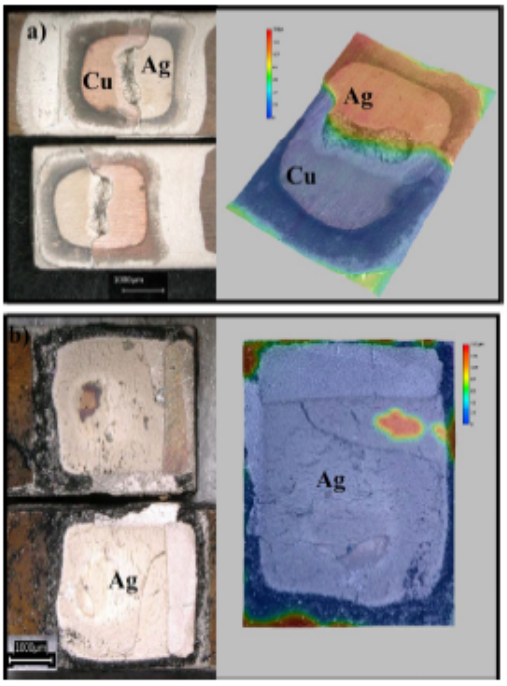

Fig. 7. Fracture of sheared-off samples a) at 100 °C and b) at 165 °C

was observed due to raised process pressure. In addition, an enhancement above 27 MPa was measured when the copper base was sputtered on one side. In the case of two-side pre-sputtering before the sintering the mean value of the shear strength reached more than 50 MPa.

Furthermore, at temperatures lower than 140 °C, fracture occurred at the Ag/Cu interface either at the top or the substrate side (Fig. 7.a). At higher temperature fracture crack propagated through the Ag-layer (Fig. 7.b).

3.2. Relaxation

The stress relaxation curves of the examined samples at room temperature, 100 °C, and 140 °C showed similar behavior. Compared to lower temperature, at 165 °C a stronger stress relaxation process is observed (Fig. 8).

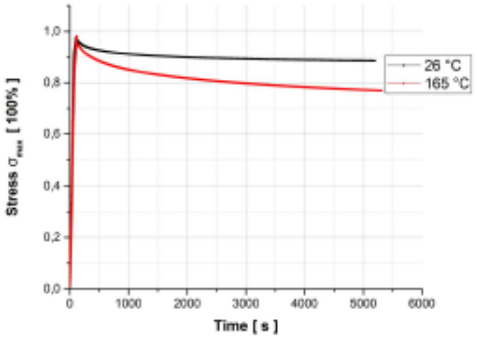

Fig. 8. Stress relaxation mean values compared at room temperature and 165 °C.

The relaxation can be represented by the power-law creep equation

$$\frac{d\varepsilon}{dt} = A.e^{K}.\sigma^{n} \qquad (1)$$

where t stands for time, ε is the strain, σ is the applied stress, n is the stress exponent, A is a material constant and K is

$$K = -\frac{Q}{R.T} \qquad (2)$$

with T being the absolute temperature, Q the activation energy and R the Boltzmann's constant.

For the attainment of creep behavior data the samples were loaded up to 120 N and hold at that position and stress vs time curves were obtained. In order to compare the samples at the steady state region, the stress relaxation data after 5% stress drop were considered for calculation of the stress exponent. As samples show a variation range of shear strength (compare maxima and minima in Fig. 6) and yield limit, this deviation is also seen in the relaxation data. The obtained stress exponent n for the measured samples at room temperature were between 28 and 78, whereas a lower n value around 20 is related to 165 °C (Table 1).

Similar creep strain tests were reported by Xin Li et al. [5]: Lap-shear joints with an area of 2 mm^2 and bondline thickness of 50 µm were sintered at 280 °C for 30 min by using nano-scale paste with particles size smaller than 50 nm (comparing with the micro-scaled Ag particle size of < 20 µm of this study). The drawn stress exponents for tests between 315 °C and 225 °C were in the range 4 and 11. That would lead to a stress exponent about 18 for 165 °C and around 45-50 for room temperature, which corresponds also to our calculated mean values from in Table 1.

Temp.	Steady phase 95 % of σ_{max} reached after t [s]	Stress exponent n (for Δt = 60 min)
26 °C	570 s	77.92
26 °C	839 s	45.15
26 °C	218 s	28.78
165 °C	250 s	22.24
165 °C	228 s	20.28
165 °C	96 s	20.10
165 °C	126 s	9.55

Table 1. Comparison of the stress exponents obtained from experimental data for various samples at room temperature and at 165 °C: n is related to the reciprocal variation of temperature.

3.3. Fatigue

The used three-point-bending fatigue test as described in section 2.3 is a time saving method to determine the lifetime of the interconnection. The results at room temperature for the two pre-sputtered series, Cu-Ag-Cu(Ag) and Cu(Ag)-Ag-Cu(Ag) samples, are presented in Fig. 9 as a failure probability plot. Especially from the former type almost half of the samples outlived the runout limit of $1.5 \cdot 10^8$ loading cycles. The chart also includes the fatigue data corresponding to the PbSnAg die attach solder joints which were tested by using the same set-up as reported in [4].

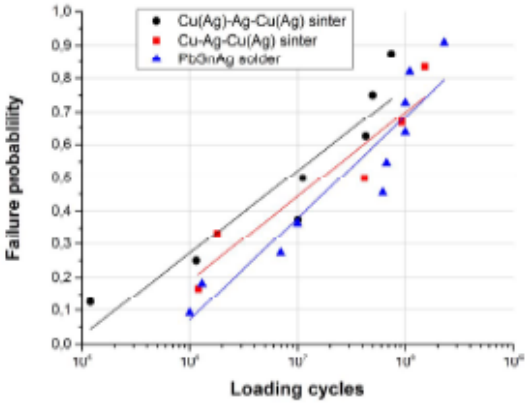

Fig. 9. Probability of failure as a function of loading cycles for two types (Cu-Ag-Cu(Ag) marked as red squares and Cu(Ag)-Ag-Cu(Ag) marked as black circles) of silver sinter joints in comparison to lead-tin-silver alloy solder joints (marked as blue triangle) [4].

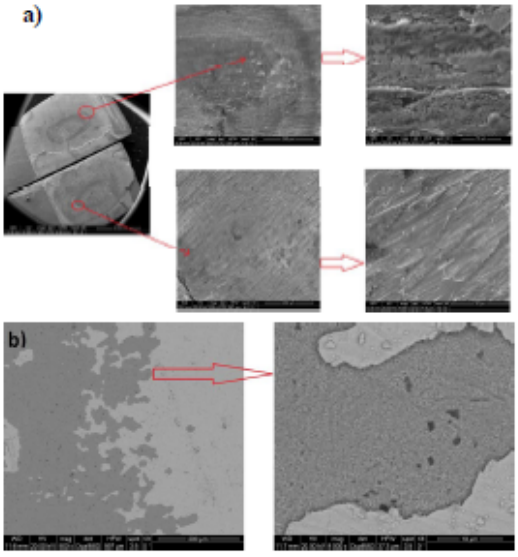

Fig. 10. Samples of surface fracture microstructure a. after shearing and b. after detachment due to fatigue of mechanical cycling.

Analysis of the fracture surface was conducted with scanning electron microscopy. Fig. 10a shows a

depicted example of a couple sheared-off at 100 °C with the typical shear patterns. Fig. 10 b represents a typical partial interfacial delamination of a sample which failed due to detachment of the copper top from the substrate after mechanical fatigue at room temperature.

4. Conclusion

For copper-silver-copper lap-joints it has been confirmed that the interconnection withstands a higher shear stress when the Ag-paste is sintered in air rather than in nitrogen atmosphere. Also a stronger bond for less Ag-thickness (100 µm vs. 200 µm stencil printing) was measured. An increase of shear strength can be gained by raising the process pressure. Augmenting the sintering pressure above 50 MPa leads to a reduction in the porosity of the silver layer to less than 5% from 40% of pressureless sintering. Further, a higher shear resistance was attained when both sides of the copper were pre-sputtered with silver on the junction layers. A decrease in shear strength was observed with increasing the test temperature. From the relaxation investigation of strained samples at 26 °C and at 165 °C stress exponents are obtained according to creep law. For the latter a stronger relaxation is observed with a mean value of 18 for *n*, and 50,6 for room temperature. Furthermore, shearing the samples below 140 °C resulted in fracture near the Ag-Cu interface whereas at higher temperatures failure occurred through the Ag-bulk. Fatigue failure at room temperature occurred mainly due to interfacial delamination. The resultant failure probability plots for silver-sintered copper bonds show similar trend with the strong lead-tin-silver alloy solders joints.

Acknowledgement

The financial support by the Austrian Federal Ministry of Science, Research and Economy and the National Foundation for Research, Technology and Development is gratefully acknowledged. We would like to thank Prof. J. Fleig from Div. Electrochemistry CTA–TU Wien for providing the facility and A. Viernstein for sputtering of the samples.

References

[1] Kim S.Siow, "Are Sintered Silver Joints Ready for Use as Interconnect Material in Microelectronic Packaging?" Journal of Electronic Materials, Vol. 43, No. 4, 2014, pp 947–961

[2] W. Schmitt, L. May Chew, D. Schnee, "Silver sinter paste for SiC bonding with improved mechanical properties"; EMPC 2017, European Microelectronics Packaging Conference , 10-13 September 2017, Warsaw, Poland, www.empc2017.pl, pp. 1-6.

[3] Kim S.Siow, "Mechanical properties of nano-silver joints as die attach materials", Journal of Alloys and Compounds Vol. 514, January 2011, pp. 6-19.

[4] A. Betzwar Kotas, G. Khatibi, "Isothermal bending fatigue response of solder joints in high power semiconductor test structures", Microelectronics Reliability, Vol. 76-77, 2017, pp. 357-361.

[5] Xin Li et al., "Creep properties of low-temperature sintered nano-silver lap shear joints", Materials Science and Engineering A 579, September 2013, pp. 108–113

[6] S. Hascoët, C. Buttay, D. Planson, R. Chiriac, A. Masson, "Pressureless Silver Sintering Die-Attach for SiC Power Devices", ECSCRM, Sep 2012, St Petersburg, Russia. trans tech publications, 4p, 2012

5.2. Behaviour of Silver-Sintered Joints by Cyclic Mechanical Loading and Influence of Temperature

Zeynep Gökdeniz[1)], Golta Khatibi[1)], Johann Nicolics[2)], Andreas Steiger-Thirsfeld[3)]

[1)] Christian Doppler Laboratory for Lifetime and Reliability of Interfaces in Complex Multi-Material Electronics, Inst. for Chemical Technologies and Analytics, TU Wien, Getreidemarkt 9, 1060 Vienna, Austria

[2)] Dep. of Electronic Materials, Inst. of Sensor and Actuator Systems, Gusshausstraße 27-29, TU Wien, Austria

[3)] USTEM, TU Wien, Wiedner Hauptstr. 8-10, A-1040 Wien

Phone: +43-1-58801-164391, E-mail: zeynep.goekdeniz@tuwien.ac.at

Abstract

Devices in power electronics operate at high temperatures and demand controlled power loss density, while the trend leads to low temperature bonding methods in the packaging procedure. As an alternative to using Pb-alloys and Cu-Sn transient liquid phase soldering, Ag-sintering is a promising bonding technology. Silver with its high thermal and electrical conductivity is an advantageous joining material for different applications (e.g. die attach in power modules). One of the main advantages of this joining technology is the low processing temperature in combination with the high melting point of silver. It is also compatible with multilayer processing. The features of the bonding silver layer affect the elastic and thermo-mechanical behavior of the whole devices. A thorough investigation of the properties of Ag-sintered joints in relationship with their microstructure at various temperatures is essential for an appropriate lifetime prediction. This work investigates the low cyclic fatigue of Cu-Ag-Cu la joints at room and elevated temperature prior and subsequent to thermal treatment. Furthermore, the ratcheting behaviour of the joints as a part of the plastic-creep phenomenon has been evaluated. SEM investigations were performed to determine the porosity of the silver bonding layer and to analyze the fracture surface of the failed samples.

Key words: low temperature silver sintering, temperature effect, shear strength, low cycle fatigue, lifetime

INTRODUCTION

While high temperature Pb-solders are still exempted from RoHS regulations for high power semiconductors with specific applications, industry is seeking for reliable alternative solutions. A leadfree alternative is silver sintering, which has the advantage of being a low temperature bonding method. Additional, regarding the device operation temperature, Ag sintered joints are supposed to be insensitive with respect to high temperature (melting point of Ag 960 °C) than conventional solder. Pure silver having high thermal (430 W/(m·K) and electrical conductivity ($60 \cdot 10^6$ S/m) is an outstanding material for different applications in the field of power electronics.

Formulations of silver paste compositions from various suppliers have a broad range containing Ag-particles from flake-shaped to drop-form and from micron to nanosize. They are used to form silver joints by pressureless sintering and sintering under pressure [1] and under atmosphere such as air or nitrogen. The thermo-mechanical behavior of the sintered joints depends on parameter such as their geometry (e.g. thickness of the paste and applied area) and sintering conditions, which affect the porosity and hence the performance of the bonding layer. Based on the microstructure, thermal and mechanical properties of Ag-sintered components are topics of ongoing studies for lifetime prognosis. In this study a commercial silver paste from Heraeus (specified particle size 1 µm – 20 µm) developed for pressure sintering on copper substrate [4] was used.

EXPERIMENTAL

Sample preparation

To perform tests on silver sintered Cu-Ag-Cu lapjoints, samples were prepared as followed: copper stripes of 1 mm thickness, 50 mm length and 3 mm width were grinded and polished to remove the surface oxidation, put in isopropyl for rinsing by ultrasonic bath and dried by air blowing. First a silver layer of approximately 500 nm was sputtered on both mating copper surfaces. Then the Ag-paste was applied by stencil printing (mask thickness

Presented at the European Microelectronics and Packaging Conference and Exhibition (EMPC)®

100 µm) on both strips, forming a pad area of ca. 10 mm² on each side. The Ag-paste was dried at 130 °C under nitrogen flow. Sintering was performed under pressure of 70 MPa for 30 minutes at 230 °C in air (Figure 1).

After sintering some samples were heat treated at 250 °C up to 250 h in air and in protective atmosphere in order to study the effect of aging on the mechanical properties and evolution of pores and grain size.

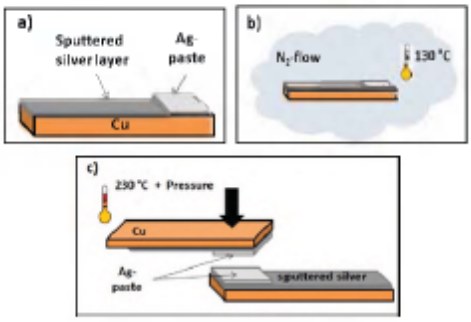

Figure 1: a) Preparation and application of Ag-paste by stencil printing b) Drying under nitrogen-flow c) Sintering of the lapjoints.

Microstructure

Mainly the sintering conditions including temperature, pressure, and time lead to a difference in the microstructure hence in mechanical behavior of the joint. Typical overview of an Ag-sintered lapjoint in Figure 2.a shows that sintering for 30 minutes under 70 MPa pressure leads to a relative dense Ag-layer. The thickness of the silver layer in the lapjoint was reduced from 200 to 70 µm after the sintering process. However, due to the geometrically induced lower bonding pressure at both sides of the joints, the porosity of a marginal area was around 40 % (Figure 2.b) [5]. Nanoindentation tests were performed to determine the Young's modulus of the samples, leading to a value of about 70 GPa for the Ag-joint. The E-Modulus of the porous area was around 45 GPa.

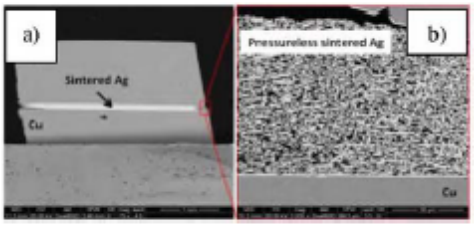

Figure 2: SEM image of the cross-section of a sintered Cu-Ag-Cu lapjoint and the microstructure of the margin area which was sintered with a lower applied pressure.

In order to reveal the microstructure of the joints and to analyze the size and distribution of the pores samples were prepared by using focused ion beam (FIB) technique as shown in Figure 3. The image analyses result in a porosity of around 6 % for the samples prior to heat treatment (for the 0-hour). Not only the total porosity but also the shape and connectivity of the pores affect the properties of a sintered part [9]. The porosity of the sintered layer seemed not to be isolated but formed an interconnected network. After heat treatment at 250°C for 250 hours a considerable change of the microstructure including rearrangement and coarsening of the pores as well as grain growth is observed (Figure 3.b).

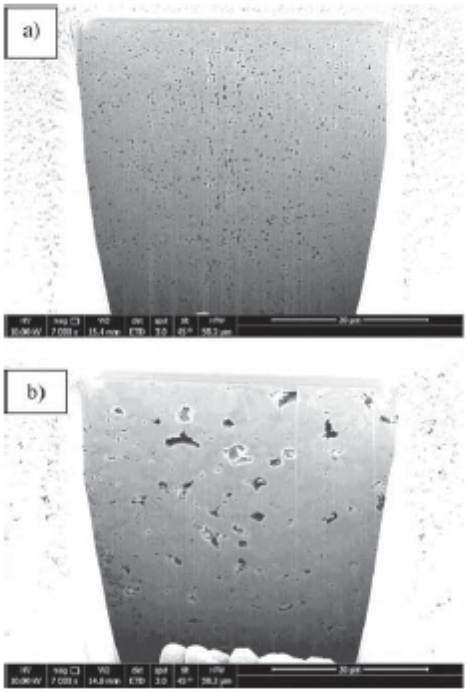

Figure 3: FIB milled section of the Ag-layer which was sintered under 70 MPa pressure a) in non-aged state and b) after aging for 250 hours at 250 °C in air.

Aging in air leads to copper-oxide formation at the Cu-Ag interface as shown in Figure 4. In our study a series of samples were protected from oxidation during the heat treatment by encapsulation in hermetically sealed glass tubes.

Tensile and fatigue test set-up

A universal testing machine from Messphysik Austria equipped with a load cell capacity of 1 kN was used for determination of mechanical properties.

Previously published in the Proceedings of EMPC-2019

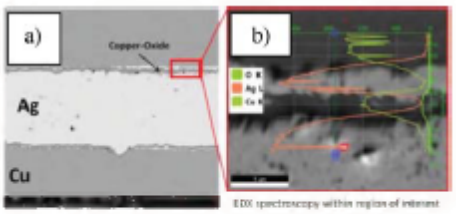

Figure 4: SEM image from the cross-section of a sample after heat treatment in air with the EDX analysis showing copper-oxide.

A thermal chamber was part of the set-up to implement the experiment also at elevated temperatures. A Laser Speckle Extensometer (LSE) system was used for contactless strain measurement of the joint area (Figure 5).

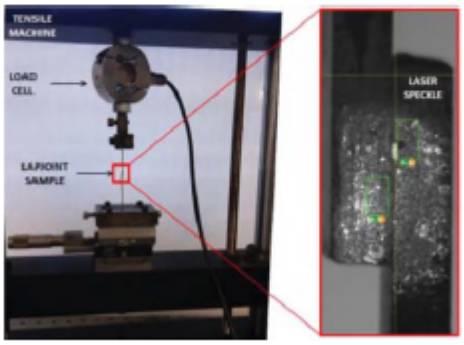

Figure 5: Tensile machine with LSE for measurements of shear strength and low cycle fatigue experiments of Cu-Ag-Cu lapjoints.

RESULTS

The effect of surface roughness of copper substrate for pressureless sintered silver on the shear strength has been investigated by Meiyu Wang et al. [7]. The pre-metallization with silver of the surface leads to a stronger interface connection compared to electroplating [6]. In a previous study, we found that using Ag-sputtered strips results in an increase of the joint strength comparing with those sintered on blank copper [8]. Therefore, in this study only sputtered samples were prepared for the fatigue investigation. All samples were half an hour and sintering pressure of 70 MPa were chosen for the samples to be investigated for mechanical cycling.
For the pre-characterization shear tests were performed on several samples resulting in a maximum shear strength of 45 MPa and a mean value of 35 MPa. A rather high scatter of shear strength in all samples was observed with 44 % of non-aged samples and 26 % of aged samples showing shear strength values below 40 MPa. These results indicate an improvement of the shear strength of Ag-sintered joints subsequent to aging. As described in the next section, low cycle fatigue tests were conducted with a maximum stress of 40 MPa.

Low cycle mechanical loading and ratcheting

Low cycle fatigue tests were performed with a cross head speed of 2 mm/min which corresponds to a testing frequency of about 0.1 Hz. The tests were conducted in tensile-tensile loading mode with a minimum stress of 8 - 10 MPa and maximum stress levels of 30, 35 and 40 MPa.

Figure 6 shows the $\sigma - \varepsilon$ relationship of a Cu-Ag-Cu lapjoint corresponding to the strain data captured with the LSE directly from the silver joint area (Figure 5) in comparison with the response of the whole system including the testing machine and the joint. For an example at a stress level of 30 MPa, the strain of the joint is about 4.5-5 % for the first five cycles with LSE, while the strain value of the whole system is around 14 %.

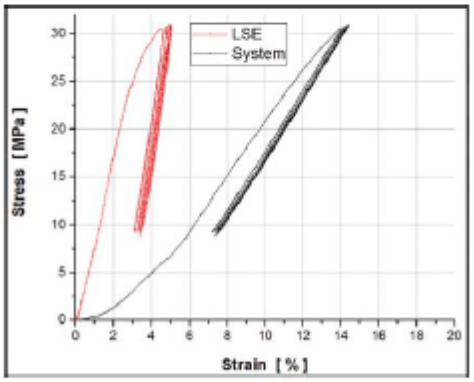

Figure 6: $\sigma - \varepsilon$ relationship of the Ag-interface captured with LSE (red plot) and of the total setup (black plot).

Ratcheting is a creep-phenomenon which occurs when the maximum of the exerted stress exceeds the elastic limit of the material. By the

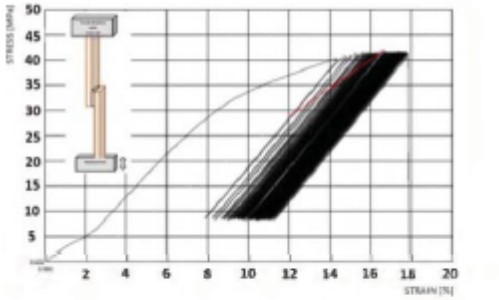

Figure 7: An example for the $\sigma - \varepsilon$ –curve of the Ag-sintered lapjoint by cycling loading.

Previously published in the Proceedings of EMPC-2019

application of cyclic stress in the tensile-tensile mode, a shift of the stress-strain hysteresis is observed due to plastic deformation. The rate of ratcheting is affected by the stress level (mean and maximum), temperature, loading history and other factors [2]. An example of this behavior for the Cu-Ag-Cu lapjoints is shown in Figure 7.

Figure 8 shows an increase of the ratcheting strain (ε_r) of the non-aged samples for stress levels of 30 and 40 MPa. A comparison of the ε_r - N_f, curves up to 300 cycles shows that a higher stress amplitude results in an increase of ratcheting strain from 14.8 % to 21.5 % (Figure 8.a). The strain rate at the first 50 cycles in both cases is higher, which gradually decreases with increasing the cycles to failure (N_f). Figure 8.b shows that the curve corresponding to a σ_{max} of 30 MPa tends to saturate after a couple of thousand cycles.

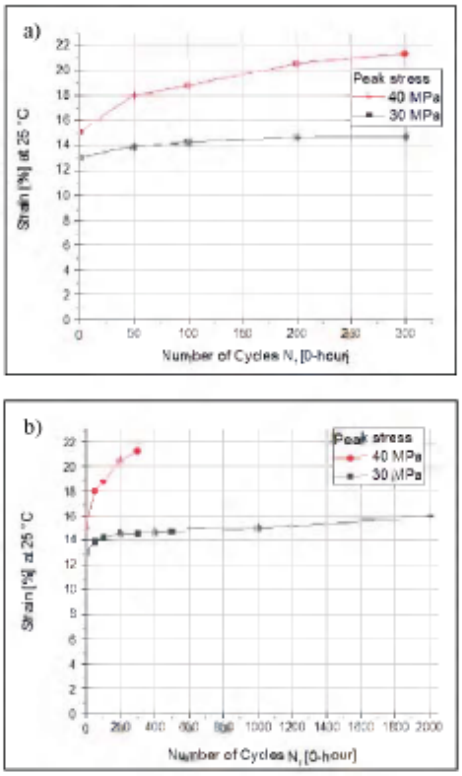

Figure 8: Average ratcheting strain at two stress levels for non-aged samples at room temperature up to N_f = 300 (a) and N_f = 2000 (b).

Influence of temperature on lifetime N_f

A comparison of the S-N curves of the non-aged lapjoints tested at 25 °C and 130 °C in the low cycle regime is presented in Figure 9. The curves are obtained in the range of maximum stress 40 to 30 MPa up to ~ 1e4 cycles to failure. Though a high scatter of data is observed in both cases, a clear shift of S-N curve with increasing the testing temperature is observed resulting in the reduction of lifetime around one order of magnitude.

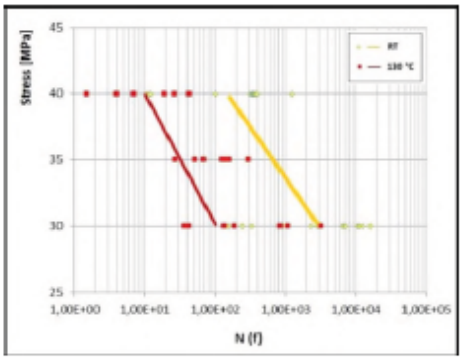

Figure 9: S-N curve for sintered Cu-Ag-Cu lapjoints

The fracture probability curves of non-aged joints at 25 °C and 130 °C in comparison with those of in air aged samples tested at 25 °C is displayed in Figure 10. All samples were tested at a σ_{max} of 30 MPa (mean stress of 20 MPa). The plots show that the aged samples have a 50 % lifetime expectation of 5.000 cycles, whereas it is 3.000 cycles for non-aged ones (Figure 10.a). Aging in a protective atmosphere results in a clear improvement of lifetime as shown in Figure 10.b for samples investigated at σ_{max} of 40 MPa (mean stress of 25 MPa). The 50 % lifetime expectation is 150 cycles versus 4.000 cycles for the non-aged and aged samples respectively.

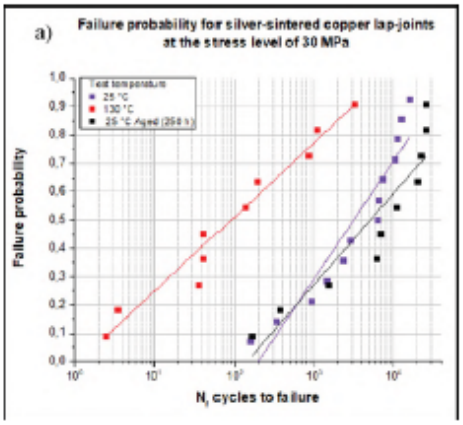

Previously published in the Proceedings of EMPC-2019

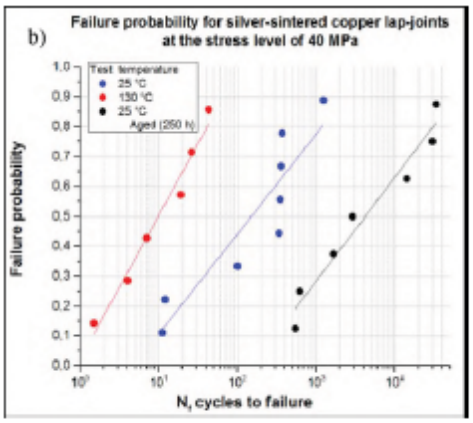

Figure 10: Failure probability plots of the Cu-Ag-Cu joints tested at elevated (red plots) and room temperature for two stress levels as shown in a) and b) and for both, 0-hour and aged sample series (blue or violet and black plots).

Fracture surface analysis

SEM investigations were performed to analyze the fracture surface of the aged and non-aged samples after shear and fatigue testing at room and elevated temperatures. Basically, two types of crack propagation were observed: One near the copper interface but mainly between sputtered and sintered silver layers (Figure 11.a), the other mainly through the Ag-sintered layer (Figure 11.b). Joints without heat treatment (0-hour samples) tested at room temperature, tend to break near Cu/Ag bonding interface. Heat treated samples which were tested at higher temperatures as well as aged samples tend to break rather in the bulk of silver sintered layer. This type of fracture was observed in the case of samples either subjected to static or cycling loading.

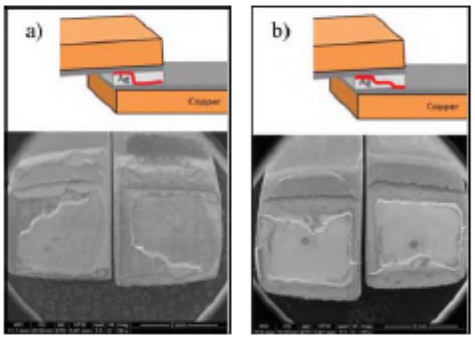

Figure 11: Exemplary SEM images and schematic crack path of fracture propagation near interface (a) and through sintered silver bulk (b).

CONCLUSION

Primarily the sintering conditions such as temperature, pressure and duration influence the microstructure of the silver sintered joints. Optimization of the manufacturing parameter includes surface treatment of the interconnecting components such as surface roughness and metallization. Mechanical properties e.g. static shear strength or fatigue behavior of the joint is affected by the porosity of the sintered bonding layer.

In this study an increase of porosity from 6 % to 40 % within the Ag-sintered joints resulted in a decrease of Young's Modulus from 70 to 45 GPa. The ratcheting behavior of the lapjoints under constant stress cyclic loading was studied. The ratcheting strain which describes the creep phenomenon of the material was found to be strongly dependent on the maximum cyclic stress at room temperature.

For non-aged samples fatigue testing at elevated temperature of 130 °C lead to a significant reduction of lifetime compared to testing at 25 °C. Long term thermal exposure in air at 250°C/250h resulted in formation of copper-oxide at the Cu/Ag interface which is believed to have a weakening effect on the joint. Furthermore a considerable grain growth and alteration of the pore shape and distribution was observed during the aging up to 250 hours. Thereby the volume percentage of the pores remained almost unchanged. Long term aging did not result in a decrease of fatigue response of the Ag-joints at room temperature. Independent of aging at air or protective atmosphere, an improvement of the lifetime was observed. In the latter case even a considerably higher lifetime was obtained. In addition, aging resulted in a change of failure mode from near interface fracture to failure in the bulk of the sintered layer due to the higher capacity of plastic deformation in the recrystallized material.

In a study on the effect of aging on the tensile behavior of sintered silver a clear trend between the mechanical response in the plastic regime and the ageing time or density was not found. This unpredictable behavior of the aged porous silver was rather related the statistically inhomogeneous distribution of the pores leading to a variation of the local density of the samples [3]. In the present work, the improvement of the fatigue strength of the aged samples at low cycle regime and high stress amplitudes seems to be related to several concurrent factors. These may include a possible completion of the sintering process during the aging, increased plasticity as result of recrystallization, increase in the mean pore spacing and improvement of the interfacial bonding strength as a result of diffusion. For a better understating of the low cycle fatigue behavior of silver sintered joints further studies are ongoing.

Previously published in the Proceedings of EMPC-2019

Acknowledgements

The financial support by the Austrian Federal Ministry for Digital and Economic Affairs and the National Foundation for Research, Technology and Development is gratefully acknowledged.

We would like to thank Prof. J. Fleig and A. Opitz from Div. Electrochemistry CTA–TU Wien for providing the sputter facility.

References

[1] Kim S. Siow, "Are Sintered Silver Joints Ready for Use as Interconnect Material in Microelectronic Packaging?" Journal of Electronic Materials, Volume 43, Issue 4, 2014, pp. 947-961.

[2] Tao Wanga, Gang Chena, Yanping Wangb et al., "Uniaxial ratcheting and fatigue behaviors of low-temperature sintered nano-scale silver paste at room and high temperatures", Materials Science and Engineering A, Volume 527, Issue 24-25, September 2010, pp. 6714-6722.

[3] P. Gadaud et al. "Ageing Sintered Silver: Relationship between Tensile Behavior, Mechanical Properties and the Nanoporous Structure Evolution" Materials Science & Engineering A 669 (2016) 379–386

[4] Ly May Chew et al., "Micro-silver sinter paste developed for pressure sintering on bare Cu surfaces under air or inert atmosphere", 2018 IEEE 68th Electronic Components and Technology Conference, 29 May - 1 June 2018, San Diego - California, USA.

[5] Wolfgang Schmitt et al., "Silver sinter paste for SIC bonding with improved mechanical properties", EMPC 2017, September 10th to 13th 2017, Warsaw University of Technology, Poland.

[6] Chen, C. et al. "High-temperature reliability of sintered microporous Ag on electroplated Ag, Au, and sputtered Ag metallization substrates", Journal of Materials Science: Materials in Electronics, Volume 29, Issue 3, 1 February 2018, pp. 1785-1797.

[7] MeiyuWang et al., "How to determine surface roughness of copper substrate for robust pressureless sintered silver in air", Materials Letters, Volume 228, 1 October 2018, pp. 327-330.

[8] Z. Goekdeniz, et. al. "Temperature Dependent Mechanical Properties of Sintered Silver-Copper Joints" ISSE 2019 1-6. 10.1109/ISSE.2018.8443659

[9] Herbert Danninger et al., "Automatic measurement of the effective load bearing cross section Ac in sintered steel", Praktische Metallographie / Practical Metallography, Volume 39, Issue 8, August 2002, pp. 414-425.

Previously published in the Proceedings of EMPC-2019

5.3. Temperature Dependent Physical Properties of Sintered Silver Layers for Power Electronics

Zeynep Gökce Gökdeniz[1)], Golta Khatibi[1)], Christian Gierl-Mayer[2)], Andreas Steiger-Thirsfeld[3)], and Martin Mündlein[4)]

[1)] Christian Doppler Laboratory for Lifetime and Reliability of Interfaces in Complex Multi-Material Electronics, Inst. for Chemical Technologies and Analytics, TU Wien, Getreidemarkt 9, A-1060 Vienna, Austria
[2)] Research Group for Powder Metallurgy, Inst. for Chemical Technologies and Analytics, TU Wien, Getreidemarkt 9, A-1060 Vienna, Austria
[3)] USTEM, TU Wien, Wiedner Hauptstr. 8-10, A-1040 Vienna, Austria
[4)] ESCATEC Switzerland AG, Heinrich-Wild-Strasse, CH-9435 Heerbrugg, Switzerland
zeynep.goekdeniz@tuwien.ac.at

Abstract: *Low-temperature silver sintering is a lead-free alternative interconnection technology for power modules. In addition to high electrical and thermal conductivity, silver with its moderate homologous temperature in comparison to conventional solder alloys is a promising material for applications with elevated operation temperature (above 130 °C). Therefore, investigations of the material behavior of the sintered Ag layer at various temperatures and stress conditions are essential for reliable model-based lifetime predictions. This work focuses on characterization of mechanical and electrical properties of sintered Ag coupons in relationship with their preparation and testing conditions. Simultaneous thermal analysis and residual carbon analysis are executed for the selected Ag-pastes. Dog-bone shaped specimens of Ag-paste were prepared using different sintering temperature (230 °C or 300 °C), pressure (pressureless or 70 MPa), and time (10 min, 30 min, 60 min) after drying at 130 °C for an hour under nitrogen flow. For the defined sample series, the thickness of the sintered Ag-layer and the density are quantified using microscopic techniques. Electrical resistivity at room and elevated temperature is measured using the Van-der-Pauw Method. The tensile strength is obtained for 25 °C, 130 °C, and 200 °C. Fracture surfaces of fresh and thermal treated (at 250 °C) samples are analyzed by scanning electron microscopy.*

1. Introduction

Lead containing solders have been used over decades as bonding material. Alternative lead-free interconnection technologies such as TLP systems and SnAg solders are used in applications, for example as in DCB (direct copper bonded) elements in power electronics, especially in combination with copper substrate. The emerging heat dissipation during operation can lead to mismatch due to differences of the materials' thermal expansion coefficient (CTE). To name some numbers, copper has a CTE of 16-17 µm/(m·K), DBCs with AlN or Al_2O_3 ca. 4.5 or 7-8. With a CTE of ca. 19 silver shows a better compatibility in the system than SnAg with CTE over 22 (depending on alloy, thickness or temperature).

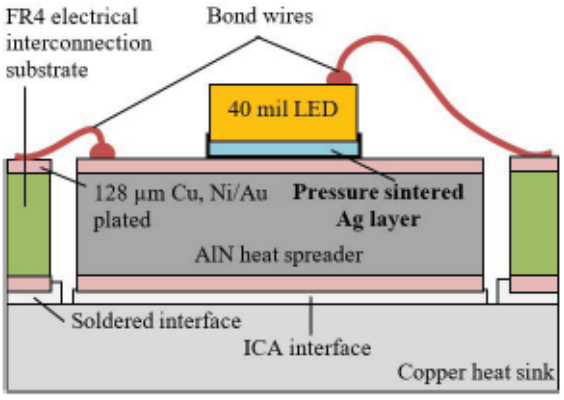

Fig. 1. Schematic structure of power LED assembly.

978-1-7281-6773-2/20/$31.00 ©2020 IEEE

Several industrial applications needing long-term stability at high operation temperature and the predictability of lifetime have provoked research on the temperature dependence of mechanical and electrical properties of the sintered silver bonding layer. In order to provide a better understanding of the importance of the bonding layer, the following example is described in some details.

The schematic build-up of a single light emitting diode (LED) used in a system is depicted in Fig. 1. Each one LED is mounted on an AlN heat spreader with 128 µm thick copper layers on top and bottom providing both, heat spreading and electrical isolation of the LEDs. The AlN substrate is attached to a copper heat sink over its comparatively large bottom face using an ICA (Isotropically Conductive Adhesive). This bonding techniques proves to be thermo-mechanically compliant even for large substrate dimensions. However, a low-enough temperature drop between LED backside and the AlN heat spreader cannot be realized using ICA technology. Moreover, for electrical interconnection of the LED chip Au wire ball bonding to a supply substrate (without thermal function) and bondings from the AlN heat spreader to this FR4 substrate are needed.

Including light-forming optical components it shows a volume of only 15 cm^3 and generates over 18.000 lm at a total electrical power of approximately 200 W and an angle of radiation of 22°. Novel 40 mil high-power LEDs are applied each operated continuously with a current of up to 3 A. At high-power operation around 65 % of this input power is converted into heat and needs to be dissipated over the backside of the LED chip. For high performance spotlight applications multiple of these LEDs are combined on one substrate with minimum distance to each other to achieve a maximum light density. The highest heat flow density appears at the LED backside (~715 W/cm^2). Therefore, the interconnection interface at that point is most relevant for thermal management. The LEDs are connected in series which requires an electrical isolation of the LED backside against each other. Due to excellent heat spreading in an AlN-based substrate the heat flux density at further interfaces is significantly reduced making them thermally less critical.

In order to comply with all requirements also from the viewpoint of manufacturability low-pressure silver sintering was considered the most promising technology for mounting the LED chips.

Investigations of the material behaviour of the sintered Ag layer at various temperatures and stress conditions are essential for reliable model-based lifetime predictions. Although there are studies about the relationships of porosity and resistivity [1] or tensile behaviour [2] based on thermal aging, there is a lack of experience relating to the parameters which impacts the bonding quality of the interconnection in combination with the metallurgical changes in the sintered layer.

2. Experimental

2.1. Sample preparation

A commercial Ag-paste from Heraeus (mAgic ASP series) was first applied with 200 µm stencil printing, dried at 130 °C for an hour under nitrogen flow in an oven with a slope profile (constant ramp rate in two slope steps: first from 25 °C to 100 °C and then slower from 100 °C to 130 °C to prevent overheating of the oven), and then sintered under various parameters. For pressureless sintering silver paste was implemented on glass substrate, for high pressure sintering on a ceramic substrate which was cleaned and coated with Bor-Nitride [1]. For the latter case an automatic Carver press machine with heating plates was used enabling a cooling procedure (adjusted to 5 minutes) after sintering while keeping the pressure.

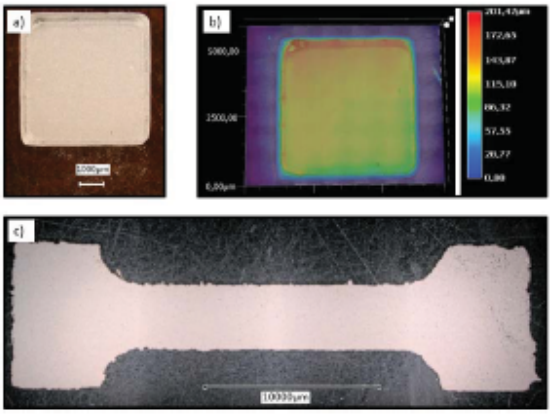

Fig. 2. Overview of samples: a) 5 mm × 5 mm square pads used for density and conductivity measurements. b) Height profile of the 200 µm stencil printed Ag after drying at 130 °C. c) The dog-bone specimens used for tensile testing.

Figure 2 shows the example of the prepared samples: a) 5 mm x 5 mm square pads were mainly used for density and conductivity measurements, and b) height profile taken after drying with a Keyence 3D-

microscope. Figure 2.c shows the dog-bone structure used for tensile testing. Samples were produced in three variations of the geometry with following measurements: either with a total length of 3 cm or 4 cm with a width of 5 mm in the middle, or total length of 2 cm with a width of 3 mm in the middle.

Based on own results on copper-silver-copper lap joints [3] and considering the thermal analysis of the dried silver paste for sintering temperature, pressure and time three main conditions are selected and named as following: A) 230 °C, 0 MPa, 30 min, B) 300 °C, 0 MPa, 30 min, and C) 230 °C, 70 MPa, 30 min.

2.2. *Thermal analysis*

Simultaneous thermal analysis (STA), including mass spectrometer (MS), thermal gravimetric (TG) and differential thermal analysis (DTA) was performed in artificial air (80 % N_2/20 % O_2) from room temperature to 500 °C with a heating ramp of 10 K/min.

The TG analysis measures the change of the weight due to reaction when temperature changes. The DTG-plot (∂TG) is the derivative of the corresponding TG-curve.

The DTA measures the temperature change (signal detection in µV) of the tested sample versus reference substance. It is an instrument to deduce the free thermal energy delivered by reactive molecules.

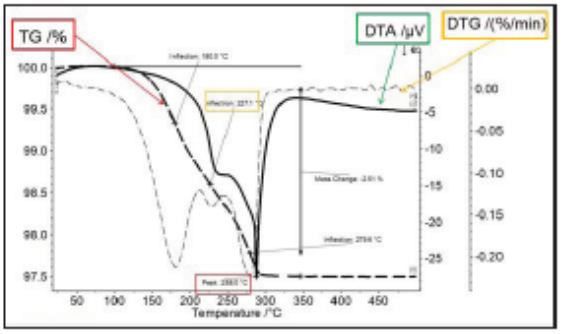

Fig. 3. Simultaneous thermal analysis for the used Ag-paste after drying at 130 °C.

The STA device was coupled to a mass spectrometer by heated (250 °C) capillary coupling. From room temperature to 300 °C mass loss occurs in three distinctive steps. The first step starts at temperatures around 180 °C and the mass loss is not clearly visible. It may be an evaporation of some remaining solvent from the drying performed at 130 °C. The second mass loss around 230 °C is only visible when DTG is taken into account. The last extremely sharp peak of DTA indicates an exothermic reaction near 290 °C. After that intense peak only a very small peak of CO_2 (mass 44) at about 380 °C and the TG shows no change until 500 °C as shown in Fig. 3.

Results of the residual carbon analysis for the used Ag-paste are as following: 0.58 % after drying at 130 °C for one hour, 0.014 % after pressureless sintering at 230 °C for 30 min and 0.0077 % after pressureless sintering at 300 °C for 30 min.

2.3. *Microstructure of samples*

The Secondary Electron Microscope (SEM) images were taken to compare the state of the silver particles after various treatments.

Figure 4 shows the flake-shaped structure of the Ag-paste in the range of a couple of micrometers after drying for an hour at 130 °C under nitrogen flow.

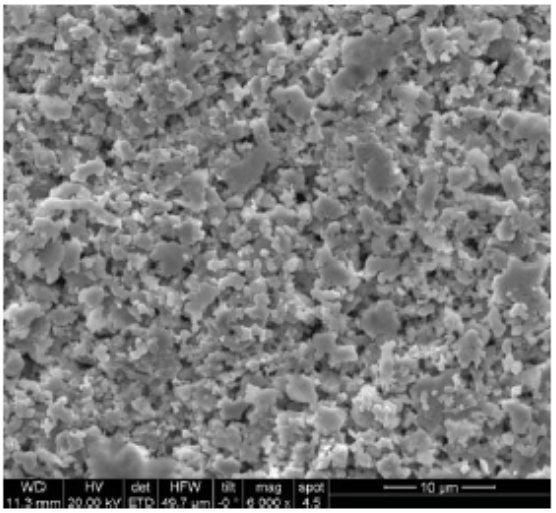

Fig. 4. Ag-paste surface after drying at 130 °C.

After sintering, some samples were heat treated at 250 °C in protective atmosphere or air ambient to measure the effect of thermal aging. The exposure time was 250 hours. Figure 5 shows two selected samples, both sintered at 230 °C. First specimen shown in Figure 5.a. was sintered pressurelessly and heat treated in protective glass: no special growth of the Ag-colloids or pores can be observed. Second specimen was fully exposed to air during heat treatment, as shown in Figure 5.b: a growth of the Ag- particles up to 5 µm can be observed.

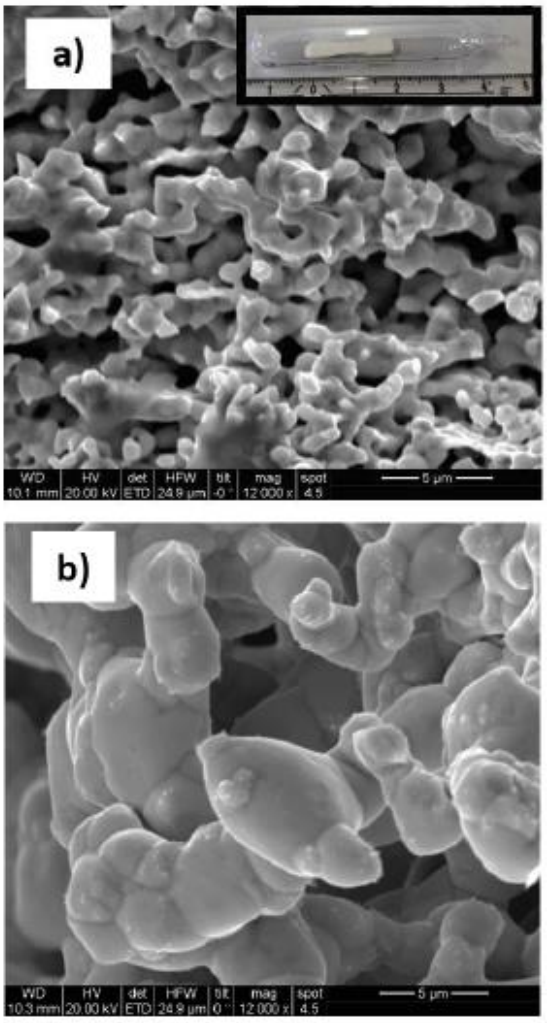

Fig. 5. Heat treatment effect on sintered silver particle sizes a) in protective glass preventing further free oxygen supply and b) in air ambient.

Further investigations on heat treatment with own samples sintered pressureless at 300 °C lead to a rather slower increase of the Ag-particles size in protective atmosphere but nevertheless recognizable up to 3 µm diameter. Other investigations of Ag-material sintered at 300 °C and under low pressure (ca. 4 MPa for 30 minutes) also reveal particle rearrangement and agglomeration into micron size clusters [4].

3. Set-up

3.1. Resistivity testing

The Van der Pauw Method is a four-point measurement technique which allows to provide an average resistivity of the specimen. Two electrodes are used to imply current and the other two electrodes to measure the voltage.

From measurements with the ohmic law gained value of the mean resistance R and the known Ag-thickness d of the sample are used to obtain the resistivity ρ:

$$\rho = R * \frac{\pi * d}{\ln(2)} \quad (1)$$

The thermal conductivity λ can be deduced by the Wiedemann-Franz-Lorenz law for metals

$$\lambda = \frac{1}{\rho} * L * T \quad (2)$$

where T is the temperature and L the Lorenz number:

$$L = \frac{1}{3} * \left(\frac{\pi * k}{e}\right)^2 \quad (3)$$

with the Boltzmann constant $k = 1.38 \cdot 10^{-23}$ J/K and the elementary charge $e = 1.6 \cdot 10^{-19}$ As.

The measurements at higher temperature were done in a Fluoric-Carbon liquid which was heated in a glass bowl placed in the heating chamber as seen in Figure 6.

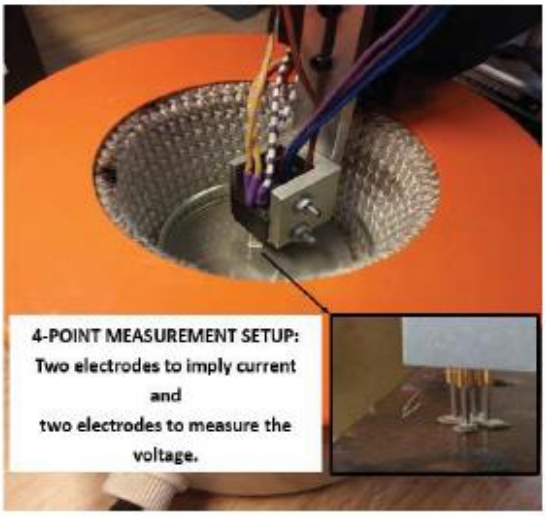

Fig. 6. Set-up for deducing the resistivity of sintered silver samples with Van-der-Pauw Method.

3.2. Tensile testing

A universal testing machine from Messphysik Austria equipped with a load cell with a resolution of 10 mN as in Figure 7 was used for determination of mechanical properties. A thermal chamber was also part of the set-up to implement the experiment at elevated temperatures.

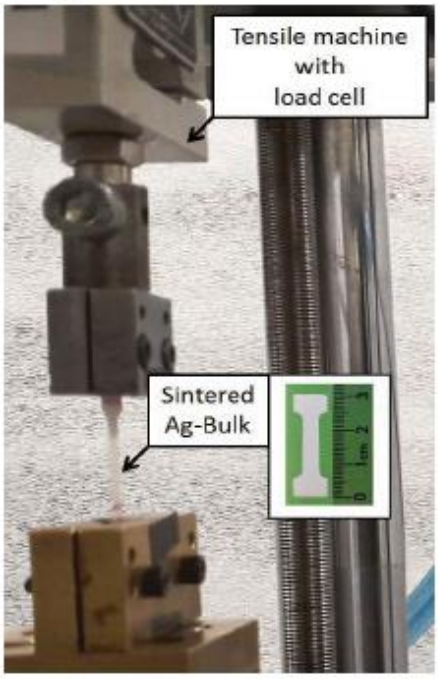

Fig. 7. Testing of sintered Ag-dogbone sample for characterizing the tensile strength and stress coefficient.

4. Results

4.1. Density measurement

For the selected series types A (pressureless PL, low temperature LT 230 °C), B (pressureless PL, high temperature HT 300 °C), and C (high pressure HP and 230 °C LT) the mean thickness values after sintering are around 115 µm, 105 µm, and 75 µm respectively.

The density of sintered silver is deduced by measuring the mass-weight and volume of the samples:

$$\varrho = \frac{m}{V} \tag{4}$$

Calculated densities as shown in Fig. 8.a are ϱ_A=3.7 g/cm^3, ϱ_B=4.4 g/cm^3 and ϱ_C=6.5 g/cm^3 and correspond, compared to pure silver (ϱ_{Ag}=10.49 g/cm^3) to Ag-content of 35 %, 42 % and 62 % respectively. An additional series of specimen (D) sintered at high pressure (70 MPa) and high temperature (300 °C) lead to the 68 % Ag-content with ϱ_D=7.2 g/cm^3.

As shown in Fig. 8.b, samples sintered at 230 °C for 30 minutes yielded a value of 6.2 g/cm^3 for 35 MPa sintering pressure and 6.55 g/cm^3 for 90 MPa.

Further measurements are done as plotted in Fig. 8.c for variations of time (10, 30, 60 min) or temperature (230 °C and 300 °C) for otherwise constant sintering parameters. The results show no significant change in the density (3.5 - 4 g/cm^3 for LT and 4 - 4.5 g/cm^3 for HT) compared to the compression taking place by pressured sintering, which also seems to slowly come to a saturation above the limit of 35 MPa.

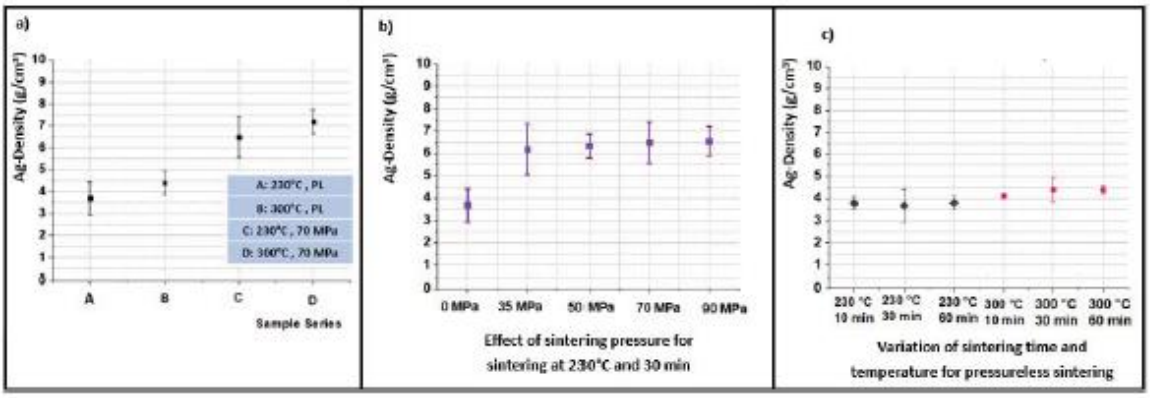

Fig. 8. Density of the sintered Ag for the selected parameter series (a). Effect of sintering pressure (b) and time or temperature on the Ag-density (c).

4.2. Resistivity measurement

Pure silver has a thermal conductivity of 430 W/(mK) and an electrical conductivity of $60 \cdot 10^6$ S/m at room temperature corresponding to an electrical resistivity of $16.7 \cdot 10^{-9}$ Ωm.

Sintered Ag has a porous structure with connection points and areas which lead to a restricted current flow path and therefore to a lower conductivity for less density. The resistivity of pressurelessly (PL) sintered samples (A: $68 \cdot 10^{-9}$ Ωm, and B: $58 \cdot 10^{-9}$ Ωm) is higher than with high pressure (HP) sintered ones at room (C: $30 \cdot 10^{-9}$ Ωm), and elevated temperature.

Metals are known for decreasing electrical connectivity at higher temperatures. Whereas the electrical resistivity for the PL-sintered silver increase to $119 \cdot 10^{-9}$ Ωm for the rising testing temperature from 25 °C to 200 °C, for the HP- sintered silver the increase is up to $44 \cdot 10^{-9}$ Ωm.

The measurements were done by using the Van der Pauw Method as described above. Two electrodes are used to imply current of 1 A and the other two electrodes detected the sample voltage in the range of several 100 µV.

4.3. Tensile measurement

Tensile strength of the dogbone shaped Ag-samples were studied at room and elevated temperatures with the testing speed of 1 mm/min.

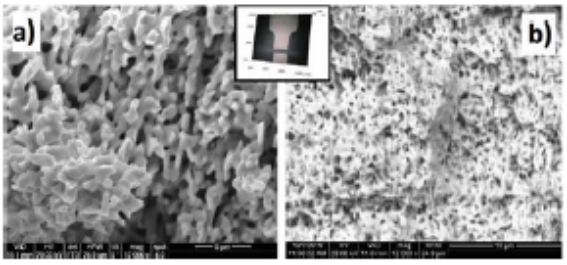

Fig. 9. Microstructure after tensile testing at room temperature: a) pressureless sintered samples (A-series) and b) high pressure sintered samples (C-series).

Figure 9 shows the cross-section of the sintered samples (in air ambient, at 230 °C) after the tensile testing at 25 °C. As shown in Figure 9.a. selected specimen type A is sintered pressureless, in comparison to the specimen type C which develops dimple-like microstructure during high pressure sintering as shown in Figure 9.b.

Not explicitly plotted here, the stress-strain curves show the clear brittle fracture of tensile testing for samples at room temperature going into a ductile fracture progression at 200 °C. The fracture mode transforming from brittle to ductile is also reported for self-manufactured Ag-paste samples (sintered at 250 °C for 1 h without pressure) after thermal aging at 250 °C for 200 hours compared to the initial state (with electrical resistivity of $8.5 \cdot 10^{-6}$ Ωcm and tensile strength of 42 MPa) [1].

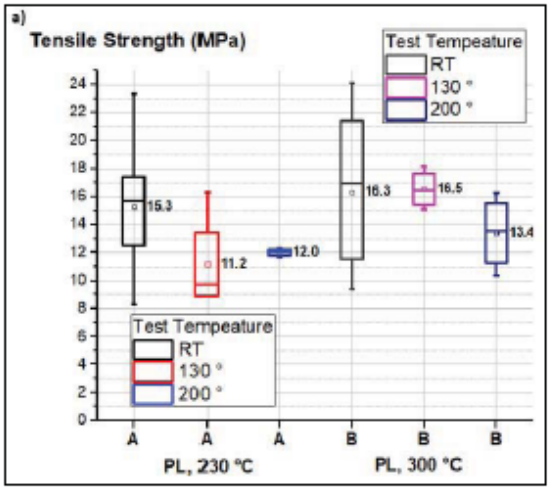

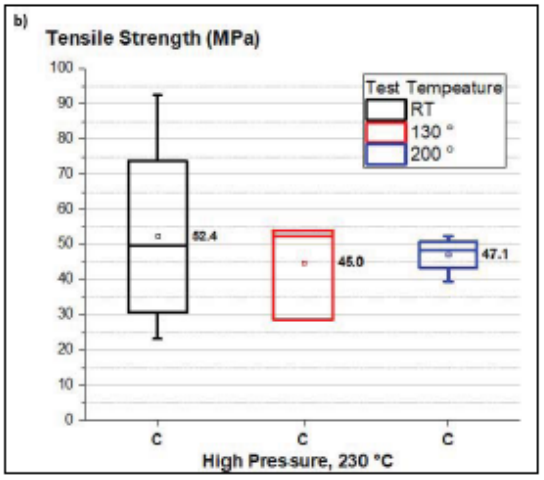

Fig. 10. Tensile strength of the a) pressureless and b) under 70 MPa sintered series are tested at 25 °C, 130 °C, 200 °C.

As shown in Figure 10, the decrease of tensile strength with rising test temperature hint at a relation with the sintering temperature: for samples prepared at the lower temperature of 230 °C the rapidly falling

values are observed rather near 130 °C (for PL samples from ca. 15 MPa to 11 MPa and HP samples from ca. 52.4 MPa to 45 MPa), while for samples prepared at higher temperature of 300 °C the falling tensile strength is observed rather near 200 °C (PL samples, from ca.16.5 MPa to 13.4 MPa).

Table 1. Comparison of tensile strength: 0-hour vs. 250 hours thermal treated at 250 °C.

Sample Series	0-hour	250 hours
A: 230 °C, PL	15.3 MPa	16.7 MPa
B: 300 °C, PL	16.3 MPa	26.8 MPa
C: 230 °C, 70 MPa	52.4 MPa	53.2 MPa

A comparison of tensile test results at room temperature for the (in protective atmosphere) heat treated samples is pointed out in Table 1. Only the specimen sintered at the higher temperature of 300 °C show a remarkable rise in tensile strength. This might be due to the increasing particle size (as mentioned in section 2.2) and accordingly larger contact area of the sintered Ag.

5. Summary

The need for a favorable interconnection technique particularly for power electronic applications is highlighted in the introduction on the example of an innovative high-performance LED multichip module. Silver sintering at temperatures even lower than needed for soldering is a promising alternative. However, for reliable model-based lifetime predictions more data from material investigations are required. In this paper temperature dependent physical properties of sintered silver layers are investigated.

The thermal analysis of the dried silver particles shows three main stages of reactions: evaoration of the remaining solvents from the past at ca. 180 °C, sintering aggregate of Ag at 230 °C and an exothermic reaction near 290 °C corresponding to a mass (44) spectrometry peak of CO_2.

For sintering parameters time, pressure and temperature three main conditions are selected: A) 30 min, 0 MPa, 230 °C, B) 30 min, 0 MPa, 300°C and C) 30 min, 70 MPa, 230 °C.

The mean thicknesses after sintering are measured and the deduced **Ag-content** values of the series lead to of 35 %, 42 % and 62 % respectively.

Further density measurements of samples sintered at 230 °C for 30 minutes are studied, indicating that between 0 and 35 MPa a saturation limit of ca. 6 g/cm^3 silver is reached and above this value the density increases only slowly (6.55 g/cm^3) with increased pressure (90 MPa). For pressureless sintering the variation of time (10, 30, 60 min) or temperature (230 °C, 300 °C) does lead to a significant change of density, for the given other parameter.

The mean electrical resistivity at room temperature decreases with decreasing porosity.

Likewise, the mean **electrical resistivity at higher testing temperature** increases more for the samples with increased density than the dense sintered ones.

After heat treatment at 250 °C for 250 hours, in protective atmosphere especially near the pressured center of the at 230 °C sintered Ag no significant grain growth can be observed (500 nm – 1 µm), unlike the heat treatment in air where an augmentation of particle diameter clearly stands out (up to > 5 µm), starting from the outer corners. Moderate enlargement of the grain clusters (< 3 µm) also occur for samples sintered at 300 °C and heat treated at 250 °C in protective glass.

The tensile strength of the pressureless sintered Ag dog-bone samples (types A and B) have mean values of around 15-16 MPa, whereas it is above 50 MPa for the samples sintered under high pressure (type C).

The tensile strength of (in protective atmosphere) heat treated samples tested at room temperature show an increasement only for those which have been sintered at 300 °C.

With **increasing test temperature**, the maximum and mean values of tensile strength show a descending tendency. The fracture behavior at 25 °C is rather brittle, whereas at 200 °C it is ductile.

The fracture surface of pressurelessly sintered specimens are flat without any plastic deformation whereas specimens sintered under high pressure show a dimple-structure after failure.

Acknowledgement

The financial support by the Austrian Federal Ministry for Digital and Economic Affairs and the National Foundation for Research, Technology and Development is gratefully acknowledged.

We would like to thank Prof. J. Fleig and A. Opitz from Div. Electrochemistry CTA–TU Wien for providing the sputtering facility.

We would like to thank Markus Lunzer, BSc. for his participation in density measurements.

REFERENCES

[1] Chanyang Choe, Seungjun Noh, Chuantong Chen, Dongjin Kim, Katsuaki Suganuma, "Influence of thermal exposure upon mechanical/electrical properties and microstructure of sintered micro-porous silver", Microelectronics Reliability, Vol. 88–90, pp.695-700, 2018.

[2] P. Gadaud, V. Caccuri, D. Bertheau, J. Carr, X. Milhet: "Ageing sintered silver: Relationship between tensile behavior, mechanical properties and the nanoporous structure evolution", Materials Science and Engineering: A., Volume 669, Pages 379-386, July 2016.

[3] Z. Gökdeniz, G. Khatibi, T. Walter, J. Nicolics "Temperature Dependent Mechanical Properties of Sintered Silver-Copper Joints", DOI: 10.1109/ISSE.2018.8443659

[4] P. Quintero, P. McCluskey, B. Koene, "Thermo-mechanical reliability of silver nano-colloid die attach for high temperature applications", Microelectronics Reliability 54, 220–225, 2014.

5.4. Temperature Dependent Relaxation Behaviour of Pressureless and Pressure Assisted Sintered Silver

2021 44th International Spring Seminar on Electronics Technology (ISSE) | 978-1-6654-1477-7/20/$31.00 ©2021 IEEE| DOI: 10.1109/ISSE51996.2021.9467547

Zeynep Gökce Gökdeniz, Martin Lederer, Golta Khatibi, and Johann Nicolics
Christian Doppler Laboratory for Lifetime and Reliability of Interfaces in Complex Multi-Material Electronics, Institute for Chemical Technologies and Analytics,
TU Wien, Getreidemarkt 9, 1060 Vienna, Austria.
zeynep.goekdeniz@tuwien.ac.at

Abstract:
In this study we investigate the creep properties of pressureless and pressure assisted sintered silver. Based on density analysis and tensile strength, the relaxation behavior of the series was observed at room temperature, at 130°C and at 200°C. A material model for mechanical properties of porous metals was derived from experimentally established time dependent material response under tensile load.

1. Introduction

Advancements in materials science allowed an increase of packaging density in power electronics applications to an incredible extent. The needs for lowering weight, size, and thermal management cost have raised the demand for packaging concepts allowing for higher operation temperature and improved predictability of lifetime and reliability of electronic assemblies. While glass fiber reinforced epoxy resin-based materials with a glass transition temperature of 200°C and more are available since recent years, interconnection techniques for such high temperatures are still a challenging hurdle. One promising industrially applicable alternative to soldering with high-lead containing solders is silver sintering. Much work has been spent in the past to explore the mechanical properties of bonding materials like SAC solder and high-lead containing solder including their temperature dependencies [1]. In particular, the conspicuous creep behavior of sintered silver layers resulting from its porous structure has been investigated [2-3] and proved to be stress relaxant. However, in order to take full advantage of silver sintering for industrially mass-produced electronic assemblies sufficiently accurate mechanical properties data need to be available during the design phase.

This work aims in formulating a material model ready for implementation in commercial finite element packages (e.g. Abaqus, ANSYS, GetFEM++) allowing to study time dependent loading cases of sintered silver layers in electronic assemblies. Starting point is a simple well-known creep model based on a Norton power law, where the tensile stress relaxation is described as the time derivative of the strain ε by

$$\dot{\varepsilon} = C \cdot e^{\frac{-Q}{kT}} \cdot q^n \qquad (1)$$

where C is a constant, $e^{\frac{-Q}{kT}}$ is called Arrhenius term (with the activation energy Q, the Boltzmann constant k and the absolute temperature T), q is the von Mises stress and n is the stress exponent. By applying this model to measurement results of the present study, features and limitations of this simple model are discussed. Furthermore, the quasi-static Gurson - Tvergaard - Needleman plasticity model [4,6,7] is extended to a creep model, whereby material parameters of the model are obtained from fits to tensile stress relaxation experiments results performed with sintered silver layers.

2. Sample Preparation

A commercial silver paste (Heraeus mAgic 338) was used to prepare dumbbell-shaped Ag samples for tensile testing as seen in Figure 1 a-b. Specimens A-type and B-type were sintered pressureless at temperatures of 230°C and 300°C, respectively, C-type specimen were pressure sintered at 70 MPa and 230°C. For all series a sintering duration of 30 minutes was used. The average thicknesses of the Ag layers of type A, B, and C after sintering were 135 µm, 105 µm, and 75 µm. Their different structures are shown in the scanning electron microscope (SEM) images of fracture surfaces with the same magnification in Figure 2.

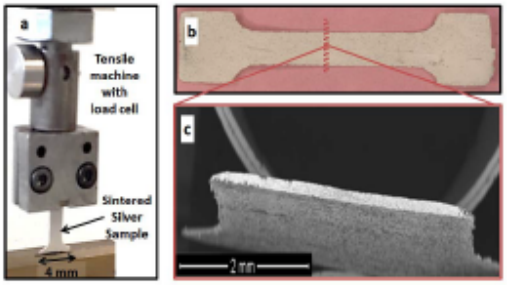

Fig. 1. Dumbbell shaped sintered silver samples (b) were tested in a tensile machine (a) and the microstructure of the cross-section was analyzed in SEM (c).

Table 1: Comparison of density for porous silver

Sample Series (sintering temp. and pressure)	Density g/cm³	Silver %
A: 230°C, 0 MPa	$\varrho_A = 3.7 \pm 0.7$	35
B: 300°C, 0 MPa	$\varrho_B = 4.4 \pm 0.6$	42
C: 230°C, 70 MPa	$\varrho_C = 6.5 \pm 0.9$	62

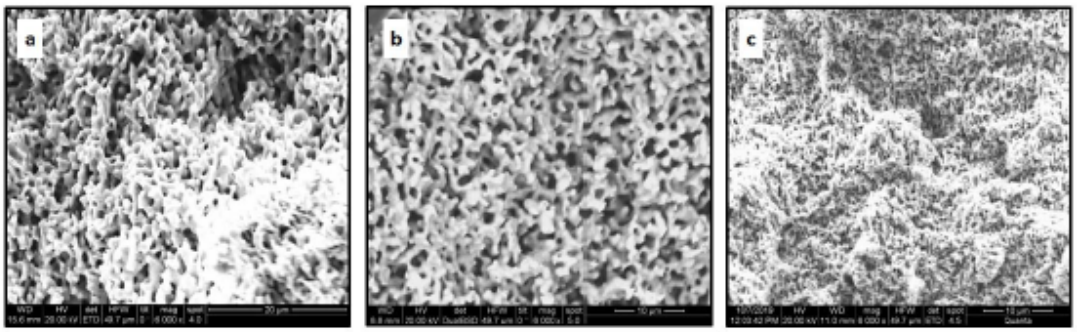

Fig. 2. SEM images from the cross-sectional area of the silver series with sintering time of 30 minutes and various sintering temperature and pressure: A) 230°C & 0 MPa, B) 300°C & 0 MPa and C) 230°C & 70 MPa.

Sintering without pressure leads to rather rounded Ag-colloids of ca. 1 µm grain size (Fig. 2.a-b), while sintering under high pressure leads to a much denser microstructure with closed pores (Fig. 2.c).

In Table 1 the average densities ϱ of specimens of the three series are listed as ratio of mass m and sample volume V

$$\varrho = \frac{m}{V} \qquad (2)$$

and as percentage of the pure Ag volume and the sample volume. The latter one was determined using a 3D-microscope of Keyence.

3. Tensile Strength and Stress Relaxation

Due to unavoidable variations in preparing the samples their tensile strength values were slightly different. In order to define the stress peak levels for performing the relaxation tests, the average tensile strength of the specimen series was taken into account.

The tensile tests for several samples to each series (A, B, C) were measured at three temperatures: 25°C, 130°C and 200°C with a testing speed of 1 mm/min. In Table 2 the mean tensile values σ_{mean} and corresponding stress peaks σ_{peak} for relaxation in average are listed.

In Figure 3 representative stress-strain curves of single tests for the series are shown to outline the brittle fraction at room temperature (Fig.3.a) and the ductile behavior at elevated temperature (Fig.3.b).

To observe the creep behavior, the samples were stretched to the defined load according σ_{peak} and then the decay of stress was measured as a function of time for 90 minutes, as shown in Figure 4.

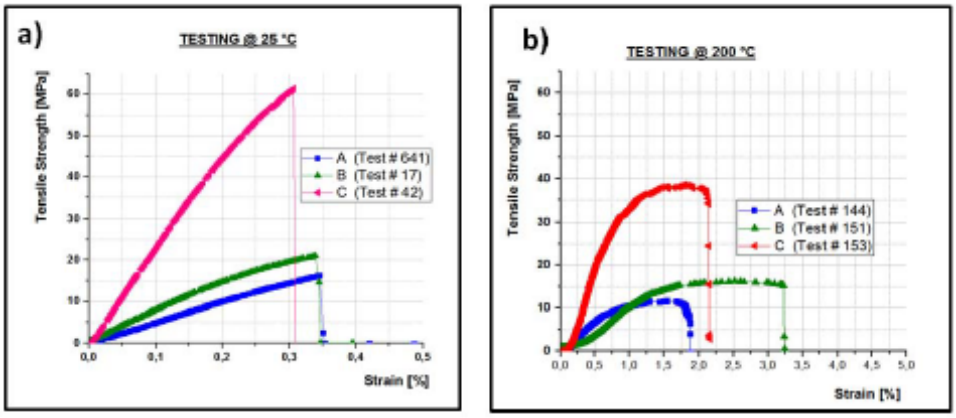

Fig. 3. Representative stress-strain curves of tensile strength for each series A (blue), B (green), C (pink/red) at testing speed of 1 mm/min and temperatures of 25°C (a) and 200°C (b), whereby (a) shows a brittle and (b) a ductile fracture behaviour.

For the pressureless (A- and B-type) and under high pressure (C-type) sintered silver, the average end-percentages of initial σ_{peak} (100%) are listed in Table 3.

The relaxation of the experimental curves could be implemented according to Norton creep described in the introduction section (1). The derived stress exponents from single test curves are used to deduce mean values for n, which were between 30-35 for the A-series, and 15-17 for the B and C series at 25°C.

Table 2: Average tensile strength values σ_{mean} and average stress peak level σ_{peak} for relaxation

A: 230°C, 0 MPa	**25 °C**	**130 °C**	**200 °C**
σ_{mean} Tensile Strength	17 MPa	11 MPa	11 MPa
σ_{peak} Av. Relaxation Stress	10 MPa	6 MPa	8 MPa
B: 300°C, 0 MPa	**25 °C**	**130 °C**	**200 °C**
σ_{mean} Tensile Strength	17 MPa	17 MPa	15 MPa
σ_{peak} Av. Relaxation Stress	11 MPa	12 MPa	9 MPa
C: 230°C, 70 MPa	**25 °C**	**130 °C**	**200 °C**
σ_{mean} Tensile Strength	57 MPa	42 MPa	42 MPa
σ_{peak} Av. Relaxation Stress	43 MPa	32 MPa	32 MPa

In general, a higher merit indicates a lower relaxation creep. At testing temperature of 130°C n was 5-8 for pressureless and 8-9 for pressure assisted sintered samples, and respectively 2-4 and 4-5 at 200°C. The more porous samples show a varying relaxation profile at elevated temperatures compared to room temperature. Unlike the already dense samples (C), the limber specimen (A, B) have more scope for displacement creep, especially with the additional thermal energy. This might lead to a posterior hardening effect with subsequent stress resistance at higher temperatures. Therefore, for porous structure more relaxation may occur, where the range of tight samples is more confined with increasing temperature.

A modified material model based on Norton creep but also inelastic behavior of the porous Ag based on Gurson plasticity should be implemented to interpret the experimental results.

Table 3: Average end-percentages $\sigma_{\%}$ after relaxation for 90 minutes from the initial stress peak of 100% for the three series A, B, C and at three test temperatures

Test Temp.	**25 °C**	**130 °C**	**200 °C**
A	78 %	12 %	2 %
B	67 %	12 %	5 %
C	65 %	34 %	18 %

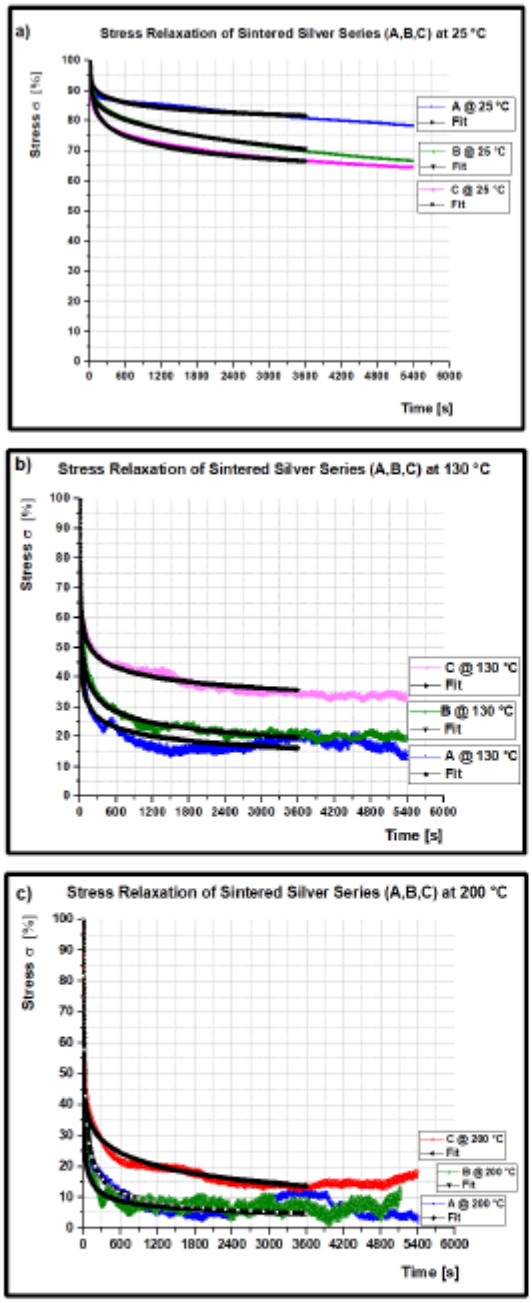

Fig. 4. Relaxation curves for each series (A-blue, B-green, C-pink) measured at testing temperatures of a) 25°C, b) 130°C and c) 200°C for 90 minutes and fit curves modelled for 60 minutes marked with black.

4. UNIFIED MODEL OF PLASTICITY AND CREEP

The density measurements of sintered silver summarized in Table 1 indicate considerable porosity of the materials. From an investigation of McClintock [5] it is known that porosity has strong influence on the plastic behavior of metals. Around pores stress concentrations are formed during ongoing deformation. Therefore, the strength of a porous metal is reduced compared to bulk material. In conclusion, Gurson [4] defined a quasi-static flow rule for porous metals, where von Mises stress and hydrostatic pressure are both influencing the plastic strain. In the present approach, this flow rule is extended to time dependent inelastic behavior. Thereby, the Norton creep equation is reformulated to include hydrostatic pressure in addition to von Mises stress. It is demonstrated that the material parameters of the model can be fitted to the stress relaxation experiments of the present study.

4.1. Gurson plasticity and Norton creep

We use the Gurson - Tvergaard - Needleman model [4, 6, 7] as starting point of our theoretical interpretation. The flow rule of this model was defined as

$$\left(\frac{q}{\sigma_y}\right)^2 + 2q_1 f \cdot \cosh\left(\frac{-3}{2}\frac{q_2 p}{\sigma_y}\right) - (1 + q_3 f^2) = 0 \quad (3)$$

where q is the von Mises stress, σ_y is the flow stress of the dense material, p is the hydrostatic pressure stress and f is the porosity, i.e. the volume fraction of the pores in the material. Further, q_1, q_2 and q_3 are material constants. In the limit of $f = 0$ for dense materials, the model reduces to von Mises plasticity. On the other hand, for materials of high porosity the hydrostatic pressure contributes significantly to the plastic deformation behavior.

However, the quasi-static flow rule (3) cannot explain the stress relaxation behavior of Figures 4 (a-c). Therefore, it is here intended to develop a creep model, which combines the principles of Norton creep and Gurson plasticity. This model shall be used for Finite Element computer simulations. Thereby, a simplification of the Gurson model is suggested in order to obtain a model which is computationally inexpensive. The hyperbolic cosine function of equation (3) can be expanded into a Taylor series, and for small strains one may truncate the Taylor series after the term of second order. This leads to an approximation, where the hyperbolic cosine is replaced

by a term, which is quadratic in p. Consequently, the flow condition under hydrostatic stress may to a good approximation be treated by analogy to flow under deviatoric stress, as will be shown in the subsequent section.

4.2. Definition of the constitutive model

In the following the orthogonal decomposition of the Cauchy stress tensor σ_{ij} into hydrostatic pressure

$$p = \frac{-1}{3} tr(\sigma_{ij}) \tag{4}$$

and deviatoric stress

$$S_{ij} = \sigma_{ij} + p \cdot I \tag{5}$$

is utilized, where I is the identity matrix and tr denotes the trace of a matrix. By analogy, the strain tensor may additively be decomposed into volumetric and deviatoric parts according to

$$\varepsilon_{ij} = \frac{1}{3} tr(\varepsilon_{ij}) \cdot I + \varepsilon_{ij}^{dev} \tag{6}$$

In short, we hereafter write

$$\varepsilon_{vol} = tr(\varepsilon) \tag{7}$$

for the volumetric strain. Furthermore, the decomposition of the total strain tensor

$$\varepsilon_{tot} = \varepsilon_{el} + \varepsilon_{ine} \tag{8}$$

into elastic and inelastic strains will be used. Thus, the strain rates

$$\left|\dot{\varepsilon}_{ine}^{vol}\right| = c_1 \cdot f \cdot e^{-Q/kT} \cdot |p|^{n_1} \tag{9 a}$$

$$\left\|\dot{\varepsilon}_{ine}^{dev}\right\| = c_2 \cdot e^{-Q/kT} \cdot \|S\|^{n_2} \tag{9 b}$$

are defined as constitutive equations of this model. The direction of inelastic flow under pressure is compressive, while flow under deviatoric stress is parallel to the deviatoric stress tensor S_{ij}. In equations (9 a, b), $|p|$ denotes the absolute value of the scalar p, and $\|S\|$ is the Euclidean norm of the tensor S. Q is the activation energy. n_1 and n_2 are the stress exponents related to hydrostatic and deviatoric parts of the stress, respectively. c_1 and c_2 are material constants. The material parameters show a dependency on the sintering conditions. It should also be noticed that a change of volumetric strain during inelastic deformation causes a change of porosity f. Consequently, conservation of mass implies the evolution equation

$$\dot{f} = (1 - f) \cdot \dot{\varepsilon}_{ine}^{vol}. \tag{10}$$

4.3. Numerical fitting

Stress relaxation experiments were performed under conditions of time dependent uniaxial tensile stress

$$\sigma_{ij}(t) = \begin{pmatrix} \sigma_{11}(t) & 0 & 0 \\ 0 & 0 & 0 \\ 0 & 0 & 0 \end{pmatrix}. \tag{11}$$

Hence, the time dependence of hydrostatic pressure writes as

$$p(t) = \frac{-1}{3} \sigma_{11}(t), \tag{12}$$

and the time dependence of the tensor norm of the deviatoric stress evaluates to

$$\|S_{ij}(t)\| = \sqrt{\frac{2}{3}} \cdot \sigma_{11}(t). \tag{13}$$

Further, both, volumetric and deviatoric parts of the strain rate contribute to the rate of the inelastic strain component $\dot{\varepsilon}_{11}^{ine}$ according to

$$\dot{\varepsilon}_{11}^{ine} = \frac{1}{3} \dot{\varepsilon}_{vol} + \sqrt{\frac{2}{3}} \cdot \|\dot{\varepsilon}_{dev}\|. \tag{14}$$

During stress relaxation, the total strain ε_{11}^{tot} of the sample was constrained to a constant value, while the inelastic strain ε_{11}^{ine} increased on the expense of elastic strain ε_{11}^{el}. Consequently, it is concluded that

$$\dot{\varepsilon}_{11}^{el} = -\dot{\varepsilon}_{11}^{ine}. \tag{15}$$

Finally, the rate of the stress σ_{11} is related to the rate of elastic strain ε_{11}^{el} by

$$\dot{\sigma}_{11} = E^{eff} \cdot \dot{\varepsilon}_{11}^{el}, \tag{16}$$

where E^{eff} is the effective Young's modulus of the porous material. Thus, we are in the position to express the time dependence of stress σ_{11} as ordinary differential equation of first order. The stress rate $\dot{\sigma}_{11}$ is a function of the strain rates (9 a, b), which depend on the value of σ_{11} and on the fit parameters of the model.

The activation energy Q of creep was found to be 133 kJ/(mol K). The remaining fit parameters of this material model were considered as temperature dependent: The best fits are shown in Figure 4 (a-c). The fit parameters used are summarized in Table 4. In spite of obvious agreement between experimental results and model fits, it is here suggested to perform additional experiments under pure deviatoric stress in order to obtain unique values for the material parameters.

Table 4: Material parameters used for numerical fits shown in Fig 4 a-c. Stresses are in units of MPa.

Series A	c_1	c_2	n_1	n_2
RT	96	$2.08 \cdot 10^{-15}$	10	35
130°C	$1.08 \cdot 10^{12}$	$8.74 \cdot 10^{-3}$	6	10
200°C	$2.26 \cdot 10^{9}$	2.45	3	7.9

Series B	c_1	c_2	n_1	n_2
RT	$3.59 \cdot 10^{12}$	$2.08 \cdot 10^{-15}$	8	35
130°C	$1.21 \cdot 10^{10}$	$8.74 \cdot 10^{-3}$	6	10
200°C	$6.78 \cdot 10^{9}$	2.45	4	7.9

Series C	c_1	c_2	n_1	n_2
RT	3.29	$4.16 \cdot 10^{-81}$	16	62.2
130°C	$2.3 \cdot 10^{4}$	$1.22 \cdot 10^{-2}$	10	10
200°C	$1.29 \cdot 10^{7}$	3.92	3	7.9

5. SUMMARY-CONCLUSION

To analyze the creep behavior of porous silver as interconnection material in packaging technology, pressureless and pressure assisted sintered-Ag samples were produced. The mass/volume densities of the sample series were determined (35% - 62%) and the ultimate tensile strength was measured at room and elevated temperatures. In order to observe the creep behavior at various testing temperatures (25°C, 130°C and 200°C), samples were exposed to uniaxial stress and the stress relaxation over time at constant sample length was monitored.

The theoretical interpretation of the material behavior was based on a combination of Norton creep and Gurson plasticity. Owing to the high porosities of the samples, it was necessary to consider the influence of hydrostatic pressure on plastic deformation. A constitutive material model was formulated, which makes use of an orthogonal decomposition of stress and strain tensors into volumetric and deviatoric parts. Consequently, the time dependent inelastic deformation of the material was described by a system of two equations. It was demonstrated that the material parameters of the model can be fitted to stress relaxation experiments. Nevertheless, it was suggested to perform additional experiments under pure deviatoric stress to obtain unique solutions of the fit parameters. For this purpose, data of stress relaxation experiments under shear stress is already planned to be implemented in a subsequent publication.

ACKNOWLEDGEMENT

The financial support by the Austrian Federal Ministry for Digital and Economic Affairs and the National Foundation for Research, Technology and Development is gratefully acknowledged.

REFERENCES

[1] E.W. Hare, R.G. Stang, **"Stress Relaxation Behavior of Eutectic Tin-Lead Solder"**, Journal of Electronic Materials, Vol. 24, No. 10, 1995

[2] Gang Chen et al. **"High-Temperature Creep Behavior of Low-Temperature-Sintered Nano-Silver Paste Films"**, Journal of Electronic Materials, Vol. 41, No. 4, 2012

[3] C. Weber, M. van Dijk, H. Walter, M. Hutter, O. Wittler, K-D Lang, **"Combination of experimental and simulation methods for analysis of sintered Ag joints for high temperature applications"**, 66th Electronic Components and Technology Conference, IEEE, ECTC 2016.

[4] A. L. Gurson, **"Continuum Theory of Ductile Rupture by Void Nucleation and Growth: Part I - Yield Criteria and Flow Rules for Porous Ductile Materials"**, Journal of Engineering Materials and Technology, vol. 99, pp. 2–15, 1977.

[5] McClintock, F.A., 1968. **"A criterion for ductile fracture by growth of holes"**, Transactions of the ASME Journal of Applied Mechanics 35, 363–371.

[6] V. Tvergaard: **"On localization in ductile materials containing spherical voids"**. Int J Fracture 1982;18:237–52.

[7] V. Tvergaard, A. Needleman **"Analysis of the cup-cone fracture in a round tensile bar"** Acta Metall 1984;32:157–69.

5.5. Temperature Dependent Relaxation Behaviour of Ag-Sintered Copper Joints

Zeynep Gökce Gökdeniz, Martin Lederer, Golta Khatibi, and Johann Nicolics
Christian Doppler Laboratory for Lifetime and Reliability of Interfaces in Complex Multi-Material Electronics,
Inst. for Chemical Technologies and Analytics, TU Wien, Getreidemarkt 9, 1060 Vienna, Austria
Email: zeynep.goekdeniz@tuwien.ac.at

Abstract—In the field of power electronics device function leads to high operating temperatures. High stresses and strains are induced as a result of mismatch in Coefficient of Thermal Expansion (CTE) leading to plastic deformation in constrained joints. The thermomechanical stresses stimulate mechanisms such as dislocation glide or creep. Especially when the homologous temperature increases, time dependent creep failure becomes a dominant issue in the joint reliability. This work is devoted to the development of a temperature dependent material model for pressure assisted silver sintered joints. This model is validated on the basis of stress relaxation experiments aside from measurements of shear strength and mechanical fatigue. For this purpose, Ag-sintered copper joints were manufactured (0-hour) and heat treated at 250 °C for 250 hours in air and in protective atmosphere. Investigations of microstructure were made by scanning electron microscopy (SEM). Shear and stress relaxation tests were conducted in a tensile machine with thermal chamber at temperatures of 25 °C, 130 °C and 200 °C. For lifetime estimation of the samples Weibull probability plots for low cycle fatigue were determined. Further, Norton power law was employed to determine material parameters such as stress exponent *n* and creep activation energy *Q*. In conclusion, a unified model of plasticity and creep was established.

Keywords—Silver sintering; shear strength; lifetime reliability; stress relaxation; Norton power law; Gurson model

I. Introduction

In power electronics packaging besides the mechanical properties such as hardness or tensile and shear strength, characterization of the time and temperature dependent behavior of the interconnection materials is important for fatigue investigations and reliable lifetime estimation. As the most commonly used interconnect technology of last decades the properties of conventional lead containing or lead-free solders such as SAC have been extensively investigated, also on their creep behaviour [1, 2]. Due to its high melting point and good thermal and electrical conductivity sintered silver is a promising alternative joining technology.

In the past, mechanical properties of sintered silver were often described by constitutive models, which have actually been developed for materials without significant amount of porosity. Yu et al. [3] determined appropriate material parameters of the viscoplastic Anand model [4] for sintered nano-silver. The Anand model was also applied to sintered silver by Chen et al. [5], who compared the model predictions with a plasticity model of kinematic hardening. Indeed, there are many experiments, which can successfully be interpreted in this way. In the case of a material with high porosity, however, a different material response is expected. In the quasi-static deformation regime, porous materials are well described by the Gurson – Tvergaard – Needleman [6-8] model (GTN model). An interesting extension of the GTN model to rate dependent plastic deformations was proposed by Yao and Gong [9], who used an approach of McDowell et al. [10] in order to derive a unified model of plasticity and creep. This model of Yao and Gong was validated through shear experiments.

In the present study, we are aiming at a phenomenological material model unifying the ideas of Gurson plasticity and creep. Thereby, it must be considered that porous materials show a pronounced pressure dependence of the material response. In contrast to plastically incompressible von Mises materials, porous materials can be subjected to both inelastic deformation types, to deviatoric and to volumetric plastic deformations. Therefore, the determination of appropriate material parameters should involve experiments showing deviatoric and volumetric plastic deformations.

In this article, we will focus our interest on shear experiments, which are representing purely deviatoric deformations. In a second study to be published elsewhere [11], additional experiments under tensile load are performed with sintered silver.

II. Sample Preparation

A. 0-hour Samples

Cu-Ag-Cu lap-joints samples were prepared as follows: as shown in Fig. 1 a, first ca. 1 µm silver was sputtered on cleaned surface of copper stripes of 50 mm length and 3 mm width with a thickness of 1 mm, then the Ag-paste was applied by stencil printing (mask thickness 100 µm) forming a pad area of ca. 10 mm². The Ag-paste was dried at 130 °C prior to sintering at 230 °C and under the pressure of 70 MPa for 30 minutes to perform the joint as in Fig. 1 b. Unlike the edge corners of the sample with more porous parts as shown in Fig.1.c, the middle section of the sintered silver has a dense microscopic structure with an average thickness of ca. 70-75 µm after sintering as shown in Fig. 1 d. The weight/volume density of the sintered silver corresponds to ca. 6.5 g/cm^3 with over 60 % Ag content. These lap-joints manufactured as described are called 0-hour samples.

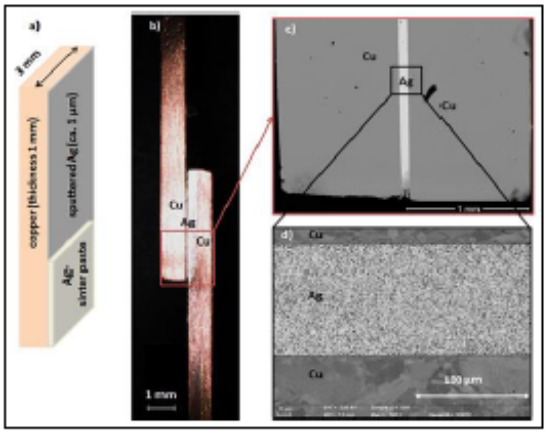

Fig. 1. Cleaned copper surface is first sputtered with silver (ca. 1 µm), then a pad of Ag-paste (100 µm) is applied (a) to sinter the copper joints (b). Images of the lap-joint are showing the dense middle section of the sample (c), and the regular microscopic structure of the sintered Ag (d).

B. *Thermal Treatement*

The samples obtained immediately after sintering are here called 0-hour samples. In comparison, 250-hours specimens were produced as follows: two kinds of lap-joint series were heat treated at 250 °C up to 250 h. One kind has undergone thermal treatment in regular air; the change of the microscopic structure is shown in Fig. 2 a. The second series were put in protective sealed glass as in Fig. 2 b to prevent further oxygen flow, and its microstructure is shown in Fig. 2 c. For the former case, coarsening of the pores as well as grain growth is observed. Further, on the sputtered junction layer between copper and silver formation of copper-oxide was detected, which was not observed in the latter case of thermal treatment without oxygen flow. These lap-joints manufactured as described are called 250-hours air-aged or glass-aged samples, respectively.

III. Shear Strenght, Mechanical Lifetime and Stress Relaxation

For determination of force-displacement measurements a universal testing machine from Messphysik Austria equipped with a load cell (resolution 0.1 mN) was used. With the help of a thermal chamber experiments could be performed at elevated testing temperatures.

A. *Shear Strength*

For lap-joint samples tested on shear strength at room temperature values were mainly observed between 25-40 MPa leading to an average of ca. 32 MPa as shown in Fig. 3 a. Increasing the testing temperature to 130 °C led especially for the 250-hours glass-aged samples to a decrease of shear strength as shown in Fig. 3 b.

B. *Mechanical Lifetime*

Cyclic mechanical fatigue tests were performed in shear mode in the stress range of 10-30 MPa with a cross head speed

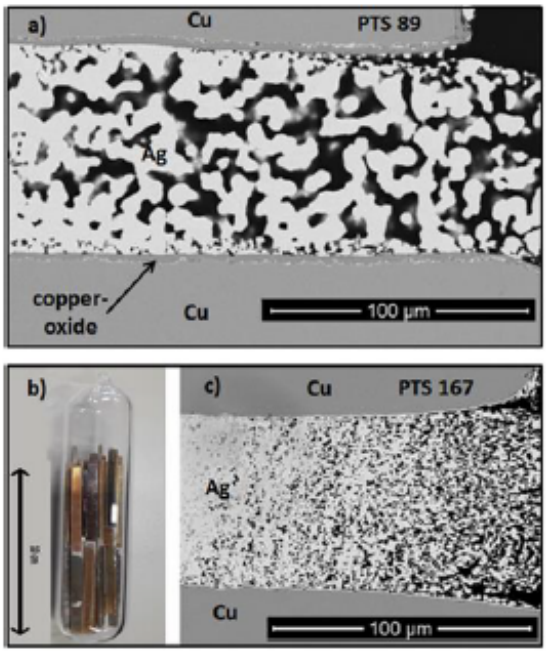

Fig. 2. Especially on the edge of the lapjoints where access to oxygen is easy possible, heat treatment leads to grain growth and coarsening of pores; further CuO layer formation is detected (a). After heat treatment with preventing oxygen flow, such as in a protective glass atmosphere (b), no significant change in microstructure is observed (c).

of 2 mm/min corresponding to a testing frequency of about 0.1 Hz. The lifetime N_f was captured for 0-hour samples in comparison to glass-aged and air-aged specimens at room temperature as plotted in Fig. 4. The Weibull fracture probability curves show that the 250-hours specimens have a higher 50 % lifetime expectation of ca. 5.000 (glass-aged) and 7.000 (air-aged) cycles, compared to 3.600 cycles for non-aged ones; i.e., heat-treatment at 250 °C for 250-hours results in a clear improvement of lifetime.

C. *Stress Relaxation*

To observe the creep behavior of the Ag-sintered copper lap-joints, the decay of stress σ was measured as a function of time after the samples were stretched to a defined load σ_{peak}, which was selected according to mean shear strength values.

The relaxation curves are plotted in Fig. 5. A power law could be implemented on the measured series according to Norton creep:

$$\dot{\varepsilon}_{cr} = C \cdot exp\left\{-\frac{Q}{R \cdot T}\right\} \cdot q^n \qquad (1)$$

For the 0-hour and 250-hours air-aged samples the selected σ_{peak} values (defined as 100 %), values for σ_{end} after 60 minutes of testing time as end-percentages, and derived values of the stress exponent n, as average of several samples, are listed in Table 1 for testing temperatures 25 °C, 130 °C and 200 °C.

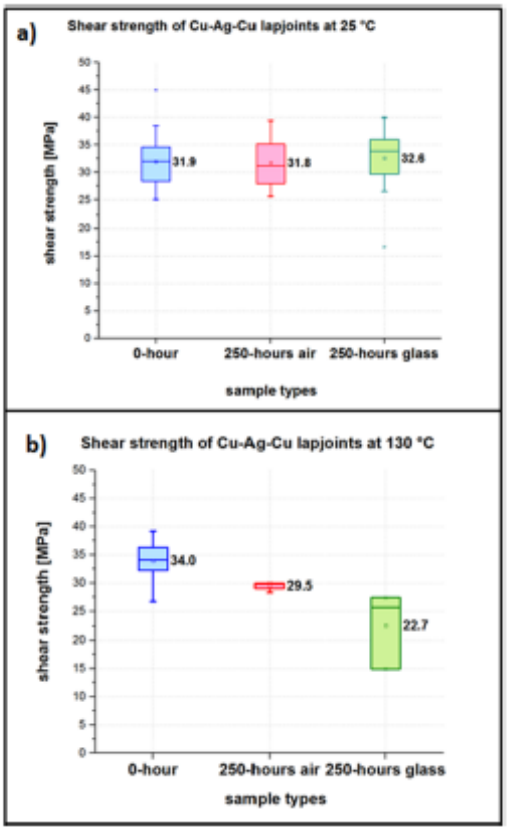

Fig. 3. Shear strength of 0-hour and 250-hours aged samples tested at room (a) and elevated temperatures (b).

D. *Creep Fracture*

While some samples relaxation behaviour was as shown in previous section, other samples, which were stressed with a force leading to a higher absolute value in σ_{peak}, were soon afflicted by total fracture as shown in Fig. 6. For these individual 0-hour samples tested at 200 °C the shear creep lifetime was not significant more than 10 minutes.

According to an analysis of McClintock [12] and Rice and Tracey [13], stress concentrations occur at the holes of porous metals, as in this case of sintered silver, which induce plastic deformation and finally lead to rupture. Therefore, a unified model of Gurson plasticity and Norton creep is here developed.

IV. Unified Model of Plasticity and Creep

The model proposed here utilizes an orthogonal decomposition of stresses into hydrostatic and deviatoric parts. In the present article, the material parameters related to deviatoric deformations will be determined from fits to shear experiments. The determination of the remaining material parameters from fits to experiments under tensile load can be found in reference [11].

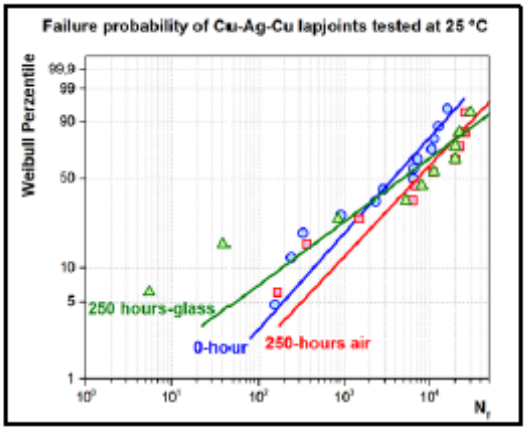

Fig. 4. Failure probability as Weibull plot of the 0-hour (blue) and 250-hours aged (red in air and green in glass) Cu-Ag-Cu lapjoints, tested at room temperature with a stress level σ_{max} of 30 MPa.

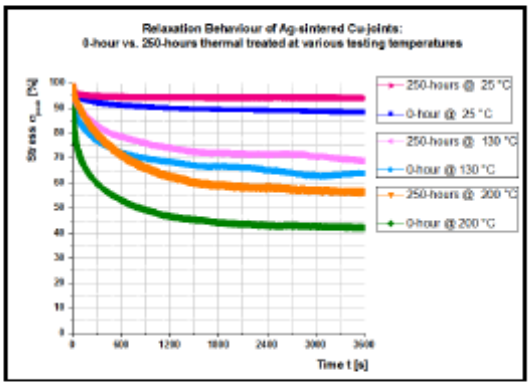

Fig. 5. Creep behaviour of Cu-Ag-Cu lap-joints as a function of time: 0-hour samples show a stronger stress relaxation than 250-hours air-aged samples for three testing temperatures.

A. *Constitutive equations*

The flow rule of the GTN model writes as

$$\Phi = \left(\frac{q}{\sigma_y}\right)^2 + 2q_1 f \cdot \cosh\left(-\frac{3}{2}\frac{q_2 p}{\sigma_y}\right) - (1 + q_3 f^2) = 0 \qquad (2)$$

where σ_y is the flow stress of the dense material, q is the von Mises stress, p is the hydrostatic pressure stress and the porosity f is the volume fraction of the pores. Thus, the rate of plastic strain consistent with this flow rule becomes [14]

$$\dot{\varepsilon}_{pl} = \dot{\lambda}\frac{\partial \Phi}{\partial \sigma} = \dot{\lambda}\left(-\frac{1}{3}\frac{\partial \Phi}{\partial p} I + \frac{3}{2q}\frac{\partial \Phi}{\partial q} S\right) \qquad (3)$$

where $\dot{\lambda} > 0$ is called plastic multiplier. Here

$$S = \sigma + p \cdot I \qquad (4)$$

is the deviatoric stress tensor, σ is the Cauchy stress tensor and I is the unity matrix.

Previously published in the Proceedings of EMPC-2021

TABLE 1: SHEAR STRESS PEAK VALUES σ_{peak} (DEFINED AS 100%) FOR RELAXATION, END PERCENTAGE LEVEL OF STRESS σ_{end} AFTER 60 MIN. AND STRESS EXPONENT VALUES N FOR THE SELECTED SAMPLES TESTED AT ROOM AND ELEVATED TEMPERATURES

0-hour	**25 °C**	**130 °C**	**200 °C**
$\sigma_{peak\ Shear\ Stress}$	30 MPa	30 MPa	23 MPa
σ_{end}	89 %	64 %	42 %
n	62	14	8
250-hours air-aged	**25 °C**	**130 °C**	**200 °C**
$\sigma_{peak\ Shear\ Stress}$	30 MPa	30 MPa	21 MPa
σ_{end}	94 %	69 %	57 %
n	101	15	9

Following Tvergaard [7], we will hereafter assume that $q_3 = q_1^2$. In absence of hydrostatic pressure p, equation (1) simplifies to

$$q^2 = \sigma_y{}^2(1 - q_1 f)^2 \tag{5}$$

For simplicity, we here assume $q_1 = 1$, as suggested by Gurson [6]. In conclusion, the material behavior under purely deviatoric stress is equivalent to a von Mises material, where the flow stress is reduced in proportion to the porosity. In this case, equation (2) reduces to

$$\dot{\varepsilon}_{pl} = \dot{\lambda}\frac{3}{\sigma_y{}^2}S \tag{6}$$

This equation may now be combined with the Norton creep law

$$\|\dot{\varepsilon}_{cr}\| = C \cdot (1 - f) \cdot exp\left\{-\frac{Q}{R \cdot T}\right\} \cdot q^n \tag{7}$$

where the porosity f is considered in the constitutive equation. Here, C is a material constant, Q is the activation energy of creep, R is the gas constant of 8.314 $J\ mol^{-1}K^{-1}$ and n is the stress exponent. T is the absolute temperature in K, and $\|\dot{\varepsilon}_{cr}\|$ is the Euklidean norm of the tensor $\dot{\varepsilon}_{cr}$.

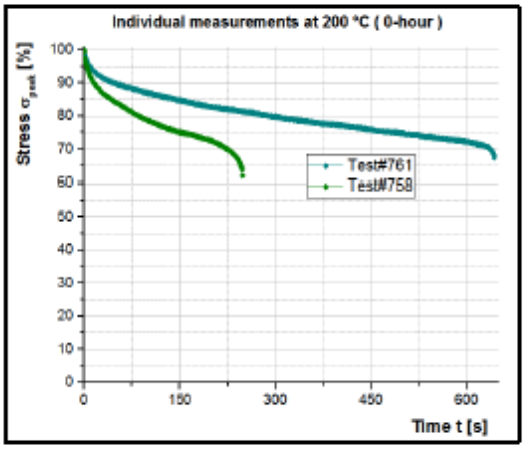

Fig. 6. Creep fracture of individual Ag-sintered Cu-lap-joints at elevated test temperature.

On the other hand, the term of $-\frac{1}{3}\frac{\partial \Phi}{\partial p}I$ in equation (3) predicts a plastic volume change for cases, where hydrostatic stresses are present. This effect is due to void growth under triaxial tension. The contribution of this effect to inelastic deformations will be analyzed in reference [11].

B. Numerical fitting

Now, the model parameters of equation (7) are fitted to the experimental results of stress relaxation tests performed in shear mode. It is assumed that the entire sample length remains constant, while the plastic shear in the sintered silver increases on the expense of elastic strains. Thereby, the geometry of lap-joints consisting of a thin silver layer connecting two pieces of copper base material must be taken into account. During stress relaxation, the change of sample length caused by shear strain in the thin silver layer is to a good approximation compensated by reduction of elastic strain in the copper base material:

$$\Delta\varepsilon_{Ag} \cdot Th_{Ag} \cong -\Delta\varepsilon_{Cu}^{elast} \cdot L_{Cu} \tag{8}$$

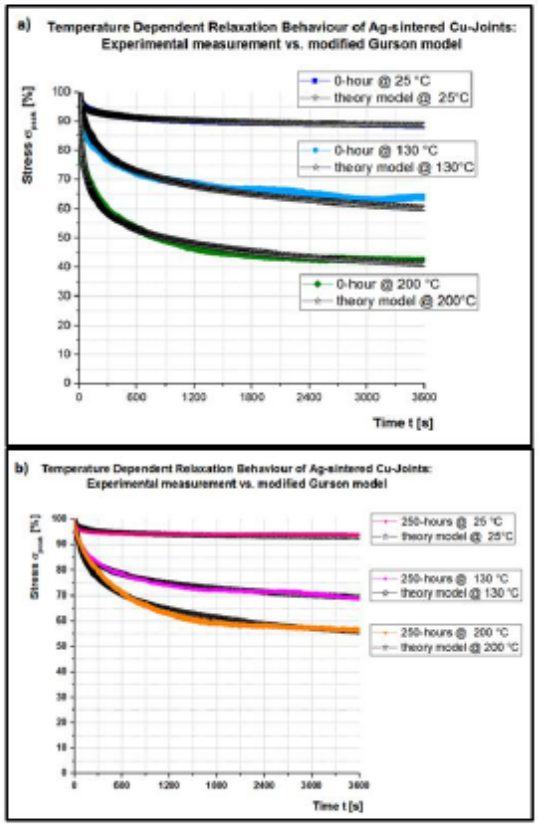

Fig. 7. The measurements of the temperature dependent relaxation behavior of silver sintered copper joints are described through fit parameters (as in Table 2) of modified Gurson model for 0-hour (a) and 250-hours air-aged (b) Cu-Ag-Cu samples.

where Th_{Ag} is the thickness of the silver layer and L_{Cu} is the length of the copper pieces above and below the joint. The approximate values for the elastic compliance of the whole sample were confirmed by FEM analyses. Thus, the numerical fits of stress relaxation experiments depicted in Figure 7 led to the material parameters summarized in Table 2.

TABLE 2: MATERIAL PARAMETERS (C, Q, n) ACCORDING TO FIT CURVES OF THE MEASURED STRESS RELAXATION BEHAVIOUR FOR AG-SINTERED COPPER JOINTS WHICH WERE SHEAR STRESSED AT THREE TESTING TEMPERATURES.

0-hour	**25 °C**	**130 °C**	**200 °C**
C	$1.5 \cdot 10^{-86}$	$2 \cdot 10^{-5}$	$4 \cdot 10^{8}$
Q (kJ/(mol K))	133	133	133
n	62.2	10	7.9
250-hours	**25 °C**	**130 °C**	**200 °C**
C	$8 \cdot 10^{-154}$	$2.5 \cdot 10^{-12}$	$4 \cdot 10^{7}$
Q (kJ/(mol K))	133	133	133
n	101	15.2	8.2

SUMMARY

The mean shear strength of the as-sintered samples (0-hour) and those treated at 250 °C for 250 hours (in air and protective atmosphere) varied mainly around 32 MPa at room temperature; however, the mechanical cyclic tests revealed a considerable increase in lifetime of the latter joints.

In the case of air-aged samples the microstructural investigations in SEM revealed an enlargement of grain size especially on the corners of the sintered silver area where immediate inflow of oxygen is possible. Further, on the Ag-sputtered junction layer between copper and silver, formation of copper-oxide was detected, which was not observed in the case of thermal treatment with no oxygen flow.

A comparison between the stress relaxation curves at three different testing temperatures (25 °C, 130 °C and 200 °C) shows a higher relaxation rate of 0-hour samples compared to 250-hours air-aged specimen. For the plotted curves a power low could be implemented according to Norton creep, and corresponding stress exponents n were deduced. The less the n number is, the more distinct is the relaxation.

Further a unified material model of plasticity and creep was implemented to designate the specific material constant C in various thermal testing conditions and define the creep activation energy Q = 133 kJ/(mol K).

ACKNOWLEDGMENT

The financial support by the Austrian Federal Ministry for Digital and Economic Affairs & the National Foundation for Research, Technology and Development is gratefully acknowledged.

We would like to thank Prof. J. Fleig and A. Opitz from Div. Electrochemistry CTA–TU Wien for providing the sputtering facility.

REFERENCES

[1] Song, H.G., Morris, J.W. & Hua, F., "The creep properties of lead-free solder joints", JOM 54, 30–32, 2002.

[2] M. Rollig, S. Wiese, K. Meier and K. Wolter, "Creep measurements on SnAgCu solder joints in different compositions and after mechanical and thermal treatment", EuroSimE 2008 - International Conference on Thermal, Mechanical and Multi-Physics Simulation and Experiments in Microelectronics and Micro-Systems, 2008

[3] Dun-ji Yu, Xu Chen, Gang Chen, Guo-quan Lu, Zheng-qiang Wang, "Applying Anand model to low-temperature sintered nanoscale silver paste chip attachment", Materials and Design 30 (2009) 4574–4579

[4] L. Anand, "Constitutive equations for hot working of metals", Int J. Plasticity 1985;1:213–31.

[5] Gang Chen, Ze-Sheng Zhang, Yun-Hui Mei, Xin Li, Dun-Ji Yu, Lei Wang, Xu Chen: Applying viscoplastic constitutive models to predict ratcheting behavior of sintered nanosilver lap-shear joint, Mechanics of Materials 72 (2014) 61–71.

[6] A. L. Gurson, "Continuum theory of ductile rupture by void nucleation and growth: Part I - Yield Criteria and Flow Rules for Porous Ductile Materials", Journal of Engineering Materials and Technology, vol. 99, pp. 2–15, 1977.

[7] Tvergaard V., "Influence of voids on shear band instabilities under plane-strain conditions", Int J Fracture 1981;17:389–407.

[8] Tvergaard V, Needleman A., "Analysis of the cup-cone fracture in a round tensile bar", Acta Metall 1984;32:157–69.

[9] Yao Yao, He Gong, "Damage and viscoplastic behavior of sintered nano-silver joints under shear loading", Engineering Fracture Mechanics 222 (2019) 106741.

[10] McDowell DL, Miller MP, Brooks DC., "A unified creep-plasticity theory for solder alloys", Fatigue Electron Mater: ASTM Int 1994.

[11] Z. G. Gökdeniz, M. Lederer, G. Khatibi, J. Nicolics, "Temperature dependent relaxation behavior of pressureless and pressure assisted sintered silver", Proc. of the ISSE 2021, in press.

[12] McClintock, F.A., "A criterion for ductile fracture by growth of holes", Transactions of the ASME Journal of Applied Mechanics 35, 363–371, 1968.

[13] Rice, J.R., Tracey, D.M., 1969. On the ductile enlargement of voids in triaxial stress fields. Journal of the Mechanics and Physics of Solids 17, 201–217.

[14] ABAQUS 6.13 Theory Manual, Dassault Systems, 2013.

5.6. Constitutive Equations for Strain Rate and Temperature Dependent Mechanical Behaviour of Porous Ag-sintered Joints in Electronic Packages

Microelectronics Reliability 126 (2021) 114209

Contents lists available at ScienceDirect

Microelectronics Reliability

journal homepage: www.elsevier.com/locate/microrel

Constitutive equations for strain rate and temperature dependent mechanical behaviour of porous Ag-sintered joints in electronic packages

M. Lederer [a,b,*], Z. Gökdeniz [a,b], G. Khatibi [a,b], J. Nicolics [b]

[a] Christian Doppler Laboratory for Lifetime and Reliability of Interfaces in Complex Multi-Material Electronics, TU Wien, Getreidemarkt 9, 1060 Vienna, Austria
[b] Institute for Chemical Technologies and Analytics, TU Wien, Getreidemarkt 9, 1060 Vienna, Austria

ARTICLE INFO

Keywords:
Finite element analysis
Creep
Sintered silver

ABSTRACT

Sintering of silver attracts increasing attention in electronic packaging owing to superior bonding quality and high operation temperatures. However, the mechanical properties of sintered joints strongly depend on fabrication parameters like sintering temperature, pressure or organic solvents in the silver paste. In consequence, the mechanical characterization of this material is a challenging task. In the present article, unified constitutive equations for plasticity and creep of sintered silver are established. Thereby, particular interest is devoted to the influence of porosity on the mechanical properties. The assumptions of the model are validated by mechanical tests carried out with samples prepared under constant sintering conditions. The model parameters are fitted to test results performed in tension mode, in shear mode and under conditions of stress relaxation. This material model is implemented in the commercial software ABAQUS through user subroutines UMAT and VUMAT. In conclusion, the constitutive material model can be used as prerequisite for reliability predictions of Ag-sintered joints in electronic packages.

1. Introduction

In the last decade sintering of silver paste at temperatures comparable to those of soldering processes received increasingly attention as novel interconnection technique with particular features like superior bonding properties also at high operation temperatures, the impossibility of formation of quality-degrading intermetallic layers, and the avoidance of flux enclosures [1]. The combination of these features predestine silver sintering as a replacement of soldering for both, embedding and surface attachment of power devices and attracts more and more power electronics manufacturer, since this technique allows double-sided cooling [2], promises a further significant step towards saving weight, reducing package dimensions, parasitic impedances, and cost, while improving ecological measures by avoiding of lead-containing alloys [3]. As consequence of the low sintering temperatures the bonding silver layer exhibits an extremely porous structure which, in turn, is responsible for a conspicuous creep behaviour making it favorable as a highly reliable stress releasing and compliant bonding layer [4,5]. However, since the mechanical properties of this bonding layer strongly depend on fabrication parameters and operation conditions, full use of advantages requires accurate numerical modelling of assemblies during their design phase based on adequate temperature and time dependent material models.

In recent years, several constitutive models were applied to sintered nanosilver. Yu et al. [6] preferred the viscoplastic Anand model [7], because of its temperature and strain rate dependence. Chen et al. [8] also applied the Anand model and compared it to a kinematic hardening model with temperature dependent material parameters. Finite Element simulations showed good agreement between those two models on the one side and experiments on the other. A drawback of the here mentioned models might be that the porosity of sintered silver was not considered in detail. A model including porosity was proposed by Yao and Gong [9]. They started their investigation from the Gurson model [10] and extended it to a model of unified creep and plasticity.

In the present study, a constitutive model is developed from the phenomenological point of view. Mechanical tests were performed in tension, in shear, under cyclic load and under conditions of stress relaxation. Consequently, a constitutive material model is elaborated, which is in accordance with all relevant experiments.

* Corresponding author.
E-mail address: martin.lederer@tuwien.ac.at (M. Lederer).

https://doi.org/10.1016/j.microrel.2021.114209
Received 25 May 2021; Accepted 17 June 2021
Available online 11 October 2021

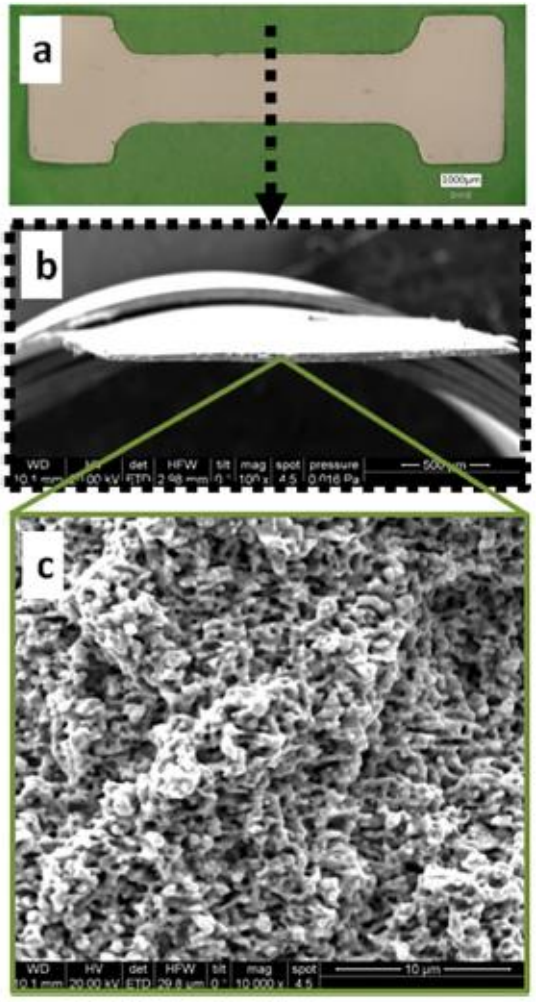

Fig. 1. (a) Dumbbell shaped specimen, (b) and (c) SEM micrographs of its fracture surface.

2. Experimental

Two main types of samples were prepared for mechanical tests. Firstly, dumbbell shaped specimens of sintered silver were produced for uniaxial tensile tests and for stress relaxation after tensile loading. The tests were performed by using a micro tensile machine equipped with a laser speckle extensometer, with load cell capacities of 100 N for the dumbbell shaped samples and 1000 N for the lap-joints. The dumbbell shaped samples had a parallel length of about 30 mm, a width of 4 mm and a thickness of approximately 75 µm. The shape of a sample before testing is depicted in Fig. 1 (a), while Fig. 1 (b) and (c) show the cross section of a tensile sample after rupture.

Secondly, lap-joints connecting two pieces of copper base material with sintered silver were prepared for shear tests under monotonic and cyclic loading, and for testing under conditions of stress relaxation. The pieces of copper base material had a cross section of 3 × 1 mm and a length of 50 mm each. The overlap length of a lap-joint was typically between 4 and 5 mm, and the thickness of the sintered silver layer was in the range between 45 µm and 70 µm, as shown in Fig. 2 (a, c). An EBSD scan of its microstructure is depicted in Fig. 2 (d). Fig. 2 (b) shows a lap-joint sample mounted onto the tensile machine, and the illuminated red dots indicate the position of laser beams of the laser speckle extensometer, which was used for strain measurements.

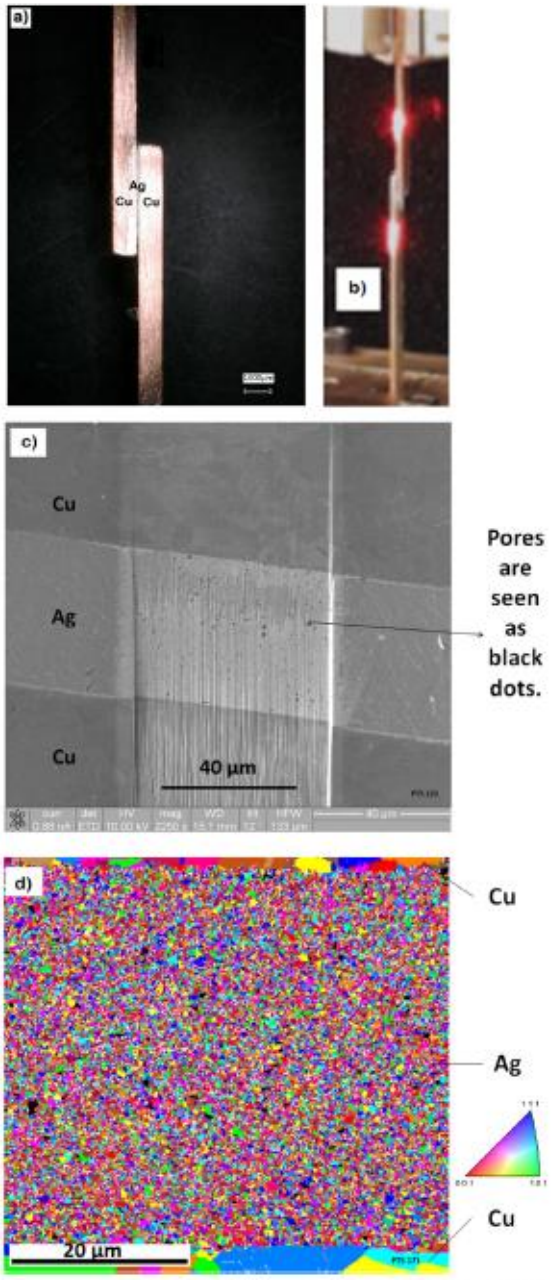

Fig. 2. (a) Cu-Ag-Cu lap-joint, (b) mounted onto a tensile machine, (c) SEM micrograph showing its porosity. (d) EBSD scan showing its grain sizes and orientations.

Table 1
Summary of averaged values for tensile strengths of dumbbell shaped samples and shear strengths of lap-joints.

Test temperature	Dumbbell shaped tensile strength	Lap-joints shear strength
RT	53.2 MPa	33.8 MPa
403 K	42.1 MPa	34 MPa
473 K	42.2 MPa	26.9 MPa

The dumbbell shaped samples and the lap-joints were produced with use of the commercial silver paste Heraeus mAgic 338 under equivalent sintering conditions at a pressure of 70 MPa and a temperature of 503 K, respectively.

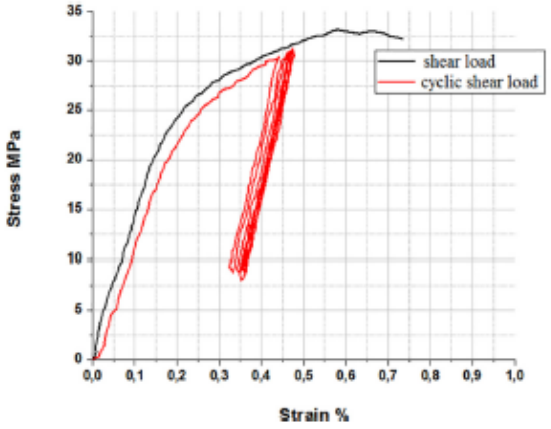

Fig. 3. Stress-strain curves representing the relative longitudinal elongation of a Cu-Ag-Cu lap-joint measured between two points with initial distance of 23 mm.

A metallographic examination confirmed that dumbbell shaped samples and lap-joints showed the same porosity and microstructure. By gravimetric analysis, the porosity was determined as 30%. Further details of the production process used for sintering may be found in references [4,5]. The average tensile and shear strength of the samples at different test temperatures are summarized in Table 1. In stress relaxation experiments, samples were at first loaded to about 75% of their ultimate strength, and thereafter the decay of stress was measured for 1 h. In addition, experiments of cyclic loading and unloading were performed with lap-joints, as shown in Fig. 3.

A collection of cyclic shear experiments with Ag-sintered lap-joints and a detailed description of the setup are included in reference [4].

3. Constitutive model

3.1. Fundamental assumptions

An advanced material model for sintered silver is developed here, whereby meaningful ideas of already existing theories are merged in order to derive optimized accordance with relevant experiments. At first, it is recognized that stress-strain curves of sintered silver under cyclic loading show qualitative agreement with experiments for cyclic loading of metallic fcc bulk material. Such behaviour of cyclic hardening and ratcheting has well been described by a combination of kinematic and isotropic hardening [11]. Therefore, we will take over this method for the present model.

Further, the stress relaxation curves of the present study are in qualitative agreement with experiments of Kariya et al. [12], who fitted this behaviour with the Garofalo model. Moreover, the tensile test data of the present study also show a similarity with experiments, which were successfully interpreted with the Anand model [6,7]. In conclusion, the temperature dependent strain rates are well described by a hyperbolic sine creep law.

Furthermore, it is noticed here that stress relaxation experiments show more compliance under tensile load compared to relaxation under shear load. This behaviour seems to be a consequence of porosity. According to analyses of McClintock [13], Rice and Tracey [14] there occur stress concentrations at the holes of porous metals, which induce plastic deformation and finally lead to rupture. Such stress concentrations increase, when hydrostatic and deviatoric stresses are superimposed. This effect is well described by the Gurson model [10]. In the model of the present study, an orthogonal decomposition of stresses in hydrostatic and deviatoric parts will be utilized to account for this behaviour.

3.2. Constitutive equations

The hydrostatic pressure in a solid is defined as

$$p = -\frac{1}{3}tr(\sigma) \tag{1}$$

where tr denotes the trace of a tensor and σ is the Cauchy stress. The deviatoric stress reads as

$$S = \sigma + p \cdot \mathbf{I}, \tag{2}$$

where I is the unity matrix. Further, the volumetric strain is defined as

$$\varepsilon_{vol} = \frac{1}{3}tr(\varepsilon) \cdot \mathbf{I}, \tag{3}$$

while the deviatoric strain writes as

$$\varepsilon_{dev} = \varepsilon - \varepsilon_{vol}. \tag{4}$$

It is assumed that the strain tensor

$$\varepsilon = \varepsilon_{el} + \varepsilon_{ine} \tag{5}$$

can additively be decomposed into an elastic part ε_{el} and an inelastic part ε_{ine}. The accumulated inelastic strain at time t_1 is here defined as

$$\varepsilon_{acc}^{ine} = \int_0^{t_1} \left\| \dot{\varepsilon}_{ine} \right\| dt, \tag{6}$$

where $\|\varepsilon\|$ denotes the Euklidean norm of the tensor ε. The derivative with respect to time is written according to the dot notation. Next, we define the effective stress

$$\sigma_{eff} = \sigma - \chi \tag{7}$$

where χ is called backstress. The backstress in the material occurs in consequence of the dislocation structure developed during plastic deformation. The backstress follows the time evolution.

$$\dot{\chi} = \chi_0 + k_1 \dot{\varepsilon}_{ine} - k_2 \cdot \varepsilon_{acc}^{ine} \cdot \chi, \tag{8}$$

where k_1 and k_2 are material constants. χ_0 is the initial value of backstress. In context with isotropic hardening, we need to define the deformation resistance

$$D = D_1 \cdot \left(1 - \exp\{ -D_2 \cdot (\varepsilon_{acc}^{ine} + \varepsilon_0) \} \right), \tag{9}$$

where D_1 and D_2 are material constants, and ε_0 is the initial value of plastic strain. A value of $\varepsilon_0 > 0$ is needed to obtain a finite value of the deformation resistance in the initial state. Furthermore, a temperature dependent scalar threshold value of

$$\sigma_{th}(T) = A \cdot \left(1 - \exp\left\{ -\frac{Q}{k_B T} \right\} \right) \tag{10}$$

is defined for the stress, below which creep deformation does not occur. Here, Q plays the role of an activation energy, k_B is the Boltzmann constant, $A > 0$ is a material parameter and T is the temperature in units of Kelvin. Thus, we are in the position to define the creep rate of the viscoplastic model. With use of an orthogonal decomposition into volumetric and deviatoric parts, we define the rates of creep strain

$$\left\|\dot{\varepsilon}^{in}_{vol}\right\| = c_1 \cdot \exp\left\{-\frac{Q}{k_B T}\right\} \cdot \sinh\frac{\left(c_3 \cdot f \cdot \left(\sqrt{3}\,\|p_{eff}\| - \sigma^{vol}_{th}\right)\right)^{n_1}}{D} \tag{11a}$$

$$\left\|\dot{\varepsilon}^{in}_{dev}\right\| = c_2 \cdot \exp\left\{-\frac{Q}{k_B T}\right\} \cdot \sinh\left(\frac{\|S_{eff}\| - \sigma^{dev}_{th}}{D}\right)^{n_2} \tag{11b}$$

for

$$\|\sigma_{eff}\| > \sigma_{th} \tag{11c}$$

with

$$\sigma^{vol}_{th} = \frac{\sqrt{3}\|p_{eff}\|}{\|\sigma_{eff}\|}\sigma_{th} \tag{11d}$$

and

$$\sigma^{dev}_{th} = \frac{\|S_{eff}\|}{\|\sigma_{eff}\|}\sigma_{th}, \tag{11e}$$

where σ^{vol}_{th} and σ^{dev}_{th} are the volumetric and deviatoric parts of the threshold stress. Further, c_1, c_2 and $c_3 > 0$ are material constants and f is the porosity, i.e., the volume fraction of pores in the material. n_1 and n_2 are the stress exponents of the hyperbolic sine creep law. S_{eff} is the deviatoric part of the effective stress σ_{eff}. Due to inelastic volume change in view of porosity, there also occurs a hydrostatic part of the backstress, and in consequence an effective hydrostatic pressure p_{eff}. The volumetric part of strain rate causes compression under positive effective pressure and in the opposite case it leads to expansion. The direction of the deviatoric strain rate is parallel to the effective deviatoric stress S_{eff}. Finally, conservation of mass implies an evolution of porosity according to

$$\dot{f} = (1-f) \cdot \mathrm{tr}\left(\dot{\varepsilon}_{in}\right) \tag{12}$$

3.3. Damage accumulation

The equations describing the evolution of stresses, strains and porosity of the material are a prerequisite for the formulation of lifetime models. In addition, a rule of damage accumulation is required to obtain reliability assessments based on FEM simulations. In metal plasticity, it is usually assumed that the hydrostatic pressure stress has a small influence on plastic yielding, but a large influence on ductility [13–15]. Under triaxial tension, significant void growth is observed, and this effect appears to be particularly relevant for materials of high porosity. In the case of monotonic loading, the inelastic strain leading to fracture can be described by an equation of the form

$$\varepsilon_f = h_1 \cdot \exp\{-h_2 \cdot p_{eff}\} \tag{13}$$

where h_1 and $h_2 > 0$ are material parameters, while the effective pressure p_{eff} has the same meaning as in Eqs. (11a) and (11d). Further, damage accumulation follows the rule

$$H = \sum \frac{\Delta\varepsilon}{\varepsilon_f}, \tag{14}$$

where H plays the role of a damage variable. Fracture is initiated, when the value of the damage variable H approaches the value of 1. Eqs. (13) and (14) represent a simplified version of a fracture criterion proposed by Johnson and Cook [15].

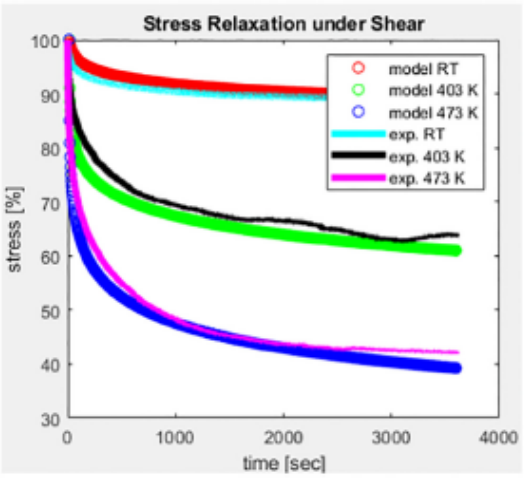

Fig. 4. Shear stress relaxation curves of the model compared to experimental results.

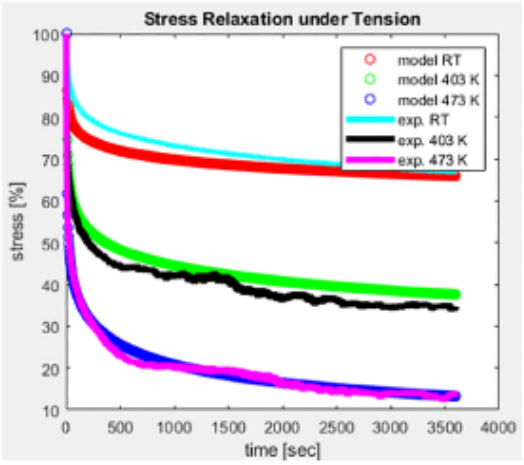

Fig. 5. Stress relaxation curves after tensile loading. Model calculations were fitted to experimental results.

For the case of cyclic loading under steady-state conditions, we here suggest a modified Coffin Manson lifetime model, where the number N_f of loading cycles to failure is expressed as

$$N_f = a\left(\frac{\Delta\varepsilon_{ine}}{\varepsilon_f^{mean}}\right)^b, \tag{15}$$

where a and b are material parameters, $\Delta\varepsilon_{ine}$ is the inelastic strain increment per loading cycle, and ε_f^{mean} is defined as

$$\varepsilon_f^{mean} = h_1 \cdot \exp\left\{-h_2 \cdot p_{eff}^{mean}\right\} \tag{16}$$

Here, p_{eff}^{mean} is the mean value of effective hydrostatic pressure, which is averaged over one period of cyclic deformation. Owing to a temperature dependence of ductility, the parameters a, b, h_1 and h_2 are

Table 2
Material parameters used for the plots of Figs. 4 and 5.

Temperature	Shear modulus	Bulk modulus
298 [K]	8460 [MPa]	18,333 [MPa]
403 [K]	7920 [MPa]	17,167 [MPa]
473 [K]	7580 [MPa]	16,417 [MPa]

Isotropic hardening	D_1	D_2	ε_0
Parameter	16 [MPa]	3	0.09

Kinematic hardening	k_1	k_2
Parameter	20 [MPa]	7

Activation energy	Threshold stress value A	Initial porosity
133 kJ/ (mol K)	2.0 [MPa]	0.38
p		

Creep	c_1	c_2	c_3
Coefficients	3e11	2e9	0.22

Stress	n_1 (volumetric)	n_2 (deviatoric)
Exponents	1.9	3.5

considered as temperature dependent.

3.4. Numerical fitting of material parameters

The material parameters of the model are determined from fits to mechanical tests under tension and shear loads.

The numerical fits shown in Figs. 4 and 5 were based on the assumption that the sintered material is homogeneously deformed so that conditions of uniaxial tension and simple shear are fulfilled to a good approximation. The fitting procedure was at first performed for shear tests, because this state of stress is purely deviatoric, and therefore the number of relevant fit parameters is reduced from the beginning. Thereafter, the remaining parameters were determined from fits to tests under tensile load.

Fig. 4 shows fits to stress relaxation experiments performed with lap-joints in shear mode at temperatures of RT, 403 K and 473 K. The initial shear stresses of these experiments were 30 MPa, 30 MPa and 23 MPa, respectively. Thus, fits at equivalent temperatures were performed for stress relaxation of dumbbell shaped samples after tensile loading, as depicted in Fig. 5. The initial tensile stresses of these experiments were 43.2 MPa, 30.7 MPa and 31.7 MPa respectively. The parameters determined through the fits of Figs. 4 and 5 are summarized in Table 2. The values of elastic material constants were chosen in agreement with literature data [17] for sintered silver of the same porosity.

4. FEM implementation in ABAQUS

The constitutive equations for the evolution of stresses, strains and porosity are now implemented in the commercial software ABAQUS Standard through user subroutine UMAT and in ABAQUS Explicit through user subroutine VUMAT [18], respectively. The implementation in ABAQUS Explicit is straightforward, but when applied to long time scales it gets computationally expensive. On the other hand, the implementation in ABAQUS Standard is more difficult to achieve, because the stiffness matrix of a nonlinear material has to be calculated. However, with use of this algorithm larger time increments can be evaluated, and therefore the computation is faster.

For simplicity, we here start with the algorithm used for the subroutine VUMAT: This subroutine is called for every increment of the simulation. The interface of the user subroutine to the main program is defined in the sense that stresses and state variables, which are valid at the beginning of the increment, are passed in by the main program together with incremental values dt for time and $\Delta\varepsilon$ for strain, respectively. The subroutine has to return the updated values for the stress tensor and the state variables at the end of the increment. The 8 state variables used in this algorithm are the components of the backstress tensor, the value of accumulated inelastic strain and the updated value for the porosity of the material.

In the first step of the algorithm, a trial stress

$$\sigma_{trial} = \sigma_{Inl} + C \cdot (\varepsilon_{fin} - \varepsilon_{ine}) \tag{17}$$

is calculated, where C represents the elastic tensor. Further, the mean stress

$$\sigma_{mean} = \frac{1}{2}(\sigma_{Inl} + \sigma_{trial}) \tag{18}$$

representing the time average of stress active in this increment is calculated. Next, the effective mean stress

$$\sigma^{eff}_{mean} = \sigma_{mean} - \chi_{Inl} \tag{19}$$

is evaluated by subtraction of the backstress. Here, the backstress χ_{Inl} for the beginning of the increment is inserted. Thus, the effective mean stress is decomposed into hydrostatic and deviatoric parts, and the correlated Euklidean norms of these tensors are calculated. Then, it is checked whether the inequality of Eq. (11c) is satisfied. In the case that the effective stresses are below the threshold value for creep, σ_{trial} is used as result for the stress at the end of the increment. Otherwise, the values for the volumetric and deviatoric strain rates are calculated according to Eqs. (11a) and (11b). In fact, the time increments used by ABAQUS Explicit are extremely small. Therefore, strains may be interpolated linearly within the increment, and one receives.

$$\Delta\varepsilon^{Inl}_{vol} = \dot{\varepsilon}^{Inl}_{vol} \cdot dt \tag{20a}$$

and

$$\Delta\varepsilon^{Inl}_{dev} = \dot{\varepsilon}^{Inl}_{dev} \cdot dt. \tag{20b}$$

Consequently, the stress at the end of the increment becomes

$$\sigma_{fin} = \sigma_{trial} - 2G\Delta\varepsilon^{Inl}_{dev} - K\Delta\varepsilon^{Inl}_{vol}, \tag{21}$$

where G and K are shear modulus and bulk modulus of an isotropic elastic material, respectively. Finally, the state variables are updated according to the equations

$$\chi_{fin} = \chi_{Inl} + k_1 \cdot \Delta\varepsilon_{ine} - k_2 \cdot \|\Delta\varepsilon_{ine}\| \cdot \chi_{Inl} \tag{22}$$

$$\varepsilon^{Inl}_{acc,fin} = \varepsilon^{Inl}_{acc,Inl} + \|\Delta\varepsilon_{ine}\| \tag{23}$$

$$f_{fin} = f_{Inl} + (1 - f_{Inl}) \cdot \Delta\mathrm{tr}(\varepsilon_{ine}) \tag{24}$$

This update of the state variables completes the subroutine VUMAT.

Next, the subroutine UMAT for ABAQUS Standard is explained: The algorithm used for UMAT divides the time increment dt into N intervals, whereby every interval is evaluated according to the algorithm, which was already described in Eqs. (17) to (24). Thereby, N serves as solution parameter, and a value of $N = 10$ intervals proved to be useful. Further, the stresses and state variables at the end of every interval are used as start values for the subsequent interval. In consequence, one finally obtains the update for the stresses and state variables at the end of the time increment.

Furthermore, the 36 components of the material Jacobian matrix $\frac{\partial\Delta\sigma_{ij}}{\partial\Delta\varepsilon_{kl}}$ at the end of the increment are to be evaluated. This is done numerically with use of the stress update algorithm in combination with an increased strain increment $\Delta\varepsilon = \varepsilon_{fin} - \varepsilon_{Inl}$. This procedure is carried out for every component of the strain tensor, whereby an additional strain increase of at least 10^{-12} per strain component was assumed.

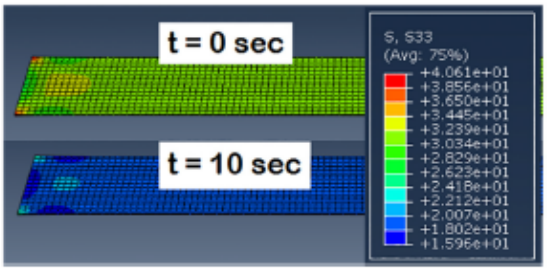

Fig. 6. Plot of tensile stress [MPa] for two time steps at 403 K. The stress relaxation within the first 10 s at constant sample length is shown.

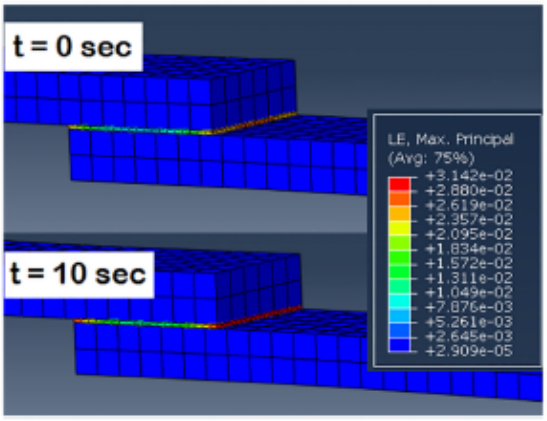

Fig. 7. Plot of first principal logarithmic strain for two time steps during stress relaxation at room temperature. An increase of inelastic strain within the sintered material is observed.

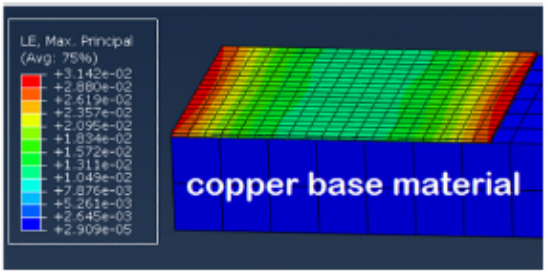

Fig. 8. Distribution of first principal logarithmic strain in the sintered material after 10 s of stress relaxation.

5. Simulation results

Examples of FEM simulations performed with subroutine UMAT are shown in Figs. 6–8. Fig. 6 shows the stress relaxation of a tensile specimen at 403 K using the material parameters of Table 2. For simplicity, only the parallel length of the sample was simulated. Prior to relaxation, the sample was loaded to 30.7 MPa within 8 s. Thereupon, the sample was kept at constant length. In Fig. 6, $t = 0$ indicates the time step of maximum stress at the onset of stress relaxation. 10 s later, a considerable stress reduction is observed. The material behaviour seen in the FEM simulation is in good agreement with the numerical results of Fig. 5, which was derived for a homogeneously deformed sample.

In Fig. 7 one can see the stress relaxation of a lap-joint at room temperature. The entire sample including the copper parts of 50 mm length was simulated. The Figure shows the region in the vicinity of the sintered area. The time step of $t = 0$ indicates the onset of stress relaxation after loading. Thereupon, further increase of inelastic strain is observed in the sintered material.

The cut view depicted in Fig. 8 shows the strain distribution in the sintered silver after 10 s of stress relaxation at room temperature.

Obviously, the distribution of strain is not homogeneous. Nevertheless, the amount of tensile stress reduction at the ends of the lap-joint appeared to be plausible with respect to experimental data. In conclusion, the material parameters of Table 2 can be used for modelling of sintered silver without need of further optimization.

6. Summary and conclusions

In summary, a unified material model for sintered silver was developed, which can be applied to reliability assessments of sintered joints in electronic packages. Lifetime estimates are usually deduced from models of damage accumulation, whereby damage develops in dependence of the accumulated inelastic strain observed during simulation of electronic assemblies [16]. In praxis, simplified material models as for instance bilinear kinematic hardening are used for this purpose. In this context, advanced material models for the sintered joints may provide more accurate estimates for expected lifetimes of electronic modules. However, follow up studies seem to be necessary in order to obtain further insight into damage accumulation. In particular, it is planned to study ageing effects of the sintered material in future investigations.

Declaration of competing interest

We have no conflict of interest regarding the manuscript submission: "Constitutive equations for strain rate and temperature dependent mechanical behaviour of porous Ag-sintered joints in electronic packages" for publication in Microelectronics Reliability, special issue of the ESREF conference!

Acknowledgements

The financial support by the Austrian Federal Ministry for Digital and Economic Affairs and the National Foundation for Research, Technology and Development is gratefully acknowledged.

References

[1] Jan A. Oestreicher, T. Röhrich, J. Wilden, M. Lerch, A. Jakob, H. Lang, An innovative method for joining materials at low temperature using silver (nano) particles derived from [AgO2C(CH2OCH2)3H], Appl. Surf. Sci. 265 (15) (2013) 239–244.
[2] Ch. Neeb, L. Böttcher, M. Conrad, R. de Doncker, innovative and reliable power modules, IEEE Ind. Electron. Mag. (2014) 6–16. Sept.
[3] L. Boettcher, S. Karaszkiewicz, D. Manessis, A. Ostmann, Embedded die packages and modules for power electronics applications, IMAPS 2016 (2016) 001918–001947.
[4] Z. Gökdeniz, G. Khatibi, J. Nicolics, A. Steiger-Thirsfeld, Behaviour of silver-sintered joints by cycling mechanical loading and influence of temperature, in: IEEE Proc. of 22nd EMPC, 2019.
[5] Z. Gökdeniz, G. Khatibi, T. Walter, J. Nicolics, in: 41st International Spring Seminar on Electronics Technology (ISSE), 2018.
[6] Yu. Dun-ji, Xu. Chen, Gang Chen, Lu. Guo-quan, Zheng-qiang Wang, Applying Anand model to low-temperature sintered nanoscale silver paste chip attachment, Mater. Des. 30 (2009) 4574–4579.
[7] L. Anand, Constitutive equations for hot working of metals, Int J. Plasticity 1 (1985) 213–231.
[8] Gang Chen, Ze-Sheng Zhang, Yun-Hui Mei, Xin Li, Dun-Ji Yu, Lei Wang, Xu Chen, Applying viscoplastic constitutive models to predict ratcheting, Mech. Mater. 72 (2014) 61–71.
[9] Yao Yao, He Gong, Damage and viscoplastic behavior of sintered nano-silver joints under shear loading, Eng. Fract. Mech. 222 (2019) 106741.
[10] A.L. Gurson, J. Eng. Mater. Technol. 99 (1977) 2–15.

[11] J.L. Chaboche, A review of some plasticity and viscoplasticity constitutive theories, Int. J. Plast. 24 (2008) 1642–1693.
[12] Y. Kariya, H. Yamaguchi, M. Itako, N. Mizumura, K. Sasaki, J. Smart Process. 2 (2013) 160.
[13] F.A. McClintock, A criterion for ductile fracture by growth of holes, Am. Soc. Mech. Eng. 35 (1968) 363–371.
[14] J.R. Rice, D.M. Tracey, On the ductile enlargement of voids in triaxial stress fields, J. Mech. Phys. Solids 17 (1969) 201–217.
[15] G.R. Johnson, W.H. Cook, Fracture characteristics of three metals subjected to various strains, strain rates, temperatures and pressures, Eng. Fract. Mech. 21 (1) (1985) 31–48.
[16] P. Rajaguru, H. Lu, C. Bailey, Sintered silver finite element modelling and reliability based design optimisation in power electronic module, Microelectron. Reliab. 55 (2015) 919–930.
[17] J. Carr, X. Milhet, P. Gadaudb, S.A.E. Boyer, G.E. Thompson, P. Lee, Quantitative characterization of porosity and determination of elastic modulus for sintered micro-silver joints, J. Mater. Process. Technol. 225 (2015) 19–23.
[18] ABAQUS User Subroutine Manual Dassault Systemes.

CHAPTER 6

DISCUSSIONS and SUMMARY

Previous chapter contains six published papers. This chapter is devoted to the summary of results of our investigations with complementary plots and to the main discussion points including comparisons with outcomes of other research works.

6.1. Porosity Measurement

One of the challenges surely is the density evaluation for the porous structure of a sintered material, here silver, with various shapes and sizes of cavities. Especially when sintering is performed under pressure the outer margin of a lap-joint has another density than the tighter mid-inside section (as shown in Fig.2 in section 5.5.). This might be a result of the stencil printing where the Ag-paste forms a lowering profile on the boundary due to viscosity (as shown in Fig.3.2.a and Fig.3.3.a-b in section 3.1.). Furthermore, the conjunction and thoroughfare of the pores shaped during sintering are structured randomly, which might affect the penetration dept of the oxygen, which again plays an effective role in the aggregation of the connecting silver necks, enlargement of the grain size (as shown in Fig.4.17 in section 4.2.) and reshaping the pores in case of elevated temperature (as shown in Fig.4.11 in section 4.2.).

W. Rmili et al. [68] reconstructed the 3D tortuosity of two sintered samples from ca. 100 image slices each, for the volumes of ca. 13 µm x 19 µm x 11 µm and 13 µm x 15 µm x 12.5 µm. The sintering parameters are not given, but the porosities are deduced with 56 % and 16 % respectively. The connectivity of the pores was given with 99.9 % and 90.7 %.

James Carr et al. [52] had a 3D study on the pores' connectivity after sintering (under 10 MPa for 3 min. with a final step at 240 °C) and after ageing for 1500 hours in air at 125 °C considering the size and distribution. It was found that some areas after ageing were almost free of pores, whereas other areas displayed large pores. Yutai Su et al. [53] evaluated within a region of 60 µm x 35 µm four areas with porosities from 11 % to 23 % as shown in Fig.6.1.

Therefore, especially in case of a microscopic analysis of the density it is important to clarify the local position of the observation and if it is representative for the material in general.

In our research, for the samples of free-standing Ag-coupons both the optical and mass/volume measurements of the densities were investigated. For the lap-joints the optical evaluation was made for three disclosure methods of the sintered Ag-area: revealed surface after fracture, lateral grinding after embedding in resin and vertical FIB treatment. Another possibility would be the selective etching of the copper to reach the silver layer, but this last method was not specially followed up in this work.

For the lap-joints, the grinding of the pressureless sintered area on copper lead to a silver density evaluation between 61-63 %. For the under pressure sintered area the density increased to 88-94 %. For the FIBed section of the latter the value was around 94 % for both 0-hour and A-Aged samples, and between 90-94 % for G-Aged ones, which means there was no significant change in the optically established density after heat treatment for the under high pressure sintered silver within the copper joint.

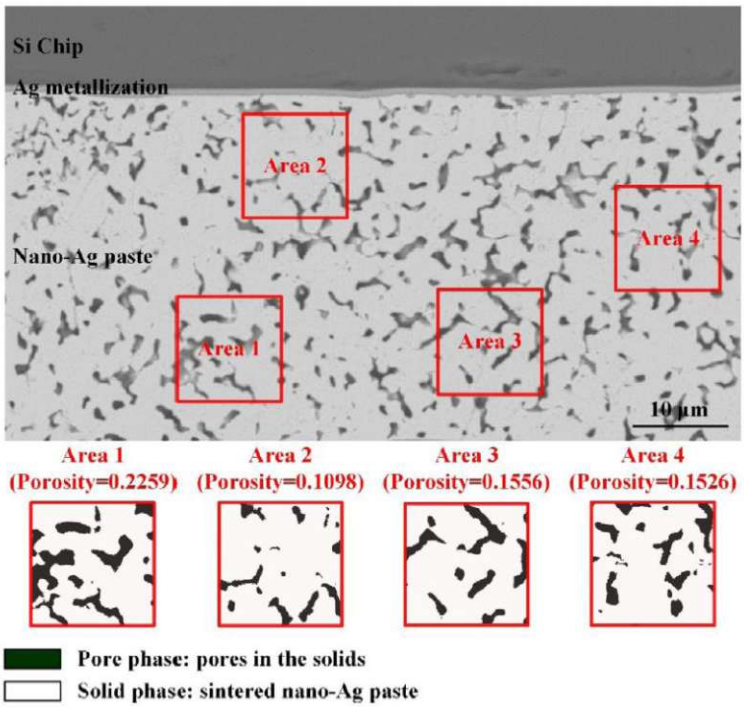

Fig. 6.1: Sintered nano-silver paste with micro-porous morphology [53].

Keisuke Wakamoto et al. [51] investigated the porosity-dependent mechanical properties of the pressure sintered silver films. The densities were determined using SEM cross-sectional images and were in the range of 75 – 95 % for the sintering pressures between 5 MPa and 60 MPa. These values are in accordance with our measurements for the grinded silver surface of the lap-joints.

L. Signor et al. studied the evolution of thermal conductivity of sintered silver joints with their porosity [54]. Specimen#1 was as sintered and the mass/volume density was 8 g/cm^3 corresponding to a porosity of ca. 23.7 %, Specimen#2 was heat treated and the mass/volume density was 7.8 g/cm^3 corresponding to a porosity of ca. 25.6 %. Respectively, the 3D image analysis yielded 10.5% and 17.2 % porosities for the two specimens, much less than the mass/volume method.

Fig. 6.2.a shows a section from the fracture surface of a pressureless sintered Ag-dumbbell of our research. The susceptible point is the conversion of the 3D topography into a plain monochromacy. Not all the through automatic conversion black marked areas are actual pores. The comparison of Fig.6.2.b and Fig.6.2.c reveals the scope of the threshold setting for the circumference (red filled areas), one leading to a porosity of 10 % and the other to 36 %.

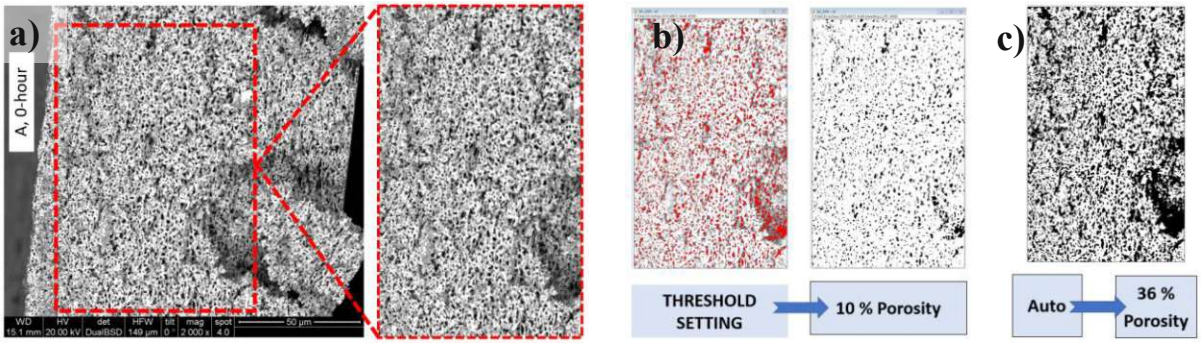

Fig. 6.2: The porous microstructure of the sintered silver (a) and manual threshold setting as red marked areas (b) vs. automatic recognition of the voids on the fracture surface (c) with the monochromatic mapping as black marked areas for optical density evaluation.

The depiction for the sample series is given in the Appendix section A.2. To give the overview, the optical analysis of the fracture surface of the pressureless sintered silver resulted in a silver density between 64-90 % depending on the threshold setting as described, and between 62-85 % for pressure assisted sintered silver. Regarding that pressureless sintering and sintering under high pressure could not engender a similar porosity in that vast range, the method of optical evaluation was considered as not fully reliable.

The mass/volume measurements however delivered evident values of 35 % and 42 % Ag-density depending on sintering temperature 230 °C and 300 °C for pressureless sintering, 62 % and 68 % Ag-density for pressure assisted sintering. Therefore, the parameters of the developed material model were based on the latter (as published in section 5.3.). The manufacturing of the dumbbell-shaped using the 200 µm stencil led to different mean thicknesses of the Ag layer after sintering: above 100 µm for 0 MPa and around ca. 70 µm under 70 MPa, as shown in Fig.6.3.

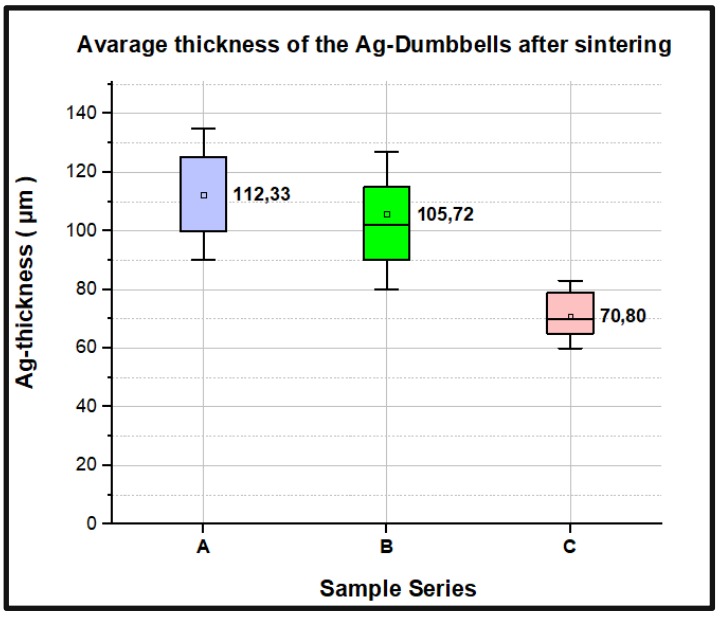

Fig. 6.3: Average thickness of the silver after pressureless (A at 230 °C and B at 300 °C) and pressure-assisted (C at 230 °C) sintering, measured with a micrometer screw.

6.2. Effect of Temperature on Porosity and Related Properties

Keisuke Wakamoto et al. [55] measured the E-modulus of the sintered silver for various testing temperatures between 25 °C and 150 °C. The samples were manufactured with a sintering pressure of 60 MPa, similar to our series, and the porosity of 5 % was determined with the optical method which is similar to our results obtained by optical measurements.
Further, the E-modulus was determined from the slope of the stress-strain curve and given with 45 GPa at room temperature and 15 GPa at the elevated temperature of 120 °C. Further, a 10 µm thick pure silver (99.99% Ag) was shaped by laser cutting in the same configuration as the sintered Ag specimen. A comparison with the pure silver delivered over 60 GPa and 30 GPa as E-modulus, higher than the ones for the sintered silver at the named temperatures respectively. In other words, a decrease of the elastic modulus was found for both the increase of porosity and the increase of testing temperature.

As shown in Fig.4.7-4.9, the stress-strain measurements delivered also in our case decreasing values of the E-modulus for the 250-hours aged samples in comparison to the 0-hour samples. A decreasing tendency was also observed for the elevated test temperature of 200 °C, more distinguished for the specimen sintered at 230 °C.
For the brittle-ductile transition of the fracture characteristics during the increase of testing temperature with the decrease of UTS, the increase of the flow ability of Ag grains enabling large plastic strains was considered.

T. Suzuki et al. [56] prepared samples with pressureless and pressure assisted sintering and found the porosities of 45 % and 25 % with the mass/volume method. The E-modulus was determined to 20 GPa and 40 GPa from the slope of the tensile stress-strain curves, respectively.
These values correspond to our result of ca. 40 GPa for the E-modulus measured with LSE for the pressure assisted sintered C-series (0-hour).

Tomofumi Watanabe et al. [57] investigated pressureless sintered silver for die-attach. The tensile stress-strain curves of the sintered Ag dumbbells were measured after storage at 250 °C for 250 h, 500 h and 1000 h. Elastic modulus of the sintered silver, independent of storage time, was calculated as 14 GPa before and after the isothermal storage.
V. Caccuri et al. [58] performed tensile tests using an Instron E1000 with a strain gage extensometer and determined the E-modulus around 25 GPa for the silver with the density of around 7 g/cm^3, which can be again compared with our series sintered under high pressure.
P. Gadaud et al. [59] measured the tensile strength of sintered silver at 25 °C and 125 °C, and investigated the effect of isothermal aging in air ambient at 125 °C up to 1500 hours. The density was measured over the mass/volume method and was for the as sintered samples 7.7 g/cm^3 with a

final thickness of 50-60 µm. It was concluded that the elastic properties of E-modulus and yield strength did not change significantly after the ageing as described.
Similarly, James Carr et al. found densities of 7.8-8 g/cm^3 for the 'as sintered' specimen whereby this range remained the same after ageing for 1500 hours at 125 °C [52].
However, Hao Zhang et al. [63] reported a decrease in the porosity from 24.3 % to 21.2 %, based on the evaluation of the FIBed cross-section of the microstructure of a pressureless sintered silver after ageing for 1000 hours at 250 °C. C. Choe et al. [46] also reported a decrease in the porosity for the pressureless sintered silver after ageing at 250 °C.

The reports considering thermal treatment temperatures below 130 °C and at 250 °C are in accordance with the outcome of our Thermo-Gravemetric-Analysis of the ASP-338 Ag-paste series, where 180 °C seem to be a reaction threshold temperature in the sintering process after the evaporation of the volatile components from the paste [4].

We could also observe a decrease in the porosity for the pressureless sintered silver series A and B from ca. 65 % and 58 % to ca. 52 % and 41 % respectively after heat treatment at 250 °C for 250 hours, measured with the mass/volume method.
Furthermore, a decrease in the E-modulus (Table 4.1.b-c) with the aging time at a temperature beyond the reaction temperature is evident. This result was expected and is in accordance with many other metals where a thermal treatment is applied to anneal internal stress.

In Fig.6.4 the porosities for the main four series A, B, C, and D (which were prepared as described in section 3.1.) are plotted versus the electrical resistivities at 25 °C and at 200 °C. The resistivity decreases with the decrease of the porosity, i.e. with the increase of the Ag-density. The resistivity increases with the elevating temperature, as expected. The mean and deviation values at room and elevated testing temperatures are listed in Table 6.1.

Table 6.1:
RESISTIVITY in 10^{-9} Ωm

25 °C	
A	70,18 ± 1,19
B	58,32 ± 3,3
C	30,33 ± 4,82
D	24,72 ± 4,23

200 °C	
A	113,58 ± 10,46
B	98,63 ± 7,28
C	42,98 ± 3,23
D	42,53 ± 8,96

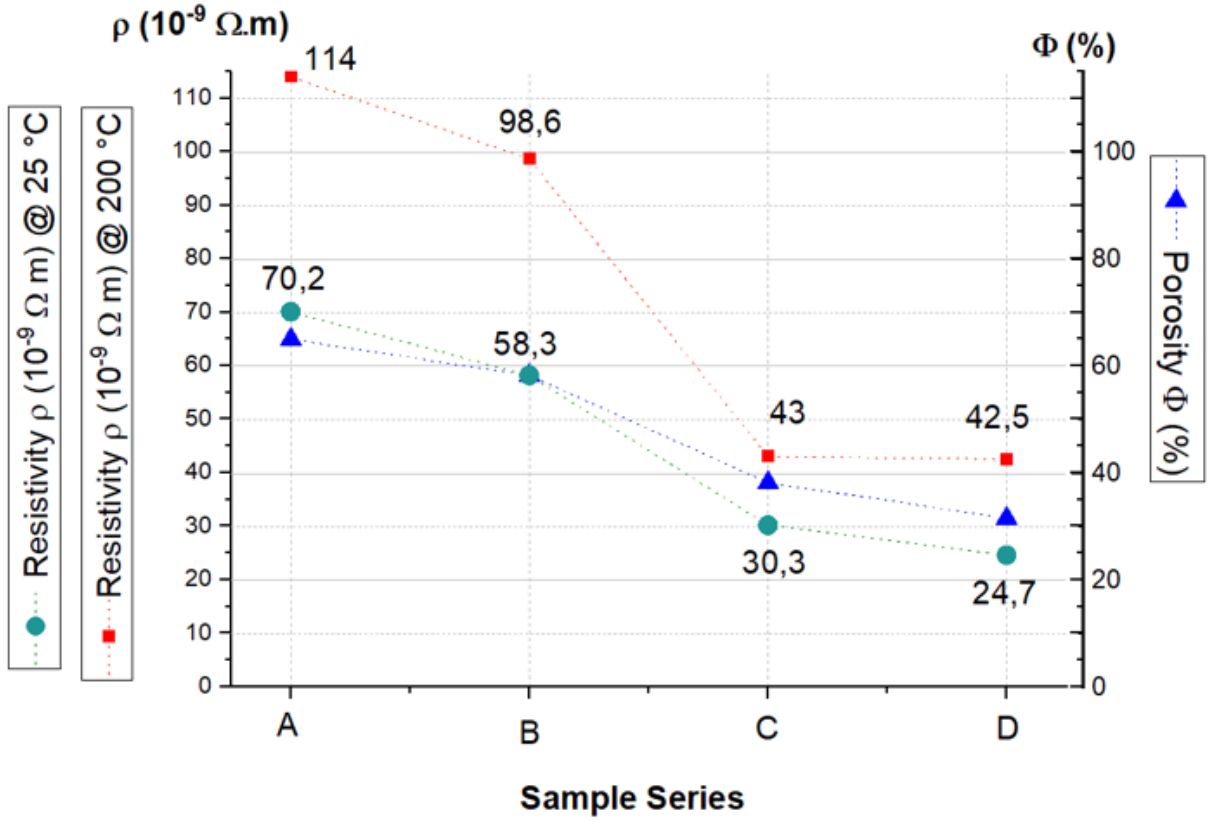

Fig. 6.4: Two plots with the scale on the left side showing the resistivity measurement of the pressureless (A and B) and under pressure (C and D) sintered Ag-series for room (green circles) and elevated testing temperature (red squares) vs. the plot of m/V density as percent (blue triangles) with the scale on the right side.

6.3. Shear Characteristics, Cyclic Lifetime and Creep Behaviour

The shear strength of the lap-joints was measured with a testing speed of 2 mm/min. The first results for the tested samples' quantity number up to ten were published as in section 5.1. A mean strength of around 16 MPa of the specimen was assessed, which correspond to the series named PT as described in section 3.2.

However, during further experiments more samples (over twenty for the PT series) were tested and an updated overview showing the deviation is plotted in Fig.6.5.a. For the 200 µm Ag stencil print on blank copper, increasing the sintering pressure from 25 MPa to over 70 MPa and decreasing the sintering time from 60 min. to 30 min at 230 °C (the PTP series) resulted in the increase of mean shear strength up to 28 MPa. Further, when copper substrates were Ag-sputtered on both sides of the joint an increase in the mean shear strength from ca. 23 MPa to ca. 50 MPa was observed for the button samples, sintered for 60 min. at 230 °C with 50 MPa sintereig pressure for the 100 µm Ag stencil print (Kap 5.1, Fig.6). Regarding this ascertainment, the PTS series with Ag-sputtered copper strips sintered at 70 MPa and 230 °C for 30 min. were manufactured. These parameters also correspond to those for the C-series of the Ag-dumbbells, which were tensile tested.

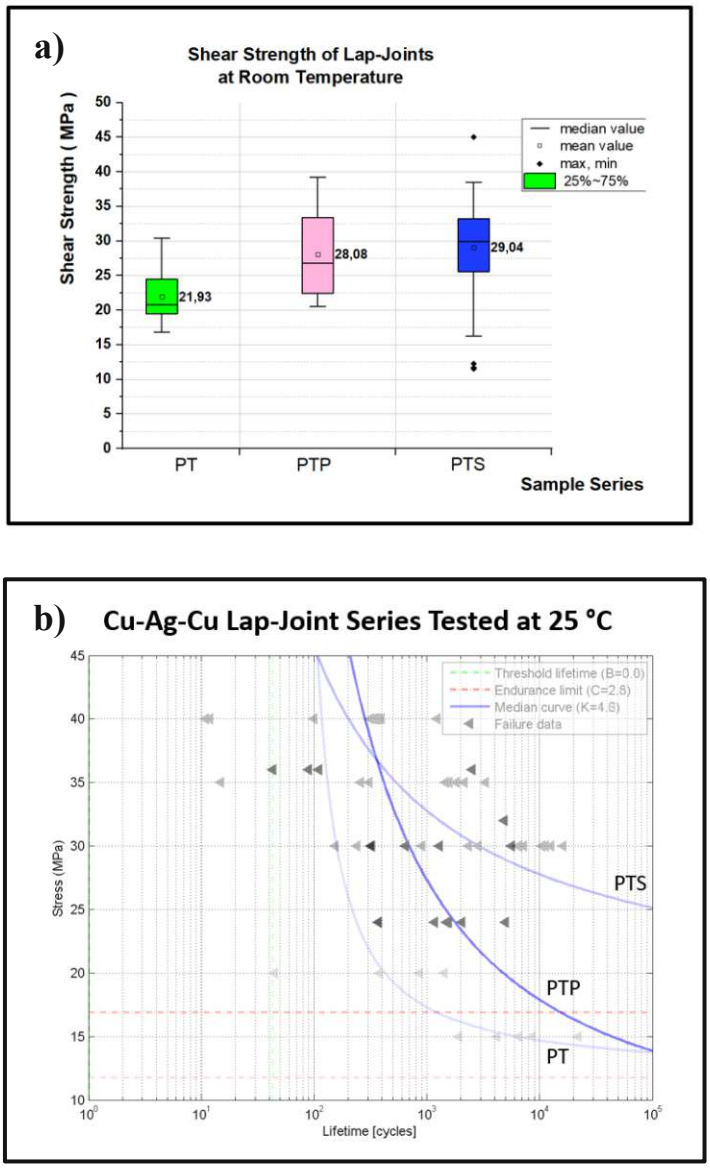

Fig. 6.5: Shear strength of three lap-joint series (a) and corresponding mechanical cyclic lifetime with the exerted stress maxima τ (b) at room temperature.

The Wöhler plot for the mechanical cyclic lifetime of the specimen-series PT, PTP, and PTS at room temperature is given in Fig 6.5.b.

Yansong Tan et al. [50] investigated the shear behaviour of Ag-sintered lap joints and stress-strain hysteresis of cyclic loading effected by various amplitude levels and elevated temperature. The shear strength of ca. 28 MPa decreased with increasing testing temperatures 125 °C, 225 °C and 325 °C. The area of the hysteresis loop is generated by the difference of the energy loss created between deformation during cyclic loading and recovery in the lattice. Increase of the hysteresis loop area with increasing cycle number at the given loading, the increase of the stress amplitude and the increase of testing temperature indicates that more plastic energy was consumed in these cases.

Long, X et al. [60] reported a hardening phenomenon for the sintered Ag, i.e. an increase of the tensile yield strength with the increase of the applied loading rate, at a typical temperature of 150 °C, based on the strain [61] and stress loading [62] measurements.

A preview of mechanical lifetime, tested at room temperature, for the named three series of the lap-joints (PT, PTP, and PTS) is plotted in Fig. 6.5.b. The τ-N_f curves represent the maximum shear stress to which the samples are strained over the number of cycles until end of life, i.e. detachment of the silver joint at the corresponding stress levels. The stars mark the 50 % probability points for the total fracture failure. In comparison, the Ag-presputtered lap-joint specimen (PTS) yielded higher values and were chosen for the subsequent experiments under various thermal conditions. The results of the latter are plotted and discussed in the sections 4.2. and 5.2.

Zheng Zhang et al. [64] sintered silver on bare copper at various temperatures at atmospheric conditions. SEM images of the joints' cross-sections showed that no rough oxide layer was formed on copper at 180 °C and only a portion of the Ag particles bonded on the Cu substrate. On the other hand, with the sintering at 250 °C and 300 °C an oxide layer of 30 µm - 100 µm interconnected silver particles tightly with the copper base. The High-Resolution TEM investigations revealed copper-oxide nanoparticles on both sides of the intermediate oxide layer, forming a robust bond on the interface between the Cu side and the matching silver nanoparticles on the Ag side which are released during sintering in air at elevated temperature.

This is in accordance with our results as shown in section 4.2., where we also observe an increase of the cyclic lifetime for the thermal treated specimen [2]. Heat treatment prior to mechanical testing improved the cyclic lifetime of lap-joints, however, the cyclic fatigue life was significantly reduced, when samples were tested at elevated temperature.

Further, stress relaxation experiments at 25 °C, 130 °C and 200 °C were pursued to examine the creep properties of the defined pressureless and pressure assisted sintered samples. Thereby, the temperature dependence was described by an Arrhenius term as in section 2.2.2. The results of the performed tests and analyses could be fitted by the parameters of a theoretical material model based on a combination of Norton creep and Gurson plasticity, as published in 5.4 - 5.6. The constitutive equations of the model describe the creep properties of sintered silver in dependence of its porosity. Using an activation energy Q for sintered silver of 133 kJ/(mol K), the

material model was implemented in the commercial software of ABAQUS through user subroutine UMAT and can now be used as helpful tool for reliability assessment of Ag-sintered copper joints.

6.4. Summary

In this work, the thermo-mechanical and electrical properties of sintered Ag were characterized, which are influenced by the porous structure arising in consequence of sample preparation and sintering conditions. Defined series of samples were either produced by pressureless or by pressure assisted sintering and the correlated microstructure of the porous silver was investigated. Characteristic features such as density and electrical resistivity were determined. Moreover, the mechanical behaviour of pure materials and sintered joints was measured in tensile and shear tests, by stress relaxation tests and by cyclic fatigue experiments at various testing temperatures.

An overview of the main parameters of the investigations for the pressure assisted sintered specimens (at 70 MPa and 230 °C for 30 min), 0-hour and 250-hours heat treated samples, are given in Table 6.2 with selected results of testing at room temperature. Further, the summary of the results is described as follows:

Table 6.2: Overview of the main parameters of the selected Ag-specimens sintered under the pressure of 70 MPa at 230 °C for 30 min.

PARAMETER	COMMENT	0-hour specimen measurement @ 25 °C	250-hours specimen measurement @ 25 °C
Mean Tensile Strength	mean UTS	56,5 MPa	48,5 MPa
Mean Shear Strength		29 MPa	33 MPa
Density	optical measurement	88-94 %	90-94 %
	m/V measurement	62 %	(could not be measured due to bending of structure)
Electr. Resistivity		30 nΩm	
Young's modulus	LSE	38 GPa	
50 % Weibull Probability of the Mechanical Cyclic Lifetime	Stress maximum τ_{max} 30 MPa	3600 cycles	> 5000 cycles
	Stress maximum τ_{max} 40 MPa	220 cycles	8500 cycles
Stress Relaxation (Lap-joint)	Stress Relaxation Level after 60 min., Stress exponent n	100 % → 89 %, 62	100 % → 94 %, 101

Dumbbell shaped specimens of silver sintered without pressure for 30 min. exhibited a mean tensile strength of ca. 14 MPa or 17 MPa when sintered at 230°C, or 300 °C, respectively. Further, the specimens sintered under pressure of 70 MPa for 30 min. at 230 °C showed a mean tensile strength of ca. 56,5 MPa when tested at room temperature. A decrease of ultimate tensile strength was observed for higher testing temperatures of 130 °C and 200 °C. With increase of temperature, the ductility of the material improved changing the brittle fracture characteristics of low temperatures into a ductile behavior at elevated temperature. Tensile strength of ca. 48,5 MPa was measured for the G-Aged specimen, heat treated for 250 hours at 250 °C in sealed glass protection with restricted oxygen content.

The mean shear strength of the Cu-Ag-Cu lap-joints sintered under 70 MPa for 30 min. at 230 °C was ca. 29 MPa for specimens without additional heat treatment. On the other hand, lap-joints heat treated either in air or in sealed glass exhibited mean shear strengths around 33 MPa at room temperature, and showed reduced strengths at 130 °C.

The Young's modulus of the dumbbell shaped samples prepared without heat treatment was measured by a setup including a laser speckle extensometer, which enabled contactless strain measurement of the sintered silver. At room temperature, values of ca. 9 GPa and 5.5 GPa were measured for the specimens sintered pressureless at 230 °C and 300 °C, respectively, and ca. 38 GPa were found for the specimens sintered at 70 MPa at 230 °C for 30 min.
Furthermore, for the purpose of comparing, the Young's modulus was also evaluated over the stress-strain measurement of the tensile strength. In conclusion, samples aged for 250 hours showed a reduced elastic modulus compared to samples, which were not heat treated. A decreasing tendency of the Young's modulus was also observed with increasing test temperature, even more pronounced for the specimens sintered at 230 °C.

For the density measurement of the porous silver two methods were used: the mass/volume method and the optical method of digital image processing. For the latter, to reveal the cross-sectional surface, the samples were either fractured in liquid nitrogen or grinded. A local cut with focused ion beam (FIB) enabled the insight into the porous structure below the surface showing pitch holes of the Ag-layer.

The density obtained from digital image processing applied to the grinded area (2D) of the pressureless sintered silver was ca. 61-63 %, while the density of the grinded area sintered under 70 MPa pressure was evaluated to ca. 88-94 %. For the latter specimens derived by pressure assisted sintering, the FIB cut (3D) showed a density around 94 % for samples without heat treatment or heat treated in air, while between 90 and 94 % density were obtained for samples heat treated under glass protection, i.e. at significantly reduced oxygen. In conclusion, no significant change in density arising from heat treatment at 250°C could be measured with the optical method.

In comparison, lower density values were measured with use of the mass/volume method: 35 % and 42 % Ag-density were found for samples sintered pressureless at 230 °C and 300 °C, respectively. On the other hand, 62 % density were obtained for pressure-assisted sintering. For the former, the pressureless sintered specimens, after ageing at 250 °C for 250 hours, a change in the densities was observed: 48 % density for samples sintered at 230 °C, and 59 % for samples sintered at 300 °C.

The electrical measurements delivered increasing resistivity with increasing porosity: ca. 70 nΩm and 58 nΩm for at 230 °C and 300 °C pressureless sintered specimens, respectively, and ca. 30 nΩm for samples sintered with pressure assistance at 230°C, all electrically measured at room temperature. With increasing testing temperature (200 °C) an increase of the electrical resistivity was observed, as expected.

The mechanical cyclic lifetime was determined for various specimens of the Cu-Ag-Cu lap-joints sintered at 230 °C, for 30 min. or 60 min., under 25 MPa or under 70 MPa. Finally, the samples of which the copper substrate was pre-sputtered with a thin Ag-layer, then stencil printed with Ag-paste and sintered at 70 MPa and 230 °C for 30 min. were selected for the main test series. The fatigue behaviour of samples without heat treatment were compared to 250-hours aged samples at room and elevated temperatures, at a frequency of ca. 0.1 Hz. The number of cycles to failure N_f were analyzed with Weibull probability plots. In general, the cyclic fatigue life was reduced, when samples were tested at 130 °C. However, heat treatment at 250 °C prior to mechanical testing room temperature improved the cyclic lifetime of lap-joints significantly.

The creep properties of the defined pressureless and pressure assisted sintered samples were examined with stress relaxation experiments at 25 °C, 130 °C and 200 °C. For this purpose, the samples were stretched to defined stress levels, depending on the ultimate strength of the specimen series, and the stress relaxation was observed for over an hour.
The dumbbell shaped samples of the pressureless sintered series A and B, and samples of the series C sintered with pressure, were stressed in tensile mode. For the latter specimens, a more distinguished relaxation characteristic was observed at room temperature. At elevated temperatures, the behaviour was reversed; the A and B series showed a steeper relaxation slope.
For the lap-joints, of which the sintering parameter correspond to the C-series, the stress relaxation was measured in shear mode. The as sintered 0-hour samples showed a higher relaxation rate compared to the 250-hours A-Aged samples for testing at room and elevated temperatures.

The values for the stress exponent n were evaluated to compare the inclination of the relaxation. Thereby, the temperature dependence was described by an Arrhenius term using an activation energy Q for sintered silver of 133 kJ/(mol K).

The results of the performed tests and analyses could be fitted by the parameters of a theoretical material model based on a combination of Norton creep and Gurson plasticity.
The constitutive equations of the model describe the creep properties of sintered silver in dependence of its porosity. The material model was implemented in the commercial software of ABAQUS through user subroutine UMAT and can now be used as helpful tool for reliability assessment of Ag-sintered copper joints.

To sum up, Ag sintering is a lead-free alternative interconnection technology with a relatively well matching CTE with copper, which is commonly used in power modules as DCB boards. In addition to high electrical and thermal conductivity, silver with its high melting temperature in comparison to conventional solder alloys is a promising material for applications with elevated temperature.
This thesis followed systematic experiments to elaborate temperature dependent behaviour and mechanical properties of the sintered, porous silver. Statical and cyclic characteristics are investigated. Results could be implemented in finite element simulation for material modeling. Fatigue lifetime was determined for a selected test speed; further interest lies in research at various (especially lower) strain rates (at elevated temperatures).

REFERENCES

[1] Z. Gökdeniz, G. Khatibi, T. Walter and J. Nicolics: **"*Temperature Dependent Mechanical Properties of Sintered Silver-Copper Joints*"**; IEEE, 41st International Spring Seminar on Electronics Technology (ISSE) 2018, pp.1-6.

[2] Z. Gökdeniz, G. Khatibi, J. Nicolics and A. Steiger-Thirsfeld: **"*Behaviour of Silver-Sintered Joints by Cyclic Mechanical Loading and Influence of Temperature*"**; IEEE, 22nd European Microelectronics and Packaging Conference & Exhibition (EMPC) 2019, pp.1-6.

[3] Gökdeniz, Zeynep; Khatibi, Golta; Nicolics, Johann: **"*Low-cycle fatigue of low-temperature sintered Ag interconnections*"**; **"*Ermüdungsverhalten hoch-belasteter Ag-Sinterverbindungen*"**; Elektronische Baugruppe und Leiterplatten (EBL), 10.DVS/GMM-Tagung 18-19 Feb. 2020, Tagungsband GMM-Fb. 94: EBL 2020.

[4] Z. G. Gökdeniz, G. Khatibi, C. Gierl-Mayer, A. Steiger-Thirsfeld and M. Mündlein: **"*Temperature Dependent Physical Properties of Sintered Silver Layers for Power Electronics*"**; IEEE, 43rd International Spring Seminar on Electronics Technology (ISSE) 2020, pp. 1-8.

[5] Z. Gökce Gökdeniz, M. Lederer, G. Khatibi and J. Nicolics: **"*Temperature Dependent Relaxation Behavior of Pressureless and Pressure Assisted Sintered Silver*"**; IEEE, 44rd International Spring Seminar on Electronics Technology (ISSE) 2021, pp.1-6.

[6] Z. G. Gökdeniz, M. Lederer, G. Khatibi and J. Nicolics: **"*Temperature Dependent Relaxation Behavior of Ag-Sintered Copper Joints*"**; IEEE, 23nd European Microelectronics and Packaging Conference & Exhibition (EMPC) 2021, pp.1-5.

[7] M. Lederer, Z. Gökdeniz, G. Khatibi, J. Nicolics: **"*Constitutive equations for strain rate and temperature dependent mechanical behaviour of porous Ag-sintered joints in electronic packages*"**; Microelectronics Reliability, Volume 126, 114209, November 2021, 114209, ISSN 0026-2714.

[8] M. Lederer, Z. Gökdeniz, G. Khatibi, J. Nicolics: **"*Temperaturabhängigkeit mechanischer Eigenschaften von Niedertemperatur-Silber-Sinterschichten und deren Modellierung für die Nutzung in Finite-Elemente-Simulationen*"**; Elektronische Baugruppe und Leiterplatten (EBL), 11.DVS/GMM-Tagung 02-03 Mar. 2022, Tagungsband.

[9] Kim S.Siow: "**Die-Attach Materials for High Temperature Applications in Microelectronics Packaging; Materials**"; Processes, Equipment, and Reliability", Springer 2019.

[10] Gerhard Fasching: "**Werkstoffe für die Elektrotechnik: Mikrophysik, Struktur, Eigenschaften**"; ISBN 3-211-22133-6 SpringerWienNewYork, 4.Auflage 2005, p182.

[11] John H. Lau: **"State of the Art of Lead-Free Solder Joint Reliability"**; ASME. J. Electron. Packag. June 2021; 143(2): 020803.

[12] Arunachalam Lakshmanan: **"Sintering Techniques of Materials"**; IntechOpen, 2015, http://dx.doi.org/10.5772/58496

[13] Dagdelen T, Abdel-Rahman E, Yavuz M.: **"Reliability Criteria for Thick Bonding Wire"**; Materials (Basel). 2018 Apr 17;11(4):618.

[14] DA5 Customer Presentation 2021 06 04, www.infineon.com/dgdl/DA5_customer_presentation_1612016.pdf?fileId=5546d4616102d26701610905cfde0005&redirId=63139

[15] Marco Schaal, Markus Klingler, Bernhard Wunderle: **"Silver Sintering in Power Electronics: The State of the Art in Material Characterization and Reliability"**; 7th Electronic System-Integration Technology Conference (ESTC), 2018, 18 p.

[16] Ly May Chew, W. Schmitt, Ch. Schwarzer, J. Nachreiner: **"Micro-silver sinter paste developed for pressure sintering on bare Cu surfaces under air or inert atmosphere"**; IEEE 68th Electronic Components and Technology Conference, ECTC 2018, pp. 323-330.

[17] C. Qian et al.*:* **"Thermal Management on IGBT Power Electronic Devices and Modules"**; in IEEE Access, vol. 6, pp. 12868-12884, 2018

[18] B. J. Baliga: **"The IGBT Device: Physics, Design and Applications of the Insulated Gate Bipolar Transistor"**; Norwich, NY, USA: William Andrew, 2015.

[19] Guofeng Bai: **"Low-Temperature Sintering of Nanoscale Silver Paste for Semiconductor Device Interconnection"**; PhD (Materials Science and Engineering), Department of Materials Science and Engineering, Virginia Polytechnic Institute and State University Blacksburg, Virginia, October 2005, p.46.

[20] Suk-Joong L.Kang: **"Sintering Densification, Grain Growth, and Microstructure"**; 2005, https://doi.org/10.1016/B978-0-7506-6385-4.X5000-6

[21] Chen, C., Yeom, J., Choe, C. et al.: **"Necking growth and mechanical properties of sintered Ag particles with different shapes under air and N_2 atmosphere"**; J Mater Sci 54, 13344–13357, 2019.

[22] P.C. Angelo, R. Subramanian: **"Powder Metallurgy; Science, Technology and Applications"**; PHI Learning, New-Delhi, 2009, p.127.

[23] Zhang Lei et al.: **"Effect of the Silver with Different Morphologies on the Performance of Electrically Conductive Adhesives";** Rare Metal Materials and Engineering, Volume49, Issue5, May 2020.

[24] Hanpin Lim, Stephen W Hoag: **"Plasticizer Effects on Physical–Mechanical Properties of Solvent Cast Soluplus® Films";** AAPS PharmSciTech, May 2013.

[25] W. H. Bang, K. H. Oh, J. P. Jung, J. W. Morris, and F. Hua: **"The correlation between stress relaxation and steady-state creep of eutectic Sn-Pb";** J. Electron. Mater., vol. 34, no. 10, pp. 1287–1300, Oct. 2005.

[26] Xin Li et al.: **"Creep properties of low-temperature sintered nano-silver lap shear joints";** Materials Science and Engineering: A, Volume 579, 1 September 2013, Pages 108-113.

[27] Julien MAGNIEN: **"Investigation of Mechanical Behavior and Failure Mechanisms in Miniaturized Solder Interconnects"**; Dissertation, Universität Wien, 2015.

[28] Morrow, J.: **"Cyclic Plastic Strain Energy and Fatigue of Metals"**; Internal Friction, Damping, and Cyclic Plasticity; ASTM Special Technical Publication No. 378, 1964, pp. 45-87.

[29] Günter Lange, Michael Pohl: **"Systematische Beurteilung technischer Schadensfälle"**; 6.Auflage 2014 Wiley-VCH Verlag & Co. KGaA, p278.

[30] Yu Lu, Alice A. Miller, Ruth Hoffmann and Christopher W. Johnson: **"Towards the Automated Verification of Weibull Distributions for System Failure Rates"**; International Workshop on Formal Methods for Industrial Critical Systems and Automated Verification of Critical Systems (FMICS-AVoCS 2016) at: Pisa, Italy; September 2016.

[31] Na Liu et al.: **"Optically-controlled digital electrodeposition of thin-film metals for fabrication of nano-devices"**; Optical Materials Express Vol. 5, Issue 4, pp. 838-848, 2015.

[32] Johanna Zikulnig, Ali Roshanghias, Lukas Rauter and Christina Hirsch: **"Evaluation of the Sheet Resistance of Inkjet-PrintedAg-Layers on Flexible, Uncoated Paper SubstratesUsing Van-der-Pauw's Method"**; Sensors MDPI Published:23 April 2020.

[33] Josef Náhlík, Irena Kašpárková, Přemysl Fitl: **"Study of quantitative influence of sample defects on measurements of resistivity of thin films using van der Pauw method"**; Measurement 44, pp 1968-1979, 2011.

[34] Toru Matsumura, Yuichi Sato: **"A Theoretical Study on Van Der Pauw Measurement Values of Inhomogeneous Compound Semiconductor Thin Films"**; Journal of Modern Physics, Vol.1 No.5, pp. 340-347, November 2010.

[35] L.J. van der Pauw: **"A method of measuring specific resistivity and Hall effect of discs of arbitrary shape"**; *Philips Research Reports* Vol.13.No.1,: 1-9, 1958.

[36] Cheng, Z., Liu, L., Xu, S. et al.: **"Temperature Dependence of Electrical and Thermal Conduction in Single Silver Nanowire"**; Sci Rep 5, 10718, 2015.

[37] Rogachev, A.S., Kuskov, K.V., Moskovskikh, D.O. et al.: **"Effect of mechanical activation on thermal and electrical conductivity of sintered Cu, Cr, and Cu/Cr composite powders"**; Dokl. Phys. 61, 257–260, 2016.

[38] Magdalene Dlapka, Herbert Danninger, Christian Gierl, Björn Lindqvist: **"Pycnometric investigation of the transition between open and closed porosity for different iron based PM materials"**; EuroPM Copenhagen, 2009.

[39] H. F. Fischmeister: **"Powder Metallurgical Review 9 – Characterization of Porous Structures by Stereological Measurements"**; Powder Metallurgy International Vol. 7, No. 4, 1975.

[40] Herbert Danninger et al.: **"Automatic measurement of the effective load bearing cross section A_c in sintered steel"**; Praktische Metallographie / Practical Metallography, Volume 39, Issue 8, August 2002, pp. 414-425.

[41] Herbert Danninger et al.: **"Characterization of Pressed and Sintered Ferrous Materials by Quantitative Fractography"**; Praktische Metallographie / Practical Metallography, Volume 31, Issue 2, 1994, pp. 56-69.

[42] Andrew A. Wereszczak et al.: **"Properties of Bulk Sintered Silver As a Function of Porosity"**; ORNL/TM-2012/130, June 2012.

[43] Andi Wijaya, Barbara Eichinger, Martin Mischitz and Roland Brunner.: **"3D Characterization of Porous Copper Thin Films"**; Microsc. Microanal. 25 (Suppl 2), 2019.

[44] Chuantong Chen, Chanyang Choe, Dongjin Kim, Zheng Zhang, Xu Long, Zheng Zhou, Fengshun Wu, Katsuaki Suganuma: **"Effect of oxygen on microstructural coarsening behaviors and mechanical properties of Ag sinter paste during high-temperature storage from macro to micro"**; Journal of Alloys and Compounds Volume 834, 5 September 2020, 155173.

[45] Chuantong Chen, Shijo Nagao, Katsuaki Suganuma, Jinting Jiu, Hao Zhang, Tohru Sugahara, Tomohito Iwashige, Kazuhiko Sugiura, and Kazuhiro Tsuruta: **"Self-healing of cracks in Ag joining layer for die-attachment in power devices"**; Appl. Phys. Lett. 109, 093503, 2016.

[46] C. Choe, S. Noh, C. Chen, T. Ishina, S. Nagao and K. Suganuma: **"Thermal effect on material properties of sintered porous silver during high temperature ageing"**; *18th International Conference on Electronic Packaging Technology (ICEPT),* 2017, pp. 1492-1496.

[47] Jie Li, Xin Li, LeiWang, Yun-Hui Mei, Guo-Quan Lu: **"A novel multiscale silver paste for die bonding on bare copper by low-temperature pressure-free sintering in air"**; Materials and Design 140 (2018) 64–72.

[48] S. Kırtay and D. Dıspınar: **"Effect of Ranking Selection on the Weibull Modulus Estimation"**; Gazi University Journal of Science, vol. 25, no. 1, pp. 175-187, Jan. 2012

[49] Peter Lorenz, Wolfgang Gattermayr et al.: **"Leitfaden: Verfahren zur Abschätzung von Hochwasserkennwerten"**; Bundesministerium für Land- und Forstwirtschaft, Umwelt und Wasserwirtschaft 1030 Wien, December 2011, info.bml.gv.at/service/publikationen/wasser/Leitfaden--Hochwasserkennwerten.html

[50] Yansong Tan, Xin Li, Xu Chen: **"Fatigue and dwell-fatigue behavior of nano-silver sintered lap-shear joint at elevated temperature"**; Microelectronics Reliability, Volume 54, Issue 3, 2014, Pages 648-653, ISSN 0026-2714.

[51] Keisuke Wakamoto, Yo Mochizuki, Takukazu Otsuka, Ken Nakahara, Takahiro Namazu: **"Tensile mechanical properties of sintered porous silver films and their dependence on porosity"**; Japanese Journal of Applied Physics58, SDDL08 (2019), pp. 1-5.

[52] James Carr, Xavier Milhet, Pascal Gadaud, Severine A.E. Boyer, George E. Thompson, Peter Lee: **"Quantitative characterization of porosity and determination of elastic modulus for sintered micro-silver joints"**; Journal of Materials Processing Technology, Volume 225, 2015, Pages 19-23, ISSN 0924-0136.

[53] Yutai Su, Guicui Fu, Changqing Liu, Kun Zhang, Liguo Zhao, Canyu Liu, Allan Liu, Jianan Song: **"Thermo-elasto-plastic phase-field modelling of mechanical behaviours of sintered**

nano-silver with randomly distributed micro-pores"; Computer Methods in Applied Mechanics and Engineering, Volume 378, 2021, 113729, ISSN 0045-7825.

[54] Signor, L., Kumar, P., Tressou, B., C. Nodor-Martin, Jose´ Miranda-Ordonez, J. Carr, K. Joulain, and X. Milhet: **"Evolution of the Thermal Conductivity of Sintered Silver Joints with their Porosity Predicted by the Finite Element Analysis of Real 3D Microstructures"**; J. Electron. Mater. 47, 4170–4176, 2018.

[55] Keisuke Wakamoto, Yo Mochizuki, Takukazu Otsuka, Ken Nakahara, Takahiro Namazu: **"Temperature Dependance on Tensile Mechanical Properties of Sintered Silver Film"**; *Materials* 2020, *13*(18), 4061.

[56] T. Suzuki *et al.*: **"Effect of Loading Type on Fatigue Lifetime of Sintered-Silver Die Attach"**; in *IEEE Transactions on Device and Materials Reliability,* vol. 18, no. 3, pp. 350-358, Sept. 2018.

[57] Tomofumi Watanabe, Masafumi Takesue, Tomoki Matsuda, Tomokazu Sano, Akio Hirose: **"Thermal stability and characteristic properties of pressureless sintered Ag layers formed with Ag nanoparticles for power device applications"**; J Mater Sci: Mater Electron (2020) vol. 31, pp. 17173–17182.

[58] V. Caccuri, X. Milhet, P. Gadaud, D. Bertheau, and M. Gerland: **"Mechanical Properties of Sintered Ag as a New Material for Die Bonding: Influence of the Density"**; Journal of Electronic Materials, Vol. 43, No. 12, 2014.

[59] P. Gadaud, V. Caccuri, D. Bertheau, J. Carr, X. Milhet: **"Ageing sintered silver: Relationship between tensile behavior, mechanical properties and the nanoporous structure evolution"**; Materials Science & Engineering A, Vol. 669, 2016, pp. 379–386.

[60] Long, X., Guo, Y., Su, Y. et al.: **"Constitutive, creep, and fatigue behavior of sintered Ag for finite element simulation of mechanical reliability: a critical review"**; J Mater Sci: *Mater Electron* **33**, 2293–2309, 2022.

[61] D.J. Yu, C. Xu, C. Gang, G.Q. Lu, Z.Q. Wang: **"Applying Anand model to low-temperature sintered nanoscale silver paste chip attachment"**; Mater. Des. 30(10), 4574–4579, 2009.

[62] W. Tao, C. Gang, Y. Wang, C. Xu, G.Q. Lu: **"Uniaxial ratcheting and fatigue behaviors of low-temperature sintered nanoscale silver paste at room and high temperatures"**; Mater. Sci. Eng. A 527(24–25), 6714–6722, 2010.

[63] Hao Zhang, Chuantong Chen, Jinting Jiu, Shijo Nagao, Katsuaki Suganuma: **"High-temperature reliability of low-temperature and pressureless micron Ag sintered joints for die attachment in high-power device"**; Journal of Materials Science: Materials in Electronics, 2018, 29:8854–8862.

[64] Zheng Zhang, Chuantong Chen, Yang Yang, Hao Zhang, Dongjin Kim, Toru Sugahara, Shijo Nagao, Katsuaki Suganuma: **"Low-temperature and pressureless sinter joining of Cu with micron/ submicron Ag particle paste in air"**; Journal of Alloys and Compounds 780 (2019) 435-442.

[65] Calvin M. Stewart: **"Fatigue Analysis For Extreme Environments, Stress-Life Approach"**; MECH 5390-6390 Presentation, Spring 2021; Shigley's Mechanical Engineering Design.

[66] Cyril Buttay, Dominique Planson, Bruno Allard, Dominique Bergogne, Pascal Bevilacqua, Charles Joubert, Mihai Lazar, Christian Martin, Hervé Morel, Dominique Tournier, Christophe Raynaud: **"State of the art of high temperature power electronics"**; Materials Science and Engineering: B, Volume 176, Issue 4, 2011, Pages 283-288, ISSN 0921-5107

[67] Joachim Rösler, Harald Harders, Martin Bäker, "**Mechanisches Verhalten der Werkstoffe**", 3.Auflage 2008, Vieweg+Teubner | GWV Fachverlage GmbH, Wiesbaden, pp.333.

[68] Rmili, W., Vivet, N., Chupin, S. et al. .: **"Quantitative Analysis of Porosity and Transport Properties by FIB-SEM 3D Imaging of a Solder Based Sintered Silver for a New Microelectronic Component"**; J. Electron. Mater. 45, 2242–2251, 2016.

[69] Khazaka, R., Mendizabal, L. & Henry, D.: **"Review on Joint Shear Strength of Nano-Silver Paste and Its Long-Term High Temperature Reliability"**; J. Electron. Mater. 43, 2459–2466, 2014.

[70] X. Li, X. Chen, D. Yu, and G-Q. Lu, 11th International Conference on Electronic Packaging Technology & High Density Packaging, 2010.

[71] P. Ning, Ph.D. thesis at the faculty of the Virginia Polytechnic, 2010.

[72] G-Q. Lu, J.N. Calata, and G. Lei, IEEE 8th International Conference on Thermal, Mechanical and Multiphysics Simulation and Experiments in Micro-Electronics and Micro-Systems, EuroSime 2007, pp. 609–613.

[73] N. Heuck, S. Muller, G. Palm, A. Bakin, and A. Waag, IMAPS International Conference and Exhibition on High Temperature Electronics (HITEC), 2010.

[74] Richard G. Budynas and J. Keith Nisbett: **"Shigley's Mechanical Engineering Design"**; Ninth edition, Physical Constant of Materials.

[75] Smith DR, Fickett FR.: **"Low-Temperature Properties of Silver"**; J Res Natl Inst Stand Technol. 1995 Mar-Apr, 100(2):119-171, DOI: 10.6028/jres.100.012; H. Ledbetter, private communication (Ref.134).

[76] Smith DR, Fickett FR.: **"Low-Temperature Properties of Silver"**; J Res Natl Inst Stand Technol. 1995 Mar-Apr, 100(2):119-171, DOI: 10.6028/jres.100.012; J. R. Neighbours and G. A. Alers, Phys. Rev. 111, 707 (1958).

[77] Georgi Genov: **"Revisiting the Rule-of-Thumb Dependencies of the Shear Strength and the Hardness on the Yield and Ultimate Strengths"**; Journal of Materials Research and Technology 17.11.2020, DOI:10.13140/RG.2.2.24105.72807

[78] www.substech.com/dokuwiki/doku.php?id=fine_silver; 30/10/2022.

APPENDIX

A.1. FRACTURE BEHAVIOUR OF THE SINTERED LAP-JOINTS

This chapter intends to give an overview over the fracture characteristics of the Cu-Ag-Cu lap-joints being sheared either by monotonic shear testing or cycling loading at room temperature (RT) or above 130 °C. To reveal the main bonds of the carrier area a couple of samples, 0-hour and A-Aged, were ruptured in liquid nitrogen. Samples have been prepared, named, and tested as described in chapter 3. The microscopic images of the fracture surfaces for the sample series 0-hour, G-Aged, and A-Aged are shown in the figures of the following sections.

Mainly two fracture pathways have been observed. One type starting on the copper-silver interface and then mainly going through the stencil printed and sintered Ag-paste as drawn in Fig.A.1.1.a. This might base on the rather high interfacial strength created due to binding oxidation layer between sintered silver and copper. Another type of fracture starting at the Cu-Ag interface and then mainly following it along as drawn in Fig.A.1.1.b. On the fracture surface,

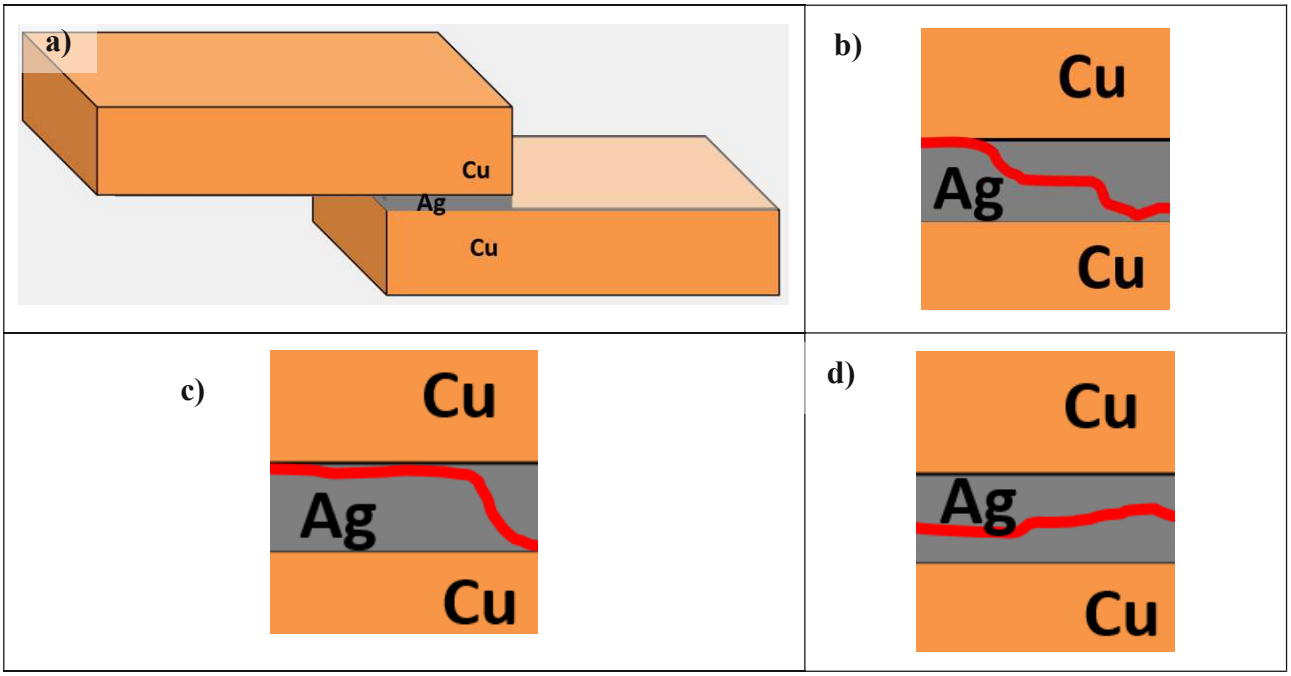

Fig. A.1.1: Sketch of the lap-joint (a) and main fracture propagation types FP-1 (b), FP-2 (c), and FP-3 (d) for the sintered silver interface.

when there was a rupture between the copper and silver interface, the stencil printed Ag-layer of one side detached from the Cu-interface and added on to the sintered silver layer of the other side. To mark this condition of the silver after shearing the notation Ag+ have been used in some of the microscopic pictures.

In some samples there was also a third kind of miscellaneous crack propagation throughout the porous silver as in Fig.A.1.1.c. These three types have been named as FP-1, FP-2 and FT-3. The investigated samples have been categorized correspondent to the surface fracture and listed accordingly in the Table A.1.1 to outline the distribution.

Table A.1.1: Fracture Propagation Types and Distribution of the Investigated Samples

	FP-1	**FP-2**	**FP-3**
Fracture in Liquid Nitrogen			
SHEAR @ 25 °C, 0-hour	(PTS 72)	(PTS 32) (PTS 106) (PTS 189) (PTS 196)	(PTS 182)
SHEAR @ 25 °C, G-Aged	(PTS 163)		
SHEAR @ 25 °C, A-Aged	(PTS 150)		
SHEAR @ 130 °C, A-Aged	(PTS 262) (PTS 179)		(PTS 179)
CYCLIC @ 25 °C, 0-hour	(PTS 17) (PTS 93) (PTS 68)	(PTS 97) (PTS 35) (PTS 200) (PT 59) (PT 06)	(PTS 73) (PT 05) (PT 02)
CYCLIC @ 25 °C, A-Aged	(PTS 102)		
CYCLIC @ 130 °C, 0-hour		(PTS 49)	(PTS 45)

FRACTURE TOPOGRAPHY OF SAMPLES RUPTURED IN LIQUID NITROGEN

Fracture @ -196 °C, 0-hour

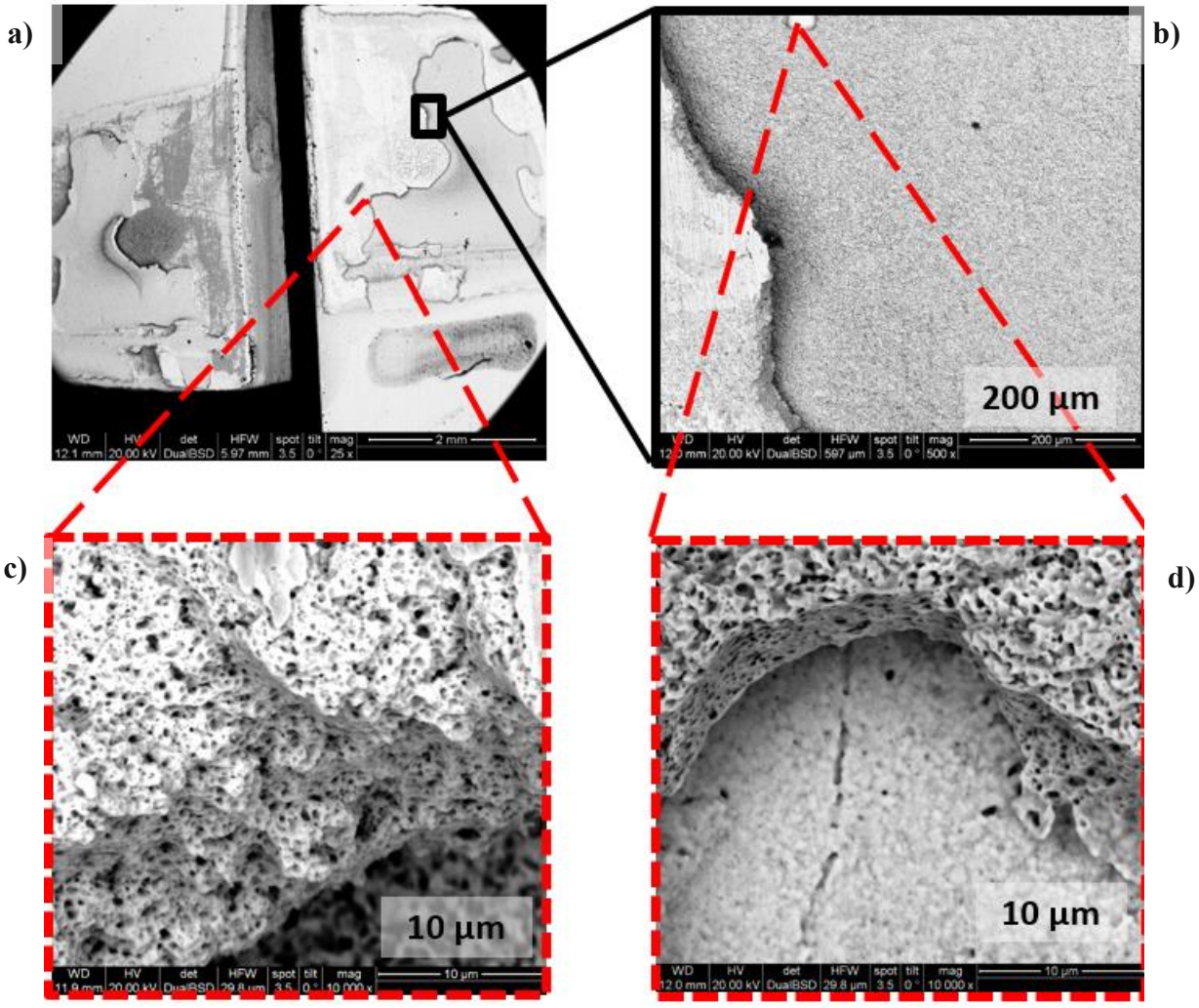

Fig. A.1.2: Fracture surface of an 0-hour PTS-type sample breached in liquid nitrogen (a) showing the SEM image of one part (b) at the top side (c) and bottom side (d) of the sintered silver.

Fracture @ -196 °C, A-Aged

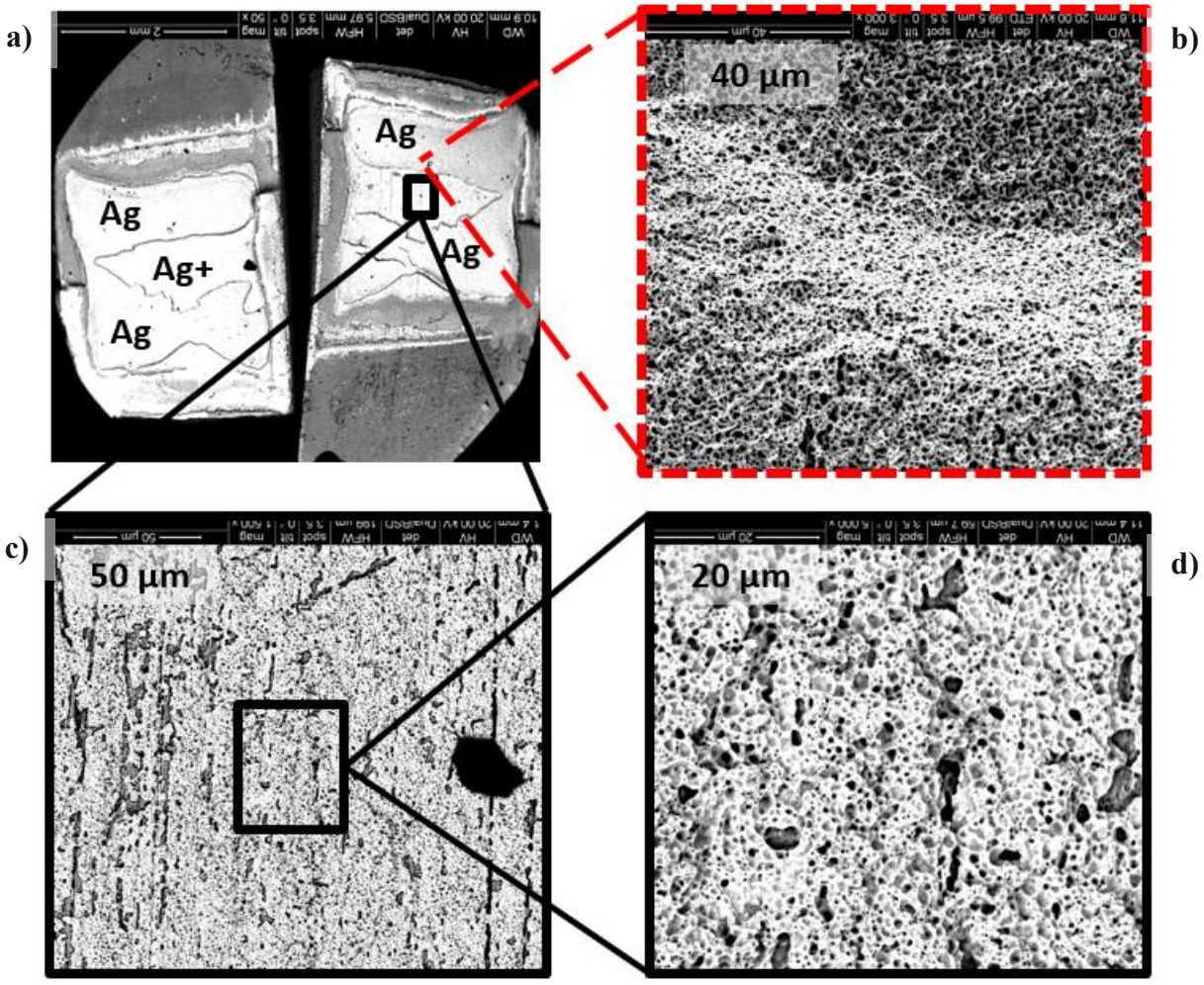

Fig. A.1.3: Fracture surface of an PTS-type sample, which has been thermal treated at 250 °C for 250 hours, ruptured in liquid nitrogen (a) with SEM images from the sintered silver bulk interface (b) and from the bottom copper-silver junction (c-d) at various magnifications.

SHEAR

Shear @ 25 °C, 0-hour

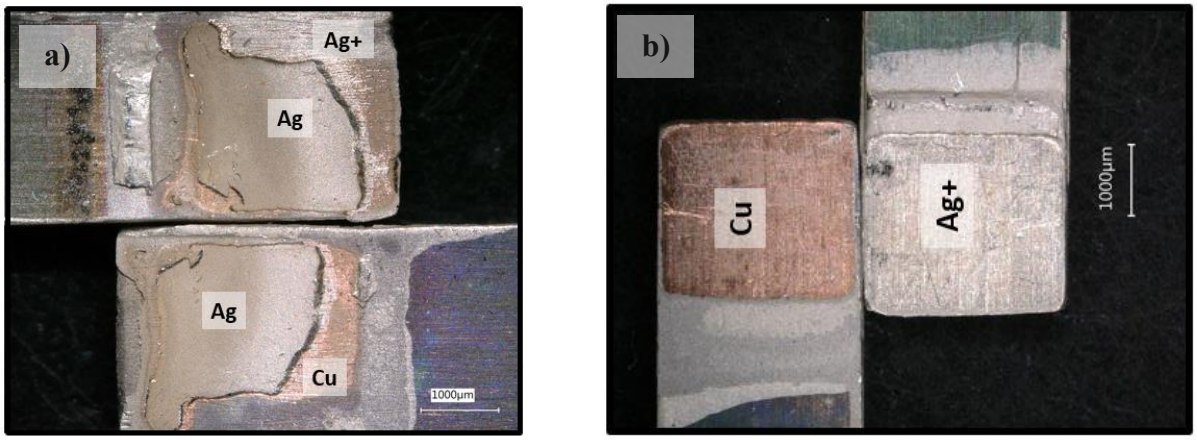

Fig. A.1.4: Microscopic images of two lap-joint samples for fracture characteristic FP-1 (a) and FP-2 (b).

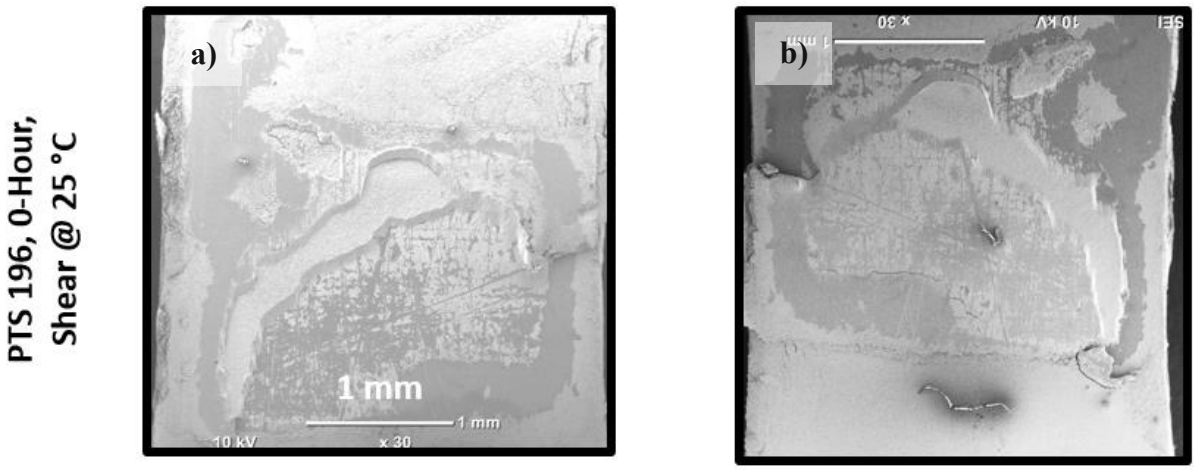

Fig. A.1.5: SEM images of the fracture surfaces from both sides (a-b) of the lap-joint at the same magnification.

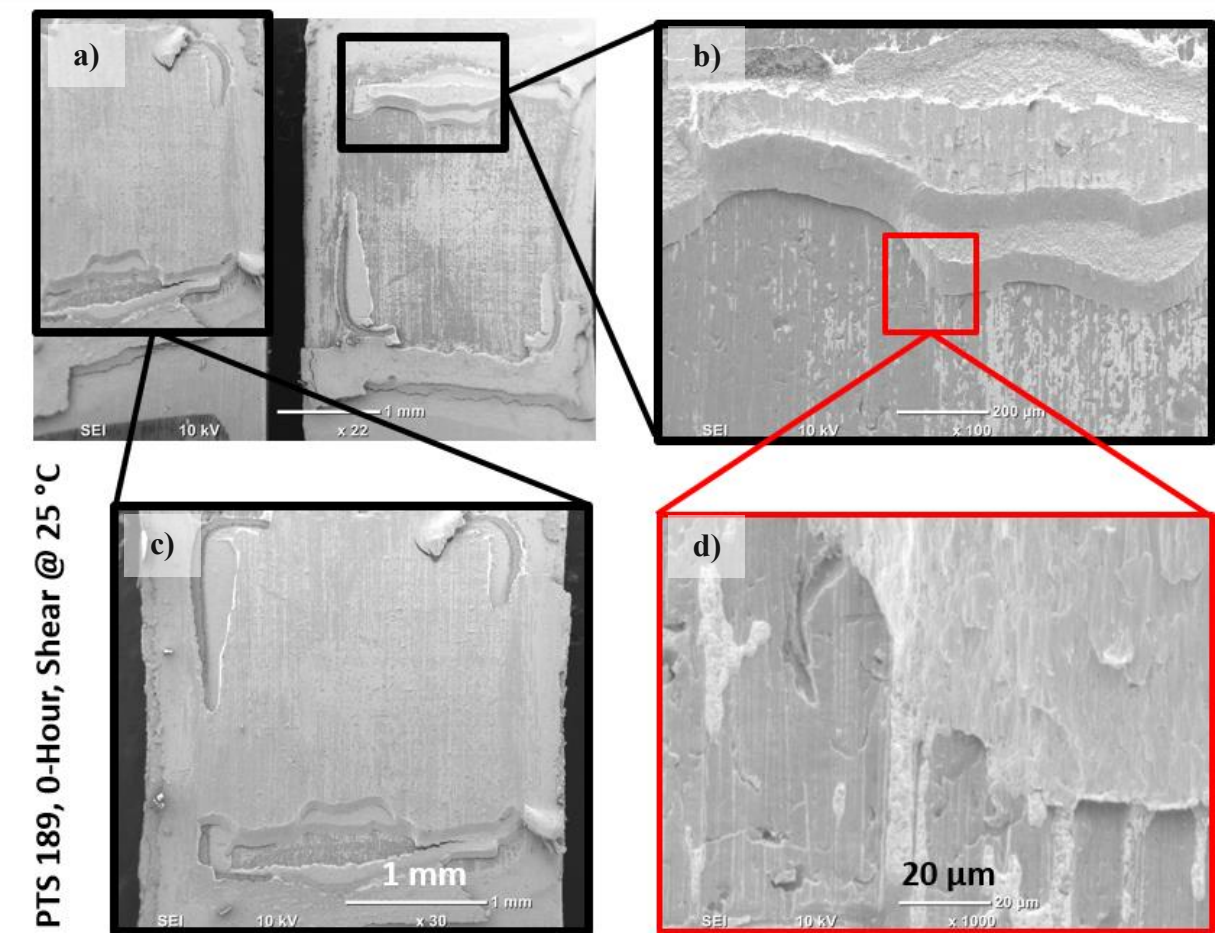

Fig. A.1.6: SEM image from both sides of the lap-joint (a) and various magnifications of the fracture surfaces (b-d).

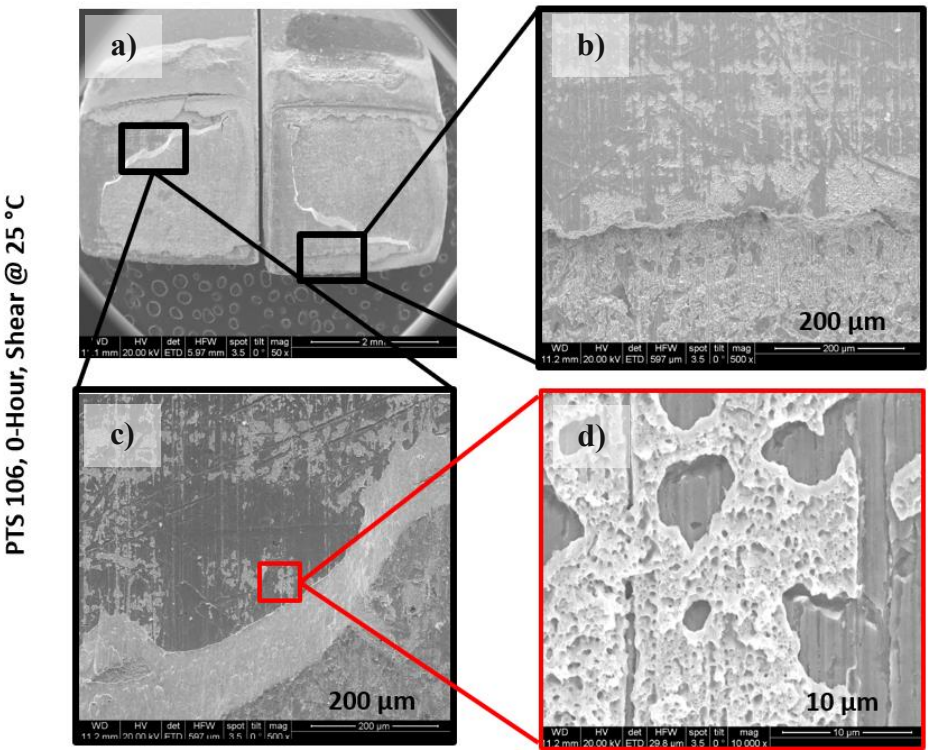

Fig. A.1.7: SEM image from both sides of the lap-joint (a) and various magnifications of the fracture surfaces (b-d).

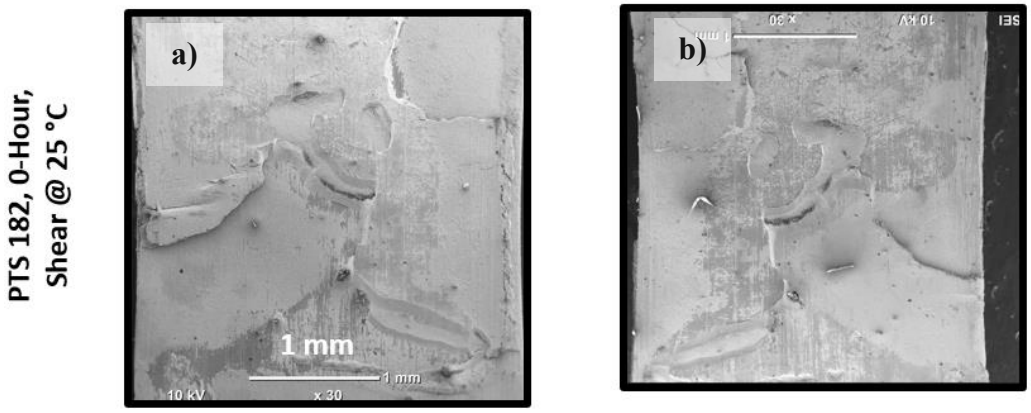

Fig. A.1.8: SEM images of the fracture surfaces from both sides (a-b) of the lap-joint at the same magnification.

Shear @ 25 °C, G-Aged

PTS 163, G-Aged, Shear @ 25 °C

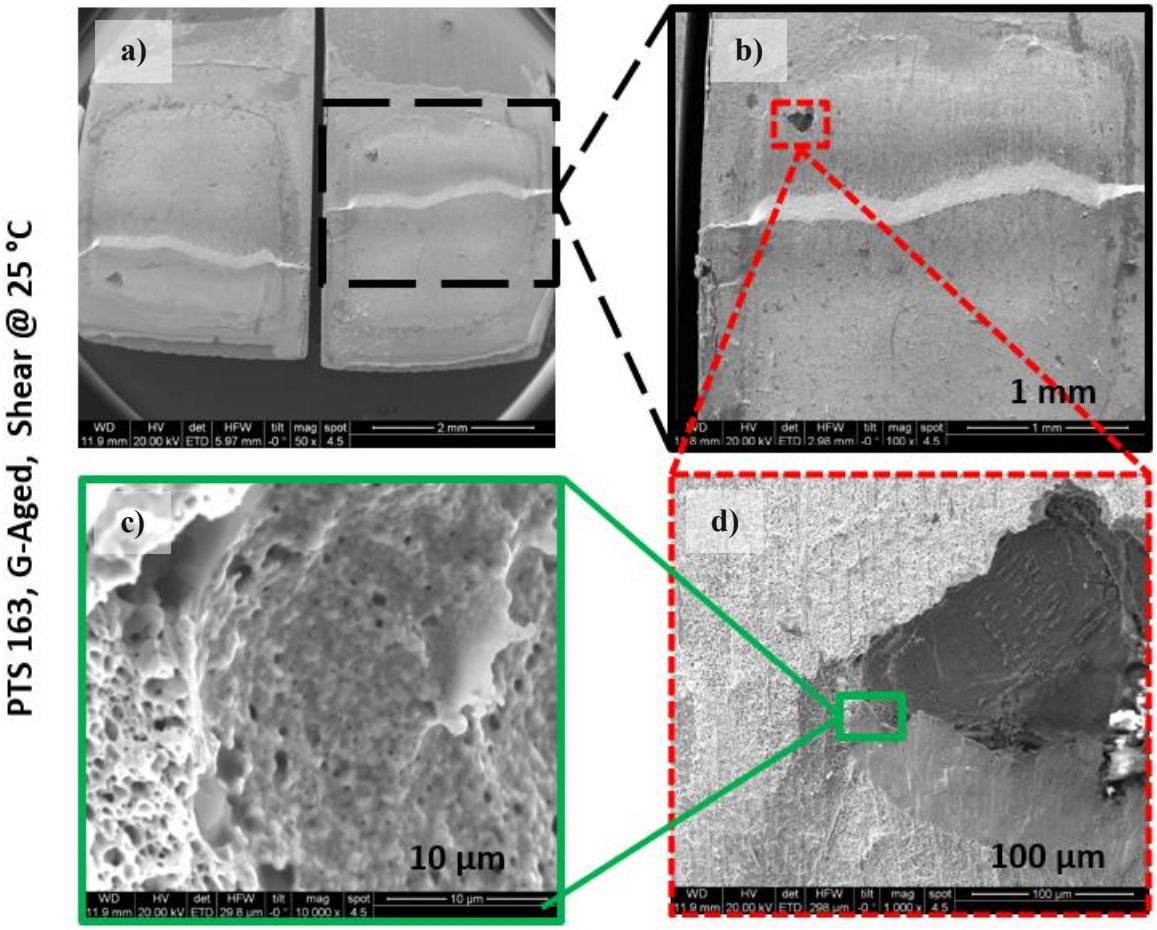

Fig. A.1.9: SEM images from the sheared lap-joint (a) and of the fracture surface at various magnifications (b-d).

Shear @ 25 °C, A-Aged

PTS 150, A-Aged, Shear @ 25 °C

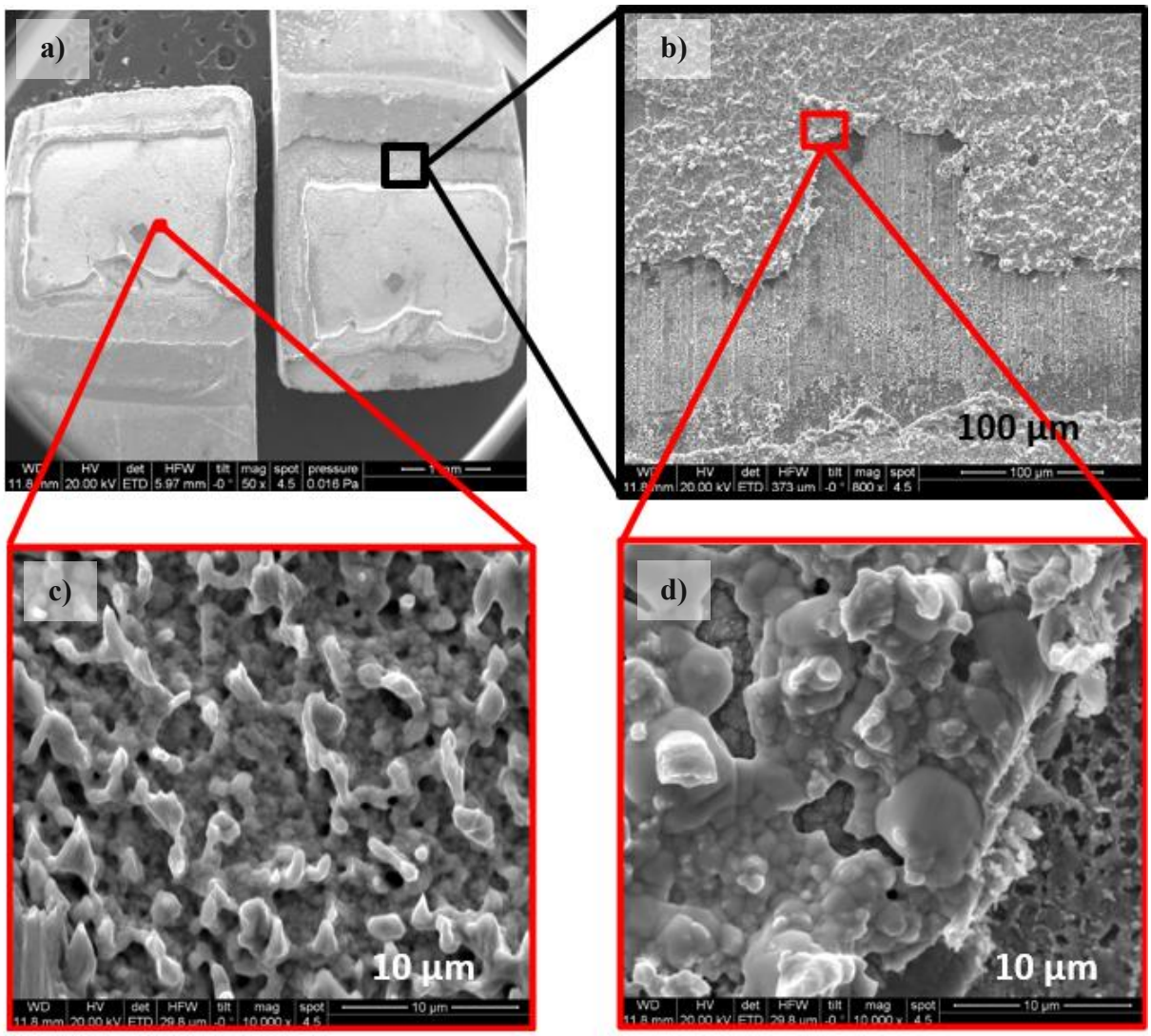

Fig. A.1.10: SEM images from the sheared lap-joint (a) and of the fracture surfaces (b-d) at various magnifications.

Shear @ 130 °C, A-Aged

PTS 179, A-Aged, Shear @ 130 °C

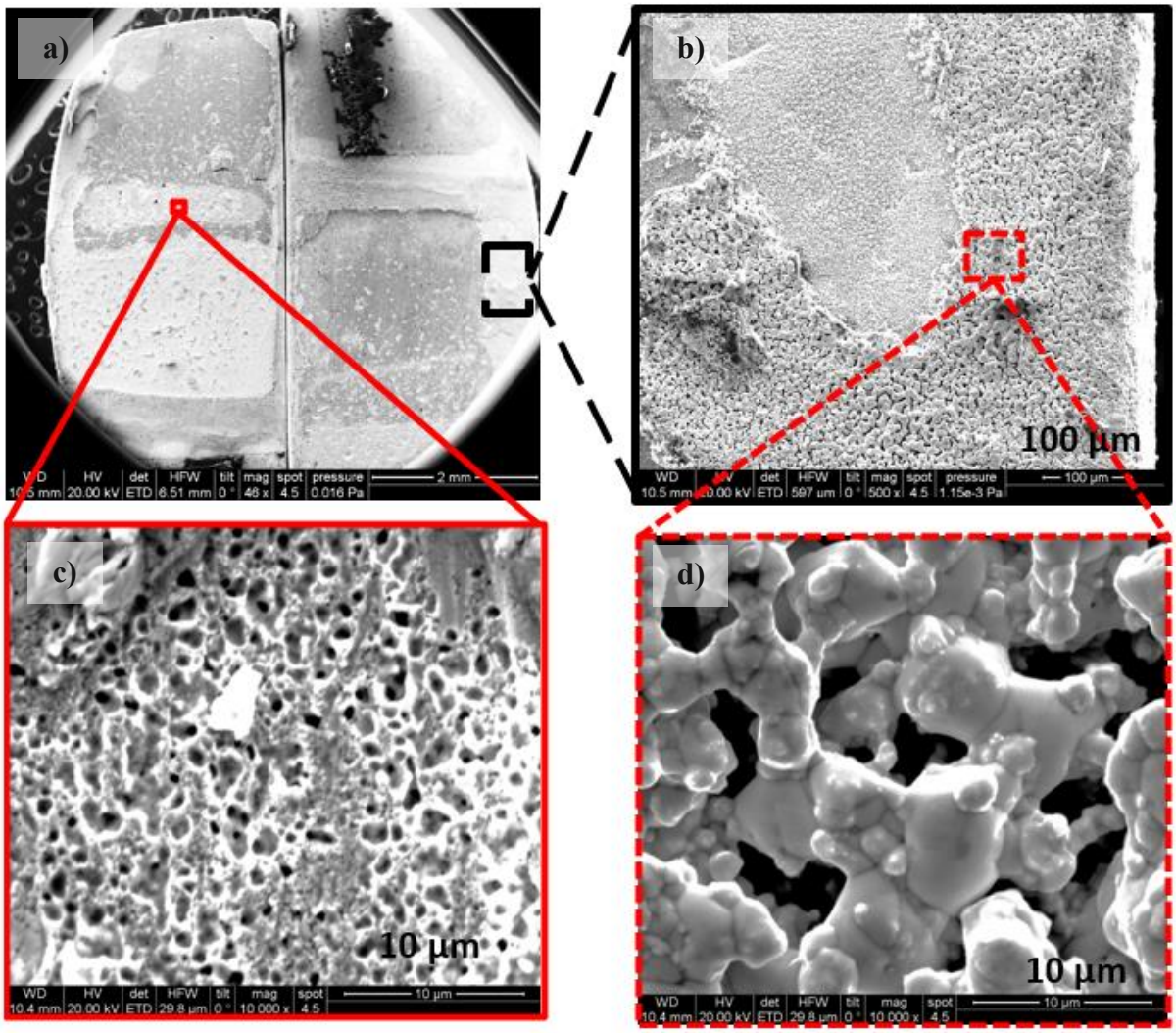

Fig. A.1.11: SEM images from the sheared lap-joint (a) and various magnifications of the fracture surfaces (b-d).

PTS 262, A-Aged, Shear @ 130 °C

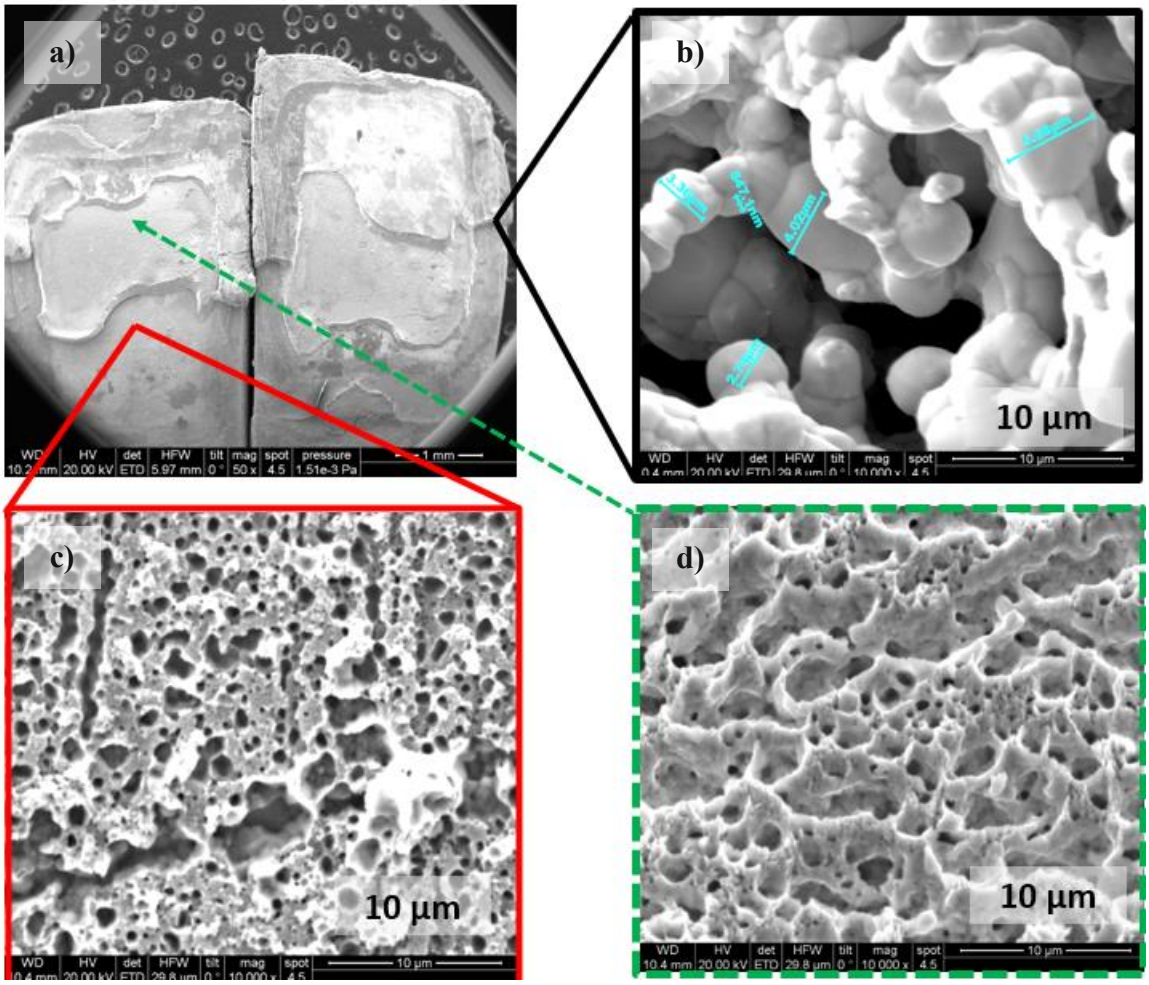

Fig. A.1.12: SEM images from the sheared lap-joint (a) and the fracture surfaces on the corner (b), on the Cu-Ag interface (c), and in the middle of the sintered silver (d) all at the magnification of 10K.

CYCLIC

Cyclic @ 25 °C, 0-hour

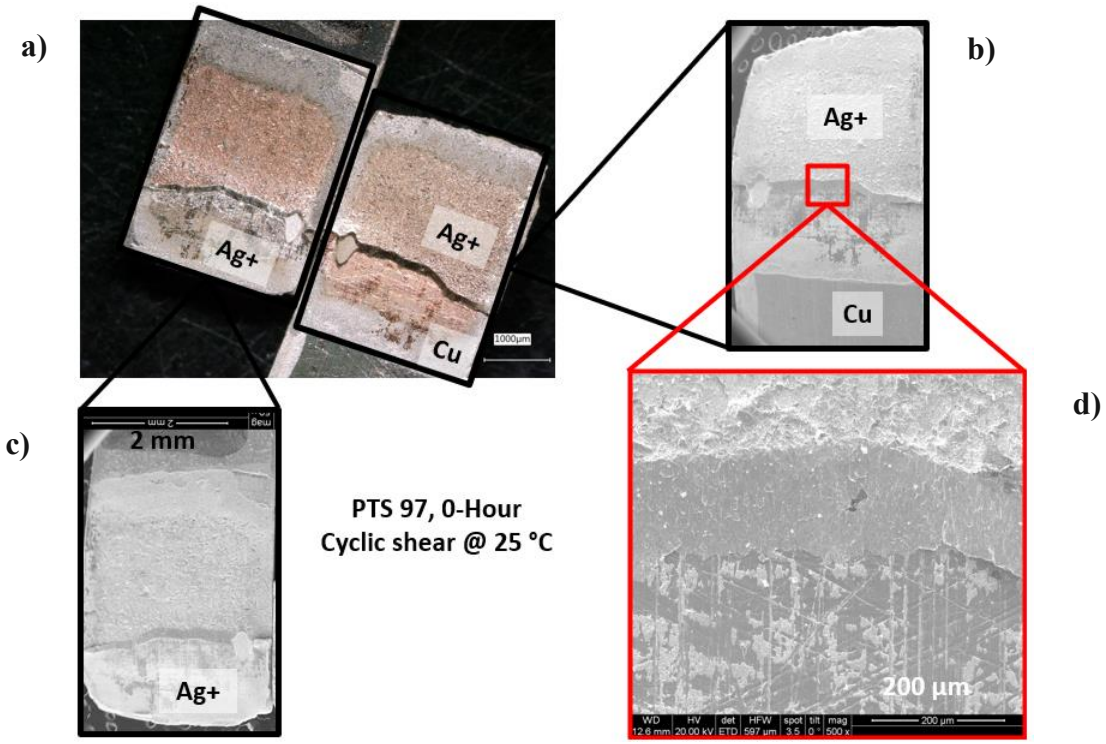

Fig. A.1.13: Microscopic image from the lap-joint (a) and SEM images of the fracture surfaces at various magnifications (b-d).

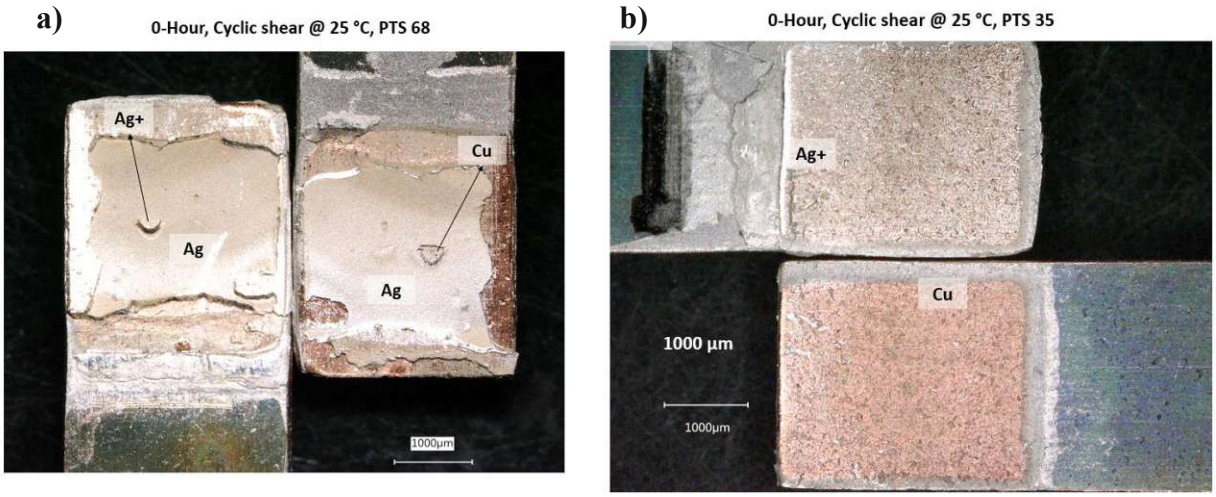

Fig. A.1.14: Microscopic images from two lap-joints (a-b) showing the fracture surfaces.

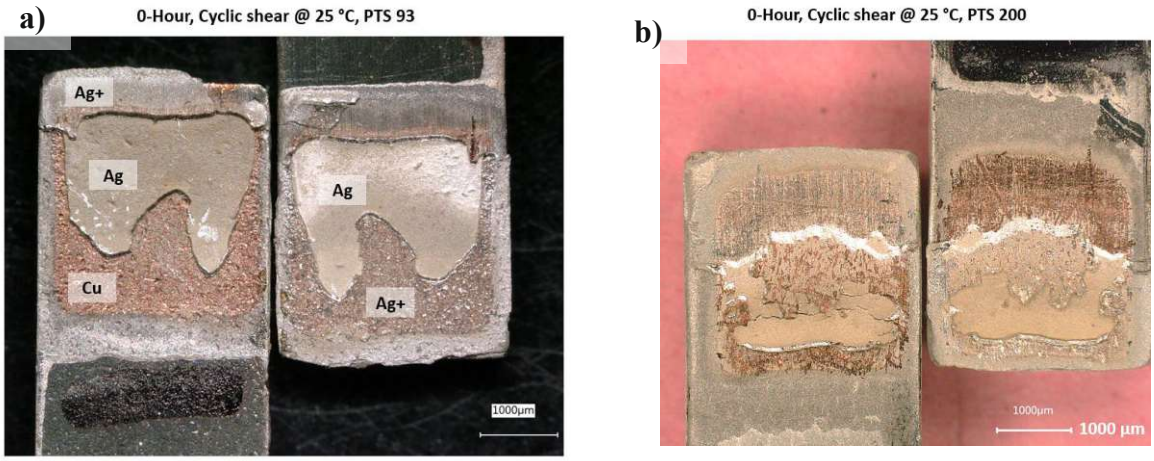

Fig. A.1.15: Microscopic images from two lap-joints (a-b) showing the fracture surfaces.

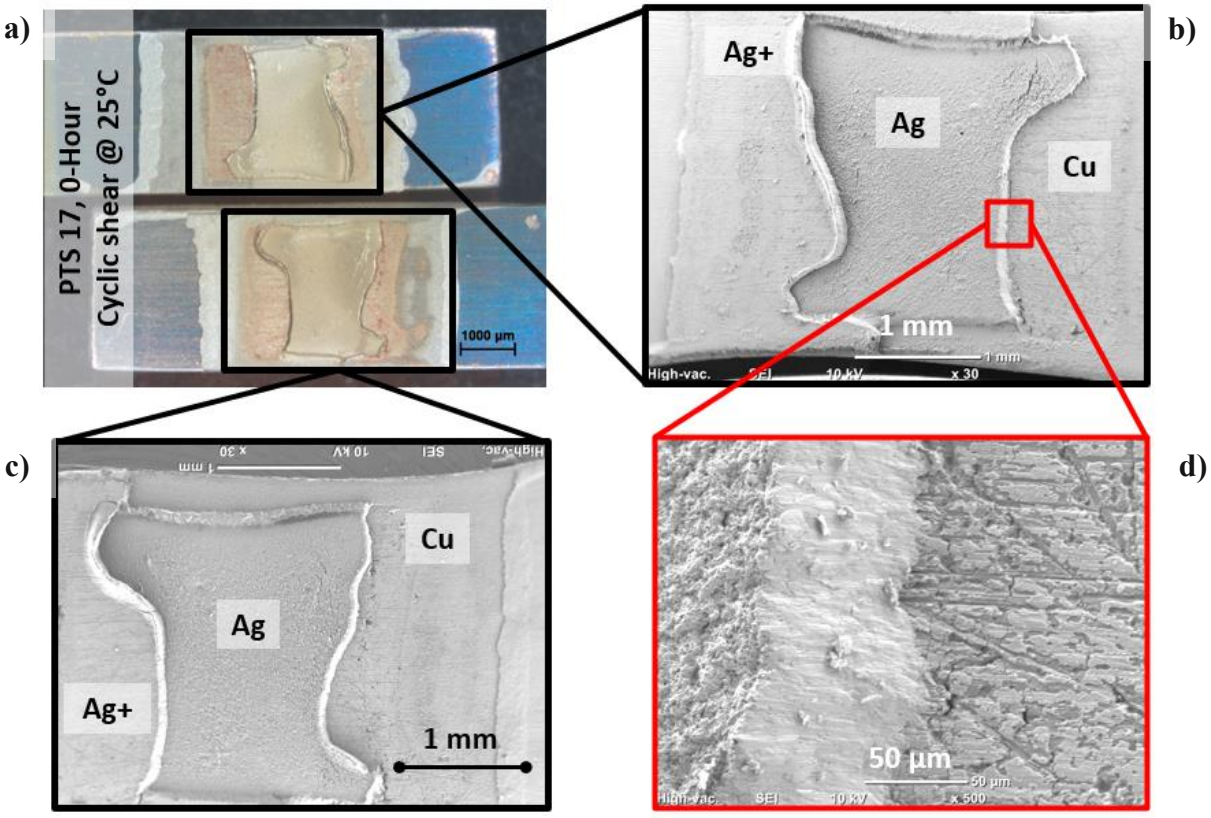

Fig. A.1.16: Microscopic image from the lap-joint (a) and SEM images of the fracture surfaces at various magnifications (b-d).

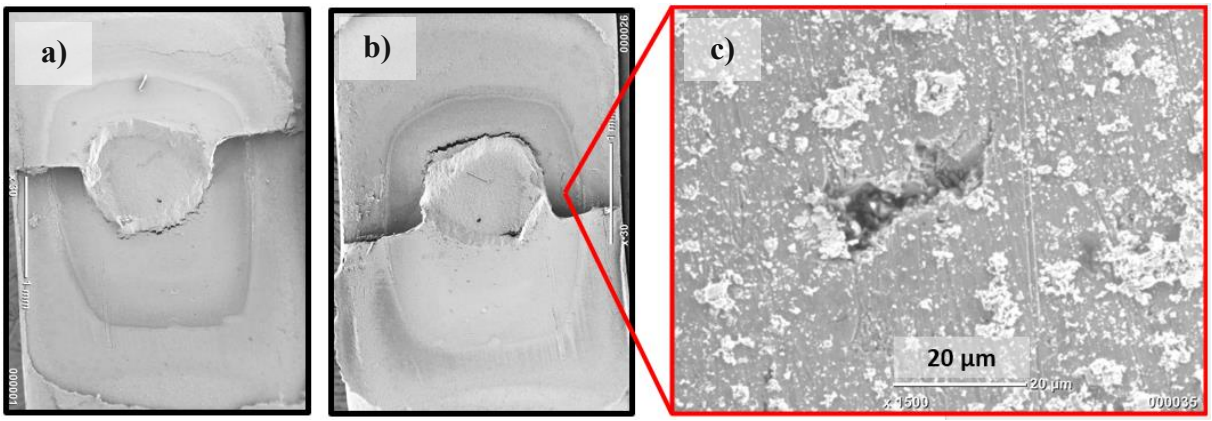

Fig. A.1.17: SEM images from both sides of the sheared lap-joint (a-b) and magnified fracture surface on the copper side (c).

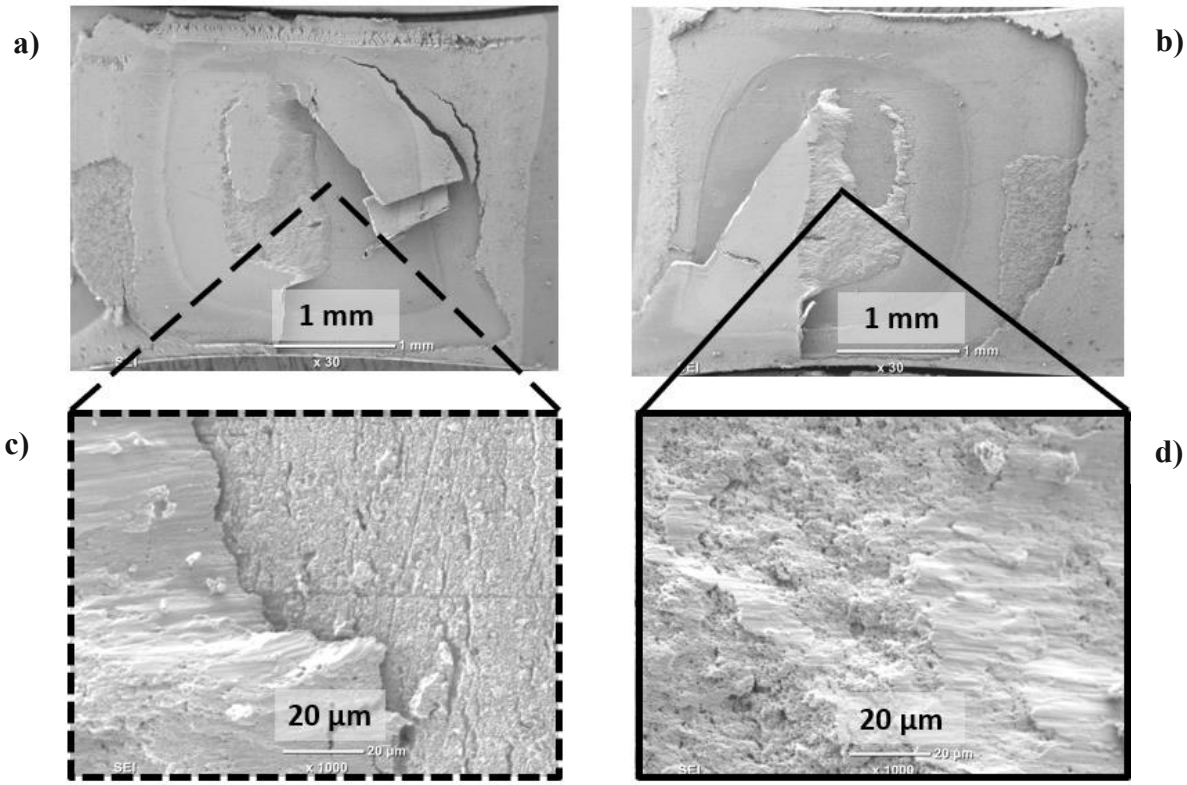

Fig. A.1.18: SEM images from both sides of the lap-joint (a-b), magnified fracture surface on the copper side (c) and shear surface of the sintered silver (d).

Cyclic @ 25 °C, A-Aged

PTS 102, A-Aged, Cyclic shear @ 25 °C

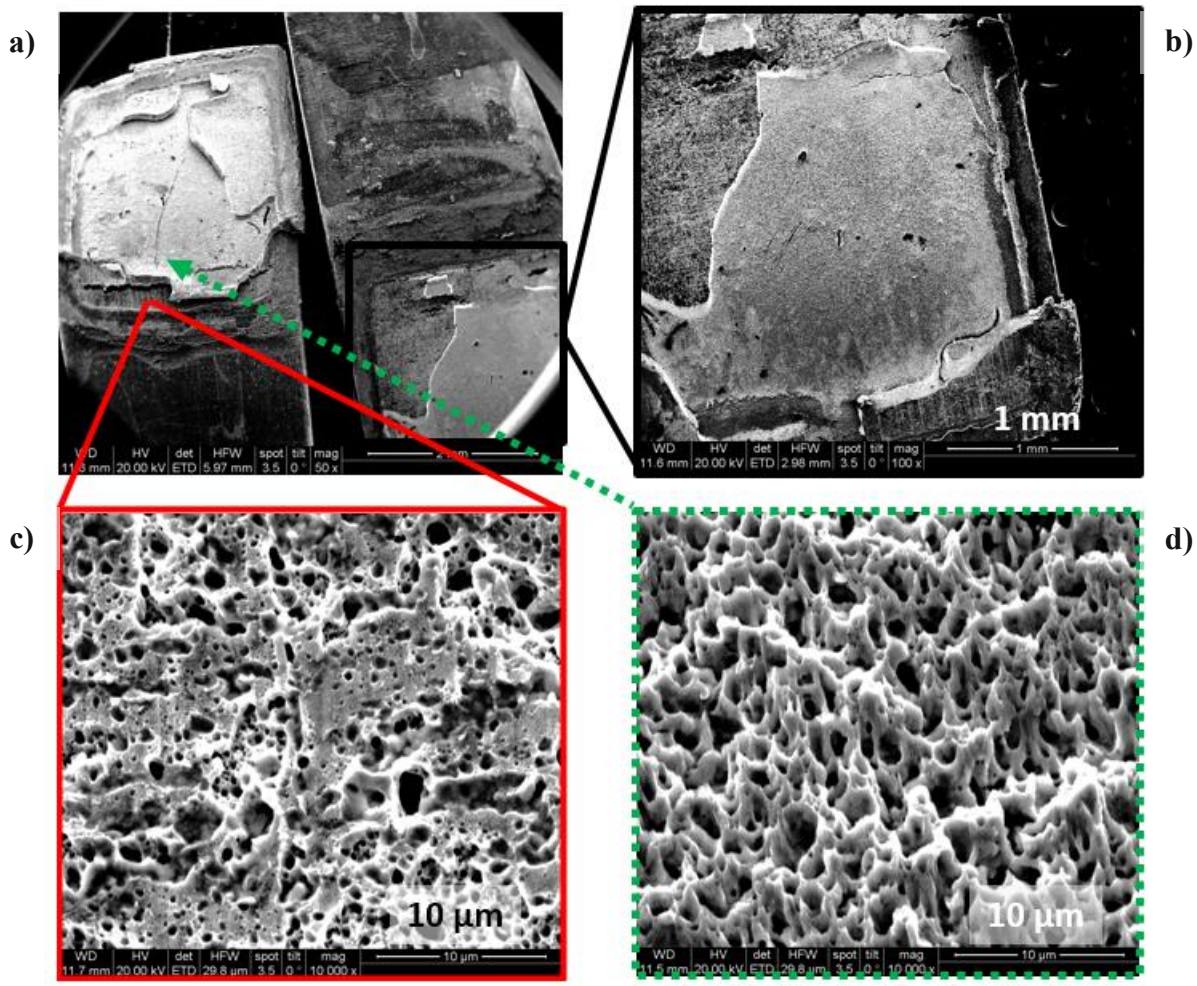

Fig. A.1.19: SEM images from the lap-joint (a) and of the fracture surfaces at various magnifications (b-d).

Cyclic @ 130 °C, 0-hour

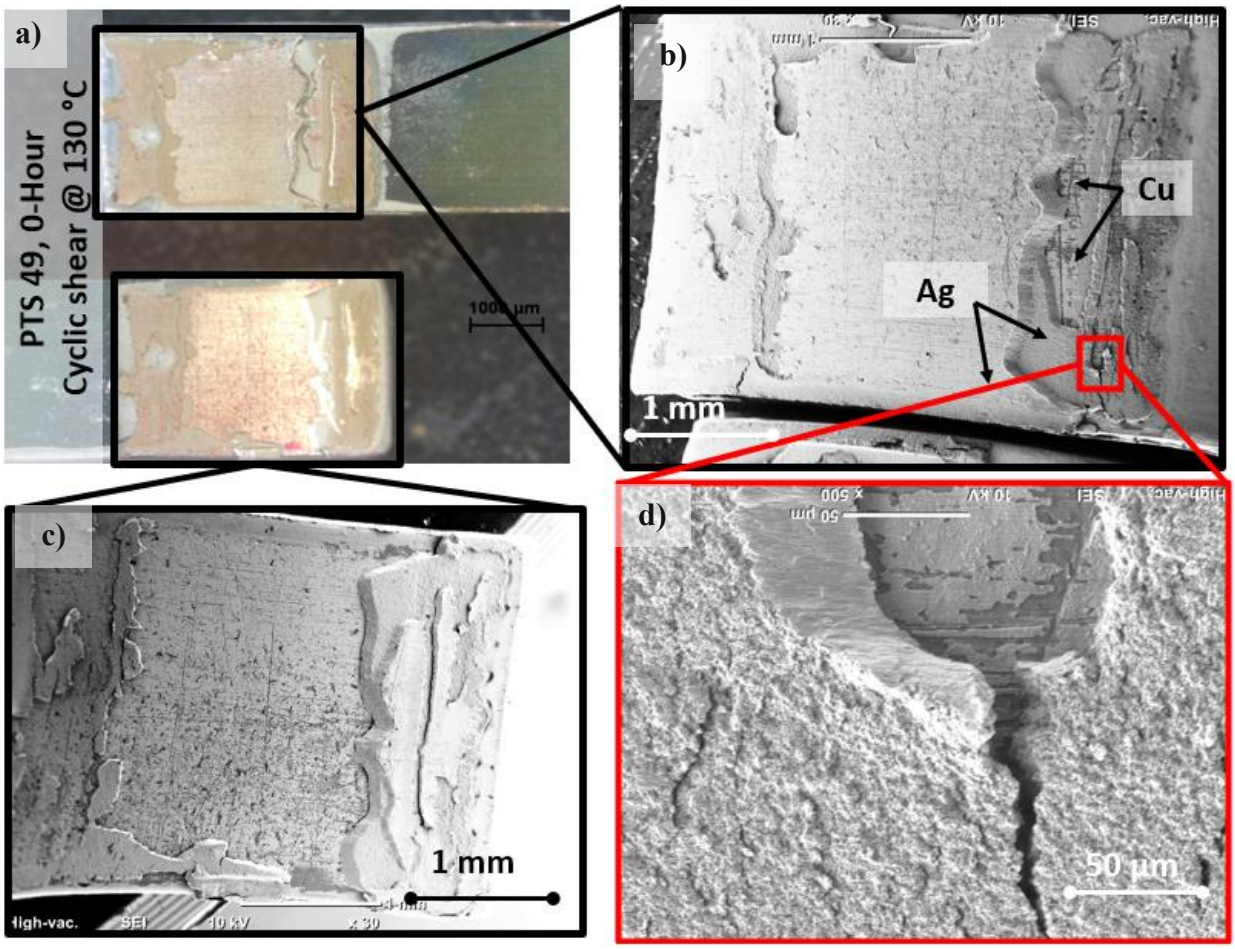

Fig. A.1.20: Microscopic image from the lap-joint (a) and SEM images of the fracture surfaces at various magnifications (b-d).

PTS 45, 0-hour, Cyclic @ 130 °C

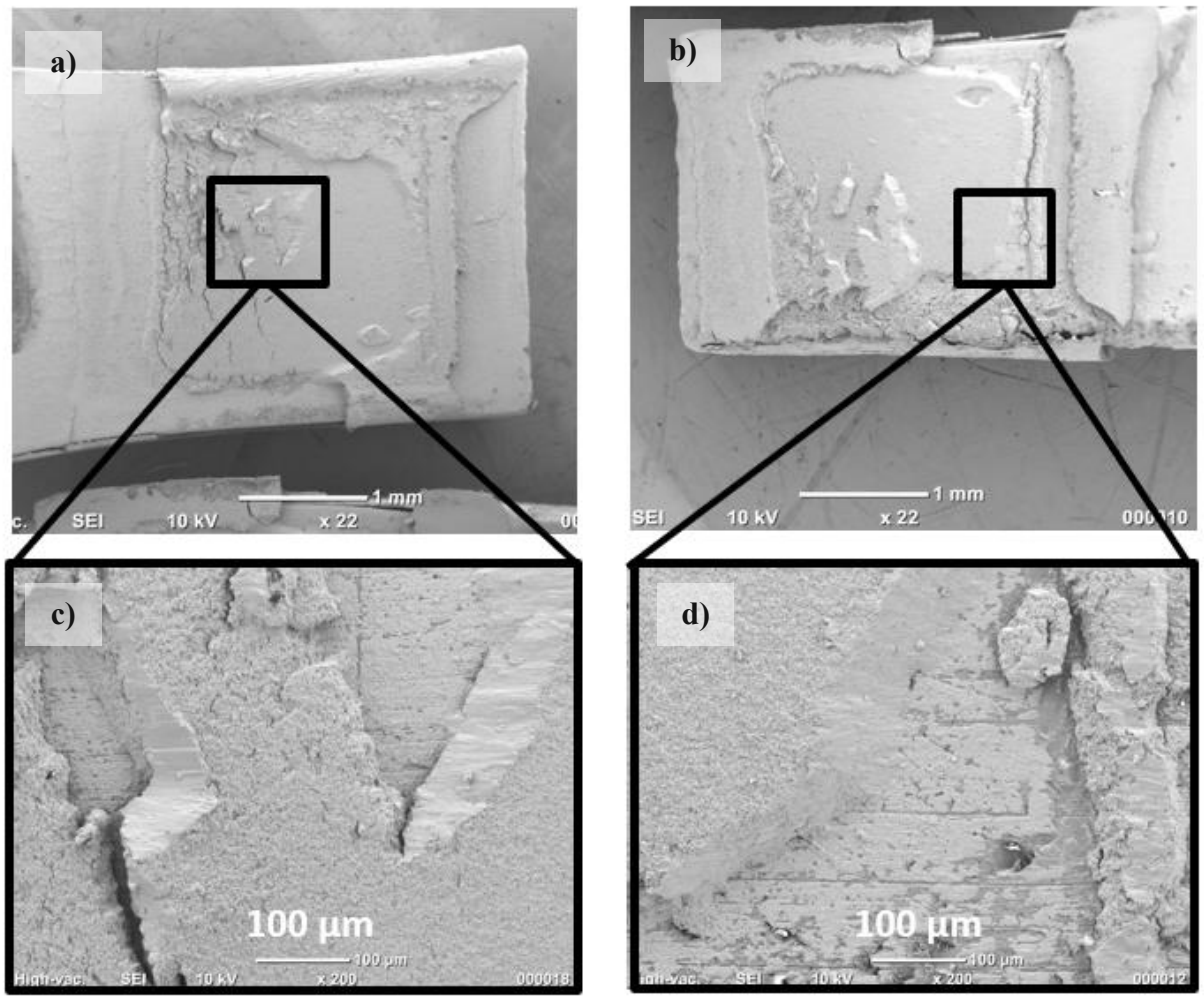

Fig. A.1.21: SEM images from both sides of the lap-joint (a-b) and fracture surfaces at a higher magnification (c-d).

A.2. MONOCHROMATIC DENSITY EVALUATION

This chapter intends to give the background information on the optical density evaluation of the sintered silver, and the derivation of the values discussed in chapter 5.

The sample series A, B, and C of the free-standing Ag-coupons and the sample specimen PTS of the lap-joints were investigated. The cross-sectional grinded area and fracture surface were analyzed. The digital image processing of the porous structure into black marked regions is based on the images taken with the electron microscope and was executed with the open source software ImageJ. The total monochromatic area of the pores is given in percentage compared to the whole zone. It should be noted that the automatic setting of the threshold for the conversion of the image from the 3D structured sintered silver into a black-and-white 2D image can lead to non-reliable evaluation of the surface area, as outlined in the figures below.

In the following sections the nomenclature used in previous chapters is maintained: 0-hour means the condition as sintered, Aged means thermal treated (at 250 °C).

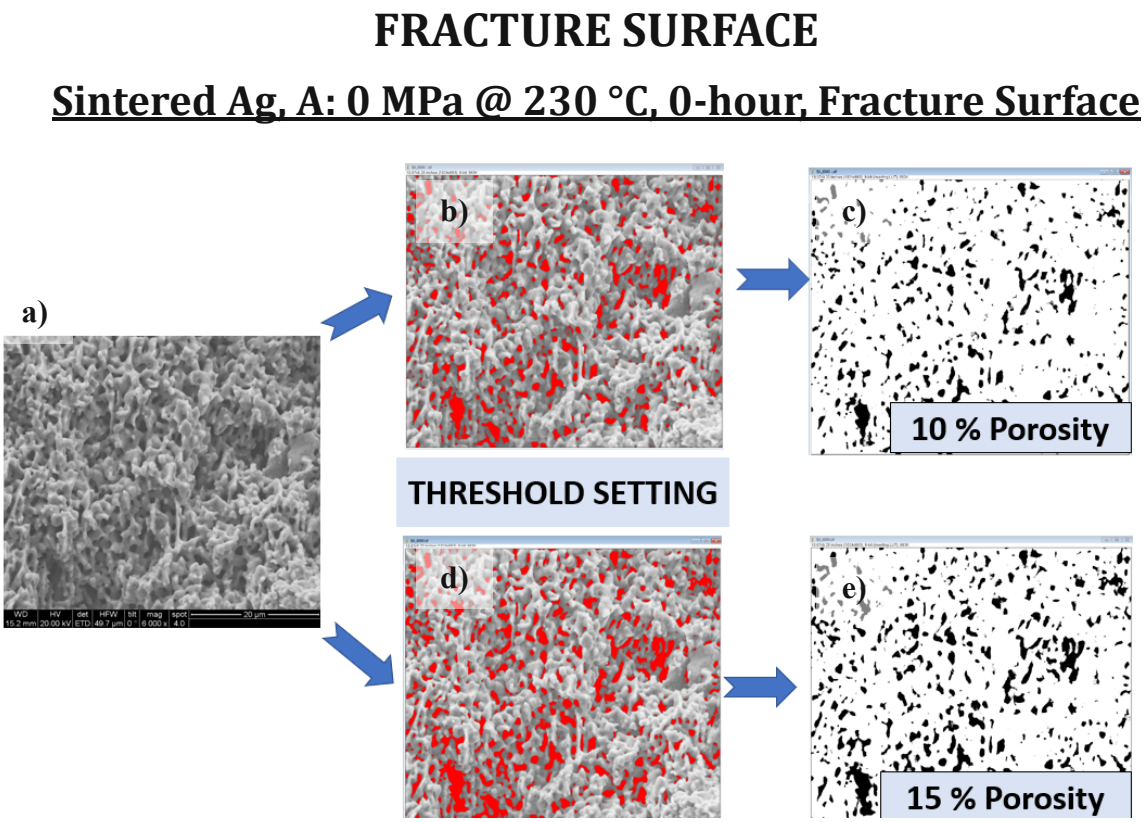

Fig. A.2.1: Cross-section of a free-standing Ag-coupon (type A) at a magnification of 6K (a) and varying threshold settings of the pores' boundaries (b, d) leading to different evaluation figures (c, e) for the density.

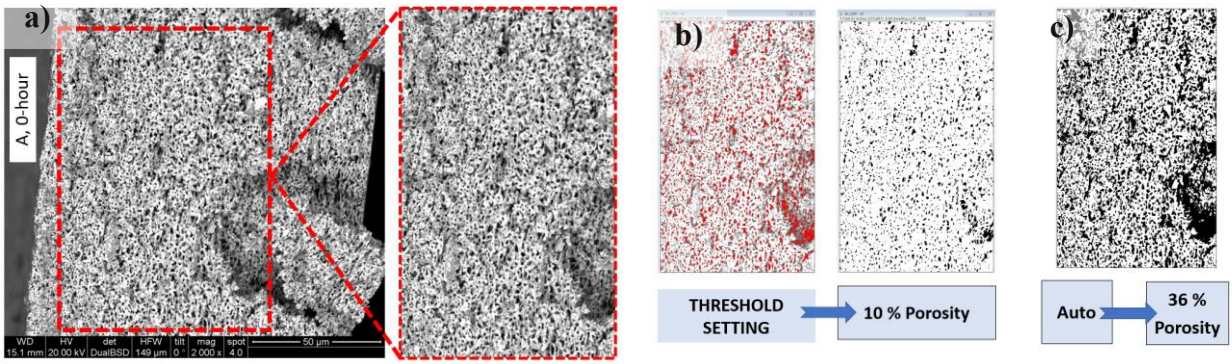

Fig. A.2.2: The porous microstructure of the sintered silver at a magnification of 2K (a) and manual threshold setting as red marked areas (b) vs. automatic recognition of the voids on the fracture surface (c) with the monochromatic mapping as black marked areas.

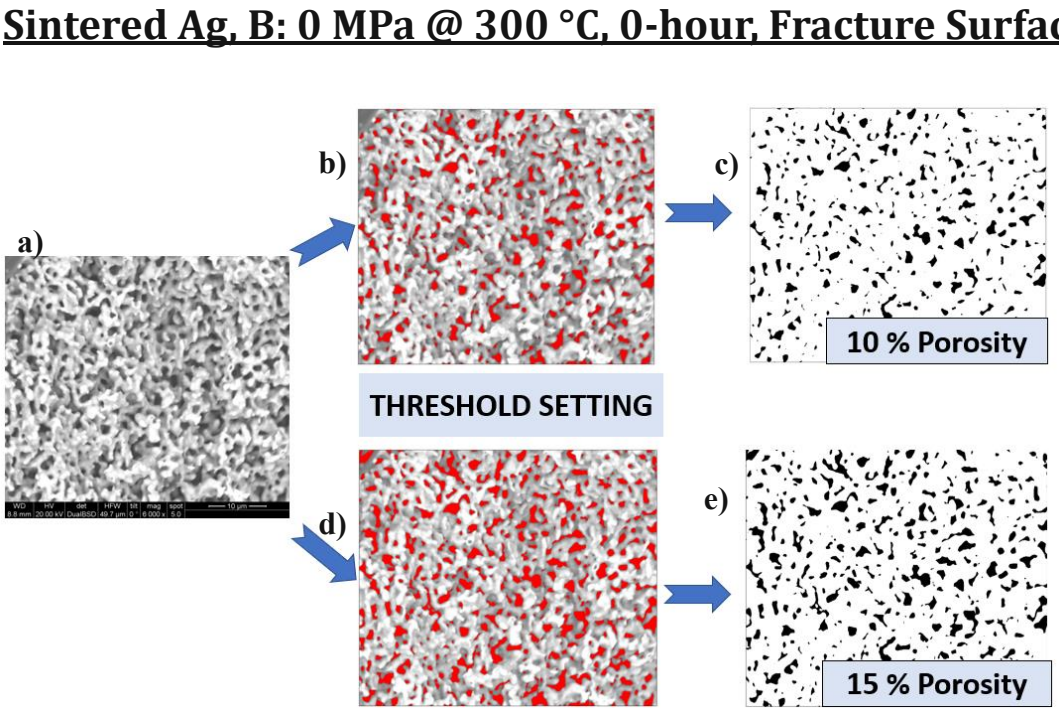

Fig. A.2.3: Cross-section of a free-standing Ag-coupon (type B) at a magnification of 6K (a) and varying threshold settings of the pores' boundaries (b, d) leading to different evaluation figures (c, e) for the density.

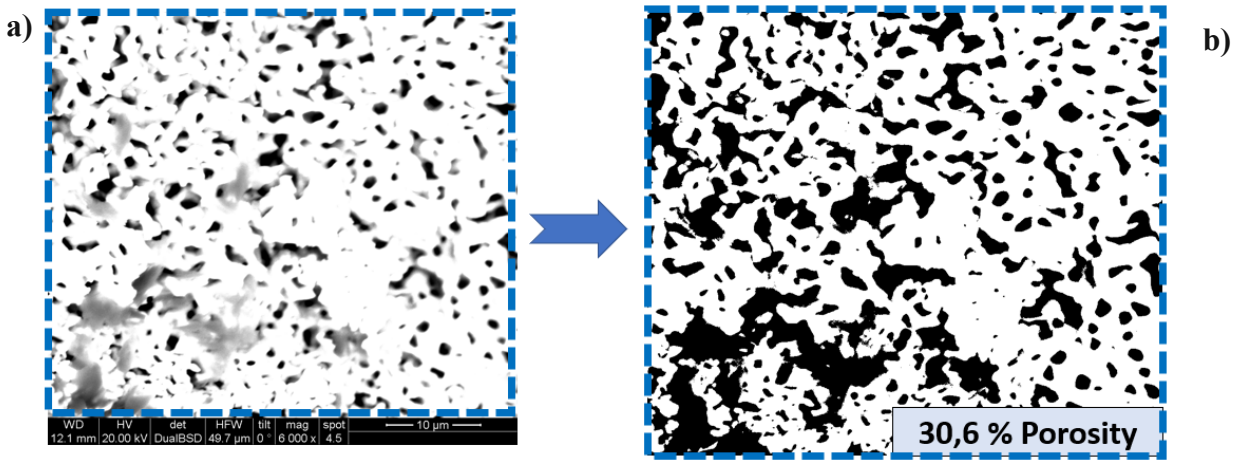

Fig. A.2.4: Cross-section of a free-standing Ag-coupon (type B) at a magnification of 6K (a) and automatic conversion by the software into a monochromatic image (b).

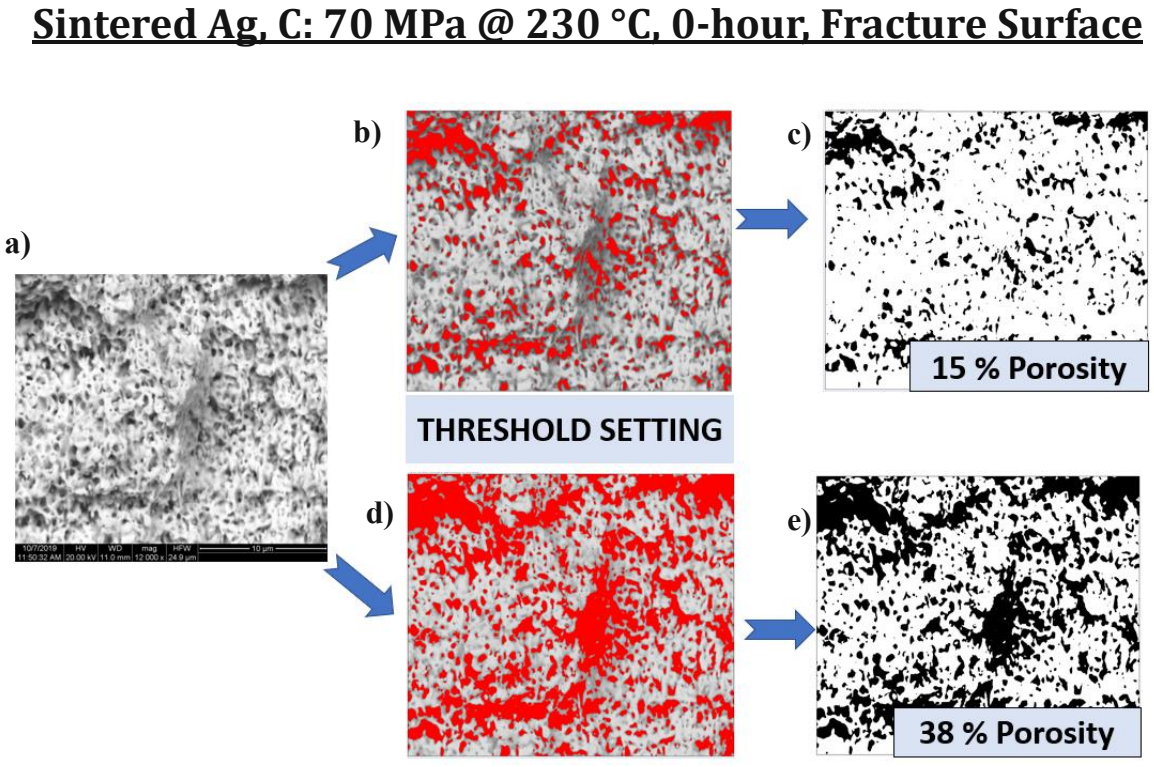

Fig. A.2.5: Cross-section of a free-standing Ag-coupon (type C) at a magnification of 12K (a) and varying threshold settings of the pores' boundaries (b, d) leading to different evaluation figures (c, e) for the density.

Sintered Ag, A-Aged, Fracture Surface (automatic)

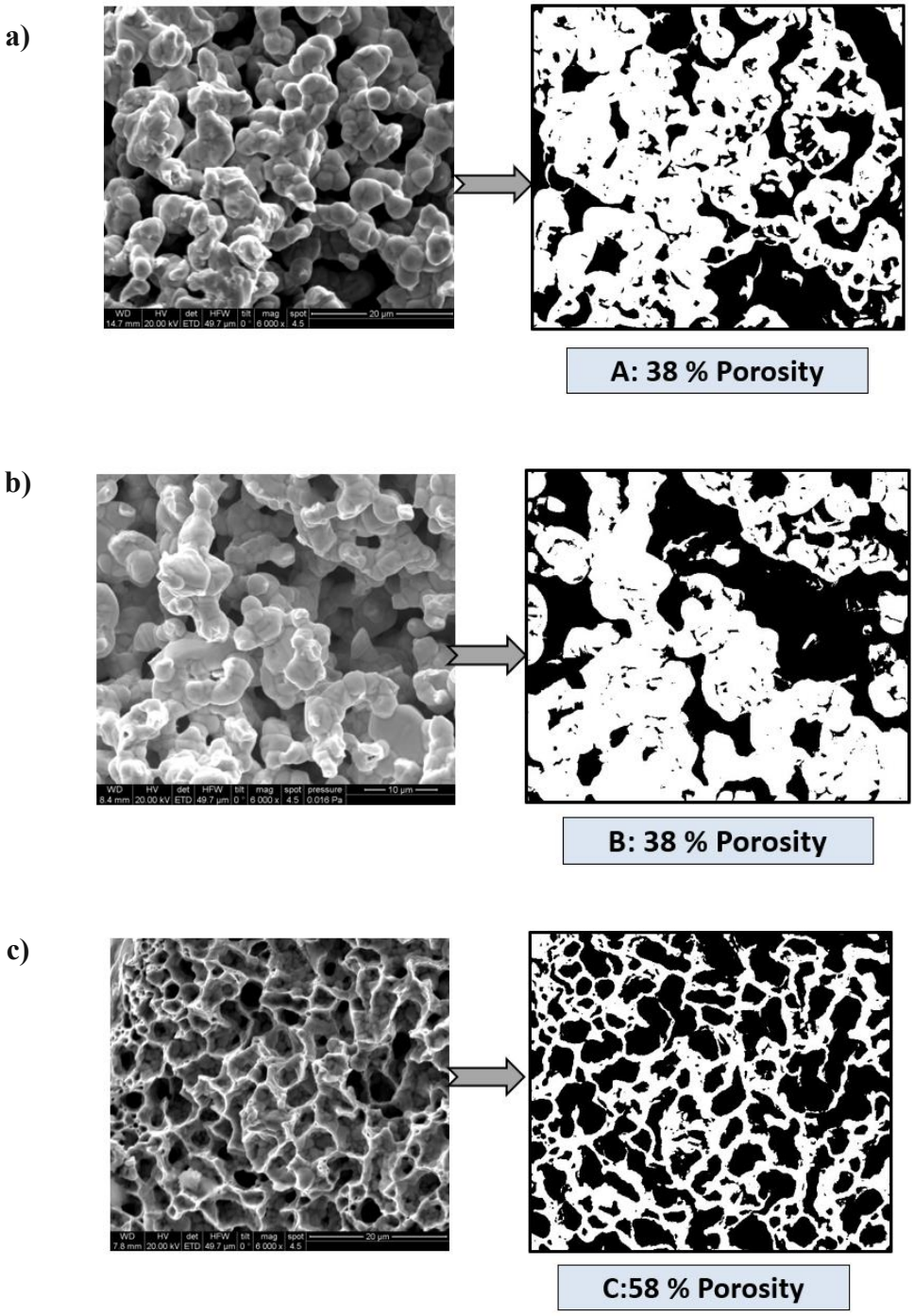

Fig. A.2.6: Automatic conversion of the fracture surface into monochromatic images for the sintered silver of type A (a), B (b) and C (c).
It should be noted that the automatic setting of the black-white threshold for the conversion can, and as shown in this case have led to a non-reliable density evaluation: the under pressure sintered dense samples of type C cannot have more porosity than the pressureless sintered types A and B.

PTS 153, 70 MPa @ 230 °C, 0-hour, Fracture Topography of Samples Ruptured in Liquid Nitrogen

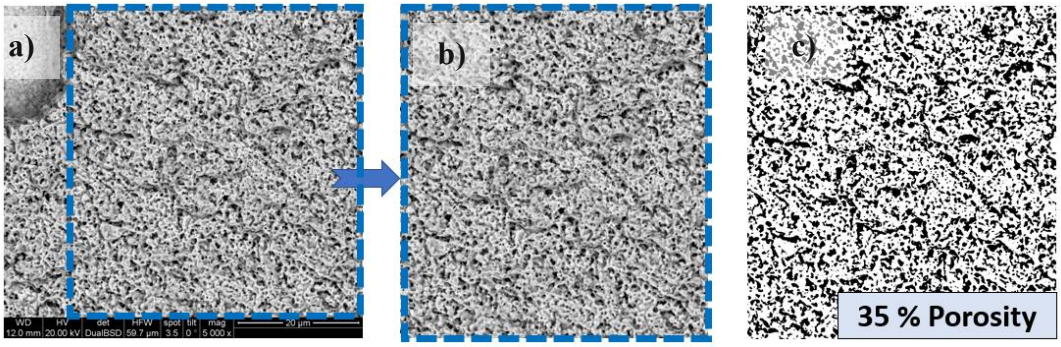

Fig. A.2.7: Fracture surface of the sintered Ag from a lap-joint at a magnification of 5K (a) and selection of the area (b) for automatic image conversion (c).

PTS 154, 70 MPa @ 230 °C, Aged, Fracture Topography of Samples Ruptured in Liquid Nitrogen

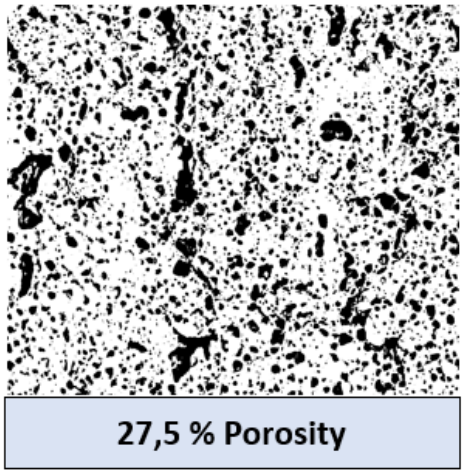

Fig. A.2.8: Monochromatic image of the Ag-surface from a lap-joint being fractured in liquid nitrogen to reveal the carrying neckings and surrounding pores.

GRINDED SURFACE and FIBed SECTION

0 MPa @ 230 °C, 0-hour, Grinded Surface

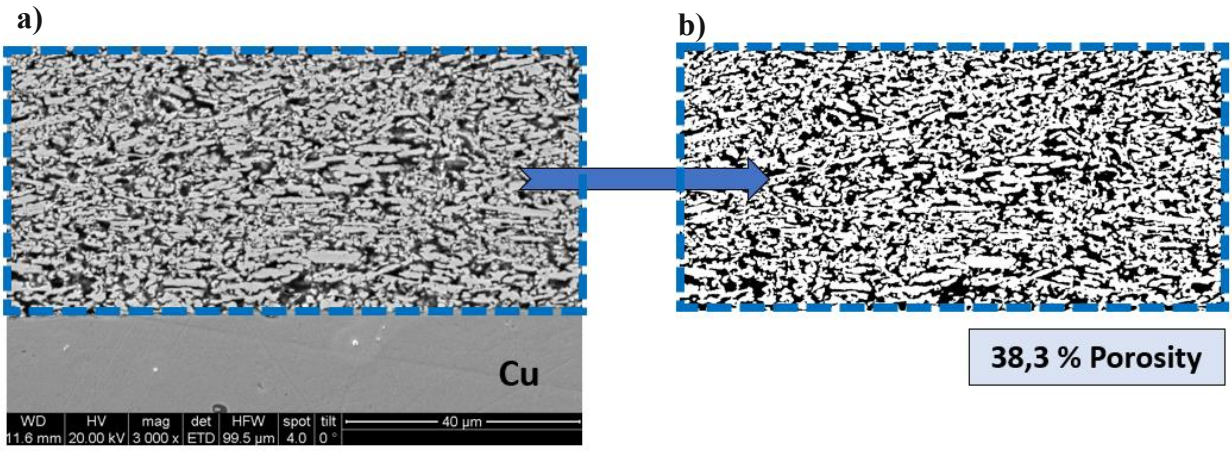

Fig. A.2.9: The selected area from the lap-joint at a magnification of 3K, showing the silver section which is sintered without pressure (a) and automatic image conversion leading to the marked porosity value (b).

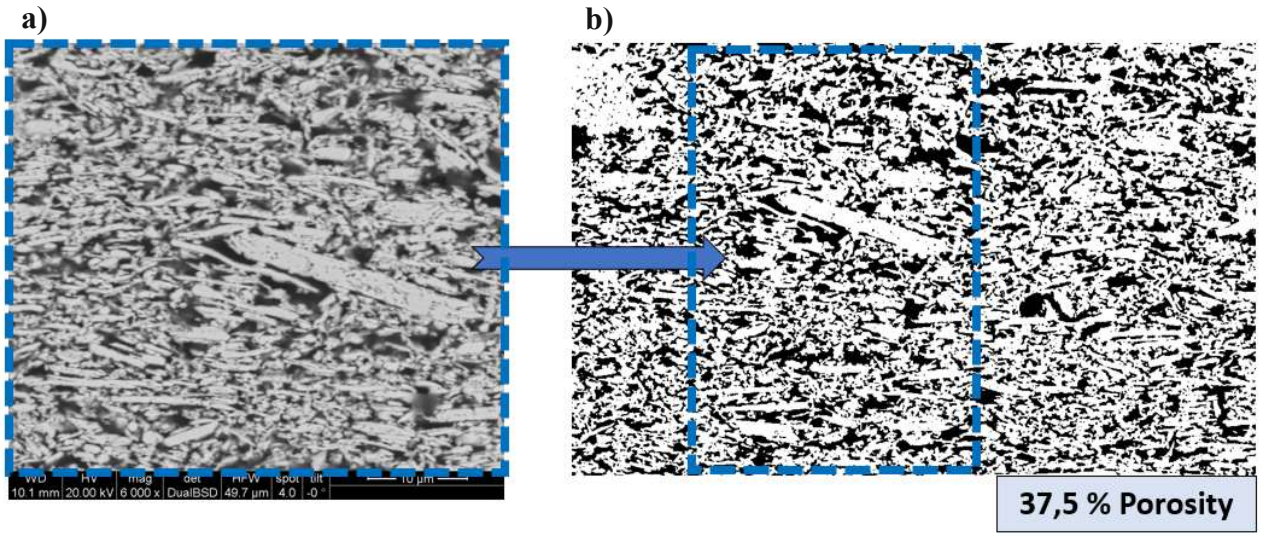

Fig. A.2.10: The selected area of the silver sintered without pressure at a magnification of 6K (a) and automatic porosity evaluation of the marked section (b).

70 MPa @ 230 °C, 0-hour, Grinded Surface

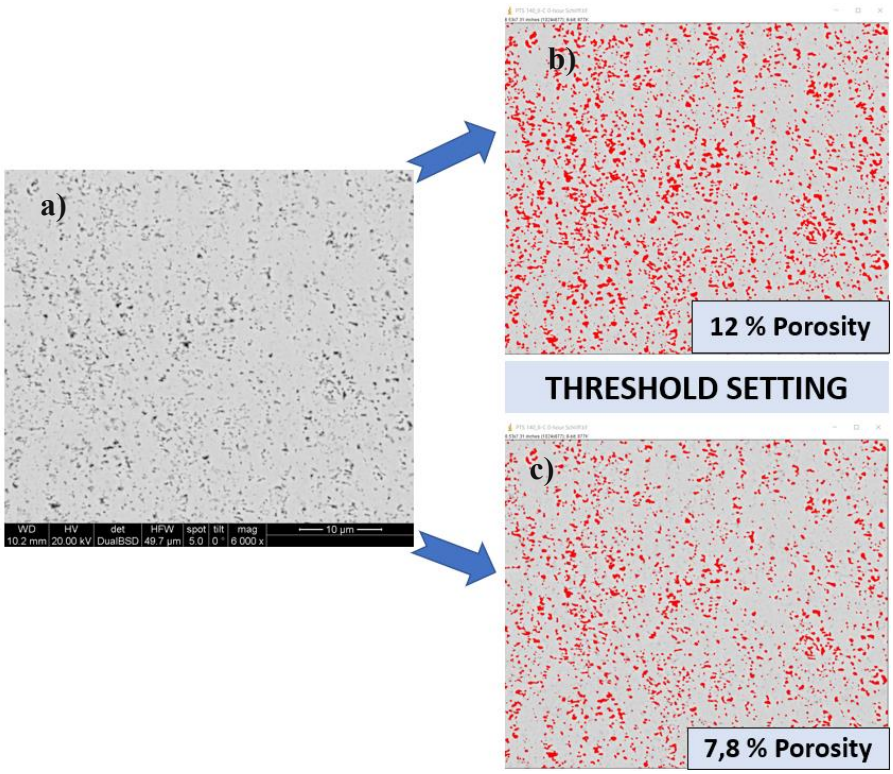

Fig. A.2.11: The grinded surface of the sintered silver in the dense middle zone of a lap-joint (a) and varying threshold settings for monochromatic conversion leading to different porosity values (b-c).

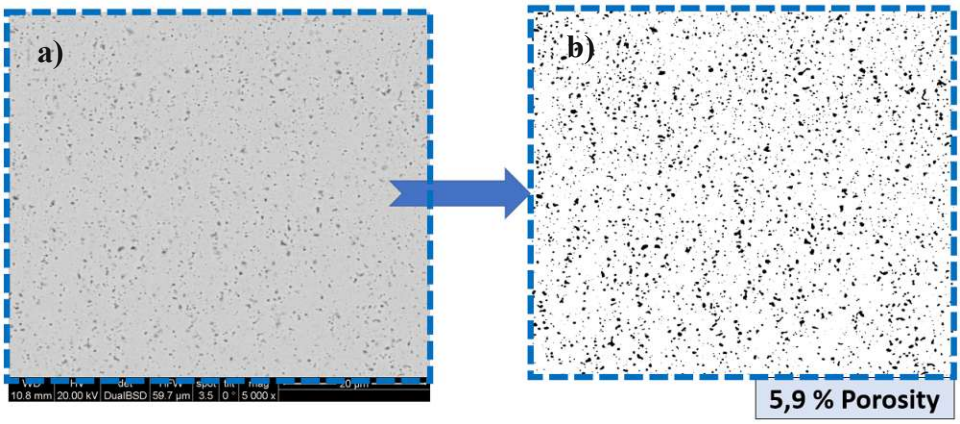

Fig. A.2.12: The grinded surface of the silver sintered under high pressure (a) and automatic porosity evaluation (b).

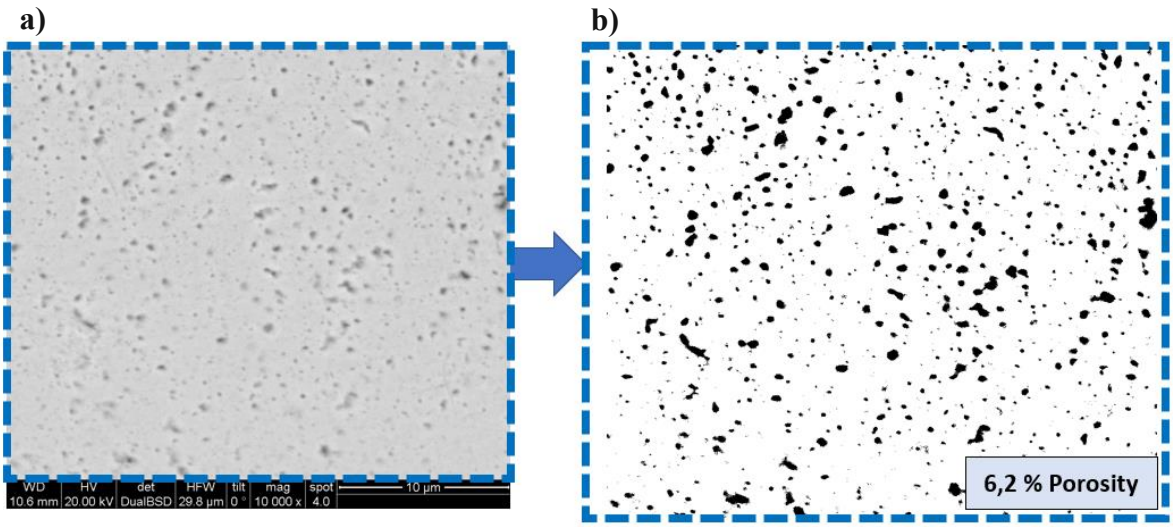

Fig. A.2.13: The grinded surface of the silver sintered under high pressure (a) and automatic porosity evaluation (b).

70 MPa @ 230 °C, 0-hour, FIBed Section

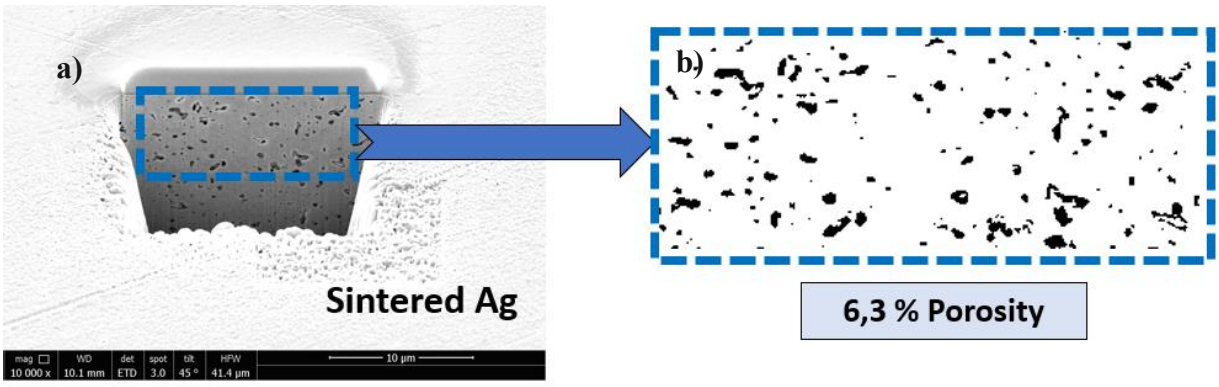

Fig. A.2.14: The FIBed section of the silver sintered under high pressure (a) and automatic porosity evaluation for the marked zone (b).

70 MPa @ 230 °C, G-Aged (250 hours), Grinded Surface and FIBed Section

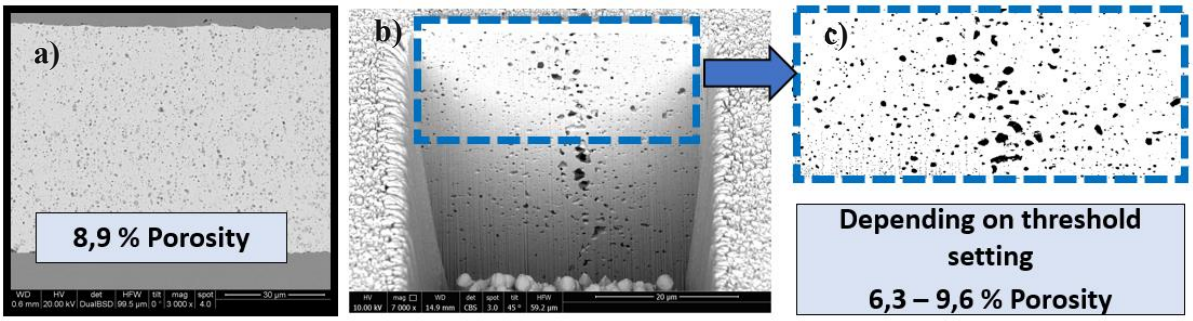

Fig. A.2.15: Cross-section of a thermal treated Cu-Ag-Cu lap-joint at the magnification of 3K (a), the FIBed section of the sintered silver from the middle zone (b) and automatic porosity evaluation for the marked area (c).

70 MPa @ 230 °C, A-Aged (250 hours), Grinded Surface and FIBed Section

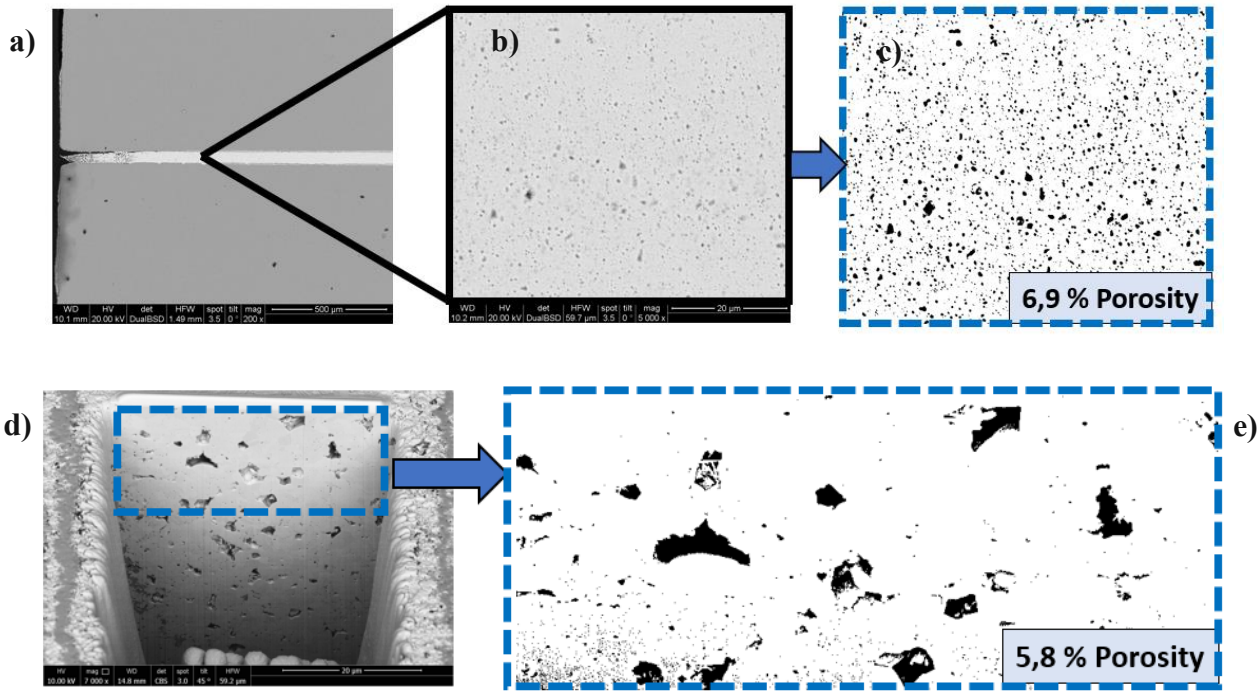

Fig. A.2.16: Cross-section of a thermal treated Cu-Ag-Cu lap-joint (a) with the sintered silver region (b) and the FIBed section of the sintered silver (d) with automatic porosity evaluation of the marked areas (c), (e).

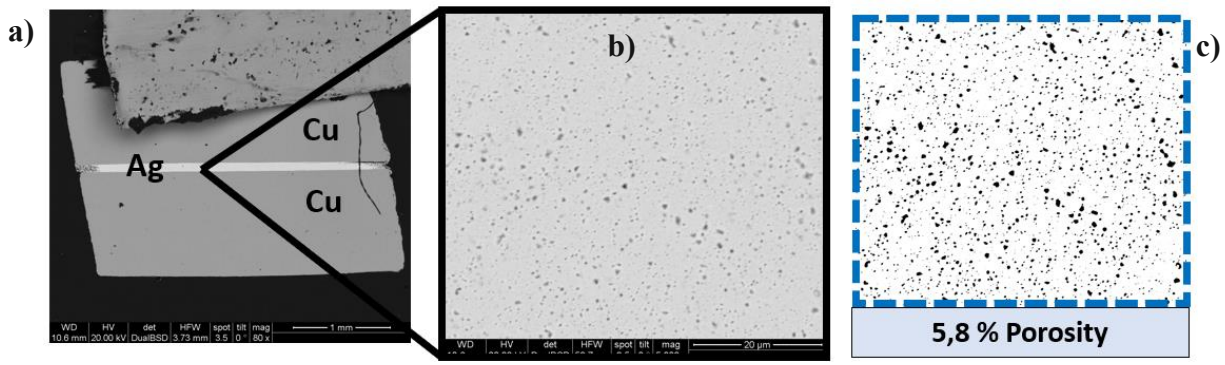

Fig. A.2.17: Cross-section of a thermal treated Cu-Ag-Cu lap-joint (a) with automatic porosity evaluation (c) of the under high pressure sintered silver (b).

70 MPa @ 230 °C, A-Aged (500 hours), Grinded Surface and FIBed Section

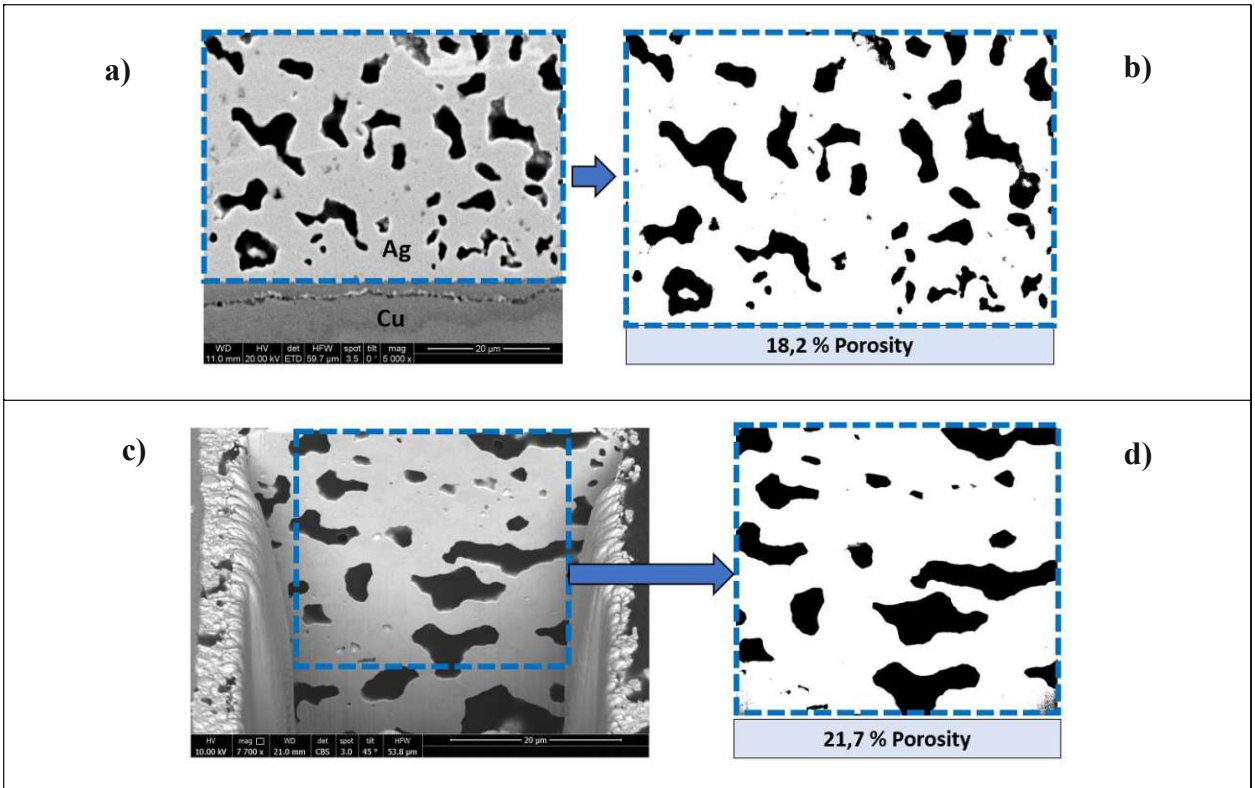

Fig. A.2.18: Grinded surface (a) and FIBed section of the sintered silver (c) from a lap-joint sample which is thermal treated in air ambient for 500 hours at 250 °C. Corresponding monochromatic images with automatic density evaluation values (b), (d).

A.3. NOMENCLATURE and ABBREVIATIONS

A-Aged	Thermally Aged in Air Ambient
CTE	Coefficient of Thermal Expansion
DC	Direct Current
DCB	Direct Copper Bonded
DTA	Differential Thermal Analysis
DUT	Device Under Test
EBSD	Electron Backscatter diffraction
EDX	Energy Dispersive X-ray
EELS	Electron Energy Loss Spectroscopy
EOL	End Of Life
FEM	Finite Element Method
FIB	Focused Ion Beam
G-Aged	Thermally Aged in Sealed Glass Tube
HCF	High Cycle Fatigue
IC	Integrated Circuit
IEEE	Institute of Electrical and Electronics Engineers
IGBT	Insulated Gate Bipolar Transistor
ISO	International Organization for Standardization
LCF	Low Cycle Fatigue
LED	Light Emitting Diode
LSE	Laser Speckle Extensometer
PCB	Printed Circuit Board
RoHS	Restriction of Certain Hazardous Substances
ROI	Region Of Interest
SEM	Scanning Electron Microscope
TEM	Transmission Electron Microscope
TGA	Thermo Gravimetric Analysis
UTS	Ultimate Tensile Strength
0-Hour	As Sintered, No Thermal Aging
2D	Two Dimensional
3PB	3-Point-Bending